

LRP 703/01

August 2001

**Fast transient transport phenomena
measured by soft X-ray emission in TCV
tokamak plasmas**

I. Furno

Che cos' è il genio?
É fantasia, intuizione, decisione e velocità di esecuzione

P. Noiret in "Amici Miei" by M. Monicelli

Version abrégée

La compréhension du transport de la chaleur et des particules dans les plasmas confinés magnétiquement en présence de chauffage additionnel est une question cruciale pour la réalisation d'un futur réacteur à fusion thermonucléaire. Le *Tokamak à Configuration Variable* (TCV) a créé des plasmas avec chauffage électronique cyclotronique (ECH) et entraînement de courant (ECCD) permettant d'étudier ce transport dans les plasmas ohmiques ainsi que avec de la puissance ECH/ECCD, en général en présence de dents de scie. Les dents de scie sont des relaxations périodiques du plasma qui sont observées dans beaucoup de tokamaks. Elles ont un impact important sur le confinement du plasma puisque, à chaque relaxation, de l'énergie et des particules sont expulsées de la région centrale du plasma, définie par le rayon d'inversion des dents de scie, conduisant à un aplatissement des profils centraux de température et de densité.

Un ensemble étendu de mesures a été utilisé pour caractériser les dents de scie sur une échelle temporelle plus rapide que la durée de ces relaxations, typiquement inférieure à 100 μ s sur TCV. Le système de tomographie de rayons x-mous de 200 canaux a été un instrument clé pour la mesure de l'émission des rayons x-mous du centre de plasma. Un système de bolométrie rapide a également été développé pour mesurer la puissance totale rayonnée permettant l'étude de phénomènes transitoires jusqu'à présent inaccessibles avec des techniques bolométriques habituelles.

Un certain nombre d'outils d'analyse ont été développés. En particulier, la décomposition en valeurs singulières de l'émissivité de rayons x-mous inversée tomographiquement a permis d'extraire la structure poloïdale des oscillations du plasma. Cette technique a également été employée pour déterminer le rayon d'inversion des dents de scie. Une méthode modifiée d'inversion d'Abel a été appliquée aux mesures interférométriques multicanal pour obtenir la densité locale des électrons.

Un but important de TCV est d'étudier les effets de la forme du plasma sur le confinement et la stabilité magnétohydrodynamique. Le comportement des dents de scie a été étudié dans une grande variété de décharges ohmiques à mode de bas confinement (mode L) comprenant des formes avec une élongation jusqu'à 2.54 et une triangularité entre -0.5 à +0.7. L'effet principal des dents de scie est la limitation de la concentration des profils de courant, de pression ou de température à l'intérieur du rayon d'inversion, au moins lorsque, comme dans les plasmas ohmiques en mode L de TCV, la période des dents de scie est plus courte que le temps effectif de diffusion résistive du courant et le temps de confinement de l'énergie. Nous observons que le rayon d'inversion normalisé est déterminé seulement par le profil normalisé du courant, indépendamment de la forme

du plasma et de la densité électronique. Ce résultat étend les précédentes lois d'échelle du rayon d'inversion dans les plasmas à section circulaire. Les profils de température et de densité électronique suivent également la même dépendance sur le profil de courant normalisé.

La description relativement simple de l'activité des dents de scie dans les plasmas ohmiques est compliquée en présence de puissance ECH et d'ECCD. On observe différents types de relaxation centrale selon la position de déposition de la puissance: (1) des dents de scie normales, c'est à dire triangulaires, semblables à celles observées en régime ohmique; (2) des dents de scie saturées en présence de déposition centrale de puissance ECH; (3) des dents de scie géantes et des oscillations humpback lorsque la puissance est déposée près du rayon d'inversion. Les nouvelles mesures à résolution temporelle élevée prouvent que la forme différente des dents de scie et leurs signatures dans les profils de température électronique sont compatibles avec une forte localisation du dépôt de puissance associée à la convection et le transfert de l'énergie thermique des électrons dûs à la présence d'un îlot magnétique. L'îlot produit un déplacement hélicoïdal de l'axe magnétique qui est décrit par une fonction de déplacement déduite des données expérimentales de la tomographie de rayon x-mous. Les différents types de dents de scie sont simulés en utilisant un modèle qui décrit l'évolution de la température électronique en présence des sources de chaleur localisées et d'un îlot magnétique.

Un phénomène intrigant de transport des particules, nommé 'pumpout', a été mis en relation au déplacement hélicoïdal de l'axe magnétique. On observe le pumpout dans plusieurs tokamaks et stellarators avec ECH et ECCD. Celui-ci conduit à une déplétion en particules au centre de plasma, produisant des dents de scie inversées sur la densité centrale et menant à des profils creux de densité en absence de dents de scie. Il semble que sur TCV ce phénomène est qualitativement conforme à la diffusion thermique néoclassique en présence de particules localement piégées, comme dans les stellarators.

En conclusion, l'activité des dents de scie dans les plasmas fortement façonnés dans le tokamak TCV a été étudiée en conditions ohmique et ECH. Cette étude a démontré que le transport de la chaleur et des particules est fortement influencé par la présence d'un îlot magnétique causant la perte de la configuration axisymétrique du tokamak idéal. Davantage de progrès pourraient être apportés par l'amélioration de la compréhension de la dynamique de l'îlot et du transport néoclassique dans une géométrie à trois dimensions.

Abstract

Understanding of heat and particle transport in magnetically confined plasmas in the presence of additional heating is a crucial issue for the feasibility of a future thermonuclear fusion reactor. The Tokamak à Configuration Variable (TCV) has been used with powerful electron cyclotron resonance heating (ECH) and current drive (ECCD) to study the physics of heat and particle transport in ohmic and ECH/ECCD plasmas in the presence of sawteeth. Sawteeth are periodic relaxations of the plasma which are observed in many tokamak experiments. They have a significant impact on plasma confinement since, at each relaxation event, energy and particles are expelled from the central region of the plasma, defined by the so-called sawtooth inversion radius, resulting in a flattening of central temperature and density profiles.

An extensive set of diagnostics was used to monitor sawteeth on a time scale faster than the duration of these relaxations (sawtooth crash) which is typically less than 100 μs on TCV. The 200 channel soft x-ray tomography system was the key diagnostic for measuring the soft x-ray emission from the plasma core. A fast bolometry system for measuring the total radiated power was also developed which allows the study of transient phenomena hitherto inaccessible with standard bolometric techniques. A number of analysis tools have been implemented. The singular value decomposition of the tomographically inverted soft x-ray emissivity has been used to extract the poloidal mode structure of plasma oscillations. This technique was also used to determine the sawtooth inversion radius of the soft x-ray emission. A modified Abel inversion method was also developed to obtain the local electron density from the multichord interferometer diagnostic.

An important goal of TCV is to investigate the effects of plasma shaping on confinement and magnetohydrodynamic stability. The behaviour of sawteeth has been studied in a wide variety of ohmic, low confinement mode (L-mode) discharges including plasma configurations with elongation up to 2.54 and triangularities in the range -0.5 to $+0.7$. The main effect of sawteeth is to limit the peaking of the current and pressure or temperature profiles inside the sawtooth inversion surface at least when, as in TCV ohmic L-mode plasmas, the sawtooth period is shorter than both the current resistive diffusion time and the energy confinement time. We observe that the normalised sawtooth inversion radius is determined solely by the normalised current profile independently of the poloidal cross section of the plasma and the electron density. This result extends previous scalings of the sawtooth inversion radius in circular plasma cross sections. Profiles of electron temperature and density also show the same dependence on the normalised current profile.

The relatively simple picture of sawtooth activity in ohmic plasmas is complicated in the presence of ECH and ECCD. Different types of central relaxation oscillations are observed depending on the location of the deposited power. Standard sawteeth, i.e. triangular sawteeth similar to ohmic sawteeth, and saturated sawteeth are observed with central ECH power deposition, while giant sawteeth and humpbacks occur when the power is deposited close to the sawtooth inversion radius. New measurements with high temporal resolution show that the different sawtooth shapes and their features in the electron temperature profiles are compatible with the strong localisation of the power deposition region and the advection and mixing of electron thermal energy associated with the presence of a magnetic island. The island produces a helical displacement of the magnetic axis which is described by a displacement function inferred from the experimental soft x-ray tomography data. The different types of sawteeth are simulated using a model which describes the evolution of the electron temperature in the presence of localised heat sources in the region of a magnetic island.

An intriguing particle transport phenomenon, termed 'pumpout', has been linked to the helical displacement of the magnetic axis. Pumpout is observed in several tokamak and stellarator experiments with ECH and ECCD. It results in the depletion of particles in the plasma centre, causing inverted sawteeth of the central density in sawtooth discharges and leading to hollow density profiles in the absence of sawteeth. Experimental evidence from TCV show that this phenomenon is qualitatively consistent with neoclassical thermodiffusion in the presence of locally trapped particles, as in stellarators.

In conclusion, sawtooth activity in strongly shaped plasmas in the TCV tokamak has been studied in ohmic and ECH conditions. This study has demonstrated that both heat and particle transport are strongly influenced by the presence of a magnetic island causing the loss of the axisymmetrical configuration of the ideal tokamak. Further progress will depend on improved understanding of island dynamics and neoclassical transport in a fully 3-dimensional geometry.

Table of Contents

Version abrégée	i
Abstract	iii
Table of Contents	v
1 INTRODUCTION	1
1.1 World energy demand and nuclear fusion	1
1.2 Magnetic confinement	3
1.3 The tokamak concept	4
1.4 Plasma heating	7
1.5 Fusion plant considerations	8
1.6 The TCV tokamak	11
1.6.1 TCV plasmas	12
1.6.2 Electron Cyclotron Heating system on TCV	14
1.7 Sawtooth activity in tokamak plasmas	15
1.8 Outline of the thesis	19
2 THEORY OF PLASMA EMISSION	23
2.1 Introduction	23
2.2 Radiation processes in plasmas	24
2.2.1 Bremsstrahlung radiation	24
2.2.2 Recombination radiation	26
2.2.3 Line radiation	29
2.3 Types of ionisation equilibrium	30

2.3.1	Local thermal equilibrium model	33
2.3.2	Steady state corona model	34
2.3.3	General time-dependent equilibrium model	37
2.4	Ionisation equilibrium codes	39
2.5	Conclusions	42
3	DIAGNOSTICS ON TCV	45
3.1	Soft x-ray tomographic system	45
3.1.1	Hardware set-up.	45
3.1.2	Detector array	47
3.1.3	Acquisition system.....	49
3.2	The tomographic problem	50
3.2.1	Definition of the problem	50
3.2.2	Tomographic inversion methods	54
3.2.2.1	Expansion in basis functions	54
3.2.2.2	Pixel methods	57
3.3	Other diagnostics	62
3.3.1	Interferometry	62
3.3.1.1	Modified Abel inversion of interferometer data	64
3.3.2	Magnetic measurements	68
3.3.3	Thomson scattering system	68
3.3.4	Soft x-ray photodiodes: MHD activity and central electron temperature	68
3.3.5	Metal foil bolometry	72
3.4	Fast AXUV bolometric system	72
3.4.1	Diagnostic design.....	73
3.4.2	Comparison of the AXUV system to standard bolometry.....	75
3.5	Concluding remarks	80

4	ANALYSIS OF SOFT X-RAY DATA	83
4.1	Singular value decomposition (SVD)	83
4.1.1	Some properties of the SVD	86
4.2	Application of the SVD to TCV soft x-ray signals	88
4.2.1	Mode identification	89
4.2.2	The determination of the sawtooth inversion radius	90
4.3	Determination of the effective ion charge from soft x-ray emission	94
5	DEPENDENCE OF SAWTOOTH INVERSION RADIUS AND PROFILES ON PLASMA PARAMETERS	99
5.1	Introduction	99
5.2	Experimental observations in ohmic TCV plasmas	100
5.3	Current profile modelling	104
5.4	Scaling of the sawtooth inversion radius	107
5.5	Profile shape dependence on plasma parameters	111
5.6	Experimental observations in ECH plasmas	115
5.7	Summary and discussion	119
6	SAWTOOTH ACTIVITY IN ECH PLASMAS IN TCV	123
6.1	Introduction	123
6.2	Experimental set-up	124
6.3	Experimental observations and heuristic understanding	125
6.3.1	Standard sawteeth	126
6.3.2	Saturated sawteeth	131
6.3.3	Heating close to the sawtooth inversion surface	134
6.4	Theoretical model	140
6.4.1	Derivation of the model	142
6.5	Simulation results	149

6.5.1	Standard sawtooth	150
6.5.2	Saturated sawtooth.....	153
6.5.3	Deposition close to the sawtooth inversion surface.....	153
6.6	Concluding remarks.....	155
7	PARTICLE TRANSPORT WITH HIGH POWER CENTRAL ECH AND ECCD	159
7.1	Introduction	159
7.2	Experimental observations.....	159
7.3	Discussion and interpretation.....	169
8	SUMMARY	175
	Acknowledgements	181
	Curriculum vitae	183

1 INTRODUCTION

1.1 World energy demand and nuclear fusion

Over the years, energy demand has increased in concert with the growth of the global economy and the world population. For instance, during the last decade, the world's consumption of primary energy, i.e. petroleum, natural gas, coal, and electric power (hydro, nuclear, geothermal, solar, and wind), increased from $3.5 \cdot 10^{20}$ J/year in 1988 to $4.0 \cdot 10^{20}$ J/year in 1997. Presently, the Far East (with 60% of the world population) consumes about 25% of the energy in the world, with an average annual growth of 5% over the 10 years [1]. The rest of the world has an annual growth of 1.5%. Recently, projections of energy consumption over the next few decades have been reported, predicting a substantial increase in energy use over the next 20 to 30 years [2]. Even though their scenarios incorporate slightly different assumptions about future population growth, future economic growth, changes in energy efficiency, innovations in technology, the sizes of known fuel reserves, and energy pricing, a demand rise of more than 50% is predicted by 2020 or a 34% to 44% rise in demand by 2010 by projection spanning a shorter time period. Despite rising levels of consumption, estimates of world energy reserves have increased significantly over the past 20 years. Present proven recoverable reserves are given in Table 1.1 together with an estimate of the period still available to use a specific source at the current rate of consumption [3].

Fuel	Proven Reserves	Years of use at current consumption
Coal	$1.0 \cdot 10^{12}$ tons	270
Crude Oil	$950 \cdot 10^9$ barrels	40-50
Natural gas	$120 \cdot 10^{12}$ m ³	60-70
Uranium	$2.0 \cdot 10^6$ tons	2400-3000

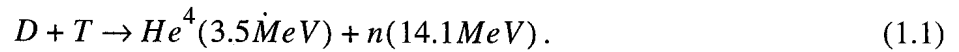
Table 1.1 Estimated world energy reserves

However, one has to be very careful with these numbers as there lie huge political and economic interests behind them which might lead to under- or over-estimates depending on who is providing the data. In addition, large parts of the world are not yet prospected, and this could result in future updates of these numbers. From this table is evident that the energy demand in the next few decades could be satisfied by burning fossil fuels which presently provide about 90% of the energy

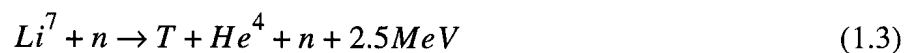
production. However, this option entails the risk of the release of gigantic quantities of CO₂ into the atmosphere. Although the consequences to our environment are difficult to predict, there is general consensus among the specialists that this will cause global warming of the planet by the greenhouse effect [4] with the possibility of dramatic climatic changes. In this context, other sources of energy will be needed to meet the long term world energy demand.

Large-scale conventional nuclear power plants are the most promising sources of primary electricity and their production is estimated to increase slightly in the next decade as existing and planned constructions come to completion. At the current consumption rate of nuclear electricity, assuming the use of advanced schemes, such as fast breeder reactors, there is about a 3000-year supply of uranium reserves to fuel these reactors (see Table 1.1). However, the exploitation of this technology suffers from the lack of acceptance due to the fears of accident and of the production of long half life time radioactive waste. However, new reactor concepts relying on passive safety systems could increase the acceptance by the general public.

Another option is controlled thermonuclear fusion which is regarded as one of the principal potential long-term, safe, and rather clean energy source. Among the different fusion reactions, the most promising one is the deuterium-tritium reaction. Deuterium and tritium nuclei fuse together to produce an alpha particle with a release of a neutron and the generation of 17.6 MeV of energy



The reason why this reaction is preferred to others is the very favourable rate coefficient ($\langle \sigma(\tilde{\nu})\nu \rangle \approx 10^{-22} m^3 s^{-1}$) at relatively low temperatures around 10 keV. The natural abundance of deuterium in hydrogen is 0.015% Mol or $4 \cdot 10^{16}$ kg of deuterium in the world ocean. In a D-T based reactor with a 30% of energy conversion efficiency this would allow for the production of 10^{22} GJ of electric power or $3 \cdot 10^{11}$ times the world annual consumption of total energy at the present rate. On the contrary, tritium, which is non-existent in nature (half-life of 12.3 years), can be bred directly from lithium using the neutron induced fusion reactions:



Since natural abundances for Li⁶ and Li⁷ are 7.4% and 92.6% respectively, lithium reserves on the

1.2 Magnetic confinement

land and in the oceans can potentially provide fuel for millions of years.

1.2 Magnetic confinement

At the temperatures required for fusion reactions to occur, the hydrogen isotopes are fully ionized. The electrostatic charge of the ions is neutralized by the presence of an equal number of electrons resulting in a neutral gas called plasma. To maintain this high temperature, the plasma has to be confined to minimise the contact with material walls. A possible method is to confine the plasma by means of a magnetic field. Owing to the Lorentz force, charged particles moving in a magnetic field B follow helical trajectories around magnetic field lines, as shown in Fig. 1.1.

The radial extent, or gyro-radius, of this trajectory for a particle of mass m_s and charge q_s , is

$$\rho_s = \frac{m_s v_{\perp}}{q_s B} \quad (1.4)$$

with v_{\perp} being the velocity perpendicular to the magnetic field.

The confinement in the direction perpendicular to the magnetic field is provided by the natural gyro-motion experienced by both ions and electrons of the plasma. However collisions among particles introduce a diffusive cross field transport and also give rise to a resistivity in the parallel direction. Confinement along the field lines is obtained by either squeezing the magnetic field at the edges of the device to produce a high field from which the particles are bounced (in the so-called mirror machines) or by using toroidal geometry to close the field lines back on themselves like in stellarators, reversed field pinch machines and tokamaks.

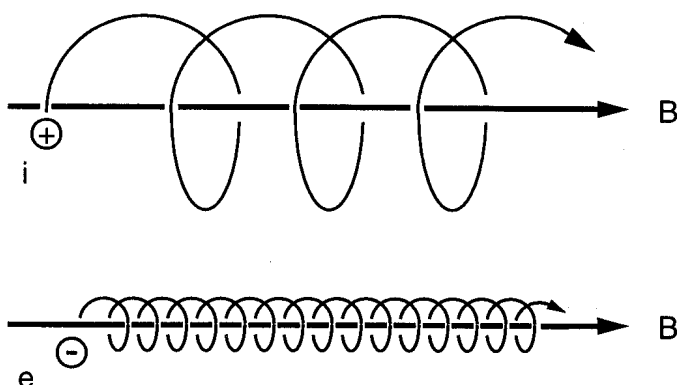


Fig. 1.1 Trajectories of charged particles in a homogeneous magnetic field B

1.3 The tokamak concept

In the Soviet Union in the early 1950s, the original idea of the tokamak configuration (from the Russian ‘Toroidalnaya Kamera Magnitnaya Katuschka’ meaning toroidal chamber with magnetic coils) was put forward by Igor Tamm and Andrei Sacharov. In 1968, the breakthrough of the tokamak concept was obtained by research performed under the leadership of Lev Artsimovich at the Kurchatov Institute where a tokamak achieved much higher plasma temperatures than were reached in any other magnetic configuration at that time [5]. In 1969, the confirmation of these results by a team from Culham Laboratory triggered a boom in tokamak experiments.

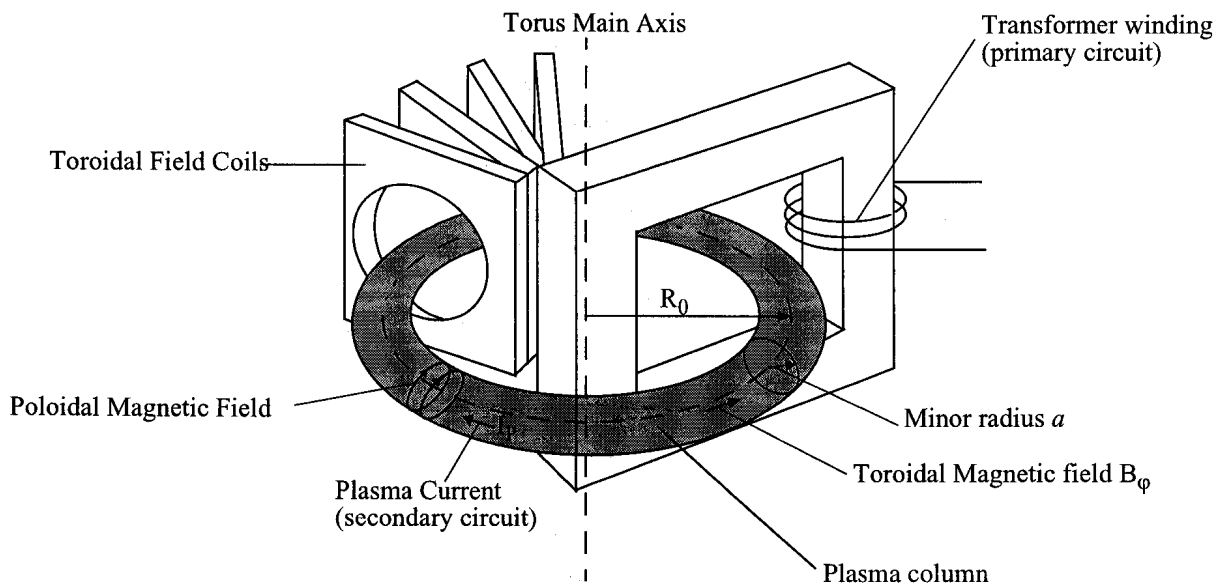


Fig. 1.2 Schematics of a tokamak. The plasma is the single secondary loop of a transformer. The induced plasma current is necessary for a stable confinement.

A toroidal plasma column with major radius R_0 and minor radius a is confined by means of an axisymmetric magnetic field \mathbf{B} . The main component of the magnetic field \mathbf{B} , which is typically of the order of 1-10 T, is a toroidal field B_ϕ produced by a number of external toroidal field coils, shown schematically in Fig. 1.2. A purely toroidal field cannot by itself confine the plasma: the toroidal curvature of the magnetic field lines, coupled with the radial decrease of B_ϕ , $B_\phi \approx B_{\phi 0} R_0 / R$ (being $B_{\phi 0}$ the vacuum magnetic field at the major radius) induces a vertical $\mathbf{B} \times \nabla B$ drift which displaces electrons and ions in opposite vertical directions. The space charge

1.3 The tokamak concept

separation generates an electric field E perpendicular to the toroidal magnetic field and the resulting $E \times B$ force drives the plasma particles outwards in major radius.

To avoid this, a weaker poloidal magnetic field B_p is applied producing magnetic field lines which have helical trajectory, so that each line passes the upper and the lower part of the torus, Fig. 1.3. Then, an averaging along the path of particles, which follow the magnetic field lines, leads to a cancelling of the vertical drift motion and avoids the build up of an electric field.

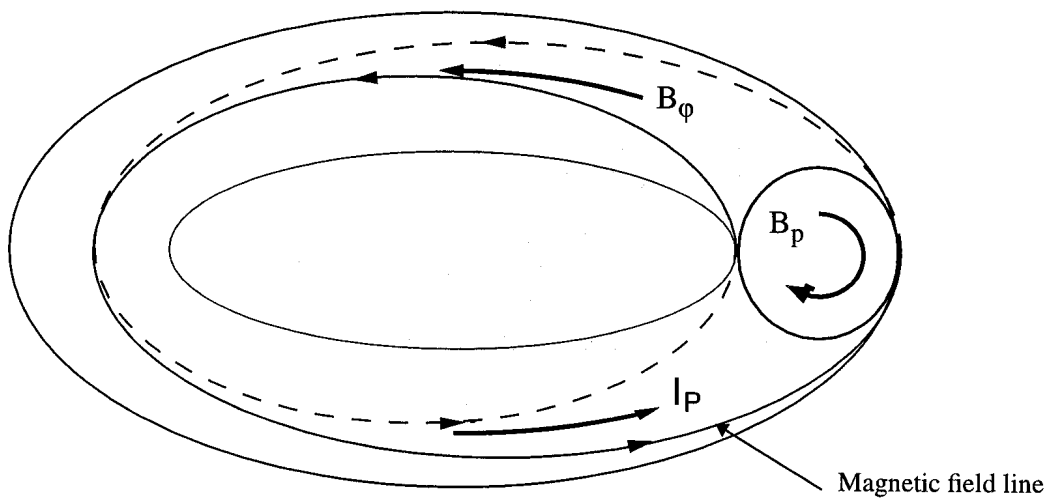


Fig. 1.3 A schematic of a magnetic field line on a $q = 2$ magnetic surface. The poloidal B_p and toroidal B_ϕ components of the magnetic field are also shown together with the plasma current I_p

The magnetic structure thus generated consists of an infinite set of nested magnetic surfaces, called *flux surfaces*. Magnetic field lines lie on these surfaces and satisfy the equation

$$\frac{Rd\phi}{ds} = \frac{B_\phi}{B_p} \quad (1.5)$$

where ds is the distance moved in the poloidal direction while moving through a toroidal angle $d\phi$. The pitch of the magnetic field lines is characterised by the *safety factor* q defined as

$$q = \frac{1}{2\pi} \oint \frac{B_\phi}{RB_p} ds \quad (1.6)$$

where the integral is carried out over a single poloidal circuit around the flux surface. For a large

aspect-ratio tokamak of circular cross section, Eq. (1.6) can be approximated as

$$q = \frac{r B_\phi}{R_0 B_p} \quad (1.7)$$

being r the minor radius of the flux surface. From Eq. (1.5), the safety factor specifies the number of complete toroidal circuits a magnetic field line makes before completing a single poloidal turn. If the safety factor is a rational number, $q = m/n$, the magnetic field line joins up on itself after m poloidal and n toroidal rotations around the torus and we refer to these magnetic field lines as *rational*, see Fig. 1.3.

A unique feature of the tokamak configuration is that the poloidal field is induced by the toroidal current I_p flowing in the plasma itself. The current is usually driven by a toroidal electric field induced by transformer action in which a central solenoid acts as primary turns and the plasma as a single secondary turn, Fig. 1.2. In addition to the toroidal and poloidal magnetic field components, a vertical magnetic field produced by external coils is also required to balance hoop forces arising from the radial decrease of the magnetic field pressure which tend to expand the plasma ring in minor radius.

Owing to the plasma resistivity caused by electron-ion collisions, the toroidal current induces ohmic heating of density

$$P_\Omega = \eta j^2 \quad (1.8)$$

where η is the resistivity of the plasma and j the current density. The necessity of avoiding disruptions imposes a constraint on the edge safety factor q_a which, for a circular plasma, is approximated by $q_a > 2$. Thus, from Eq. (1.7) $q_a = aB_\phi/R_0B_{pa}$ and from Ampere's law $B_{pa} = \mu_0 I/2\pi a$, the average current density must satisfy

$$\langle j \rangle < \frac{1}{\mu_0} \frac{B_T}{R} \quad (1.9)$$

where the brackets $\langle \rangle$ denote average over the entire plasma volume.

One constraint to the local ohmic heating, which is not strictly limited by the inequality in Eq. (1.8), arises from sawtooth activity in the central plasma region. This instability, described in detail later, tends to limit the central current density $j_0 = 2B_{\phi 0}/R_0 q_0 \mu_0$ in such a way that the safety factor on axis, q_0 , remains very close to unity. The second limitation to the local ohmic heating arises

1.4 Plasma heating

from the plasma resistivity which is mainly proportional to $T_e^{-3/2}$.

The rapid decrease of the resistivity with increasing temperatures makes the ohmic heating ineffective at temperatures above a few keV and hence additional heating methods are necessary to reach conditions required for fusion to occur.

1.4 Plasma heating

One auxiliary heating method is the electron cyclotron heating (ECH) which consists of injecting into the plasma a microwave beam with a frequency $\omega = n\omega_{ce}$, where $\omega_{ce} = eB/m_e$ is the fundamental electron cyclotron frequency and n is the harmonic number. The electrons increase their perpendicular energy through collisionless resonance absorption of the wave, while the ions are heated collisionally by the electrons. For applications in tokamak plasmas, a major advantage of the ECH is that the wave couples directly to the vacuum electro-magnetic field allowing the antenna to be located far from the plasma boundary. Particular attention must be paid to the wave polarisation in order to couple to the specific required plasma mode. For a wave that propagates perpendicular to the magnetic field ($\mathbf{k} \perp \mathbf{B}$), two different modes of propagation can be distinguished: the *ordinary* mode (O-mode), in which the incident wave electric field is parallel to the background magnetic field ($\mathbf{E} \parallel \mathbf{B}$), and the *extraordinary* mode (X-mode), where it lies in a plane perpendicular to the background magnetic field ($\mathbf{E} \perp \mathbf{B}$).

In Fig. 1.4, the *Clemmow-Mullaly-Allis* (CMA) diagram for a cold plasma illustrates the propagation and absorption properties of these two modes. In this diagram, the abscissa represents essentially the density and the ordinate the magnetic field. The propagation of these two modes is described by their index of refraction:

$$N_{ord}^2 = 1 - (\omega_p/\omega)^2 \quad (1.10)$$

$$N_{ex}^2 = (1 - (\omega_p/\omega)^2 - \omega_e/\omega) \frac{1 - (\omega_p/\omega)^2 + \omega_e/\omega}{1 - (\omega_p/\omega)^2 - (\omega_e/\omega)^2} \quad (1.11)$$

where $\omega_p^2 = n_e e^2 / (m_e \epsilon_0)$ is the electron plasma frequency. If the refractive index becomes zero the wave cannot propagate any further in the plasma and is reflected. This limit is known as *cut-off condition* and depends on both the wave harmonic number and its mode of propagation. For an O-mode wave, such a cut-off occurs for $\omega = \omega_p$ limiting the accessibility to densities below a critical density, $n_{e, cutoff}$, corresponding to the area on the left of the O-mode cut-off in the CMA

diagram. The X-mode wave is reflected at the right-hand cut-off $\omega = \omega_e/2 + [(\omega_e/2)^2 + \omega_p^2]^{1/2}$ and left-hand cut-off $\omega = -\omega_e/2 + [(\omega_e/2)^2 + \omega_p^2]^{1/2}$, which are both indicated in Fig. 1.4. For heating at the second harmonic, the cut-off condition is given by $\omega = \sqrt{2}\omega_p$ which corresponds to half of the cut-off density for the X-mode heating at the second harmonic.

In the cold plasma description, the O-mode does not possess a resonance whereas the X-mode has a resonance at the upper hybrid frequency $\omega_{UH} = [\omega_e^2 + \omega_p^2]^{1/2}$. However, both modes have resonances at the cyclotron frequency and higher harmonics if hot plasma effects are taken into account. The wave absorption at these resonances depends on the mode, the mode and the harmonic number. Generally, the second harmonic of the extraordinary mode (X2-mode) is absorbed best whereas the absorption properties of O1-, X1-, O2-, and X3-mode are somewhat weaker.

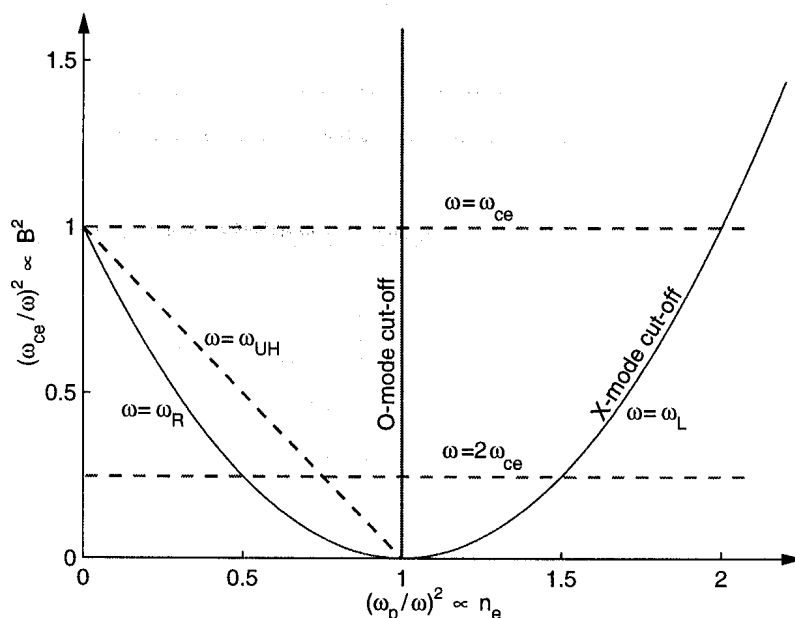


Fig. 1.4 CMA Diagram for electron cyclotron waves. Cut-offs (solid lines) and resonances (dashed lines) are shown for the ordinary and extraordinary mode.

1.5 Fusion plant considerations

In a fusion power plant, the temperature of the D-T mixture should be maintained by the energy transfer of the 3.5 MeV α -particles created by the fusion reaction of Eq. (1.1). The charged α -particles are confined by the magnetic field and can transfer their energy via Coulomb collisions.

1.5 Fusion plant considerations

It is important that they are sufficiently well confined to equilibrate their energy with the plasma bulk before leaving the plasma. In contrast to the α -particles, the neutrons leave the plasma without further interaction. They are absorbed in a blanket surrounding the reactor vessel. A blanket composed of a lithium compound can allow the breeding of tritium according to the reactions given in Eqs. (1.2), (1.3) and fuel the reactor. The heat is carried away by a suitable coolant and provides the power output for the generation of electrical power.

A power balance gives an estimate for the plasma parameters required for a fusion power plant. The reaction rate per unit volume of a 50%-50% D-T mixture, R_{D-T} , is calculated by averaging the cross section of the D-T reaction, σ_{D-T} , over a thermal velocity distribution

$$R_{D-T} = \frac{1}{4}n^2 \langle \sigma_{D-T} v \rangle_v \quad (1.12)$$

with n being the total ion density and $\langle \rangle_v$ denoting the average over the velocity distribution. The reaction rate determines the α -particle heating power density, $p_\alpha = R_{D-T} E_\alpha$, where E_α is the kinetic energy of a generated α -particle. The energy loss can be expressed by an energy confinement time τ_E

$$P_{loss} = \frac{W}{\tau_E} = \frac{\int 3nT dV}{\tau_E} \quad (1.13)$$

In Eq. (1.13), the total energy density W is expressed by the volume integral over the comprised energy density of $\frac{1}{2}nT$ per degree of freedom of the ions and of the electrons. The power balance of the whole plasma, taking into account an auxiliary heating power P_{aux} reads

$$\int \frac{1}{4}n^2 \langle \sigma_{D-T} v \rangle_v E_\alpha dV + P_{aux} = \frac{\int 3nT dV}{\tau_E} \quad (1.14)$$

If the plasma temperature can be sustained by the α -particle heating alone, the plasma ignites. Using Eq. (1.14) and assuming constant density and temperature for simplicity, a condition for ignition can be derived,

$$n\tau_E > \frac{12}{\langle \sigma_{D-T} v \rangle_v} \frac{T}{E_\alpha} \quad (1.15)$$

The condition for the product of density and confinement time has a broad minimum at 30 keV [6].

The use of this minimum value of $n\tau_E$ leads to the ignition criterion for the triple product

$$\hat{n}\hat{T}\hat{\tau}_E \geq 5 \times 10^{21} \text{ m}^{-3} \text{ keV s.} \quad (1.16)$$

Present research on magnetic fusion aims at satisfying the requirement given in Eq. (1.16) for the triple product. The achieved value of this parameter has improved by seven order of magnitude over the past 45 years and is on the verge of reactor conditions.

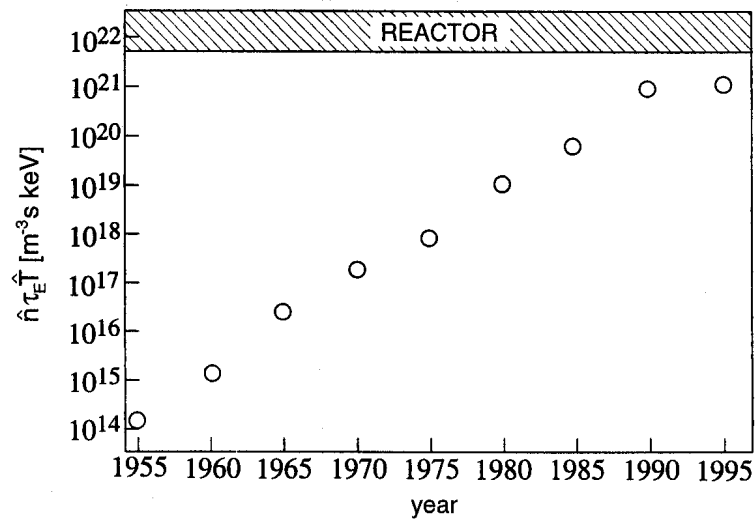


Fig. 1.5 Progress in increasing the triple product $\hat{n}\hat{T}\hat{\tau}_E$, leading towards reactor conditions.

1.6 The TCV tokamak

1.6 The TCV tokamak

The Tokamak à Configuration Variable (TCV) at the Centre de Recherche en Physique des Plasmas (CRPP) is a compact, medium size tokamak designed to investigate the effects of plasma shaping on confinement and stability [7]. The basic design parameters of the machine are listed in Table 1.2 and a schematic of the tokamak is shown in Fig. 1.6.

Parameters	Symbol	Value
Major radius	R_0	0.88 m
Minor radius	a	0.25 m
Nominal aspect ratio	$\varepsilon = R_0/a$	≈ 3.5
Vacuum vessel elongation	κ_{TCV}	2.9
Maximum plasma current	I_P	1.2 MA
Maximum central toroidal field	B_0	1.54 T
Maximum loop voltage	V_{loop}	10 V
Discharge duration		< 4 s

Table 1.2 Main TCV machine parameters

Parameters	Symbol	Value
Central electron density	n_{e0}	$1 - 20 \times 10^{19} \text{ m}^{-3}$
Central electron temperature	T_{e0}	< 1 keV (ohmic) $\leq 10 \text{ keV}$ (ECH)
Central ion temperature	T_{i0}	< 800 eV (ohmic) < 500 eV (ECH)
Electron cyclotron frequency	$f_{ce} = eB/(2\pi m_e)$	$\approx 41 \text{ GHz}$
Elongation at the edge	κ_a	1 - 2.82
Triangularity at the edge	δ_a	(-0.8) - (+0.9)

Table 1.3 Typical parameters in ohmic and ECH TCV plasmas

TCV is equipped with an air core transformer and the toroidal field is produced by 16 toroidal field coils which are connected in series. The flexibility of TCV for producing diverted and limited highly shaped plasmas is due to its unique shaping control system which uses active feedback coils

both outside and inside the vacuum vessel, Fig. 1.6. The 16 external coils are mounted in two vertical stacks on both external sides of the vacuum vessel and are driven by slow power supply. The fast internal coils (time response ≈ 0.1 ms) are placed behind the graphite tiles and allow the stabilisation of highly elongated plasmas [7].

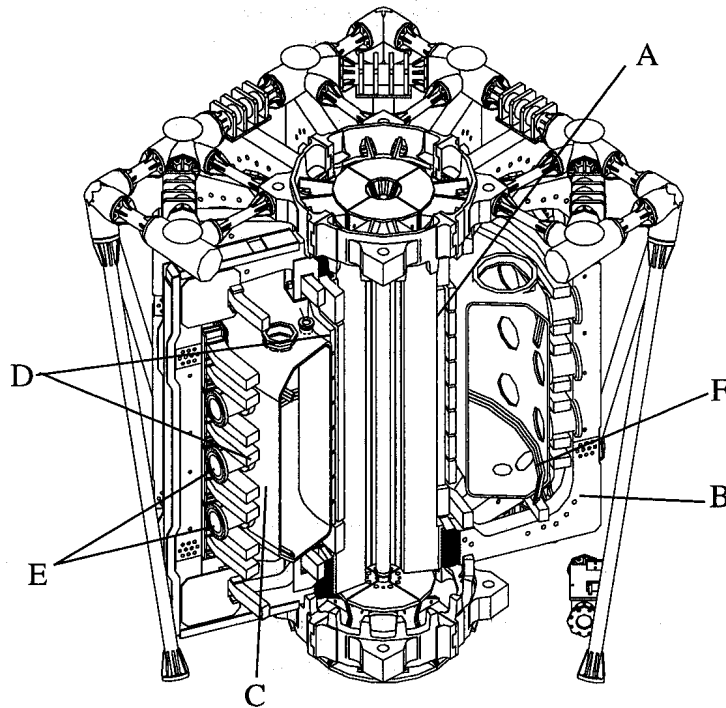


Fig. 1.6 Schematic view of the TCV tokamak: (A) the ohmic transformer coils, (B) the toroidal field coils, (C) the vacuum vessel, (D) the shaping coils, (E) observation ports and (F) internal fast shaping coils.

1.6.1 TCV plasmas

Since the beginning of the operation in November 1992, TCV has produced a wide range of limited and various diverted configurations, among them limited, single (SND) and double null diverted (DND) discharges. A selection of plasma shapes is shown in Fig. 1.7. To date, ohmic L-modes (low confinement mode) and H-mode (high confinement mode) have been obtained in both limited and diverted configurations. Plasma currents up to 1 MA have been sustained, Fig. 1.7(e), as well as up to 210kA of purely non-inductive current, Fig. 1.7(f). The plasma shapes span a wide parameters

1.6 The TCV tokamak

range with triangularities from -0.8 to 0.9 and elongations from 1 to 2.82 , Fig. 1.7(i-k). Also more exotic plasmas were produced like rectangular shapes and doublets. A list of typical values of various plasma parameters is given in Table 1.3.

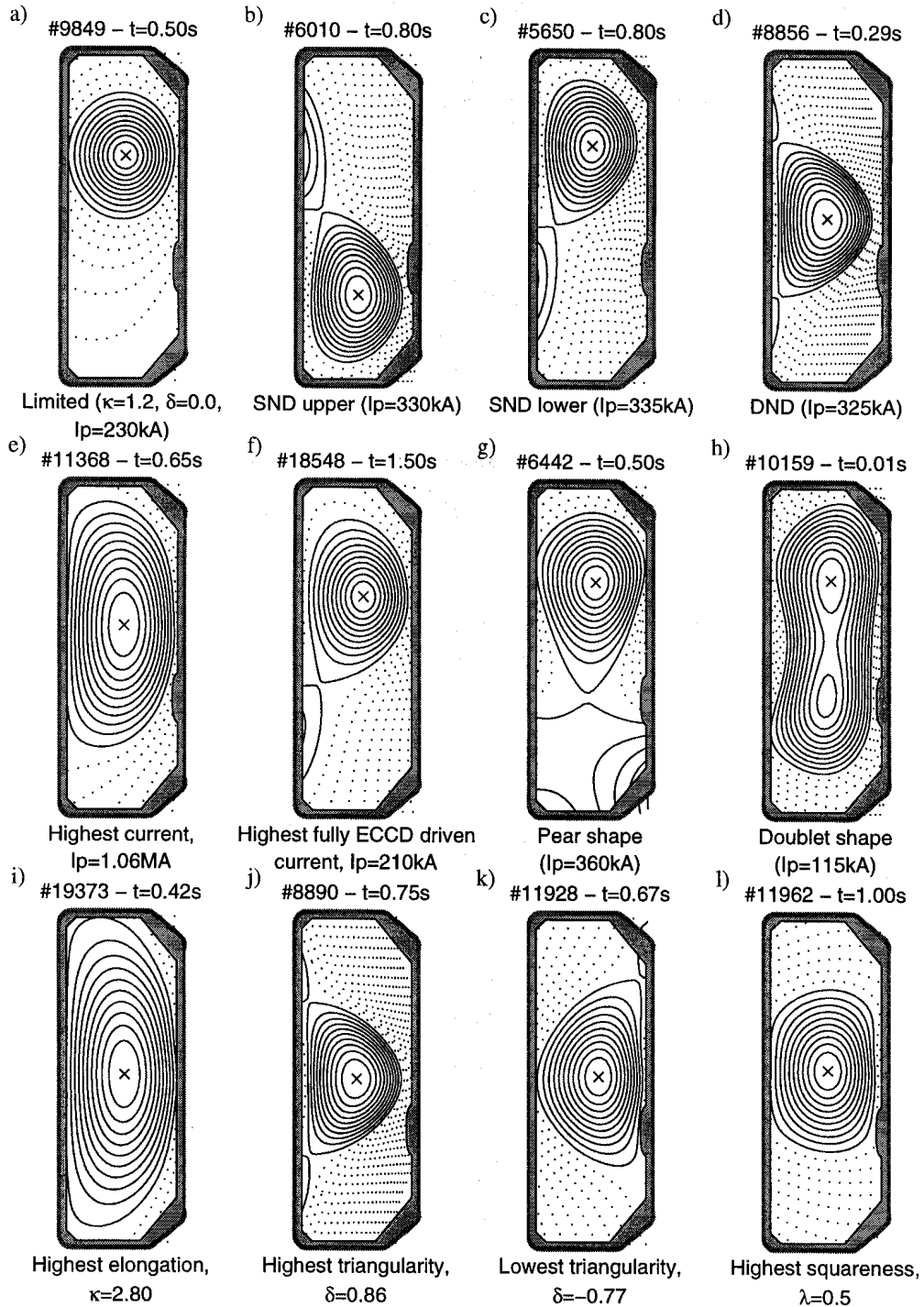


Fig. 1.7 Various plasma configurations and shapes produced in the TCV tokamak.

1.6.2 Electron Cyclotron Heating system on TCV

TCV is equipped with a very flexible electron cyclotron heating (ECH) and electron cyclotron current drive (ECCD) system which was designed to provide a maximum coverage of its wide variety of plasma shapes [8]. The system consists of six gyrotrons operating at the second harmonic frequency, $f_{2ce} = 82.7$ GHz, and three gyrotrons at the third harmonic frequency, $f_{3ce} = 118$ GHz. The nominal power for each 82.7GHz gyrotron is 465 kW and for each 118 GHz gyrotron is 480 kW, resulting in a total of radio frequency power of 4.2 MW for a maximum pulse length of 2 s. The gyrotrons are grouped in clusters of three with separate power supply for each cluster. Each gyrotron couples the electron cyclotron beam to an evacuated transmission line where it propagates to a quasi-optical launching antenna installed on the TCV vessel. The polarisation of each beam can be varied and is usually set for a propagation as an extraordinary wave (X2-, X3-mode). The cut-off density for the X2-mode propagation is $n_e \approx 4.25 \cdot 10^{19} \text{ m}^{-3}$, while the X3-mode injection extends the accessible density domain up to $n_e \approx 11.5 \cdot 10^{19} \text{ m}^{-3}$ although with a less localised power deposition region.

82.7 GHz system

For each cluster of X2 gyrotrons, there is one launcher mounted in an equatorial port (L1 and L4) and two launchers (L2, L3 and L5, L6) mounted in an upper lateral port, Fig. 1.8. Each launcher has two degrees of freedom, one of which provides steering of the microwave beam in a fixed plane during a discharge and the other allows to rotate the sweeping plane between discharges, for example to introduce a toroidal injection angle for current drive experiments. The polarisation of the wave is optimised for the launching geometry of each shot.

118 GHz system

The three gyrotrons of the X3 clusters are combined in one launcher at the top of the vessel. The microwave beam is injected nearly tangential to the resonant surface to maximise the absorption by increasing the path length through the plasma. The mirror can be displaced radially ($\Delta z = \pm a/3$) between discharges to inject the beam from either the low or high field side of the resonance, as shown in Fig. 1.8. The mirror can also be rotated during the discharge by $\pm 5^\circ$ to adjust the beam along the resonance surface.

1.7 Sawtooth activity in tokamak plasmas

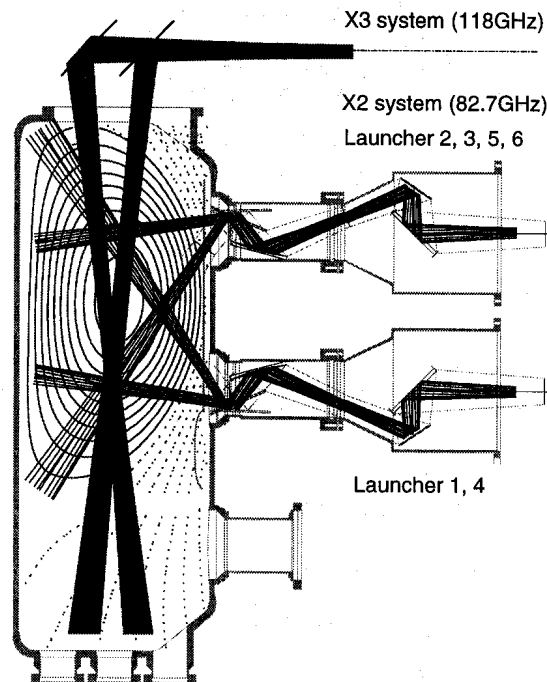


Fig. 1.8 X2 and X3 ECH system on TCV. The X2 launchers are placed on two equatorial (L1, L4) and four upper lateral (L2, L3, L5, L6) ports. The X3 launcher is mounted on the top of the vessel and can be radially displaced to view the ECH resonance on the low or high field side.

1.7 Sawtooth activity in tokamak plasmas

Sawtooth oscillations, named after the characteristic shape of their soft x-ray time traces, were first observed on the ST tokamak [9] and are present in many tokamak experiments. In ohmically heated plasmas, they consist of periodic relaxations of the central electron temperature and density which develop when the safety factor on axis, q_0 , drops below unity. A slow rise (sawtooth ramp) of temperature and density in the central region of the plasma, determined by heat deposition and transport, is followed by a rapid drop (sawtooth crash), triggered by the instability of an internal kink mode with toroidal $n = 1$ and dominant poloidal $m = 1$ mode numbers, which develops on the $q = 1$ surface. Recent results from TCV show that both ideal and resistive internal kink modes may trigger the sawtooth crash depending on the plasma shape [10]. At low triangularity and sufficient elongation, ideal MHD significantly contributes to the trigger whereas, at high triangularity and low elongation the ideal mode is stable and resistive MHD is responsible for kink

dynamics. During the subsequent sawtooth crash, reconnection of magnetic field lines occurs and particles and energy are expelled from the plasma centre resulting in a flattening of the temperature and density profiles. The current density also changes during a sawtooth period. According to the Kadomtsev relaxation model [11], the magnetic island associated with the $m/n = 1/1$ internal kink mode grows until it fills the entire plasma volume inside the mixing radius, r_{mix} , which is somewhat larger than the pre-crash $q = 1$ radius (see chapter 6). In this model, which is often referred to as complete reconnection model, the relaxed q profile equals unity on the new magnetic axis and is larger than unity elsewhere. Experimental evidence from different tokamaks indicates that Kadomtsev's model is not always consistent with experimental data even though observations from different tokamaks are somewhat inconsistent. In some experiments, the value of the safety factor on axis remains well below unity after the crash [12], [13], [14], while in other experiments it does not depart significantly from unity [15], [16].

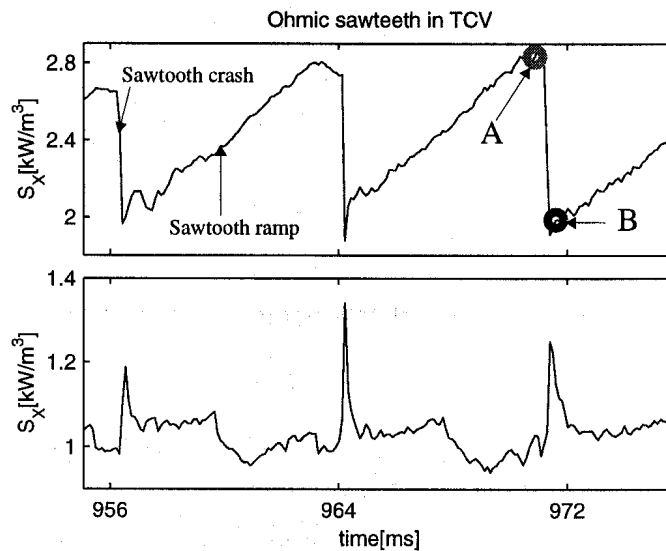


Fig. 1.9 Evolution of the soft x-ray emissivity at two radial positions during ohmic sawteeth in TCV discharge No. 19090: (a) on-axis; (b) just outside the sawtooth inversion radius.

Owing to the dependence of the soft x-ray emission on the electron density and temperature (see chapter 2), sawteeth are particularly evident on soft x-ray time traces as shown in Fig. 1.9 for the TCV ohmic discharge No. 19090. In this figure, the temporal evolution of the soft x-ray emissivity is shown at two different radial positions in the plasma. The central soft x-ray time trace, Fig. 1.9(a), shows the typical triangular shape of sawteeth which we refer to as “standard” in the following. The result of the sawtooth crash on the electron temperature profiles is shown in Fig. 1.10 for the

1.7 Sawtooth activity in tokamak plasmas

times indicated by arrows in Fig. 1.9(a). At the sawtooth crash, as a consequence of the outward transport of energy and particles, temperature (Fig. 1.10) and density (not shown here) drop inside some radius r_{inv} , called sawtooth inversion radius, and increase directly outside this radius. As seen in Fig. 1.10, sawtooth activity can involve a large fraction of the plasma volume leading to a degradation of confinement. TCV discharges, where sawteeth were stabilised using ECCD techniques, show a significant improvement in energy confinement [17].

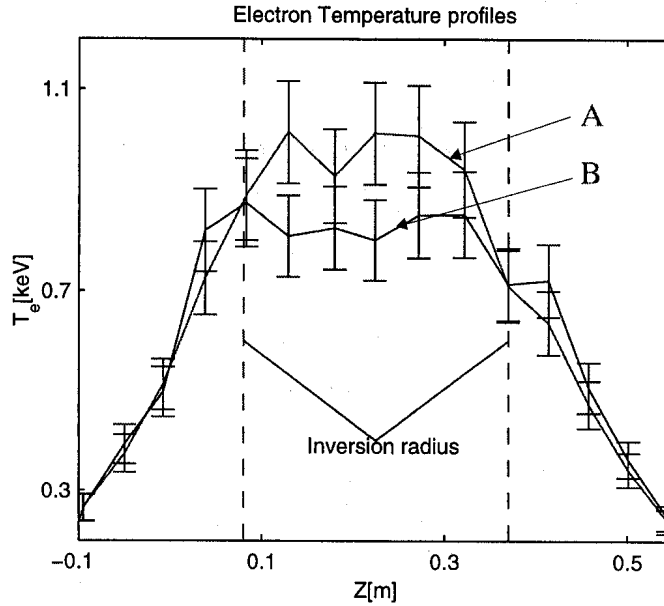


Fig. 1.10 Effect of sawtooth crash on the electron temperature profiles from the TCV Thomson scattering system. These are shown along a central, vertical cut corresponding to the different times indicated by the arrows in Fig. 1.9. Dashed lines indicate the position of the sawtooth inversion radius.

In ohmically heated plasmas, the sawtooth inversion surface $r = r_{inv}$ is close to the $q = 1$ surface but is not necessarily coincident. On different sides of the sawtooth inversion surface $r = r_{inv}$, the time traces of the soft x-ray emission invert their temporal signature as shown in Fig. 1.9(b). This can be used experimentally to determine the sawtooth inversion radius from soft x-ray measurements. Although this was the first method used for determining the sawtooth inversion radius, measurements of temperature and density profile with sufficiently high temporal resolution would define other inversion radii. From theoretical considerations, these radii do not necessarily coincide neither between themselves nor with the $q = 1$ radius and the difference depends on the pre-crash profiles and on the assumed reconnection model [18]. In this thesis, the sawtooth inversion radius is calculated from inverted soft x-ray emissivity distribution as outlined in section 4.2.2. A discussion will be presented when the difference between the $q = 1$ and the sawtooth

inversion radius is relevant in the data interpretation.

On TCV, sawtooth activity affects ohmically heated discharges operating at edge safety factor up to ≈ 10 . Both the sawtooth period τ_{ST} and the crash amplitude are observed to strongly depend on the shape of the plasma poloidal cross section. Systematic scans of plasma elongation and triangularity show small sawteeth with short periods at high elongation or low and negative triangularity, and large sawteeth with long periods at low elongation or high triangularity [10]. For example, ohmic sawteeth at $\kappa_a \approx 1.5$, $\delta_a \approx 0.2$ and typical densities of $(2 - 3) \times 10^{19} \text{ m}^{-3}$ have a period $\tau_{ST} \approx 2$ ms. Their period and crash amplitude increase up to $\tau_{ST} \approx 3$ ms and relative crash of 20% at $\delta_a \approx 0.5$. The sawtooth period also depends on particle density. For example, in a moderately shaped ($\kappa_a \approx 1.5$, $\delta_a \approx 0.2$) ohmic TCV plasma τ_{ST} increases from 1.7 ms at a central electron density $n_{e0} = 1 \times 10^{19} \text{ m}^{-3}$ to 3 ms at $n_{e0} = 5 \times 10^{19} \text{ m}^{-3}$.

As we observe from Fig. 1.9, the sawtooth crash occurs on a much faster timescale which, on TCV, is typically of the order of $\approx 100 \mu\text{s}$. The rapidity of this phase requires diagnostics with adequate time resolution.

The relatively simple picture of sawteeth given so far is complicated by the observation of ohmic sawteeth in which an $m/n = 1/1$ mode exists for a large fraction of the sawtooth period [19]. Moreover, in recent years, the use of ECH and ECCD techniques to influence sawteeth has revealed new plasma features. Examples are the observation of sharp temperature gradients just outside the sawtooth inversion radius on the RTP tokamak [20] and the multi-peaked temperature profiles observed in the TEXT upgrade [21] and RTP experiments [20]. Also, a wide ‘‘zoology’’ of sawtooth shapes appears depending on plasma and ECH / ECCD conditions [22]. These techniques are also at the origin of unexpected transport phenomena which lead to particle depletion in the plasma core [23] and result in inverted sawteeth of the central electron density [24] and therefore are potentially important in determining the particle confinement in a future reactor.

In a future fusion tokamak reactor, sawtooth activity is expected to play an important role in view of the low values of the safety factor at the edge $q_{95} \approx 3$ at which diverted discharges are intended to operate. This would lead to values of the mixing radius larger than half of the plasma minor radius. The repetitive flattening of the central temperature and density profiles over this large plasma volume would significantly reduce the confinement margin when compared with peaked profiles. Moreover, numerical simulations [25] indicate that the sawtooth period depends on whether or not complete magnetic reconnection occurs which results in different amounts of reconnected magnetic flux. Another important concern arises from the observation that sawteeth can generate seed islands which trigger neoclassical tearing modes leading to a loss of plasma confinement [26].

1.8 Outline of the thesis

1.8 Outline of the thesis

A brief introduction to nuclear fusion and the tokamak as a possible concept to exploit fusion as a future energy source has been given in this chapter. The TCV tokamak on which the work was performed and its ECH heating system have also been outlined. A brief introduction into the phenomenology of sawteeth has been given and their importance outlined for both a future fusion reactor and a better understanding of the underlying physics.

- Theory of plasma emission is reviewed in chapter 2.
- In chapter 3, the diagnostics which were used in this work are described. Special emphasis is given to those which have sufficiently high temporal resolution to resolve the dynamics of sawtooth oscillations. In particular, the soft x-ray tomographic system is detailed since it is the key diagnostic for the study of sawtooth activity in chapter 6. The foundations of the tomographic problem are outlined and main tomographic inversion techniques which are used on TCV are presented. In particular, a modified Abel inversion method is discussed which has been developed to provide electron density profiles from the TCV multichord interferometer data.

The design and first results from a bolometry system with high temporal resolution are presented. This allows the study of fast transient phenomena hitherto inaccessible to standard bolometric techniques. The development of this fast bolometric system led to a journal publication:

I. Furno, H. Weisen, J. Mlynar, R. A. Pitts, X. Llobet, Ph. Marmillod, G. Pochon, "Fast bolometric measurements on the TCV tokamak", *Rev. Sci. Instrum.* **70** (1999) 4552.

- Chapter 4 describes the basic tools for the analysis of soft x-ray data which are essential for the physics investigations in the following chapters. In particular, MHD mode identification using the singular value decomposition (SVD) analysis and an original method for the evaluation of the sawtooth inversion radius based on the SVD analysis of tomographically inverted soft x-ray data are presented.
- In chapter 5, the influence of the sawtooth activity on profile behaviour is studied in the

ohmic and ECH L-mode confinement regime for a large variety of plasma shapes which can be produced in TCV. For ohmic plasmas, the analysis resulted in the identification of the parameter $\langle j \rangle / (j_0 q_0)$ which, irrespective of plasma shape and electron density, determines the sawtooth inversion radius and the profile inverse peaking factors $\langle p_e \rangle / p_{e0}$, $\langle T_e \rangle / T_{e0}$ and $\langle n_e \rangle / n_{e0}$ for electron pressure, temperature and density, where the brackets indicate a volume averages. This dependence appears to be largely a consequence of the of the sawtooth activity which limits the core peaking of the current and the pressure or temperature. However, profile features in the confinement zone also depend on $\langle j \rangle / (j_0 q_0)$ and cannot be accounted for by sawteeth alone. In ECH L-mode plasmas, the parameter $\langle j \rangle / (q_0 j_0)$ remains the main scaling parameter for profile widths in the confinement region. Nevertheless, the profiles and the inversion radius are no longer determined by this parameter alone and they depend strongly from the ECH power deposition profile. The results of this analysis contributed to the following journal publications:

H. Weisen, I. Furno, S. Alberti and the TCV team, "Sawtooth inversion radii and profile peaking factors in TCV L-mode plasmas", *Nucl. Fusion* **41** (2001) 1227.

H. Weisen, R. Behn, I. Furno, et al. "Profile consistency features in shaped sawtooth ohmic TCV plasmas", *Plasma Phys. Control. Fusion* **40** (1998) 1803.

H. Weisen, R. Behn, I. Furno, J. M. Moret, O. Sauter, "Profile consistency features in strongly shaped ohmic tokamak plasmas", *Physics of Plasmas* **6** (1999) 1.

- Chapter 6 presents an experimental and theoretical account of different sawtooth types observed in TCV in the presence of electron cyclotron heating as a function of the location of the deposited power. New insight into the dynamics of the magnetic island associated with the resistive internal kink mode and of the magnetic reconnection during the sawtooth crash has been gained thanks to the installation of a transient recorder with maximum sustainable acquisition rate of 80 kHz for the soft x-ray tomographic system. The different types of sawteeth are simulated using a numerical code based on a theoretical model which describes the evolution of the electron temperature in the presence of localised heat sources and of a magnetic $m/n = 1/1$ island. The result of this work on TCV led to a journal publication:

I. Furno, C. Angioni, F. Porcelli, H. Weisen, R. Behn, T.P. Goodman, M.A. Henderson, Z.A. Pietrzyk, A. Pochelon, H. Reimerdes, E. Rossi, "Understanding sawtooth activity during

1.8 Outline of the thesis

intense electron cyclotron heating experiments on TCV”, *Nucl. Fusion* **41** (2001) 403.

- Chapter 7 analyses a coupled heat and particle transport phenomenon in the presence of centrally deposited electron cyclotron heating and electron cyclotron current drive in TCV. This phenomenon, known as density ‘pump-out’, is potentially important for the confinement of fusion plasmas since it leads to particle depletion from the plasma core as reported by several present and past tokamak as well as stellarator experiments. Observations in TCV show that the density pump-out is correlated with the presence of a $m/n = 1/1$ MHD mode resulting in the loss of axisymmetry. We propose that loss of axisymmetry provides the crucial physics for this phenomenon in tokamaks by permitting locally trapped particles near the helically displaced magnetic axis which are not confined in the core region, as in stellarators. The new findings were reported at two international conferences and contributed to a journal publication:

I. Furno and H. Weisen, “Observation of particle pump-out with central ECH and ECCD in TCV”, to be submitted to *Physics of Plasmas*.

H. Weisen, I. Furno, et al., “Particle Transport Phenomena in High Power ECH and ECCD Discharges in TCV”, 18th IAEA Fusion Energy Conference Sorrento, Italy, 4-10 October 2000, to be published in *Nucl. Fusion*.

I. Furno and H. Weisen, “Influence of Electron Cyclotron Heating on Electron Density Behaviour”, *Proc. 27th EPS on Controlled Fusion Plasma Physics* (Budapest 2000), P1-026.

I. Furno, et al., “Heat and Particle Transport Phenomena during Intense ECH”, *42nd Annual Meeting of the APS Division of Plasma Physics combined with the 10th International Congress on Plasma Physics* (Québec City 2000).

In chapter 8 conclusions are drawn on the presented work and proposals for future work outlined.

References

[1]International Energy Annual Report 1995, Report DOE/EIA-0219 (95) December 1996. Available at <http://www.eia.doe.gov/international>.

[2]Douglas R. O. Morrison, *Proc. 24th International Seminar on Planetary Emergencies*, 19-24 August, Erice (Italy).

[3]*Energy Statistics Yearbook 1993*, United Nations, Department of Economic and Social

Information and Policy Analysis, Statistical Division, New York, 1995.

[4]M. Verral, *Nature* **371** (1994) 274.

[5]L. A. Artsimovich, et al., *Proc. 3rd Int. Conf. on Plasma Physics and Controlled Nucl. Fusion Research* (Novosibirsk 1968), vol. 1, page .

[6]J. Wesson, *Tokamaks*, Clarendon Press, Oxford, 1987.

[7]F. Hofmann, et al., *Plasma Phys. Control. Fusion* **36** (1994) B277.

[8]T. P. Goodman, et al., *Proc. 19th SOFT* (Lisbon 1996), page 565.

[9]S. Von Goeler, et. al, *Phys. Rev. Lett.* **33** (1974) 1201.

[10]H. Reimerdes, et al., *Plasma Phys. Control. Fusion* **42** (2000) 629.

[11] B. B. Kadomtsev, *Fizika Plazmy* **1** (1975) 710; *Sov. J. Plasma Phys.* **1** (1976) 389.

[12]J. O'Rourke, *Plasma Phys. Control. Fusion* **30** (1991) 1475.

[13]F. M. Levington, *Phys. Fluids* **B 5** (1993) 2554.

[14]R. D. Gill, et al., *Nucl. Fusion* **32** (1992) 723.

[15]D. Wroblewski, et al., *Phys. Rev. Lett.* **61** (1988) 1724.

[16]H. Weisen, et al., *Phys. Rev. Lett.* **62** (1989) 434.

[17]Z. A. Pietrzyk, et al., *Phys. Plasmas* **7** (2000) 2909.

[18]Z. A. Pietrzyk, et al., including I. Furno, *Nucl. Fusion* **39** (1999) 587.

[19]H. Weisen, et al., including I. Furno, *Nucl. Fusion* **37** (1997) 1741.

[20]N.J. Lopez-Cardozo, et al., *Phys. Rev. Lett.* **73** (1994) 256.

[21]G. Cima, et al., *Plasma Phys. Control. Fusion* **40** (1998) 1149.

[22]Z. A. Pietrzyk, et al., including I. Furno, *Nucl. Fusion* **39** (1999) 587.

[23]TFTR-GROUP, *Nucl. Fusion* **25** (1985) 1011.

[24]I. Furno, et al., *42nd Annual Meeting of the APS Division of Plasma Physics combined with the 10th International Congress on Plasma Physics* (Québec City 2000).

[25]F. Porcelli, et al., *Plasma Phys. Control. Fusion* **38** (1996) 2163.

[26]O. Sauter, et al., *Phys. Plasmas* **4** (1997) 1654.

2 THEORY OF PLASMA EMISSION

2.1 Introduction

The measurement of the radiation emitted by the plasma is a powerful method to diagnose several basic plasma quantities like the electron temperature and density, and the degree of plasma purity, as well as fluctuations in these quantities. The principal objective of this chapter is to give an introduction to the theory of the plasma emission which constitutes the basis of diagnostic applications which are described in detail in chapter 3 and are extensively used in the rest of the thesis.

The main radiation processes are briefly described in this preliminary section and discussed in detail in section 2.2. Since they have been extensively treated by several authors [1], [2], only a review of the results is presented together with a discussion of the main equations, where important physical assumptions are made. In section 2.3, the main collisional processes in fusion plasmas which determine the charge state balance are presented and some general estimates of their rate coefficients are gathered together for easy reference. In the same section, a presentation of different plasma ionisation equilibrium models is provided together with the analysis of their domain of validity. Finally, an example of ionisation equilibrium on TCV is discussed in section 2.4.

Radiation emission in a plasma originate from the following main processes:

- (I) Bremsstrahlung, also called free-free radiation, arises from electron-ion Coulomb collisions which consist mainly of small-angle scattering of electrons in the electric field due to the ions. The name free-free is due to the fact that both in initial and final energy states the electrons are free. The Bremsstrahlung spectrum is thus a continuum.
- (II) Recombination radiation, produces a continuum spectrum and originates from electron-ion encounters in which electrons are captured by ions into a bound state. For this reason, recombination radiation is also called free-bound radiation.
- (III) Line radiation, originates from the transition of an electron in an excited bound state of energy E_p to another bound state of lower energy E_q resulting in the emission of a photon of energy $h\nu_{pq} = E_p - E_q$.
- (IV) Cyclotron radiation, in magnetically confined plasmas, originates from the gyration of charged particles around the magnetic field. The main contribution to the cyclotron emission comes from the electrons at multiple of the fundamental electron cyclotron frequency $\omega_e = eB/m_e$, where m_e is the electron rest mass and e is the elementary charge. For magnetic fields of the order of 1-10 T, typical for magnetic fusion experiments, the cyclotron

radiation is mainly emitted in the microwave spectral range. In a tokamak configuration, an estimate for the total radiated power can be obtained by neglecting the emission in the weakly ordinary mode and assuming that the plasma is optically thick for the spectral range of interest [3]. In this case, the radiation power per unit volume P_c emitted at the fundamental frequency at the magnetic axis, which is located at $R = R_0$, is given by

$$P_c = \frac{\omega_e^3 T_{e0}}{4\pi^2 c^2 R_0} \quad (2.1)$$

where T_{e0} is the electron temperature at $R = R_0$.

For typical plasma conditions on TCV, Eq. (2.1) gives cyclotron radiation losses of the order of 1 W/m^3 , which are small compared to other loss mechanism and therefore they can be neglected in power balance analysis.

There are other processes which could give rise to radiation from plasmas (for example Cerenkov radiation), but they can be safely ignored except under very special circumstances.

In the following, we indicate with $n_Z(g)$ the population density in the ground level g of an ion A^Z having charge Z . $n_Z(p)$ denotes the population density of the same ion corresponding to an excited level having quantum number p . The collisional processes are described by individual rate coefficients which depend only on the electron temperature T_e . This is justified since, for most plasma conditions discussed in this thesis, the distribution of velocities of the electrons is adequately represented by a Maxwellian distribution. In TCV, a suprathermal population of electrons is observed only in electron cyclotron current drive experiments where the wave beam is injected in the plasma with a significant toroidal angle [4].

2.2 Radiation processes in plasmas

2.2.1 Bremsstrahlung radiation

In fusion plasmas, the largest contribution to Bremsstrahlung radiation arises mainly from electrons scattered by ions. The contribution due to electron-electron Coulomb collisions is generally negligible since a binary collision between two identical non relativistic particles does not give rise to radiation in the dipole approximation [5]. Higher order quadrupole radiation from electron-

2.2 Radiation processes in plasmas

electron encounters become significant only for electron kinetic energies larger than 0.5 MeV [1].

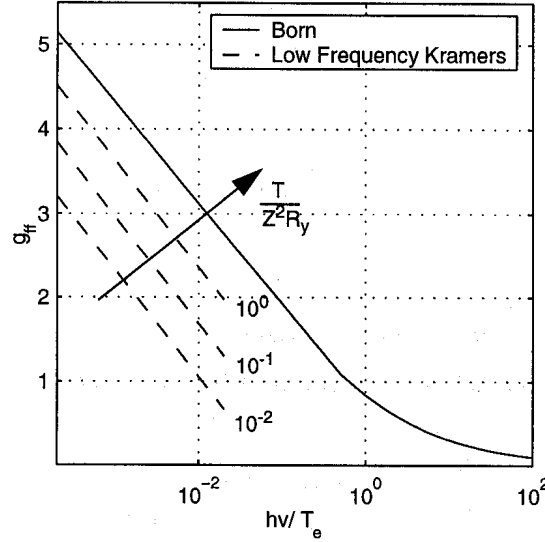


Fig. 2.1 Maxwell-averaged Gaunt factor g_{ff} as calculated from Kramers and Born analytical approximations as given respectively in Eq. (2.4) and Eq. (2.5).

Accordingly, in the following we consider only collisions between electrons and ions A^Z . Under the assumption of Maxwellian electron distribution function, the power spectral density radiated by Bremsstrahlung in the classical case can be expressed as [2]

$$j(\nu) = g_{ff} n_e n_Z Z^2 \left(\frac{e^2}{4\pi\epsilon_0} \right)^3 \frac{16\pi}{3\sqrt{3}m^2c^3} \left(\frac{2m}{\pi T_e} \right)^{1/2} e^{-\frac{h\nu}{T_e}} \quad (2.2)$$

which evaluates to

$$j(\nu) = 1.54 \cdot 10^{-38} g_{ff} n_e n_Z Z^2 \frac{e^{-\frac{h\nu}{T_e}}}{\sqrt{T_e}} \quad (\text{W} \cdot \text{m}^{-3} \cdot \text{eV}^{-1}) \quad (2.3)$$

where g_{ff} is the Maxwell-averaged Gaunt factor and n_e and n_Z are expressed in m^{-3} and T_e in eV. Modification to the classical emission given by Eq. (2.3) due to quantum-mechanical as well as relativistic effects are generally collected into corrections to g_{ff} for which formulas with different domain of applicability can be found in the literature [2], [6], [7]. Fig. 2.1 shows the Maxwell averaged Gaunt factor as a function of $h\nu/T_e$ corresponding to the following:

(a) low-frequency semi classical (Kramers) approximation [8]

$$g_{ff} = \frac{\sqrt{3}}{\pi} \ln \left| 3.24 \cdot 10^{-5} T_e [\text{keV}]^{\frac{3}{2}} h\nu [\text{keV}] Z^{-1} \right| \quad (2.4)$$

valid at low frequency for $T_e \ll Z^2 R_y$, being $R_y \approx 13.6$ eV the Rydberg constant.

(b) Born approximation, valid for $T_e \gg Z^2 R_y$

$$g_{ff} = \frac{\sqrt{3}}{\pi} K_0 \left(\frac{h\nu}{2T_e} \right) \exp \left(\frac{h\nu}{2T_e} \right), \quad (2.5)$$

where K_0 is the modified Hankel function.

For a very wide range of energies, $0.1 \leq h\nu/T_e \leq 10$, the Gaunt factor lies between 0.3 and 2. In this case, the temperature and frequency dependence of the spectral power in Eq. (2.5) is mainly contained in the $T_e^{-1/2} \exp(-h\nu/T_e)$ factor and therefore the average photon energy $\langle h\nu \rangle$ is approximately equal to the electron temperature. For plasmas of interest in thermonuclear fusion with $10 \text{keV} \leq T_e \leq 30 \text{keV}$, the Bremsstrahlung emission is mainly in the x-ray spectrum.

2.2.2 Recombination radiation

Another important contribution to the continuum spectrum arises from binary collisions between electrons and ions in which the final electron state is bound. This recombination process is accompanied by emission of radiation and, in plasmas of interest for fusion research, the most important contributions are due to radiative and dielectronic recombination, which are described in section 2.3.

The condition for recombination to occur can be obtained by a classical argument. Consider a single free-bound collision in which an electron with velocity v is captured by an ion A^Z , assumed for simplicity to be at rest. In the final bound state, the electron has a discrete spectrum of energies given by

$$W_n = -\frac{Z^2 e^4 m}{2(4\pi\epsilon_0 h)^2 n^2} = -R_y \frac{Z^2}{n^2} \quad (2.6)$$

where n is the quantum number of the recombination level. Applying the energy conservation to the recombination process, we obtain that the emitted photon has an energy $h\nu$ given by

2.2 Radiation processes in plasmas

$$h\nu = \frac{1}{2}mv^2 + R_y \frac{Z^2}{n^2}. \quad (2.7)$$

From this equation it is evident that no recombination occurs for photon energies $h\nu \leq R_y Z^2/n^2$ and conversely only those n states such that $n^2 \geq R_y Z^2/(h\nu)$ contribute to the recombination radiation at the energy $h\nu$. At the so-called recombination edges, $h\nu = R_y Z^2/n^2$ the lower n state begins to contribute. To obtain the total recombination continuum from such a plasma, the different contributions must be summed over all n for which the condition $n^2 \geq R_y Z^2/(h\nu)$ holds.

For a Maxwellian electron distribution, the power spectral density of the recombination radiation emitted during the free-bound transition into an n quantum state may be written [2]

$$j_n(\nu) = n_e n_Z Z^2 \left(\frac{e^2}{4\pi\epsilon_0} \right)^3 \frac{16\pi}{3\sqrt{3}m^2 c^3} \left(\frac{2m}{\pi T_e} \right)^{1/2} e^{-\frac{h\nu}{T_e}} \left[\frac{Z^2 R_y}{T_e} \frac{2}{n^3} G_n e^{\frac{R_y Z^2}{n^2 T_e}} \right]. \quad (2.8)$$

This equation is identical to the Bremsstrahlung Eq. (2.3), except for the term in square brackets that replaces g_{ff} . Quantum mechanical calculations show that the values for the Maxwell averaged *free-bound Gaunt factor* G_n are within the range $0.8 \leq G_n \leq 1.2$ for $h\nu < 10Z^2 R_y$. At higher frequency they decrease approximately logarithmically [9].

The relative importance of recombination radiation compared to Bremsstrahlung radiation can be determined taking the ratio of Eq. (2.8) and Eq. (2.3), which reads

$$\frac{Z^2 R_y}{g_{ff} T_e} \frac{2}{n^3} G_n e^{\frac{R_y Z^2}{n^2 T_e}}. \quad (2.9)$$

At low frequency $h\nu \leq R_y Z^2$, only very high n states contribute since $n^2 \geq R_y Z^2/(h\nu)$. Therefore, in view of the n^{-3} dependence in Eq. (2.9), recombination is negligible in this limit. However, when $h\nu \geq R_y Z^2$, all n states can contribute for $Z^2 R_y \geq T_e$ and recombination dominates whereas for $Z^2 R_y \leq T_e$ is negligible.

TCV plasmas are mainly contaminated by carbon and, to a lesser extent, boron impurities [10]. For electron temperatures $T_e \approx 1$ keV, the continuum spectrum emitted in the soft x-ray range is therefore dominated by recombination contribution.

It is important to mention that in deriving Eq. (2.8), it is assumed that the ion charge is fully screened by the bound electrons, resulting in an effective ion charge Z . However, this assumption is not valid for photons with energies that are not much larger than the ionisation potential [2]. For the lowest unfilled shell we modify the recombination formula, recognising that if the shell contains only ξ holes instead of the usual $2n^2$, then the recombination radiation is less by a factor of

$\xi/(2n^2)$. The formula arising from this assumption reads [9]:

$$j_n(\nu) = n_e n_i Z^2 \left(\frac{e^2}{4\pi\epsilon_0} \right)^3 \frac{4\pi}{3\sqrt{3}m^2 c^3} \left(\frac{2m}{\pi T_e} \right)^{1/2} e^{-\frac{h\nu}{T_e}} \left[\frac{\chi_i \xi}{T_e n^3} G_n e^{\frac{\chi_i}{T_e}} + \sum_{\mu=n+1}^{\infty} \frac{Z^2 R_y}{T_e} \frac{2}{\mu^3} G_\mu e^{\frac{R_y Z^2}{\mu^2 T_e}} \right] \quad (2.10)$$

where χ_i is the first ionisation potential for the ion considered.

In any practical case, many different ion species j of charge Z_j contaminate the plasma. The total continuum emission, including Bremsstrahlung and recombination radiation, is then the sum of contribution of the form of Eqs. (2.3), (2.10) over all different species. After evaluating the fundamental constants, the continuum emission can be written as

$$I(\omega) = 1.5 \times 10^{-38} n_e^2 \frac{e^{-\frac{h\omega}{T_e}}}{\sqrt{T_e}} \times \zeta(T_e) \quad (W \cdot m^{-3} \cdot eV^{-1}) \quad (2.11)$$

where the electron density, n_e , is given in m^{-3} and the electron temperature, T_e , in eV. The enhancement factor, $\zeta(T_e)$, can be understood as the enhancement of the radiation emission over that of a pure hydrogen plasma, with similar plasma parameters

$$\zeta(T_e) = \sum_j \frac{n_j}{n_e} [g_{ff,j} Z_j^2 + f_j] \quad (2.12)$$

where

$$f_j = Z_j^2 \left[\frac{\chi_j \xi}{T_e n^3} G_n e^{\frac{\chi_j}{T_e}} + \sum_{\nu=n+1}^{\infty} \frac{Z_j^2 R_y}{T_e} \frac{2}{\nu^3} G_\nu e^{\frac{R_y Z_j^2}{\nu^2 T_e}} \right] \quad (2.13)$$

and the summation over j has to be performed for the ionisation states of all atomic species.

When the recombination contribution becomes negligible, i.e. when $g_{ff,j} Z_j^2 \gg f_j$, from Eq. (2.12) it can be seen that, provided the Gaunt factor, $g_{ff,j}$, to be equal for all species, the total continuum emission can be expressed as

$$I(\omega) = 1.5 \times 10^{-38} \times n_e^2 Z_{eff} \frac{e^{-\frac{h\omega}{T_e}}}{\sqrt{T_e}} \quad (W \cdot m^{-3} \cdot eV^{-1}) \quad (2.14)$$

where Z_{eff} is the effective ion charge, defined as

$$\sum_j n_j n_e Z_j^2 = n_e^2 Z_{eff} \quad (2.15)$$

2.2 Radiation processes in plasmas

Z_{eff} can be thought as the factor by which the Bremsstrahlung radiation exceeds that of a pure hydrogen plasma, for which $Z_{eff} = 1$, and is also given by the formula

$$Z_{eff} = \frac{\sum n_i Z_i^2}{\sum n_i Z_i} \quad (2.16)$$

where the quasi-neutrality condition, $n_e = \sum n_i Z_i$, has been invoked in deriving Eq. (2.14).

2.2.3 Line radiation

Depending on plasma conditions, a large contribution to the total emitted power may come from line radiation emitted by ions which are not completely stripped. This contribution is usually referred to as bound-bound radiation since it requires that an electron in a bound ionic state of energy E_p make a transition to another bound state of lower energy E_q emitting a photon of energy $h\nu_{pq} = E_p - E_q$. Provided that the plasma is optically thin, the intensity of the spectral line arising from this transition is given by

$$I_{p,q} = n_Z(p) A(p,q) \cdot h\nu_{pq} \quad (2.17)$$

where $A(p,q)$ is the atomic probability of the transition $p \rightarrow q$ and $n_Z(p)$ is the density of ions with charge Z in the excited energy level denoted by its quantum number p . In order to determine the total power loss from the plasma by line radiation, the expected populations of its various excited stages in Eq. (2.17) must be evaluated. However, for tokamak plasma conditions, the density of the excited level p can be expressed as

$$n_Z(p) = n_e n_Z(g) X_Z(T_e, g, p) / \sum_{q < p} A_Z(p, q). \quad (2.18)$$

where $X_Z(T_e, g, p)$ is the collisional excitation coefficient from the ground to the excited level p . Equation (2.18) is obtained in section 2.3. Anticipating that result, the total power emitted in Eq. (2.17) can be expressed as

$$I_{p,q} = n_e n_Z(g) \frac{A(p,g)}{\sum_{p > g} A(p,g)} h\nu_{pq} \quad (2.19)$$

which only requires the evaluation of the ground state population of each ionic species. However, for weak lines or when metastable level populations cannot be neglected, one has to rely on complete excited level population calculations.

On TCV, spectroscopic measurements and modelling of the ionisation equilibrium using the IONEQ code, described in section 2.3.3, show that most of the power radiated in line emission is in the ultra soft x-ray spectral range and originates from H- and He-like carbon and to a lesser extent boron [10]. Therefore, measurements of the radiation emitted by the plasma at photon energies above ≈ 1 keV are largely dominated by the continuum spectrum contribution which has important consequences for the interpretation of the data in term of basic plasma parameters (see chapter 3).

2.3 Types of ionisation equilibrium

In the earlier section of this chapter, the theory has been outlined by which the power emitted by a plasma can be evaluated. This requires the detailed knowledge of the ionisation stage density which requires a model of the ionisation equilibrium taking into account the atomic processes for all plasma conditions. The complexity of this approach is impracticable and a number of assumptions are made on the processes, which determine the equilibrium, which restrict the applicability of a model to less general plasma conditions. The most tractable plasma models are those in which the electron density is either very high or very low. The former can be described by *local thermodynamic equilibrium* (LTE) and the latter by *corona equilibrium* (CE). We introduce these two models and examine their domain of validity. A more general time-dependent model which takes into account transport effects is discussed later.

In what follows, the principal processes relevant to the charge state balance in TCV plasmas are briefly reviewed.

(i) Collisional ionisation.

Most ionisation results from ion-electron collisions in which the electron loses kinetic energy. The process can be written



A semi empirical expression for the collisional ionisation rate can be found in Ref. [2]

2.3 Types of ionisation equilibrium

$$S_Z(T_e) = 1.7 \cdot 10^{-14} \bar{g} \left(\frac{R_y}{\chi_i} \right)^2 \left(\frac{T_e}{R_y} \right)^{1/2} \exp\left(-\frac{\chi_i}{T_e}\right) \left[1 - \exp\left(-\frac{\chi_i}{T_e}\right) \right] \quad (m^3 \cdot s^{-1}) \quad (2.21)$$

where $\bar{g} = 1 + (\sqrt{3}/\pi) \ln|1 + T_e/\chi_i|$ is the average Gaunt factor and χ_i is the ionisation potential of the considered state.

(ii) Radiative and dielectronic recombination

These processes often dominate the charge state balance and, under certain conditions, contribute significantly to the continuum spectrum emission (section 2.2.2). Radiative recombination consists of an ion A^{Z+1} of charge $Z + 1$, normally in its ground state, capturing an electron into an excited state with quantum number n of the ion of charge Z . The process is accompanied by the emission of a photon of energy $h\nu$, given by Eq. (2.7), and it can be written



The rate coefficient for radiative recombination is usually calculated using the Kramer's formula [2]

$$\alpha_Z^D(T_e) = 5.2 \cdot 10^{-20} \bar{g} Z \left(\frac{\chi_Z}{T_e} \right)^{3/2} \exp\left(-\frac{\chi_Z}{T_e}\right) Ei\left(\frac{\chi_Z}{T_e}\right) \quad m^3 s^{-1} \quad (2.23)$$

where $\chi_Z = R_y Z^2 / n^2$ is the ionisation potential from the excited level of the recombined ion, Eq. (2.6), and

$$Ei(y) = \int_y^\infty \frac{\exp(-s)}{s} ds. \quad (2.24)$$

Equation (2.24) has the following asymptotic form

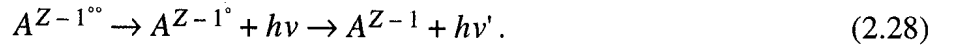
$$\exp(y) Ei(y) \rightarrow 1/y \quad \text{as } y \rightarrow \infty \quad (2.25)$$

$$\exp(y) Ei(y) \rightarrow -\ln(y) \quad \text{as } y \rightarrow 0, \quad (2.26)$$

where the former is most useful for lower quantum levels, since the temperature is usually much smaller than the ionisation energy in equilibrium.

For high- Z ions, dielectronic recombination can play a significant role in the charge state balance

and contribute significantly to the power radiated from the plasma. Recombination progresses as follows: an electron is captured into a high principal quantum number state, above the ionisation level, and simultaneously an electron of the ion A^Z is excited from a level i , with energy E_i , to a level j , with energy E_j . A very unstable, double excited $A^{Z-1^{oo}}$ ion results which can decay radiatively:



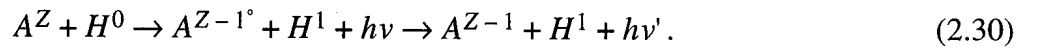
A widely used expression for the collisional rate is due to Burgess [11] and it is based on empirical fits to a variety of theoretical calculations. A simple formula is given in Ref. [2] and reads

$$\alpha_Z^D(T_e) = 8.8 \cdot 10^{-18} f_{ij} Z^{2/3} \left(\frac{R_y}{T_e}\right)^{3/2} \frac{E_{ij}}{R_y} \exp\left(-\frac{E_{ij}}{T_e}\right) \text{ m}^3 \text{ s}^{-1}. \quad (2.29)$$

where $E_{ij} = E_j - E_i$ and f_{ij} is the dimensionless oscillator strength.

(iv) **Charge exchange recombination**

A third recombination process is charge-exchange, where an electron of an hydrogen atom H^0 is captured (deuterium or tritium) by a plasma impurity ion A^Z of charge Z



The total number for charge-exchange recombination events per unit time can be expressed as

$$n_0 n_Z \alpha_Z^{CX} \quad (2.31)$$

where n_0 is the density of hydrogen atom and α_Z^{CX} is the total rate CX rate coefficient for which a universal scaled expression can be found in Ref. [12].

2.3 Types of ionisation equilibrium

2.3.1 Local thermal equilibrium model

In the local thermal equilibrium (LTE) model, it is assumed that the electron density is sufficiently high that the distribution of different ion states is only determined by particle collision processes and that the latter take place with sufficient frequency that the equilibrium responds instantaneously to any changes in the plasma conditions. With these assumptions, each atomic process is perfectly balanced by its inverse and the plasma is in thermodynamic equilibrium. The radiation emitted by the plasma has the black-body spectral energy density and the distribution of ion densities and all the excited states are given by the Saha-Boltzmann equations

$$\frac{n_{Z+1}(g)n_e}{n_Z(g)} = 2 \frac{\omega_{Z+1}(g)}{\omega_Z(g)} \left(\frac{2\pi m T_e}{h^2} \right) \exp \left[\frac{\chi_Z(g)}{T_e} \right] \quad (2.32)$$

$$\frac{n_Z(p)}{n_Z(q)} = 2 \frac{\omega_Z(p)}{\omega_Z(q)} \exp \left[\frac{\chi_Z(p, q)}{T_e} \right] \quad (2.33)$$

where $n_Z(p)$, $n_Z(q)$, $n_{Z+1}(g)$ and $n_Z(g)$ are the densities of the various level designated by their quantum number p , q and g (the last for the ground level) and ionic charge Z and $Z + 1$. The term $\omega_Z(p)$ is the statistical weight of the designated level, $\chi_Z(p, q)$ is the energy difference between levels p and q , and $\chi_Z(g)$ is the ionisation potential of the ion of charge Z in its ground level g .

Local thermal equilibrium requires high enough density for collisional transitions to dominate radiative transitions between all states. This condition, is essentially never satisfied in laboratory plasmas, though it may be approached inside stellar objects. An approximate lower limit on the density for LTE to apply may be written as [13]

$$n_e \gg 10^{19} \times \sqrt{T_e} (\Delta E)^3 \quad (m^{-3}) \quad (2.34)$$

where both the electron temperature, T_e , and the energy level difference, ΔE , are expressed in eV. As can be seen from Eq. (2.34), in magnetically confined fusion plasmas this criterion can be satisfied for principal quantum numbers, where ΔE is small, although is rarely appropriate for low-lying levels. A more general equilibrium model is therefore required. Since statistical thermodynamical arguments can not be applied, in order to calculate the ionisation states of the

plasma it is necessary to take into account all the ionisation and recombination mechanisms.

2.3.2 Steady state corona model

In the early 1950's, the *corona model* was proposed [14] to explain some observed features in the spectrum of the solar corona and it has also been useful in describing low density laboratory plasmas. The two fundamental assumptions of this model are that (1) all upward transitions (ionisation and excitation) are collisional and (2) all downward transitions (recombination and spontaneous decay) are radiative. Provided that these two assumptions are satisfied, most of the ions are in their ground states and the stationary charge state balance may be written as

$$n_e n_Z(g) S_Z(T_e, g) = n_e n_{Z+1}(g) \alpha_{Z+1}(T_e, g) \quad (2.35)$$

or equivalently as

$$\frac{n_Z(g)}{n_{Z+1}(g)} = \frac{\alpha_{Z+1}(T_e, g)}{S_Z(T_e, g)} \quad (2.36)$$

where $S_Z(T_e, g)$ is the collisional ionisation coefficient, $\alpha_{Z+1}(T_e, g)$ is the radiative recombination coefficient. Equation (2.36) shows that under the assumptions of the corona equilibrium the ion state populations are independent of electron density.

Similarly, the population densities of the excited levels are determined by a balance between the rate of collisional excitation from the ground level against the rate of the spontaneous radiative de-excitation, thus

$$n_e n_Z(g) X_Z(T_e, g, p) = n_Z(p) \sum_{q < p} A_Z(p, q) \quad (2.37)$$

where $A_Z(p, q)$ is the ionic transition probability from the energy level with quantum number p to lower energy level with quantum number q and $X_Z(T_e, g, p)$ is the collisional excitation coefficient.

Examples of calculated populations in corona equilibrium are shown in Fig. 2.2. The fractional abundances of all the ionisation states of carbon are shown as a function of the electron temperature. Ionisation to the next higher level occurs if (see for example Ref. [2])

2.3 Types of ionisation equilibrium

$$T_e > \chi_i / \ln \left| 18mc^2 / (Z^2 \chi_i) / (\chi_i / T_e) \right|. \quad (2.38)$$

This provides a qualitative understanding of the behaviour of the fractional abundances in Fig. 2.2.

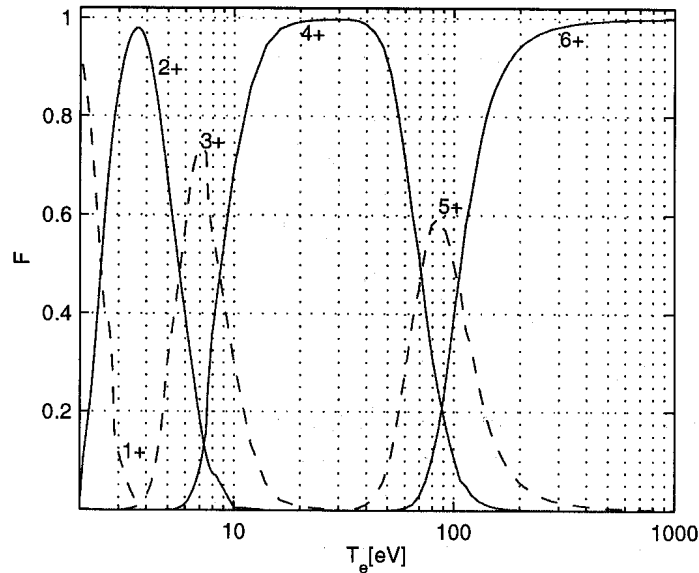


Fig. 2.2 Fractional abundances of different ionisation states of carbon in corona equilibrium as a function of electron temperature.

The significant increase in the ionisation potential for helium-like (4+) ions versus lithium-like (3+) ions explains the broad temperature range over which the helium-like is most abundant.

According to Eqs. (2.3), (2.10), (2.19), detailed knowledge of the ionisation equilibrium allows the evaluation of the different contributions to the power emitted by the plasma in a given spectral range. Fig. 2.3 shows the radiation emitted by carbon ions in the corona equilibrium of Fig. 2.2. The total radiation, summed over the different ionisation stages, has a maximum for $T_e \approx 30$ eV. For T_e approximately in the range 6-30 eV, the contribution from line radiation enhances the total emission. Fig. 2.3 shows also the plasma emission attenuated by a 47 μm beryllium filter and detected by a silicon photodiode which is used in the TCV soft x-ray tomography system. In this case, the decrease at high energy of the detected power is due to the finite thickness of the photodiode detector which becomes more transparent at photon energies above ≈ 5 keV (see chapter 3).

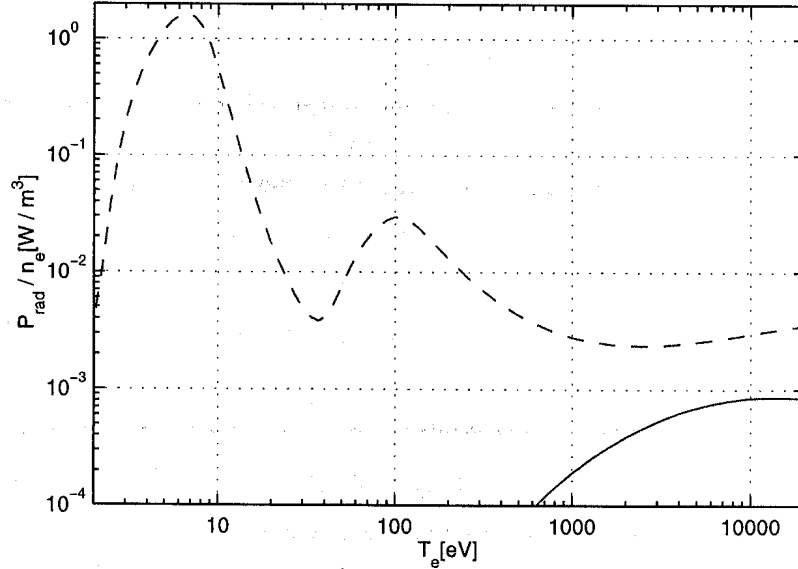


Fig. 2.3 Radiation emitted by carbon ions in corona equilibrium as a function of the electron temperature. A total carbon concentration equal to 1% of the total electron density is assumed. The power emitted is normalised to the electron density n_e and includes continuum and line radiation. The total emitted power is shown as a dashed line. The lower curve gives the corresponding power attenuated by a $47 \mu\text{m}$ beryllium filter and detected by a silicon photodiode which is used in the TCV soft x-ray tomography system.

The corona model may be applied as long as radiative de-excitation dominates over collisional de-excitation. For sufficiently high electron density $n_{e, \text{crit}}$, the collision between an excited atom or ion and an electron may cause a transition to a neighbouring excited level resulting in a reduced radiative de-excitation rate. A criterion for the applicability of the corona model can be obtained by assuming that for $n_e = n_{e, \text{crit}}$ there are as many collisional transitions out of the level p as radiative decays of level p , resulting in a line intensity which deviates by 50% from the value predicted by the corona model at the same density. This criterion can be written

$$n_{e, \text{crit}} X(T_e, p, q) \leq \sum_{s < p}^g A_Z(p, s). \quad (2.39)$$

Inspection of the dependencies of the coefficients X , A_Z on the energy levels reveals that there are always some value of p for which the criterion given in Eq. (2.39) is not satisfied. This occurs

2.3 Types of ionisation equilibrium

because with increasing principal quantum number, the probability of spontaneous decay decreases, whereas that of collisional excitation increases. As practical example, a hydrogenic ion of charge Z with a value $p = 6$ can be chosen [15] and Eq. (2.39) can be evaluated to give [13]

$$n_{e, crit} \approx 6.5 \cdot 10^{16} (Z + 1)^6 \sqrt{T_e} e^{0.1(Z+1)/T_e} \text{ (m}^{-3}\text{)}. \quad (2.40)$$

For a carbon plasma with $T_e = 100$ eV, this gives $n_{e, crit} \approx 3 \cdot 10^{22} \text{ m}^{-3}$ which is 2-3 orders of magnitude higher than electron density in tokamak experiments.

2.3.3 General time-dependent equilibrium model

The steady state corona model, described by Eqs. (2.36), (2.37), neglects not only collisional three-body recombination but more importantly the influence of bulk transport on the different ion species. Furthermore, in many situations, the populations of states are not in equilibrium and therefore a more general model has to be adopted which includes a generalisation to a time-dependent situation. However, simple estimates for the time scales of different processes relevant to the equilibrium indicate that the excited state populations can be assumed to be in equilibrium with the ground state even though the ground state of different ionisation states are not in equilibrium with one another. These estimates may be obtained as follows.

For excitation, the appropriate time scale for equilibrium between two levels i, j is the inverse of the Einstein coefficient A_{ij} [2] whose order of magnitude is given by

$$A_{ij} \approx 10^8 Z^4 \text{ (s}^{-1}\text{)}. \quad (2.41)$$

Thus, the relaxation time is of order $10Z^{-4}$ ns, a time usually extremely short compared to typical transport and pulse time in magnetically confined plasmas. For ionisation equilibrium, the recombination rate given by Eq. (2.23) which in the limit $T_e < \chi_i$ yields

$$\langle \sigma v \rangle = 5.2 \cdot 10^{-20} Z \left(\frac{\chi_i}{T_e} \right)^{1/2} \text{ (m}^3 \cdot \text{s}^{-1}\text{)}. \quad (2.42)$$

For multiple electron species, the highest ionisation stage reached in an equilibrium condition is such that the ratio χ_i/T_e is given by Eq. (2.38) which ranges from about 11 for hydrogen to about

1 at $Z = 20$. Assuming as typical value $\chi_i/T_e \approx 5$, a simple estimate for Z^2 of the highest ionisation stage is given by

$$Z^2 \approx \chi_i/R_y \approx 5T_e/R_y. \quad (2.43)$$

Substituting Eq. (2.43) into Eq. (2.42), gives an approximation for the recombination rate

$$\langle \sigma v \rangle \approx 2 \cdot 10^{-19} \sqrt{T_e/R_y} \text{ m}^3\text{s}^{-1}. \quad (2.44)$$

For example, a typical ohmic TCV plasma, with $T_e \approx 1$ keV and $n_e \approx 5 \cdot 10^{19} \text{ m}^{-3}$, the radiative recombination rate for carbon ($\chi_i \approx 0.5$ keV) is of order $n_e \langle \sigma v \rangle \approx 10 \text{ s}^{-1}$. This results in a time scale for relaxation to ionisation equilibrium of about 100 ms, which is far longer than the excitation time.

With these considerations in mind, the set of equations describing the rates at which the ground state of different ionisation stages are populated may be written as [16]

$$\begin{aligned} \frac{dn_Z}{dt} = n_e \left[n_{Z-1} S_{Z-1} - n_Z S_Z + n_{Z+1} \left(\alpha_{Z+1}^R + \alpha_{Z+1}^D + \frac{n_0}{n_e} \alpha_{Z+1}^{CX} \right) \right] + \dots \\ - n_e n_{Z+1} \left(\alpha_Z^R + \alpha_Z^D + \frac{n_0}{n_e} \alpha_Z^{CX} \right) - \nabla \cdot \Gamma_Z \end{aligned} \quad (2.45)$$

where the particle flux density Γ_Z is usually assumed of the form

$$\Gamma_Z = -D_Z \nabla n_Z + v_Z n_Z \quad (2.46)$$

being D_Z the particle diffusion coefficient and v_Z the convective velocity.

Once the equilibrium described by Eqs. (2.45) has been solved, the populations in the excited states can be calculated by using, for example, the corona model or a less restrictive model in which additional processes are included. This set of partial differential equations is usually solved numerically with experimentally determined $n_e(r)$, $T_e(r)$ profiles. The main advantage of this approach is to separate, as much as possible, impurity transport effects from uncertainties in the transport of the background plasma.

2.4 Ionisation equilibrium codes

2.4 Ionisation equilibrium codes

Once the different ion populations $n_Z(r)$ have been evaluated, the local emissivity $E = E(r)$ in a given spectral range, can be calculated using Eqs. (2.3), (2.10), (2.19). For practical purposes, it is convenient to write the plasma emissivity as

$$E(r) = \sum_z n_e(r) n_Z(r) \epsilon_Z(r) \quad (2.47)$$

where $n_e(r)$ is the electron density and the summation is over all the impurities present in the plasma. $\epsilon_Z(r)$ is the energy integrated spectral emissivity, normalised with respect to n_e and n_Z and takes into account the radiation from all the ionisation stages of the considered species of charge Z . The main advantage of Eq. (2.47) is that the emissivity $E(r)$ is related to measured local plasma parameters. The limitation in the detected spectral range which is due, for example, by transmission of the radiation through a filter and to a limited spectral sensitivity of the detector can be easily taken into account in the calculated normalised emissivity $\epsilon_Z(r)$ resulting in a simulated emissivity $E(r)$ which can be directly compared with experimental data.

On TCV, the calculation of the ionisation equilibrium and the modelling of the radiation is performed using the IONEQ [17] and the STRAHL [18] codes. For each ionisation stage of the impurity, both codes solve the system of Eqs. (2.45) in a 1-D geometry with given electron temperature and density profiles, obtained from experimental measurements. In STRAHL and IONEQ, an ansatz for the anomalous diffusivities D and radial drift velocities is used for evaluating Γ_Z and a full neoclassical impurity transport can be switched on if desired.

An illustration of STRAHL equilibrium calculation is shown in obtained from TCV L-mode discharge No. 16051 with plasma parameters $n_{e0} \approx 7.2 \cdot 10^{19} \text{ m}^{-3}$, $T_{e0} \approx 800 \text{ eV}$. This discharge offers a good opportunity to analyse the modification of the impurity distributions by transport effects. In Fig. 2.4, the radial distribution of carbon charge stages are shown as calculated by assuming corona equilibrium, Fig. 2.4(a,b), and by accounting for transport effects, Fig. 2.4(c,d), with a parabolic diffusion coefficient D which increases from $D = 0.01 \text{ m}^2\text{s}^{-1}$ in the plasma centre to $D = 6 \text{ m}^2\text{s}^{-1}$ at the plasma edge. An inward directed pinch velocity V is calculated in order to obtain a carbon total density profile which is proportional to the electron density profile. For both simulations, a total carbon concentration equal to 1% of the total electron density is assumed.

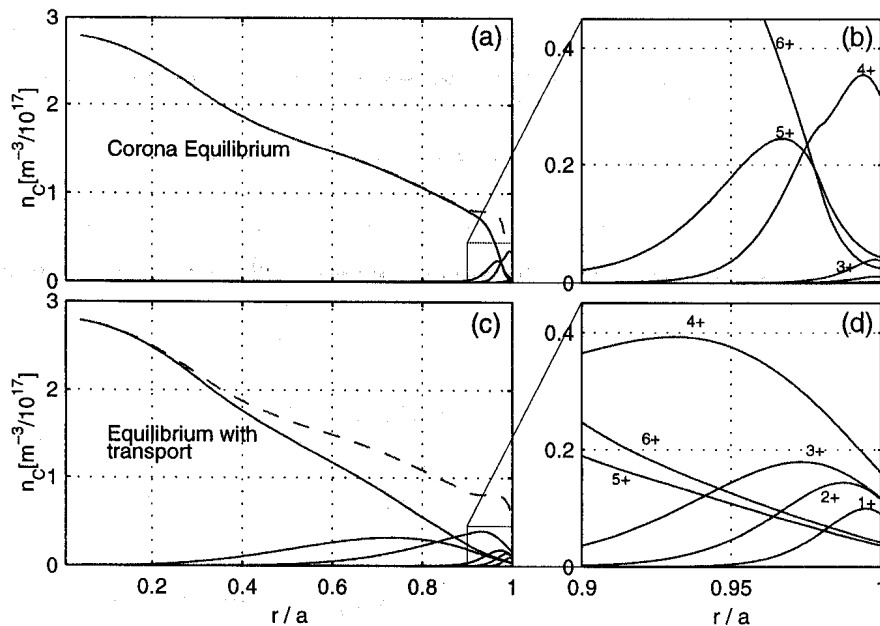


Fig. 2.4 Ionisation equilibrium for carbon in TCV discharge No. 16051 calculated using STRAHL code together with experimental electron temperature and density profiles. In the calculation, a total carbon concentration equal to 1% of the total electron density is assumed. The ionisation stage is denoted by cardinal number: +1 means singly ionised, +6 means completely ionised. The different ionisation stages are shown in corona equilibrium approximation (a) and including transport effects (b). The total carbon density is shown as a dashed line. On the right, an expanded view of the equilibrium for $r/a \in [0.9, 1]$.

For $r/a \in [0, 0.2]$, corresponding to electron temperature of approximately 800 eV, carbon is completely ionised (C6+) and the calculated profiles for all ionisation stages are almost the same for both types of equilibrium. In corona equilibrium, the lower ionisation stages are concentrated in hollow shells near the plasma periphery, typically outside $r = 0.9a$, as shown by the expanded view in Fig. 2.4(b). The distribution of these lower ionisation stages is significantly modified by transport resulting in a broadened and inward shifted distribution for all the ionisation stages.

In Fig. 2.5, the calculated emissivity profiles corresponding to the carbon ionisation stage distributions in Fig. 2.4 are shown for the total radiated power, Fig. 2.5(a), and in the soft x-ray spectral range, Fig. 2.5(b). The latter is calculated by accounting for attenuation by a 47 μm beryllium filter and for the spectral sensitivity of the photodiode detector. Emissivity profiles corresponding to corona equilibrium are shown as dashed lines.

The total radiated power is strongly enhanced by transport effects outside $r = 0.1a$ while inside

2.4 Ionisation equilibrium codes

this region it is almost unchanged. At the plasma edge, typically outside $r = 0.9a$, this enhancement is mainly due to the line radiation contribution from B-, Be- and Li-like carbon ions while for inner region, $r \in [0.1, 0.7]$, the power is mainly radiated by He- and H-like carbon ionic stages. Since line radiation from carbon is mainly emitted at energies well below the energy cut-off of the beryllium filter (≈ 1 keV), transport effects do not significantly modify the soft x-ray emissivity profile in Fig. 2.5(b).

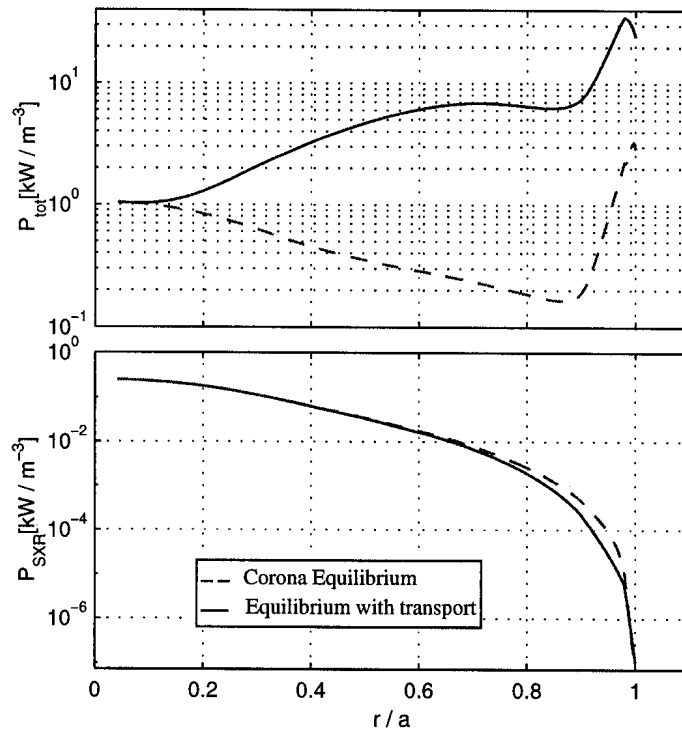


Fig. 2.5 Radiation emissivity profiles for carbon in TCV discharge No. 16051 calculated using experimental T_e and n_e profiles. Dashed lines correspond to radiation emitted in corona equilibrium. Continuous lines are calculated including transport effects with a parabolic diffusion coefficient increasing from $D = 0.01 \text{ m}^2\text{s}^{-1}$ in the centre to $D = 6 \text{ m}^2\text{s}^{-1}$ at the plasma edge. Top: total radiated power. Bottom: radiation detected in the soft x-ray range, obtained by attenuating the total emissivity by a $47 \mu\text{m}$ beryllium filter. The spectral sensitivity of the photodiode detector is also accounted for in the calculation.

2.5 Conclusions

In this chapter, a review of the main characteristic of the radiation emitted from a plasma has been given. On TCV, emission in the soft x-ray spectral range, which is extensively studied in this thesis, is largely dominated by the continuum (i.e. Bremsstrahlung and recombination) contribution for most plasma conditions. Despite the complexity of the processes involved, few relatively simple formulas relate the soft x-ray emissivity to the electron density and temperature, and to the plasma purity. Therefore, soft x-ray measurements together with ionisation equilibrium codes and additional independent diagnostics provide a powerful tool for measuring basic plasma parameters. In the following two chapters, the diagnostics and methods used in the interpretation of the soft x-ray radiation are presented.

References

- [1]G. Bekefi, *Radiation processes in plasmas*, John Wiley and Sons, New York-London-Sidney, 1966.
- [2]I. H. Hutchinson, *Principles of plasma diagnostic*, Cambridge University Press, Cambridge, 1987.
- [3]M. Bornatici, et al., *Nucl. Fusion* **23**, (1153) 1983.
- [4]S. Coda, et al., *Proc. 26th EPS Conf. on Controlled Fusion and Plasma Physics* (Maastricht 1999), Vol. 23J, page 1097.
- [5]J. D. Jackson, *Classical Electrodynamics*, John Wiley and Sons, New York, 1975.
- [6]G. Elwert, *Ann. Phys.* **34** (1939) 178.
- [7]W. Heitler, *The quantum theory of radiation*, Oxford Univ. Press, London, 1944.
- [8]H. A. Kramers, *Phil. Mag.* **46** (1923) 836.
- [9]S. Van Goeler, *Diagnostic for Fusion Experiments*, Proc. Int. School of Plasma Physics, Varenna 1978. E. Sindoni and C. Wharton, eds. London: Pergamon.
- [10]H. Weisen, et al., *Proc. 23rd EPS Conf. on Controlled Fusion and Plasma Physics* (Kiev 1996), ECA **20C** part 1, page 111.
- [11]A. Burgess, *Astrophys. J.* **141** (1965) 1588.
- [12]H. Ryufuku, et al., *Phys. Rev. A* **20** (1979) 1828.
- [13]R. P. Mc Whirter, *Plasma Diagnostic techniques*, R. H. Huddelstone and S. L. Leonard eds., New York, 1965.
- [14]G. Elwert, *Z. Naturforsch.* **7a** (1952) 432.

2.5 Conclusions

- [15]R. H. Huddlestone, *Plasma Diagnostic Techniques*, Academic Press, New York and London, 1965.
- [16]R. D. Gill, *Plasma Physics and Nuclear Fusion Research*, Academic Press, London, 1981.
- [17]A. Weller, et al., *JET Report No. JET-IR(87) 10* (1987).
- [18]K. Behringer, *JET Report No. JET-R(87) 08* (1987).

3 DIAGNOSTICS ON TCV

This chapter provides a description of TCV diagnostics that were used for this work. Owing to the dependence of the soft x-ray emissivity on n_e and T_e (see chapter 2), the effects of the sawtooth oscillations are particularly visible on the soft x-ray measurements. An overview of different soft x-ray diagnostics in TCV is given. In particular, section 3.1 details the 200 channel soft x-ray tomographic system which allows the monitoring of the sawtooth crash ≈ 10 times faster than the crash duration (typically $\approx 100 \mu\text{s}$). This system is the key diagnostic for the physical investigations of chapters 5 and 6 and provides line integrated measurements which are tomographically inverted to obtain the local soft x-ray emissivity distribution. The foundation of the tomographic inversion techniques are reviewed in section 3.2 with a particular attention to those used for TCV soft x-ray data. Section 3.3 describes other TCV diagnostics which are relevant to this thesis. In particular, the 14 chord far infrared interferometer is described which provides measurements of the line integrated electron density with a sufficiently high temporal resolution to resolve the particle pump-out phenomenon discussed in chapter 7. To obtain the local electron density from interferometer data a modified Abel inversion method was developed which is described also in this section.

In section 3.4, the design and first results are presented from a bolometric diagnostic with high temporal resolution which was developed in the course of this thesis. Although fast bolometric data were only partially exploited in the thesis they are potentially important in the study of transient phenomena such as fast MHD activity hitherto inaccessible with standard bolometric techniques. Therefore, a short overview of the main features is given for completeness.

3.1 Soft x-ray tomographic system

3.1.1 Hardware set-up.

The TCV soft x-ray tomographic system consists of 10 pinhole cameras at a single toroidal location, Fig. 3.1. Each camera is equipped with a linear array of 20 p-n junction silicon photodiodes resulting in 200 lines of sight covering the whole poloidal cross section as homogeneously as possible since plasmas of almost arbitrary shape and size can be produced in TCV. Due to the different portholes available on TCV, three different types of cameras were required which differ only in their size and the position of the detector head. The detailed design features common to all the cameras are illustrated in Fig. 3.2. The camera housing comprises three

concentric stainless steel cylinders, with water flow in the innermost gap providing active cooling of the detectors during vessel bakeout (up to 300 °C), while the gap between the outermost two cylinders can be evacuated to improve the thermal insulation.

The TCV Tomographic system

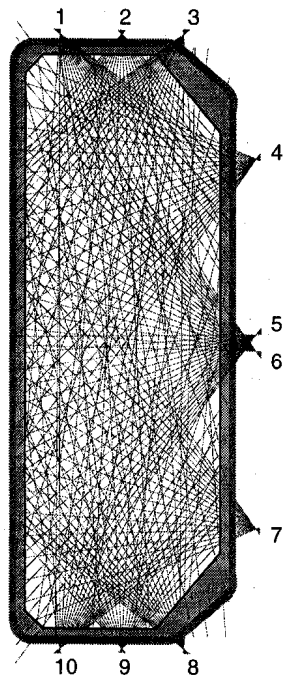


Fig. 3.1 A view of the experimental set-up of the TCV soft x-ray tomographic system. The vacuum vessel is shown, together with the carbon tiles.

A stainless steel plate, supported by short bellows and located a few centimetres behind the protective graphite tiles lining the vacuum vessel, is installed to prevent the camera interior from overheating during vessel bakeout. An aluminium plate which closes the rear camera holds a vacuum feedthrough for the electrical connections as well as the connection to the primary vacuum which is required inside the camera to avoid absorption of the x-rays between the beryllium filter and the detectors (see Fig. 3.2). The photodiode array is mounted on a circular printed circuit ($\varnothing = 55$ mm) which is fixed to the inner front plate of the camera. The current-to-voltage converters with a transimpedance gains of 2.2×10^5 VA⁻¹ and a bandwidth of 200 kHz are mounted on the seen side of the printed circuit. Preamplifiers outputs are collected by twisted pairs of cables with a ground and a signal for each photodiode grouped in a single 12-m-long shielded cable containing 22 pairs (20 signals and a ± 15 V power supply). The signals are filtered by a 3 pole

low-pass, Bessel filter with a cut-off frequency of 25 kHz and then fed to voltage amplifiers with remotely controllable gain (1, 10, 100, 1000). Both the filter and the amplification stage are housed in a standard VME rack. Separation of the torus vacuum and camera vacuum is provided by a 47 μ m beryllium foil which is bonded with an epoxy cement to the first front plate of the camera. The beryllium foil is curved to obtain equal absorber thickness for all the detectors. This is necessary to avoid an excessive dependence of the filter-photodiode efficiency on the angle of incidence and the spectrum of the incident radiation [1].

3.1 Soft x-ray tomographic system

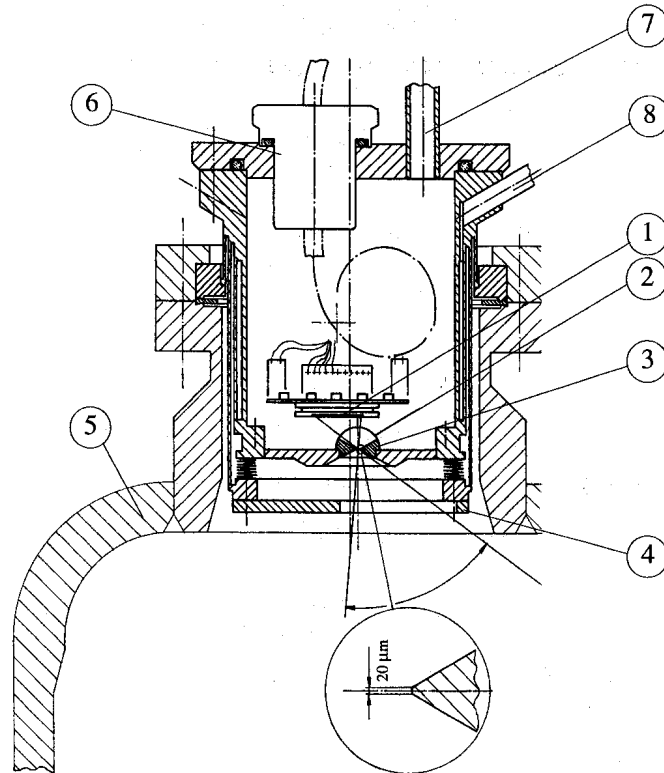


Fig. 3.2 Cross section of TCV soft x-ray pinhole camera: (1) CENTRONIC LD20-5T photodiode array with preamplifier circuit; (2) 47 μm thick curved beryllium filter; (3) poloidally limiting tungsten aperture, the details shown the trapezoidal of its edges; (4) front plate limiting the toroidal aperture; (5) TCV vessel; (6) vacuum feedthrough for electrical connections; (7) to primary vacuum pumps; (8) to the cooling system.

3.1.2 Detector array

Each camera is equipped with a LD20-5T linear array of 20 silicon p-n junction photodiodes produced by CENTRONIC, and designed for visible and ultraviolet radiation. The active surface of a single photodiode is $4 \times 0.95 \text{ mm}^2$ with a separation of 0.05 mm between neighbouring elements resulting in a total length of an array of 55 mm. The entire surface of the photodiode is covered by a 55 nm Si_3N_4 passivation layer. The photodiodes were calibrated using a tabletop soft x-ray source in order to obtain a precise relative response between detectors [1].

In the following, we briefly review the fundamental equations describing the photodiode efficiency and we summarise the typical parameters of the CENTRONIC LD20-5T array.

The efficiency η of a detector is defined as the percentage of incident photons generating electron-

hole pairs which subsequently contribute to the output signal. A formula for calculating the photodiode efficiency is given in Ref. [2]

$$\eta = \prod_i \exp(-\alpha_i d_i) [1 - \exp(\alpha V)] \times \left\{ 1 - \frac{\alpha L_p}{1 + \alpha L_p} \left[1 - \exp\left(-\frac{\alpha + 1/L_p}{D - V}\right) \right] \right\} \quad (3.1)$$

where α_i and d_i denote respectively the absorption coefficient and the thickness of the filtering materials in front of the active zone of the photodiode, $\alpha = \alpha(v)$ is the absorption coefficient of silicon, which depends on photon energy $E = hv$, V is the thickness of the depletion zone, L_p is the diffusion length of the minority carriers (electrons), D is the thickness of the n-type silicon substrate.

The efficiency η is a function of the photon energy because of the energy dependence of all the absorption coefficients α and α_i . For the TCV tomographic system, the filters in front of the photodiodes include the passivation layer ($d_{Si_3N_4} = 55$ nm), the beryllium filter ($d_{Be} = 47$ μ m) and the p^+ zone (dead layer) whose mean thickness has been found to vary from array to array between 0.6 and 0.8 μ m with an error of $\approx \pm 0.1$ μ m [1]. The values of the diffusion lengths for the LD20-5T detectors are very similar ($L_p = 200 \pm 20$ μ m) and are in agreement with an estimate by the supplier. The n-type silicon substrate thickness $D = 380$ μ m. Since the photodiodes are used in the unbiased mode, the thickness of the depletion zone can be estimated to be $V \approx 3$ μ m from the capacitance per unit surface area given in the manufacture's data sheet.

With these photodiode and beryllium filter parameters, we can determine the detection efficiency of the TCV tomographic system using Eq. (3.1). The data for the total photoabsorption cross section are taken from Ref. [3]. Fig. 3.3 shows the detection efficiency as a function of photon energy of a LD20-5T photodiode alone (dashed line) and of a LD20-5T photodiode filtered by 47 μ m Be filter (continuous line). The latter corresponds to the arrangement used in the TCV soft x-ray tomographic system. Photons of energies less than approximately 1 keV are filtered by the 47 μ m Be filter (continuous line). In both cases, the decrease of the detection efficiency at high energy is due to the finite thickness of silicon substrate, $D = 380$ μ m, which becomes more transparent at photon energies above about 5 keV. From the continuous curve in Fig. 3.3, the TCV system is most efficient for the detection of photons with energies between 1 and 10 keV which cover the thermal spectrum of most TCV plasmas.

3.1 Soft x-ray tomographic system

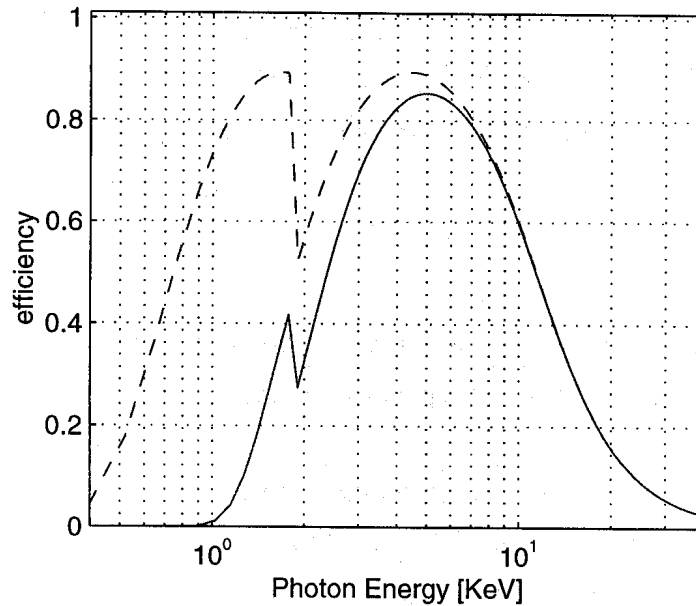


Fig. 3.3 The efficiency $\eta(\nu)$ as a function of the photon energy of a CENTRONIC LD20-5T detector alone (dashed line) and filtered by 47 μm Be filter (continuous line). The photodiode is passivated by 55 nm Si_3N_4 . A dead layer of $d_p=0.8 \mu\text{m}$ and diffusion length $L_p=200 \mu\text{m}$ are assumed.

3.1.3 Acquisition system

On TCV, the timescale of the sawtooth crash is faster than 100 μs . In the original configuration [4], data from the soft x-ray tomographic system were acquired by CAMAC modules with a maximum acquisition frequency of 10 kHz, which did not resolve the sawtooth crash phase. In the frame of this thesis, this limitation has been overcome by installing a new acquisition system, named T-REX3, which has an acquisition frequency ≈ 10 times faster than the sawtooth crash time. Since the T-REX3 was a new acquisition system first tested on TCV, a large effort was required to write the software to perform the data acquisition, retrieval and storage in the TCV database. In the following, a brief description of the system is given.

Analog-to-digital conversion and data acquisition are performed by a transient recorder based on a Vanguard 16 bit VME-based ADC which was also used to acquire the data from the fast bolometric system (see section 3.4). The transient recorder comprises 288 simultaneous A/D converters, grouped in three identical banks of 96 channels, each feeding a separated VBS bus and

a 64 Msample memory board which can acquire for up to 4 s at the maximum acquisition rate. The three modules are controlled by a SUN processor linked to the TCV tokamak data acquisition system via an Ethernet interface. Signals are digitised at the maximum acquisition rate of 80 kHz and stored on a local 2 GB disk drive. Complete data archiving in the TCV database for each discharge is impracticable so that the acquired signals are sampled down to 10 kHz with the option for higher frequency storage (up to 80 kHz) in multiple selected time windows. For all acquisition processes with an effective sampling rate < 80 kHz, anti-aliasing bandwidth reduction is performed on the local processor by a software routine, written in C-language, which implements a non-causal, non-recursive FIR filter with linear phase response and steep cut-off slopes. The choice of the low level C language for the main routines was motivated by the requirement of rapidity of the acquisition process. Data acquisition in the local memory boards, retrieval and storage in the TCV database of 288 channels, sampled at 80 kHz, during a 3 s pulse requires ≈ 700 s which is shorter than the time between two consecutive TCV discharges.

3.2 The tomographic problem

3.2.1 Definition of the problem

Much of the foundation of tomographic imaging used in plasma physics was pioneered by research in the field of medicine [5]. In both fields, the local properties of an object are to be reconstructed from line-integrated measurements. There are however some important differences between the two applications. Whereas in medical tomography the absorption of x-rays is measured, in plasma physics applications one is interested in the radiation emitted by the plasma. Although this requires different instrumentation, the mathematics of the problems remains the same. The second major difference is in the number of available measurements. Due to the difficulty of accessibility, the number of line integrated data in fusion research is usually limited to the order of some 10^2 , whereas in medical tomography some 10^5 x-ray absorption measurements are taken in a very regular pattern. This disparity has consequences on the methods, which can be optimised for solving the tomographic problem. In the following, we will formulate the tomographic problem with the emphasis on applications in fusion research.

Let us consider a system consisting of n_i detectors at one toroidal position, $\varphi = \varphi_0$, observing the plasma perpendicularly to the toroidal direction. The local emissivity of the plasma, which we assume to be isotropic, is to be reconstructed in a 2-D planar slice defined by $|\varphi - \varphi_0| \leq \Delta\varphi$, being

3.2 The tomographic problem

$\Delta\varphi$ the toroidal width defined by the collimating optics of the system. We will assume that the emissivity does not have any toroidal variation over this width (thin slice approximation). In the TCV tomographic system, the photodiode arrays view a toroidal slice about 1.5 cm thick at the plasma poloidal midplane, compared to a vessel circumference of $2\pi R_0 \approx 5.5$ m, so the thin slice approximation is valid as long as there is no MHD activity with very high toroidal mode numbers.

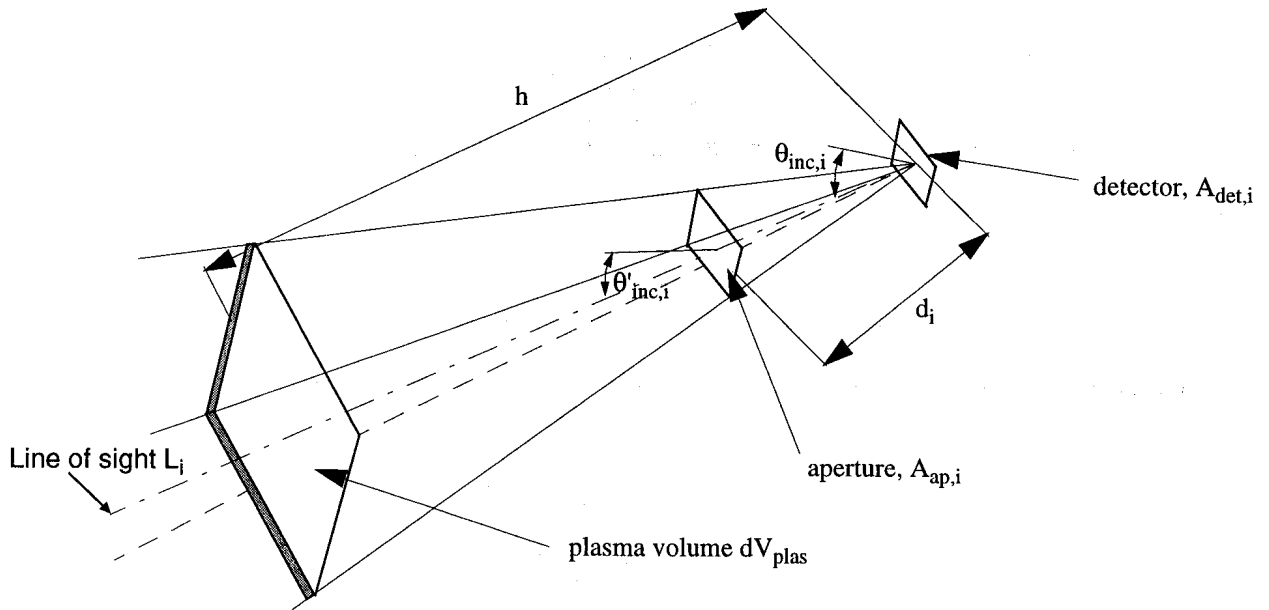


Fig. 3.4 Solid angle geometry for a detector viewing the plasma through a simple aperture.

We assume that the solid angle viewed by the detector i is defined by a single slit of area $A_{ap,i}$. The spectral range of the radiation incident on the detector is selected by a filter which does not limit the solid angle viewed by the detector. The efficiency of the detector-filter combination is given in section 3.1.2 by $\eta_i(\nu)$, being ν the frequency of the radiation.

Fig. 3.4 shows the optical arrangement for a detector of infinitesimally small area, A_i .

Provided that the plasma is optically thin for the spectral range of the detected radiation and refraction effects can be neglected, the fraction of the power emitted from an elementary volume element of plasma, dV_{plas} , which is measured by the detector is

$$dP_i = \int G(\vec{r}, \nu) \eta_i(\nu) dV_{plas} \frac{\cos(\vartheta_{inc,i}) A_{det,i}}{4\pi h^2} d\nu. \quad (3.2)$$

Here, $G(\bar{r}, \nu)$ is the local spectral emissivity at the point \bar{r} , h is the distance between the detector and the plasma volume element, and $\vartheta_{inc,i}$ is the angle between the direction perpendicular to the detector and the axis of the cone of view. In the following, the axis of this cone is referred to as 'line of sight' and indicated by L_i .

If the field of view of the detector is sufficiently narrow, we can assume that the emissivity does not vary on a surface perpendicular to the line of sight. This leads to

$$dV_{plas} = dl_i \times \frac{\cos(\vartheta'_{inc,i}) A_{ap,i} h^2}{d_i^2}, \quad (3.3)$$

where d_i the distance between the aperture and the slit (see Fig. 3.4), dl_i is measured along the line of sight L_i and $\vartheta'_{inc,i}$ is the angle between this and a direction perpendicular to the aperture. Introducing Eq. (3.3) into Eq. (3.2) allows to transform the volume integral into a line integral along the line of sight giving the following expression for the total power detected

$$P_i = \left[\frac{\cos(\vartheta'_{inc,i}) \cos(\vartheta_{inc,i}) A_{det,i} A_{ap,i}}{4\pi d_i^2} \right] \int_{L_i} dl_i \int G(\bar{r}, \nu) \eta_i(\nu) d\nu \quad (3.4)$$

where the quantity in square brackets can be taken outside the integral. This is justified by a theorem of geometrical optics [6] which states the conservation of the etendue of an optical system

$$(A\Omega)_i = \frac{\cos(\vartheta'_{inc,i}) \cos(\vartheta_{inc,i}) A_{det,i} A_{ap,i}}{d_i^2}. \quad (3.5)$$

Usually, the quantity in squared brackets in Eq. (3.4) is taken to the left side of the equality and using the definition in Eq. (3.5) the chord brightness f_i is defined as

$$f_i = \frac{P_i}{(A\Omega)_i / (4\pi)} \quad (3.6)$$

which is independent of the geometrical optical arrangement, and therefore is a suitable quantity to express line integrated data with units of $[W/m^2]$.

A further generally applied approximation is to assume that possible differences in the detector response can be allowed for by using a calibration factor c_i for every detector, which leads to

$$f_i = c_i \int_{L_i} g(\bar{r}) dl_i \quad (3.7)$$

3.2 The tomographic problem

where the emissivity

$$g(\vec{r}) = \int G(\vec{r}, \nu) d\nu \quad (3.8)$$

has been defined. Equation (3.7) is exact for spectrum independent detector efficiencies, which is not often the case as seen in section 3.1.2. On TCIV, to overcome this problem a spectrum averaged efficiency [1] is introduced which accounts for possible differences in the detection efficiencies between photodiodes in the manner proposed in Ref. [4].

From the mathematical point of view, the tomography problem consists of solving the system of inhomogeneous Fredholm integral equations of the first kind [7]

$$f_i = \int_{L_i} g dl_i \text{ for } i = 1, \dots, n_i \quad (3.9)$$

where the chord brightnesses on the left are provided by the soft x-ray experimental measurements, while on the right side, the kernel of the integral is the emissivity function, defined by Eq. (3.8), which has to be determined.

In the next section, different methods for inverting Eqs. (3.9) will be described. The following should however be noted; if the emissivity is circularly symmetric, i.e. $g = g(r)$, then Eq. (3.9) reduces to a 1-D integral commonly called the Abel transform which has a well known analytical solution [8]

$$g(r) = -\frac{1}{\pi} \int_r^a \frac{1}{\sqrt{p^2 - r^2}} \frac{d}{dp} f(p) dp, \quad (3.10)$$

where the impact parameter p is the distance between the line of sight and the origin of the coordinate system (see Fig. 3.5).

On TCIV, strongly shaped plasmas are produced and consequently the simple Abel inversion is not of much use. Also, the system described by Eqs. (3.9) is always underdetermined, since an infinite number of measurements f_i would be required to determine g over the whole space, whereas only a limited number of measurements are available. This poses severe restrictions to the spatial resolution of the system, as described in the next section.

3.2.2 Tomographic inversion methods

3.2.2.1 Expansion in basis functions

An analytical solution of the tomographic problem, defined by the system of Eqs. (3.9), was proposed in 1963 by Cormack [9], [10] who demonstrated its application in x-ray medical imaging. The merit of this method is to provide a clear description of limitations in the spatial resolution which are achievable given the finite number and arrangement of chord measurements. Since the analytical approach is well described in the literature and extensively implemented in many tokamak and stellarator experiments [11], [12], [13], [14], in the following only the main points are presented together with a brief discussion of their consequences.

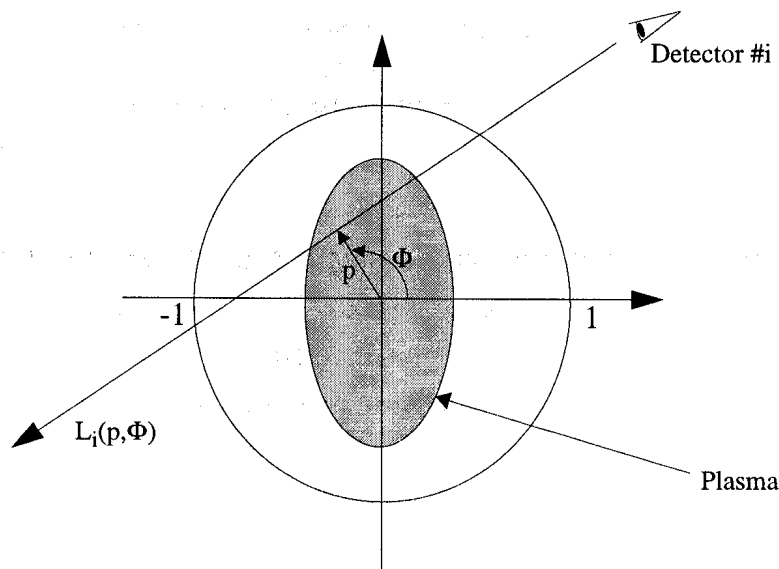


Fig. 3.5 In the optically thin plasma approximation, the signal of a detector collimated by a pin-hole is obtained by integrating the local emissivity along the line of sight $L_i(p, \phi)$. The angle ϕ and the impact parameter p define uniquely every possible chord through a circular region containing the plasma.

In Eqs. (3.9), we can define each line of sight L_i by two parameters: the impact parameter p and the impact angle ϕ as illustrated in Fig. 3.5. The pseudo coordinates (p, ϕ) span the range $0 \leq p \leq 1$ and $0 \leq \phi \leq 2\pi$. If we use a polar coordinate system (r, ϑ) in the real space, Eqs. (3.9) define an integral transformation of the local emissivity $g(r, \vartheta)$ in (r, ϑ) -space into the line

3.2 The tomographic problem

integrated brightness $f(p, \phi)$ in (p, ϕ) -space.

Cormack's method decomposes the 2-D quantities in Eqs. (3.9) into their Fourier harmonics:

$$g(r, \vartheta) = \sum_{m=0}^{\infty} [g_m^c(r) \cos(m\vartheta) + g_m^s(r) \sin(m\vartheta)] \quad (3.11)$$

$$f(p, \phi) = \sum_{m=0}^{\infty} [f_m^c(p) \cos(m\phi) + f_m^s(p) \sin(m\phi)]. \quad (3.12)$$

The coefficients $g_m^{c,s}(r)$ are further expanded into a complete set of orthogonal functions, known as Zernicke polynomials, $R_{ml}(r)$, such that

$$g_m^{c,s}(r) = \sum_{l=0}^L a_{ml}^{c,s} R_{ml}(r) \quad (3.13)$$

where

$$R_{ml}(r) = \sum_{s=0}^l r^{m+2l-2s} \frac{(-1)^s (m+sl-s)!}{s!(m+l-s)!(l-s)!}. \quad (3.14)$$

Using this expansion, a very simple solution for the Fourier components of the brightness $f_m^{c,s}(p)$ can be obtained which, after substitution into Eq. (3.12), yields a set of equations relating the expansion coefficients $a_{ml}^{c,s}$ to the measured quantities, $f(p, \phi)$:

$$f(p, \phi) = \sum_{m=0}^M \sum_{l=0}^L [a_{ml}^c \cos(m\phi) + a_{ml}^s \sin(m\phi)] \times \dots \frac{2}{m+2l+1} \sin[(m+2l+1) \cos^{-1}(p)] \quad (3.15)$$

The above harmonic decomposition gives an exact analytical solution for the emissivity coefficients $a_{ml}^{c,s}$ so long as the sums over m and l are infinite. Since this is not possible with real data because only a finite number of chord measurements are available, a truncation of the two sums, at certain maximum values, M and L , is necessary in order to solve the system of equations.

The maximum number M , which defines the poloidal resolution of the system, is determined by the number of pinhole cameras and their distribution around the poloidal cross section.

Comparing Eq. (3.15) with Eq. (3.12), it can be seen that in order to resolve the m th spatial

harmonic of the emissivity, the m th spatial harmonic of the brightness is required. In the ideal case, where N identical cameras are distributed uniformly around the poloidal cross section of the machine, the brightness is measured at $2N$ values of the impact angle ϕ for each value of the impact parameter p . The Nyquist theorem therefore limits the maximum resolvable number of poloidal harmonics to $m = N - 1$ and one component of $m = N$, while any higher harmonics cannot be resolved and will be aliased to lower spatial harmonics.

The Nyquist theorem can be similarly used to determine the maximum order of the Zernicke polynomial L which defines the radial resolution of the system. The highest Zernicke polynomial should have a node spacing about equal to chord spacing in the p coordinates.

Although the analytic solution was derived in the context of medical imaging, the complicated spatial structures in a cross section would require a huge number of harmonics in the expansion (3.15). The Zernike polynomials are thus not well adapted in describing a medical x-ray image. They are well suited for describing a circular poloidal cross section of a tokamak plasma where MHD equilibrium and instabilities are expected to consist predominantly of low poloidal mode numbers. For plasmas with non-circular poloidal cross section, methods have been developed which use magnetic flux coordinates derived from magnetic equilibrium codes [15].

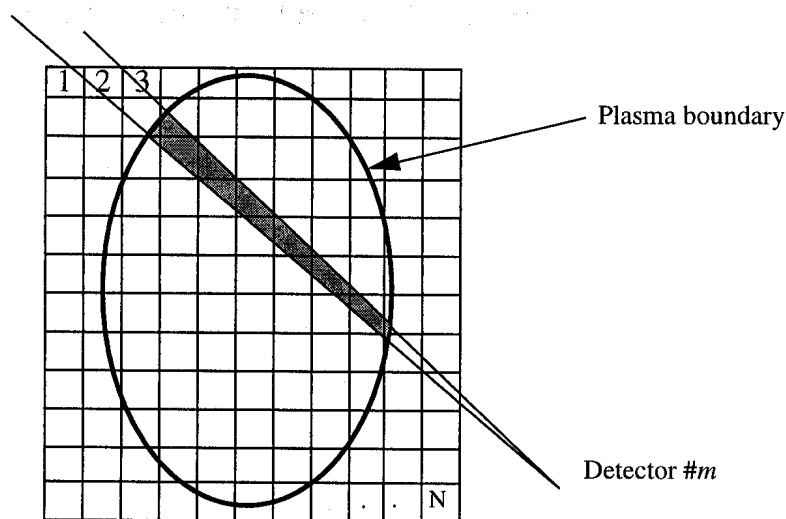


Fig. 3.6 Finite element techniques divide the cross section into pixels which can have arbitrarily complicated shapes. The transfer matrix T of the problem is calculated by adding the contribution of each pixel to each detector.

3.2 The tomographic problem

3.2.2.2 Pixel methods

Another possibility for solving the system of Eqs. (3.9) consists of approximating the line integration as a summation, as done in finite element techniques. This method begins by dividing the emitting region into a number of finite elements or “pixels” within in which the emissivity is assumed to be constant. The size of the pixels has to be sufficiently small to justify the previous ansatz and at the same time the number of pixels has to be sufficiently small to provide a tractable system of equations. The pixels have an arbitrary shape: squared pixels, radially concentric pixels with and without angular separation, concentric pixels determined by the flux surface geometry. In what follows, we restrict our analysis to the case of a rectangular grid of n_x horizontal and n_y vertical squared pixels as shown in Fig. 3.6. The total number of pixels is $n_{pixel} = n_x n_y$. This ansatz has two main advantages: the unformativeness of the assumption and the straightforward way in which the system of Eqs.(3.9) can be described by a set of algebraic equations.

Each detector views a number of squared pixels and therefore the power P_i measured by the detector i can be expressed as

$$T_{i1}g_1 + T_{i2}g_2 + \dots + T_{iN}g_N = P_i \quad (3.16)$$

where g_j is the emissivity in the j pixel and the coefficients T_{ij} represent the fraction of the radiation emitted from the pixel j which is incident on the detector i .

Using the chord brightness defined by Eq. (3.6), the set of n_i simultaneous linear Eqs. (3.16) can be arranged into the matrix form

$$\mathbf{f} = \mathbf{T} \cdot \mathbf{g} \quad (3.17)$$

where the symbol \cdot indicates the usual matrix multiplication. In the simplest approximation, the matrix element T_{ij} equals the length of the line of sight L_i in the pixels number j and the size of \mathbf{T} is $n_i \times n_{pixels}$. A straightforward inversion of the finite-elements problem, defined by Eqs. (3.17), is frequently a mathematically ill-posed problem, even for the case $n_i = n_{pixels}$. The transfer matrix \mathbf{T} may be almost singular as a result of the geometrical arrangement of the detector. This results in very large eigenvalues with consequent amplification of any experimental uncertainties.

As long as $n_i \geq n_{pixels}$, there is a well-defined unique solution, in the least squared sense, which

can be found by minimising the functional

$$\chi^2 = (\tilde{T} \cdot \mathbf{g} - \tilde{\mathbf{f}})^T \cdot (\tilde{T} \cdot \mathbf{g} - \tilde{\mathbf{f}}) \quad (3.18)$$

where the exponent T denotes transposition and the abbreviations $\tilde{T}_{li} = T_{li}/\sigma_l$ and $\tilde{f}_i = f_i/\sigma_i$ has been introduced, being σ_i the error of the chord brightness measurement f_i . The solution of the set of normal equations

$$\tilde{T}^T \cdot \tilde{T} \cdot \mathbf{g} = \tilde{T}^T \cdot \tilde{\mathbf{f}} \quad (3.19)$$

yields a least-squares-fit solution to the tomographic problem [7]. However, even though a solution exists, it does not necessarily bear any resemblance to the actual emission pattern due to the considerations above.

In the opposite case of underdetermined problem, i.e. much fewer equations than unknowns, a solution which satisfies $\chi^2 = 0$ can always be found in the $[n_{pixel} - n_i]$ -dimensional space of the kernel of Eq. (3.17). To obtain a unique and *sensible* solution, in this case, we can minimise a functional ϕ which can be written as

$$\phi = \frac{1}{2}\chi^2 + \alpha R \quad (3.20)$$

where R is a regularising functional and α is a positive definite parameter. The functional R constrains the solution \mathbf{g} to have supplementary requirements, for example smoothness, and the parameter α determines the weight between the goodness of fit, represented by χ^2 and these regularisation requirements. In the limit $\alpha \rightarrow 0$, the solution is determined by the experimental data alone, while in the case $\alpha \rightarrow \infty$ only the smoothing (or whatever we may have required) determines the solution. The most likely solution to the tomographic problem must be somewhere in between, so, once the functional R has been chosen, the first step consists in choosing the “correct” value for this regularisation parameter, and then the second step in finding a solution for a given value of α .

In the following, we will discuss in details the minimum Fisher information (MFI) method which is the method routinely used for the tomographic inversions of soft x-ray data on TCV [1]. A comparison of the performance of the different tomography algorithms for TCV soft x-ray data can be found in Ref. [1]. The MFI method was chosen since it presents the best compromise with

3.2 The tomographic problem

respect to the speed of calculation, precision and stability with respect to noisy data.

Since this method is basically a modified linear regularisation method, we begin our discussion with the latter.

In the linear regularisation algorithm, the solution \mathbf{g} of the system of Eqs. (3.17) must be a smooth function and provide a reasonable fit to the data. A measure of the “roughness” of the solution can be obtained from the gradients, therefore a suitable choice of the functional R is

$$R = \|\mathbf{g}_x\|^2 + \|\mathbf{g}_y\|^2 \quad (3.21)$$

where \mathbf{g}_x and \mathbf{g}_y denote the partial derivatives with respect to the x and y coordinate respectively. If we assume that ∇_x and ∇_y are the finite-difference matrix representations of the corresponding differential operators, we can write

$$R = (\nabla_x \mathbf{g})^T \cdot (\nabla_x \mathbf{g}) + (\nabla_y \mathbf{g})^T \cdot (\nabla_y \mathbf{g}) . \quad (3.22)$$

By defining

$$\mathbf{H} = \nabla_x^T \cdot \nabla_x + \nabla_y^T \cdot \nabla_y \quad (3.23)$$

and using Eqs. (3.18), (3.20), (3.22) the solution to the tomographic problem can be found by minimising the functional

$$\phi = \frac{1}{2}(\tilde{\mathbf{T}} \cdot \mathbf{g} - \mathbf{f})^T \cdot (\tilde{\mathbf{T}} \cdot \mathbf{g} - \mathbf{f}) + \alpha \mathbf{g}^T \cdot \mathbf{H} \cdot \mathbf{g} . \quad (3.24)$$

Setting all partial derivatives $\partial\phi/\partial g_j$ to zero in Eq. (3.24), the set of n_{pixel} normal equations can be obtained [7]

$$(\tilde{\mathbf{T}}^T \cdot \tilde{\mathbf{T}} + \alpha \mathbf{H}) \cdot \mathbf{g} = \tilde{\mathbf{T}}^T \cdot \tilde{\mathbf{f}} \quad (3.25)$$

which have to be solved for \mathbf{g} . This can be done by standard method such as LU decomposition [7]. A criterion for determining the ‘correct’ parameter α must be given which will be discussed later. Here, with the linear regularisation methodology in mind, we now introduce the MFI method.

The Fisher information of a probability distribution $g(x)$ is defined as

$$I_{Fisher} = \int \frac{g'(x)^2}{g(x)} dx \quad (3.26)$$

where the prime ' denotes the derivative with respect to the variable x . The principle of MFI is widely used in estimation theory to determine an unknown probability distribution given some of its moments or any other information on g . A wide range of applications together with some philosophical background can be found in Refs. [16], [17].

MFI is essentially a smoothing principle similar to the linear regularisation method, described above. In Eq. (3.26), the division by $g(x)$ assures particularly smooth solutions in region of low $g(x)$, whereas smoothing is less strong where $g(x)$ is large. This property of MFI is well suited for the soft x-ray tomographic problem as measurements along lines of sight through regions of low emissivity have poorer signal-to-noise ratio and therefore they should be preferentially smoothed. Conversely, the plasma centre corresponds to higher level of soft x-ray emissivity which contributes to line integrated measurements with high signal-to-noise ratio and which should not be unnecessarily oversmoothed.

In solving the problem, we exploit this feature rather than treating the fully non-linear problem as outlined in Refs. [16], [17]. Starting from the first order linear regularisation, we are free to add a diagonal matrix W , as long as all the elements are positive definite ($W_{ij} = W_{ii}\delta_{ij} > 0$)

$$H \rightarrow H^{(n)} = \nabla_x^T \cdot W \cdot \nabla_x + \nabla_y^T \cdot W \cdot \nabla_y \quad (3.27)$$

In order to minimise the Fisher information of the emissivity distribution g , the weight $1/g_i$ is not inserted directly in Eq. (3.27), thus maintaining linearity. Instead, we start with $W^{(0)} = I$, the unit matrix, and solve the set of normal equations

$$(T^T \cdot T + \alpha H^{(n)}) \cdot g^{(n+1)} = T^T \cdot f \quad (3.28)$$

with $H^{(n)}$ defined by Eqs. (3.27) and use the solution $g^{(n)}$ thus obtained to determine a new weight matrix $W^{(1)}$ such that

$$W_{ij}^{(n)} = \frac{1}{g_i^{(n)}} \delta_{ij}, \quad g_i^{(n)} > 0, \quad n > 0 \quad (3.29)$$

3.2 The tomographic problem

and

$$W_{ij}^{(n)} = W_{max} \delta_{ij}, g_i^{(n)} \leq 0, n > 0. \quad (3.30)$$

The superscript $^{(n)}$ denotes the n th iteration and W_{max} is an upper bound for the weights. This procedure continues until the solution $\mathbf{g}^{(n+1)}$ does not differ significantly from $\mathbf{g}^{(n)}$. Usually, this is already the case for $n = 2$ when a solution which minimises the Fisher information is found.

The 'correct' regularisation parameter α is determined iteratively by requiring that

$$\chi^2 \approx n_i \quad (3.31)$$

provided that the measurement errors σ_i are sufficiently well known. The condition in Eq. (3.31) provides smoothing of perturbations smaller than the error level.

The search for the parameter α is based on the following observations. For $\alpha = 0$ and $\alpha \rightarrow \infty$, the solutions of the Eqs. (3.25) can be exactly evaluated as $\mathbf{g} = \mathbf{T}^{-1} \cdot \mathbf{f}$ and $\mathbf{g} = 0$ respectively yielding $\chi^2(\alpha = 0) = 0$ and $\chi^2(\alpha \rightarrow \infty) = \mathbf{f}^T \mathbf{f}$.

In the first iteration, the Eq. (3.28) is solved for $\alpha = \alpha_1$ obtaining the solution $\mathbf{g}(\alpha_1)$, where α_1 is a first guess. Following the previous considerations, in the second iteration the regularising parameter α_2 is defined by the following rules

$$\alpha_2 = \alpha_1/2 \text{ if } \chi^2(\alpha_1) > n_i$$

$$\alpha_2 = 2\alpha_1 \text{ if } \chi^2(\alpha_1) < n_i.$$

The solution $\mathbf{g}(\alpha_2)$ and $\chi^2(\alpha_2)$ are then evaluated.

Finally, the value of α satisfying the Eq. (3.31) is obtained by evaluating the $\chi^2(\alpha) = n_i$ linearised between the values obtained from the previous iterations.

3.3 Other diagnostics

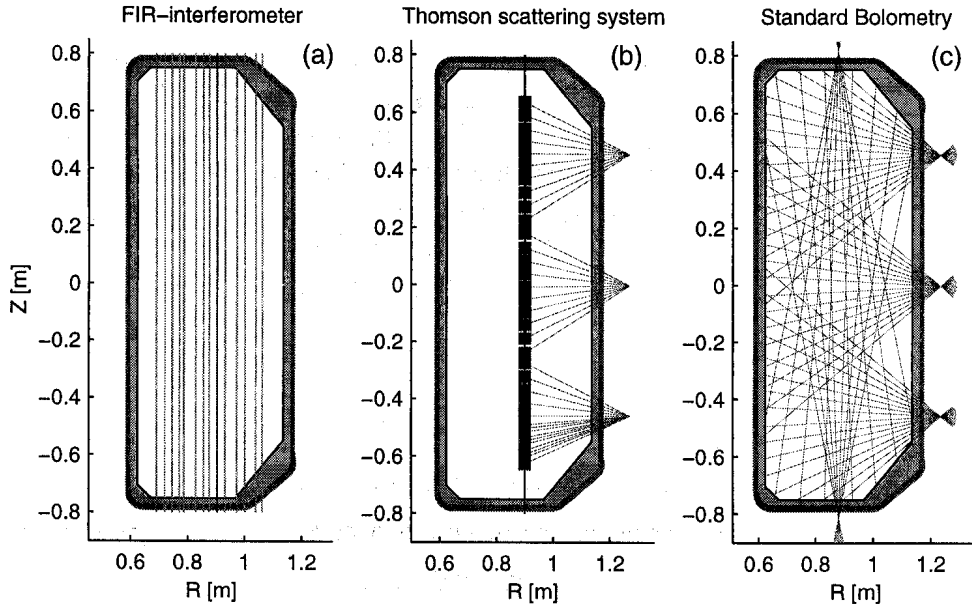


Fig. 3.7 Different diagnostics on TCV. (a) FIR: geometrical arrangement of the 14 laser beams probing the plasma. (b) Thomson scattering system: shown is one of the three almost coaxial laser beams together with the lines of sight of the detectors arranged in three lateral portholes. The scattered light is collected from 25 scattering volumes, shown as squares. (c) Standard bolometric system: the 5 pinhole cameras with a total of 64 lines of sight assure a good coverage of the whole poloidal cross section.

3.3.1 Interferometry

Let us consider an electromagnetic wave of frequency ω and wave number k which propagates through a magnetised plasma. In the case of negligible magnetic field ($\mathbf{B} \rightarrow 0$), the refractive index N is independent of the direction of propagation and can be expressed for all modes of propagation as [8]

$$N^2 = 1 - \frac{\omega_p^2}{\omega^2} \quad (3.32)$$

where $\omega_p^2 = n_e e^2 / (\epsilon_0 m_e)$ is the plasma frequency, m_e the electron mass, e the elementary charge and ϵ_0 the dielectric constant of the vacuum. If the plasma frequency exceeds the frequency of the

3.3 Other diagnostics

electromagnetic wave, $\omega_p > \omega$, then N becomes pure imaginary. This means that the wave is no longer propagating but evanescent, falling off exponentially with the distance.

If this is not the case and the plasma properties vary sufficiently slowly, $\|\nabla k\|/k \ll 1$, then the phase of the electromagnetic wave traversing the plasma is shifted by

$$(\Delta\phi)_i = \int_{L_i} k dl_i = \int_{L_i} N \frac{\omega}{c} dl_i \quad (3.33)$$

where dl_i is measured along the ray path L_i . Introducing the Eq. (3.32) in the Eq. (3.33), the phase shift can be written as

$$(\Delta\phi)_i = \frac{\omega}{c} \int_{L_i} \left[\left(1 - \frac{n_e}{n_c}\right)^{\frac{1}{2}} - 1 \right] dl_i \quad (3.34)$$

where the *cutoff density*, $n_c = m_e \epsilon_0 \omega^2 / e^2$, has been defined. If the plasma density is small compared to the cutoff density, $n_e \ll n_c$, the following expansion holds

$$N \approx 1 - \frac{1}{2} \frac{n_e}{n_c} \quad (3.35)$$

and Eq. (3.34) can be simplified to

$$(\Delta\phi)_i = \frac{\omega}{2cn_c} \int_{L_i} n_e dl_i. \quad (3.36)$$

As shown by the Eq. (3.36), the line integrated electron density, $\bar{n}_e = \int n_e dl_i$, can be derived from the phase difference, $\Delta\phi$, between a two phase coherent beams one of which probing the plasma and another beam, known as Local Oscillator (LO), having a well defined phase behaviour.

On TCV, this measurement makes use of the heterodyne or double frequency detection in a Mach-Zehnder interferometer arrangement [18]. The plasma is probed by a laser beam at the wavelength of 214.6 μm ($\omega = 1400$ GHz) produced by an optically pumped CH_2F_2 laser. The electric field of the probing beam emerging from the plasma can be represented by $E_{prob} = E_2 e^{i[\omega t + \Phi(t) + \Phi_{prob}]}$, where $\Phi(t)$ is the time-varying phase shift due to the plasma and Φ_{prob} is constant over the time. A LO beam with a slight frequency offset $\Delta\omega = 100$ kHz from the probing beam is created by Doppler diffraction from a rotating grating [19]. The electric field of the LO beam can be represented by $E_{LO} = E_1 e^{i[(\Delta\omega)t + \omega t + \Phi_{LO}]}$. The probing beam is

recombined with the LO beam and the resulting intensity can be expressed as

$$\begin{aligned} S_{prob} &= \|E_{LO} + E_{prob}\|^2 = \\ &= E_1^2 + E_2^2 + 2 \cdot E_1 E_2 \cos[(\Delta\omega)t - \Phi(t) - \Phi_{plas}] \end{aligned} \quad (3.37)$$

The phase shift $\Phi(t)$ due to the plasma can be determined by comparing the phase of the signal in Eq. (3.37) to that of a reference signal expressed as

$$S_{ref} = E_1^2 + E_2^2 + E_1 E_2 \cos[(\Delta\omega)t - \Phi_{ref}] \quad (3.38)$$

The reference signal is obtained by recombining the laser beam, which does not probe the plasma, with the LO beam. The detected phase shift, $\Phi(t) + \Phi_{plas} - \Phi_{ref}$, is the plasma induced phase shift with a constant offset due to the different optical paths of the beams.

In Fig. 3.7(a), the arrangement of the FIR on TCV is shown. Line integrated measurements are provided in a single poloidal plane along 14 vertical chords of diameter ≈ 20 mm. The detection system consists of 15 InSb hot electron bolometers in a single liquid helium cryostat. The maximum frequency response of the detectors is 750 kHz and the signals are acquired at 100 kHz. At wavelength of 214.6 μm , only minor refraction effects are present, even at high line averaged densities, $\bar{n}_e = 2.2 \cdot 10^{20} \text{ m}^{-2}$. The accuracy of the phase analysis is about 20 degrees and leads to a resolution limit of approximately $\Delta\bar{n}_e \approx 5 \cdot 10^{17} \text{ m}^{-2}$.

3.3.1.1 Modified Abel inversion of interferometer data

The far infrared interferometric system on TCV provides measurements of the line integrated phase shift $(\Delta\phi)_i$ along the optical paths $L_i = 1, \dots, 14$ of 14 beams probing the plasma. To obtain the local electron density n_e an inversion is required of the system of equations

$$p_i = \int_{L_i} n_e dl_i \text{ for } i = 1, \dots, 14 \quad (3.39)$$

where we have defined $p_i = 2cn_c(\Delta\phi)_i/\omega$.

On TCV, for the strongly shaped plasma configurations, the simple Abel solution given by Eq. (3.10), is not appropriate. Moreover, the interferometric measurements are taken along parallel

3.3 Other diagnostics

optical paths at only one impact angle ϕ limiting the poloidal resolution of the system to the $m = 0$ harmonic component, as we have seen in section 3.2.2.1. In these circumstances, additional information is required to obtain a local electron density from the system of Eqs. (3.39).

If the plasma is not perturbed by MHD activity, the electron density is expected to be constant on a magnetic flux surface and depends on the radial flux coordinate ρ alone, i.e. $n_e = n_e(\rho)$, where we have defined

$$\rho = \sqrt{\frac{\Psi - \Psi_0}{\Psi_a - \Psi_0}}, \quad (3.40)$$

Ψ_0 and Ψ_a being respectively the poloidal flux at the magnetic axis and at last closed flux surface.

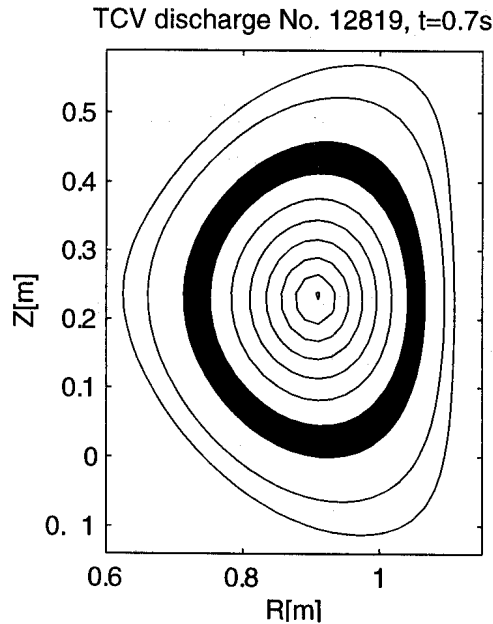


Fig. 3.8 Concentric pixels corresponding to magnetic flux surfaces which are used for the modified Abel inversion method for multichord interferometer data. Shown flux surfaces correspond to $\rho = 0.1n$, for $n = 1, \dots, 10$. The electron density is supposed to be constant in each pixel.

On TCV, the geometry of the magnetic flux surfaces is provided by the equilibrium reconstruction code LIUQE [20] which also provides the radial flux coordinate ρ on a grid of 41 equispaced points in ρ coordinate. In Fig. 3.8, an example of magnetic equilibrium reconstruction is given for the TCV discharge No. 12819. In this figure, the flux surfaces are shown at $t = 0.7$ s and correspond to $\rho = 0.1n$, for $n = 1, \dots, 10$.

One way to introduce the supplementary information provided by the flux surfaces would be to define concentric pixels determined by the geometry of the magnetic surfaces (shaded pixel in Fig. 3.8), within which the electron density is considered constant. The system of Eqs. (3.39) can thus be solved using one of the pixel methods discussed in section 3.2.2.2.

Another possibility is to expand the local electron density $n_e(\rho)$ as a linear combination of K base functions $w_k(\rho)$,

$$n_e(\rho) = \sum_{k=1}^K a_k w_k(\rho) \quad (3.41)$$

and then solve the system of Eqs. (3.39) for the unknown coefficients a_k .

The number of significant coefficients a_k could be reduced by a choice of base functions $w_k(\rho)$ which are well adapted to the physics determining the profiles. An example could be spatial eigenfunctions which are directly related to the particle transport mechanism.

In the following, we use the expansion in Eq. (3.41) with base functions

$$w_k(\rho) = e^{-\left(\frac{\rho - \rho_k}{\xi}\right)^2} + e^{-\left(\frac{\rho + \rho_k}{\xi}\right)^2} \quad (3.42)$$

where

$$\rho_k = \frac{k-1}{K-6} \text{ for } k = 1, \dots, K \quad (3.43)$$

and $\xi = 1/(K-6)$.

For these base functions, $dw_k(\rho)/(d\rho) = 0$ for $\rho = 0$ which automatically satisfies the physical condition $dn_e(\rho)/(d\rho) = 0$ for $\rho = 0$. For practical purposes, K is limited to around 30. For this value, the set of base functions in Eq. (3.42) provides good fit in the least-squares sense to most electron density profiles measured by the Thomson scattering system and therefore is also well adapted to our problem.

Substituting Eq. (3.41) into Eq. (3.39), we obtain the set of 14 simultaneous linear equations

$$p_i = \sum_{k=1}^K a_k \int_{L_i} w_k(\rho) dl_i \quad (3.44)$$

which can be arranged in matrix form

3.3 Other diagnostics

$$\mathbf{p} = \mathbf{W} \cdot \mathbf{a}, \quad (3.45)$$

where $p_i = p_i$ and $a_k = a_k$ are respectively the measurement and the coefficient vectors of the expansion in Eq. (3.41) and \mathbf{W} is a $K \times 14$ matrix whose elements $W_{ki} = \int_{L_i} w_k(\rho) dl_i$ are numerically evaluated.

The system of Eqs. (3.45) is underdetermined (14 equations and 30 unknowns) and a solution can be always found which satisfies the requirement $\chi^2 = 0$. As discussed in section 3.2.2.2, a unique solution can be found by minimising the function

$$\Phi = \frac{1}{2} (\tilde{\mathbf{W}} \cdot \mathbf{a} - \tilde{\mathbf{p}})^T \cdot (\tilde{\mathbf{W}} \cdot \mathbf{a} - \tilde{\mathbf{p}}) + \alpha \mathbf{H} \quad (3.46)$$

where the abbreviations $\tilde{W}_{ki} = W_{ki}/\sigma_i$ and $\tilde{p}_i = p_i/\sigma_i$ have been introduced, σ_i being the uncertainty of the p_i measurements. In Eq. (3.46), \mathbf{H} is a regularising functional and α a positive definite regularising parameter which is determined by imposing supplementary conditions. The functional form \mathbf{H} in Eq. (3.47) is obtained by the requirements of smoothness of the solution $n_e(\rho)$. A comparison of the performance of different regularising functional forms, which have been already presented in section 3.2.2.2, was performed on simulated and experimental data. The first derivative functional yields the most stable and precise reconstruction with respect to noisy data. Therefore, by defining

$$\mathbf{H} = \left[\frac{dn_e}{d\rho} \right]^2 = \left[\sum_{k=1}^K a_k \frac{dw_k}{d\rho} \right]^2 = \sum_{k=1}^K \sum_{j=1}^K D_{kj} a_k a_j \quad (3.47)$$

a solution of the system of Eqs. (3.45) can be found by minimising the function

$$\phi = \frac{1}{2} (\tilde{\mathbf{W}} \cdot \mathbf{a} - \tilde{\mathbf{p}})^T \cdot (\tilde{\mathbf{W}} \cdot \mathbf{a} - \tilde{\mathbf{p}}) + \alpha \mathbf{a}^T \cdot \mathbf{D} \cdot \mathbf{a} \quad (3.48)$$

where the matrix elements D_{kj} are numerically evaluated from the first derivative $dw_k/(d\rho)$ of the base functions.

A comparison between Eq. (3.48) and Eq. (3.25) shows that the unknown base function coefficients \mathbf{a} can be found by solving the system of linear normal equations

$$(\tilde{\mathbf{W}}^T \cdot \tilde{\mathbf{W}} + \alpha \mathbf{D}) \cdot \mathbf{a} = \tilde{\mathbf{W}}^T \cdot \tilde{\mathbf{p}}. \quad (3.49)$$

The regularising parameter α is calculated iteratively in the manner presented in section 3.2.2.2.

3.3.2 Magnetic measurements

MHD activity is monitored by Mirnov coils [21]. At four different toroidal locations, poloidal arrays of 38 probes are located behind the graphite tiles inside the vacuum vessel. These probes provide measurements of the component of the poloidal field tangential to the vessel wall and the poloidal number, m , of the observed MHD mode. Toroidal arrays of identical probes are located on the low-field side (16 coils) and the high-field side (8 coils) and are used to determine the toroidal mode number n . The highest sampling rate of the magnetic measurements is up to 1 MHz

3.3.3 Thomson scattering system

Thomson scattering systems provide measurements of the electron temperature and density profiles. Usually, a laser beam is injected in the plasma and the radiation scattered by the electrons is detected. The spectral broadening of the radiation which is due to the Doppler effect yields the electron temperature at the scattering position and its intensity the electron density. The TCV Thomson scattering system [22] is shown in Fig. 3.7(b). Three almost co-linear laser beams are injected from the bottom of the TCV vessel at the radial position $R = 0.9$ m. Three high power, Nd:YAG lasers at wavelength $\lambda = 1.064$ μm can operate at repetition frequencies of up to 20 Hz. The light scattered from 25 points is collected resulting in a spatial resolution of 40 mm in vertical direction and 3 mm in radial and toroidal directions. Sampling intervals down to 0.4 ms can be achieved in the so-called 'burst-mode', when the three lasers are triggered close together. This time resolution is however too small to resolve the sawtooth crash (crash duration < 100 μs) and therefore Thomson scattering measurements have to be complemented by other diagnostics like the FIR interferometer for density measurements and the foil-absorption system for temperature measurements.

3.3.4 Soft x-ray photodiodes: MHD activity and central electron temperature

The soft x-ray emissivity of the plasma is also monitored by four silicon photodiodes, equipped with a 50 μm beryllium filter, placed at the top of the vessel and equally spaced in the toroidal

3.3 Other diagnostics

direction. These detectors view the plasma along vertical chords placed at $R = 0.84$ m cutting the poloidal midplane $\cong 7$ cm from the centre of the vessel on the low field side. Their signals are acquired at frequencies up to 250 kHz. These photodiodes allows to determine toroidal mode numbers $n = 1, 2$, assuming no aliasing from toroidal mode number $n = 3$.

A fast measurement of the central electron temperature T_{e0} is derived from soft x-ray line integrated data using the foil-absorption technique [23], [24], [25], [26] which we review briefly here for reader's convenience. The local emissivity of the plasma in a given spectral range can be expressed as, Eq. (2.47),

$$E(r) = \sum_Z n_e(r)n_Z(r)\epsilon_Z(r) \quad (3.50)$$

where the summation is over all the impurities with atomic number Z and density n_Z present in the plasma. $\epsilon_Z(r)$ is the total emissivity normalised with respect to n_e and n_Z and includes the contribution of each ionisation stage for the considered atomic species.

Let us consider two detectors viewing the plasma centre and equipped by two different absorption filters (i.e. beryllium filters of different thickness) which define the spectral range of the measured radiation. Using Eq. (3.4), the total signal output P from each detector can be evaluated using

$$P = \frac{A\Omega}{4\pi} \int_{L_i} \sum_Z n_e(r)n_Z(r)\epsilon_Z(r)dl_i \propto \int_{L_i} n_e^2 \sum_Z \epsilon_Z(r)dl_i \quad (3.51)$$

where $A\Omega$ is the etendue of the detector-aperture arrangement and the integral is to be performed along the line of sight L_i viewed by the detectors. In Eq. (3.51), the assumption $n_Z/n_e = \text{const}$ is made and the different spectral sensitivities of the two filter-detector arrangements are taken into account in the normalised emissivity $\epsilon_Z(r)$.

Provided that the plasma ionisation equilibrium is described by the corona model (section 2.3.2), the normalised emissivity ϵ_Z depends only on the electron temperature. Assuming electron density and temperature profiles of the form

$$n_e = n_{e0} \left(1 - \frac{r^2}{a^2}\right)^\alpha \quad (3.52)$$

$$T_e = T_{e0} \left(1 - \frac{r^2}{a^2}\right)^\beta \quad (3.53)$$

the line integral in the Eq. (3.51) can be numerically evaluated in the appropriate geometry and the power detected can be expressed as

$$P \propto \int_{L_i} n_e^2 \sum_Z \epsilon_Z(T_e) dl = n_{e0}^2 f(\alpha, \beta, T_{e0}) \quad (3.54)$$

where f depends on the n_e and T_e profile shapes through the parameters α , β and on the central electron temperature, T_{e0} . The basis of the foil-absorption technique is contained in the Eq. (3.54). A comparison of the experimental intensity ratio, P_1/P_2 , with a numerical simulation of the function f_1/f_2 provides a measurement of the central electron temperature.

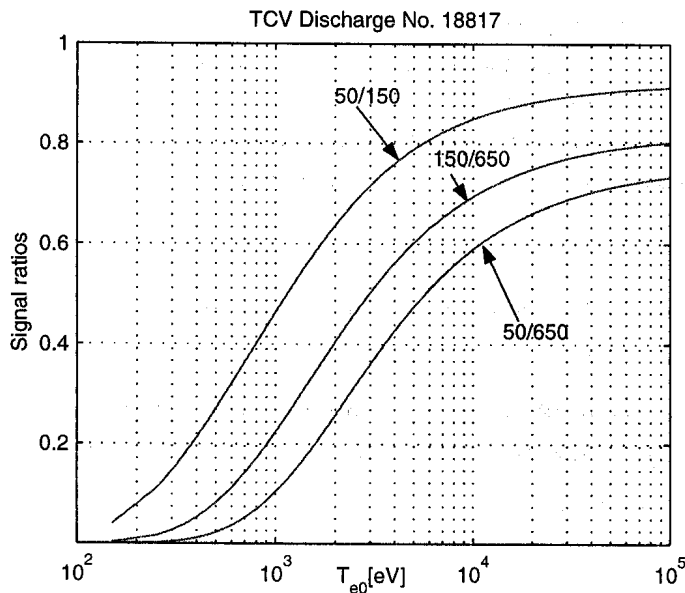


Fig. 3.9 Ratio of detector signals computed according to Eq. (3.54) for different combinations of filters as a function of the central electron temperature. Electron temperature and density profiles as in Eqs. (3.52), (3.53) are assumed with $\alpha = 1.5$ and $\beta = 0.75$.

On TCV, the foil absorption system consists of four filtered silicon photodiodes separated by 2 cm in the toroidal direction and viewing the plasma along central vertical chords. The signals are acquired at a maximum frequency of 250 kHz and the chosen absorption filters are: 50 μm Be, 150 μm Be, 650 μm Be and 62.5 μm Al + 250 μm Be. Depending on plasma parameters, different combinations of filters can be used for evaluating electron temperatures from 300 eV to 20 keV. This range covers almost all the ohmic and ECH plasmas in TCV. The choice of absorber combinations is influenced by several criteria: (1) the transmitted intensity ratio P_1/P_2 should vary sufficiently with T_e to

give adequate sensitivity to T_e changes; (2) enough radiation power should be transmitted to produce a high detector signal-to-noise ratio; (3) the transmission band of the filter should avoid strong impurity line radiation at low energy which may result in a T_e underestimate.

Fig. 3.9 shows the calculated ratio of detector signals P_1/P_2 as a function of the central electron temperature T_{e0} for three different combinations of filters. Equation (3.54) is evaluated using the

3.3 Other diagnostics

IONEQ code under the condition of corona equilibrium and assuming that most of the radiated power within the LCFS is due to carbon emission [27]. The assumption of corona equilibrium is justified for the evaluation of the soft x-ray emission, as shown in section 2.4 where the ionisation equilibria were compared as calculated with and without transport effects.

In TCV, Thomson scattering measurements indicate that the parameters α and β in Eqs. (3.52), (3.53) can range from 0.3 to 3 for most plasma conditions. For practical purposes, the ratio f_1/f_2 is evaluated using $\alpha = 1.5$ and $\beta = 0.75$. This assumption is justified if the profiles decrease monotonically with the minor radius since, in this case, the f_1/f_2 ratio is relatively insensitive to their shape. This condition is fulfilled for most of the TCV plasmas. However, in the case of hollow T_e profiles, which can form transiently after a sawtooth crash, the correct shape dependence of the f_1/f_2 ratio has to be taken into account in the T_{e0} measurement.

From Fig. 3.9, we observe that the 50 μm Be and 150 μm Be filter pair is the best suited for measurements in the T_e range from ≈ 0.3 to ≈ 1 keV. For higher electron temperatures, combinations of thicker filters are preferred due to the increased sensitivity to relative T_e changes. In this case, the reduced signal-to-noise ratio could pose severe restrictions to the applicability of the method to low density plasmas, which are also the hottest in TCV.

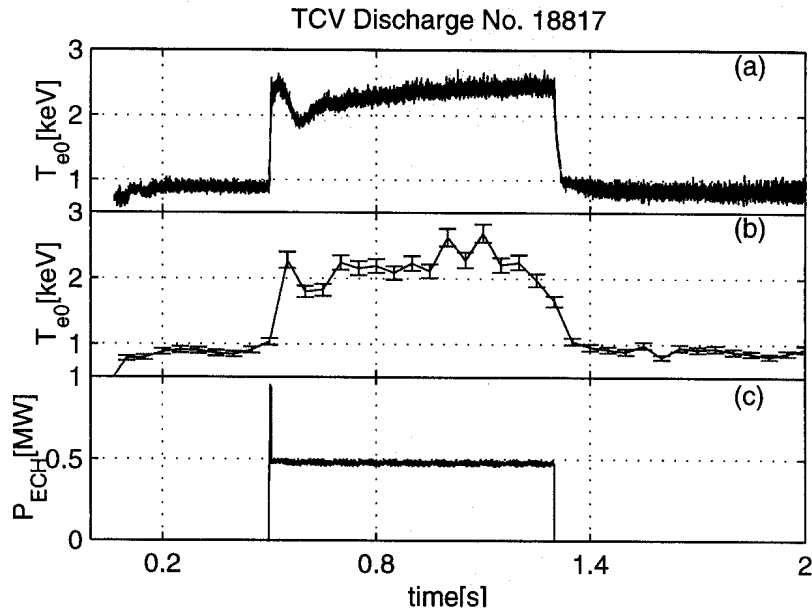


Fig. 3.10 Time evolution of the central electron temperature in an ECH TCV discharge. T_{e0} is measured using the two foil-absorption method (a) and by the Thomson scattering system (b). The total injected power is shown in (c).

In Fig. 3.10, an illustration of the performance of the foil absorption system is presented from TCV discharge No. 18817. The plasma parameters are: $\delta_a = 0.06$, $\kappa_a = 1.51$, $I_p = 140$ kA,

$\bar{n}_{e0} = 1.1 \cdot 10^{19} \text{ m}^{-3}$ and a total auxiliary ECH power $P_{ECH} = 0.5 \text{ MW}$ is centrally deposited from the gyrotron switch on at $t = 0.5 \text{ s}$. The temporal evolution of the central electron temperature from the foil-absorption system, Fig. 3.10(a), and from the Thomson scattering system, Fig. 3.10(b), are shown together with the ECH power, Fig. 3.10(c). The effect of the auxiliary heating is evident on the central electron temperature which increases from approximately 900 eV during the ohmic phase to $\approx 2.1 \text{ keV}$ in the ECH phase. Combinations of the 50 μm Be and 150 μm Be filters and of the 150 μm Be and 650 μm Be filters have been used for measuring T_{e0} with the foil absorption method respectively during the ohmic and the ECH phase. The results are in good agreement with the measurements from the Thomson system.

3.3.5 Metal foil bolometry

Precise measurements of the total radiated power are especially important in the study of heat transport in magnetically confined plasmas. On TCV, as in other tokamaks, the radiated power can be a large fraction (20-80%) of the total input power, depending on discharge conditions. To date, the most widely used technique for performing this measurement, commonly referred to as bolometry, in tokamak experiments is based on metal foil detectors [28], [29], [30].

Fig. 3.7(c) shows the TCV standard bolometric system which consists of 5 pinhole cameras at the same toroidal location with a total of 64 lines of sight. The detectors are miniaturised, low noise, metal foil resistor bolometers originally designed at the Max Planck Institut für Plasmaphysik in Garching [31] which are sensitive to electromagnetic radiation in the range from 1eV to 10 keV. The diagnostic allows tomographic reconstructions of the poloidal emissivity distribution with a spatial resolution of $\approx 4 \text{ cm}$ and a temporal resolution of $\approx 10 \text{ ms}$, limited by the integration time of the metallic resistor bolometers. This rather low time resolution is the most restrictive limitation of standard bolometric techniques [32].

3.4 Fast AXUV bolometric system

In recent years, progress in silicon deposition technology has allowed the fabrication of p-n junctions without the creation of a dead layer region at the Si-SiO₂ interface [33]. These photodiodes (also known as AXUV photodiodes) exhibit near theoretical quantum efficiency down to very low photon energy, for which the oxide absorption is negligible, permitting their use as bolometers for fusion experiments [34]. In the case of TCV these photodiodes are particularly

3.4 Fast AXUV bolometric system

attractive owing to their insensitivity to stray microwave radiation from ECH which strongly perturbs the metal foil bolometers, presumably due to direct dissipation of microwave power. Further important advantages of the AXUV photodiodes in comparison to standard bolometers are their fast time response and insensitivity to low energy (< 500 eV) neutral particles. The latter are expelled from the tokamak plasma edge as a result of charge exchange and recombination processes and can transport an important amount of power out of the plasma. Boivin et al. [35] recently reported high spatial resolution measurements of this neutral emission, using a combination of AXUV photodiode and metallic foil bolometer arrays. In this section, we will describe the application of a prototype system employing these new photodiodes to measurements on TCV [36], which has been developed in the course of this thesis.

3.4.1 Diagnostic design

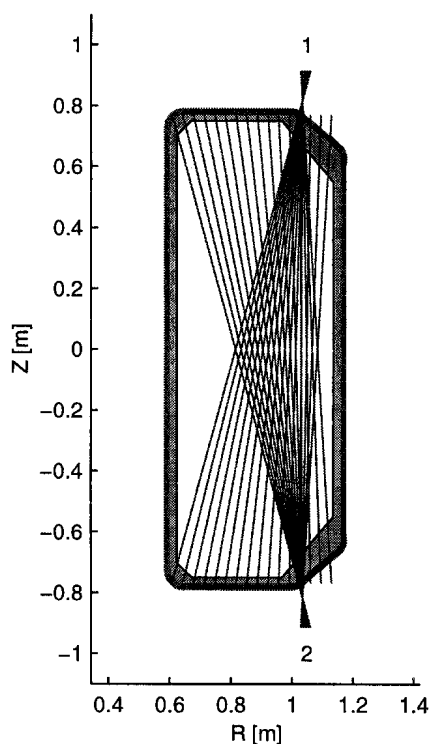


Fig. 3.11 Location and viewing chord geometry of the prototype fast bolometric system installed on TCV.

The diagnostic system consists of two pinhole cameras viewing the plasma from above and below at the same toroidal location. Each camera is equipped with a linear array of 16 photodiodes corresponding to a fan of viewing lines (Fig. 3.11) resulting in a spatial resolution of ≈ 1.5 cm at the vessel midplane. A single chord in the upper camera coincides with one of the eight chords provided by the lower foil bolometer camera and vice versa. This allows some degree of comparison between the line integrated measurements from both systems. The photodiode and foil bolometer cameras are installed at the same toroidal position on the TCV vacuum vessel.

The detailed design features of the pinhole camera are shown in Fig. 3.12. The back of the camera head consists of a flange with a built-in 40-pin electrical feedthrough (supplied by Caburn-MDC) made up of two parallel rows of 20 Iron-Nickel alloy pins (0.5 mm diameter) embedded in glass cylinders (1.5 mm diameter) providing electrical insulation between the flange and the pins. The latter are directly plugged into a ceramic socket allowing the

detector array, equipped with female connectors, to be directly mounted without any need for in-vacuum wiring. The camera housing comprises three concentric stainless steel cylinders, with water flow in the innermost gap providing active cooling of the detectors during vessel bakeout up to 300 °C while the gap between the outermost two cylinders can be evacuated to improve thermal insulation. A stainless steel plate, supported by a short bellow and located a few cm behind the protective graphite tiles lining the vacuum vessel, serves as a heat shield to prevent the camera interior from overheating during vessel bakeout. The bellow system serves to reduce conductive heat transfer from the heat shield to the concentric cylinders.

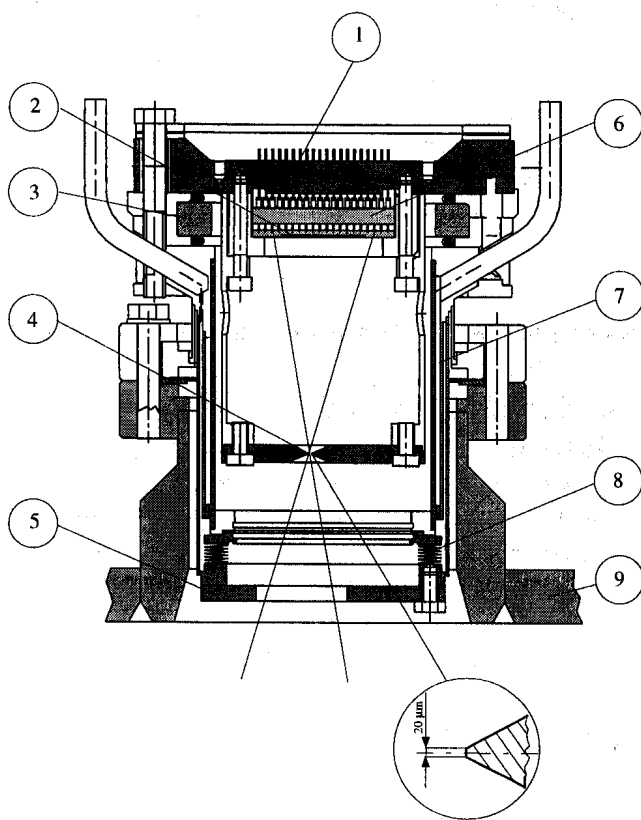


Fig. 3.12 Cross-section of the TCV pinhole camera: 1, 40-pin electrical feedthrough; 2, AXUV detector array; 3, insulating ceramic ring; 4, poloidally limiting aperture, the detail shows the trapezoidal shape of its edges; 5, front plate heat shield; 6, intermediate ceramic socket; 7, water cooled spacing between inner walls; 8, stainless steel bellow; 9, TCV vessel.

Electrical insulation between the camera housing at the torus earth potential and the head flange is ensured by an intermediate ceramic ring. A stainless steel cylinder in the camera interior fixes the detector to the ceramic socket through an intermediate plate and provides support for the pinhole aperture of dimensions 5×0.5 mm. Precise shaping of the aperture edges with minimum thickness of $20 \mu\text{m}$ is obtained by electro-erosion. The distance between the detector array and the pinhole aperture is 94.9 mm, resulting in an etendue of the aperture-detector arrangement of $\approx 3 \times 10^{-9} \text{ m}^2 \text{ sr}$. Each camera is equipped with an AXUV-16ELO linear array of 16 p-n junction photodiodes produced by International Radiation Detectors (IRD) [37] and designed for applications in the ultraviolet, extreme ultraviolet and soft x-ray spectral regions. These photodiodes are of compact design and yield high sensitivity (0.24 A/W) with near theoretical quantum efficiency over a wide range of photon energy [38]. The absence of carrier recombination at the Si-

3.4 Fast AXUV bolometric system

SiO_2 interface together with an extremely thin (4-8 nm) hard silicon protective entrance window, make these photodiodes sensitive to photon energies down to 1 eV and thus allow plasma edge phenomena to be observed [35]. The only reduction in quantum efficiency ($< 70\%$ at 8 eV) at low energies is due to the SiO_2 entrance window and is mainly for 6-50 eV photons, for which absorption in the oxide layer is non-negligible. For photon energies higher than 6 keV, the efficiency is limited by the photodiode thickness chosen for the TCV diagnostic (35-40 μm). The photodiodes are operated in unbiased mode and have a rise-time shorter than 0.5 μs [37], making measurements with high temporal resolution possible. Each detector of the array has a dedicated preamplifier located on a printed circuit board mounted at the back of the camera head as close as possible to the electrical feedthrough in order to minimise electromagnetic pick-up. The preamplifiers are current to voltage converters, based on the OP37 operational amplifier, with transimpedance gain of 1.2 MV/A and of a bandwidth of 100 kHz. Preamplifier outputs are collected by twisted pairs, with a signal and ground for each photodiode, grouped in a single, 14-m-long shielded cable containing 18 pairs (16 signals and ± 15 V power supply).

The signals are filtered by a 3 pole low-pass, Bessel filter with a cut-off frequency of 40 kHz, corresponding to the Nyquist frequency of the acquisition system. Analog-to-digital conversion and data acquisition are performed by a transient recorder based on a Vanguard 16 bit VME-based ADC which has been described in section 3.1.3 and is also used to acquire the data from the 200 channel, soft x-ray tomographic system on TCV.

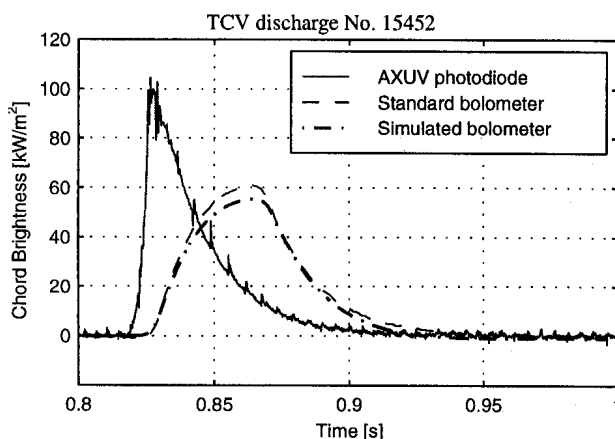


Fig. 3.13 Time evolution of the baseline subtracted chord brightness following a purely electromagnetic radiative event, caused by a piece of falling debris in TCV discharge No. 15452 at $t=0.82$ s. The full line is the AXUV photodiode signal. The standard bolometer trace (dashed line) agrees well with the simulated response (dot-dashed line).

3.4.2 Comparison of the AXUV system to standard bolometry

As has been recently reported [35], one important feature of AXUV photodiodes is their

insensitivity to low energy neutrals, unlike standard foil bolometers which cannot distinguish between power from electromagnetic radiation or by neutral particles. One way to compare the performance of the two systems is to observe the response of both to a transient, purely electromagnetic radiative event. This may occur by deliberate injection of impurities or when minute pieces of debris from the surrounding walls fall into the plasma. Since impurities reside in the TCV plasma for only ≈ 20 ms giving rise to a characteristic pulse of emission, their contribution is easily distinguishable. One such event is shown in Fig. 3.13 which illustrates the time evolution of the detected power (after background subtraction) measured along the same line-of-sight by an AXUV photodiode (full line) and by a standard bolometer (dashed line). The high temporal resolution of the photodiode allows detailed observation of the impurity penetration and subsequent expulsion from the plasma. Fast heat pulse propagation following internal disruptive instabilities (sawteeth) is also clearly visible as spikes in the measured emissivity. The much slower temporal resolution of the bolometer, even after deconvolution (rise time ≈ 20 ms, 2 kHz acquisition frequency), smooths out the time trace and such detail is lost. Using the AXUV signal to estimate the incident power on the detector due to the transient event, the corresponding metal foil bolometer signal can be simulated if its temporal response characteristic is known [31]. The result of such a calculation is also shown in Fig. 3.13 (dot-dashed line), demonstrating the excellent agreement between the two diagnostics for this special case of purely electromagnetic radiation.

An illustration of the AXUV photodiode performance is presented in Fig. 3.14 showing measurements obtained from a diverted plasma in TCV, Fig. 3.14(a), in which a transition from a low confinement (L-mode) to a high confinement (H-mode) regime occurs. This discharge also offers a good opportunity to compare the absolute values of measurements from both bolometric systems. In the same figure, the D_α emission is shown, Fig. 3.14(b), together with the line integrated central density \bar{n}_{e0} , Fig. 3.14(c), an AXUV photodiode signal from the bottom camera (channel #1) looking through the plasma edge at the outer midplane, Fig. 3.14(d), and one from the top camera (channel #2) viewing along a chord passing through the core plasma and the divertor leg, Fig. 3.14(e). The L-H transition, occurring at $t = 0.445$ s, is clearly seen in the rapid increase of \bar{n}_{e0} together with the reduction in the D_α emission (a monitor of the flux of particles leaving the plasma edge). A period of “mossy” ELMs [39] begins at $t = 0.505$ s, producing a small modulation (2% of amplitude) in the radiated power measured by the AXUV photodiode viewing the divertor region (a portion of this period is shown in the expanded view in Fig. 3.14(f).

3.4 Fast AXUV bolometric system

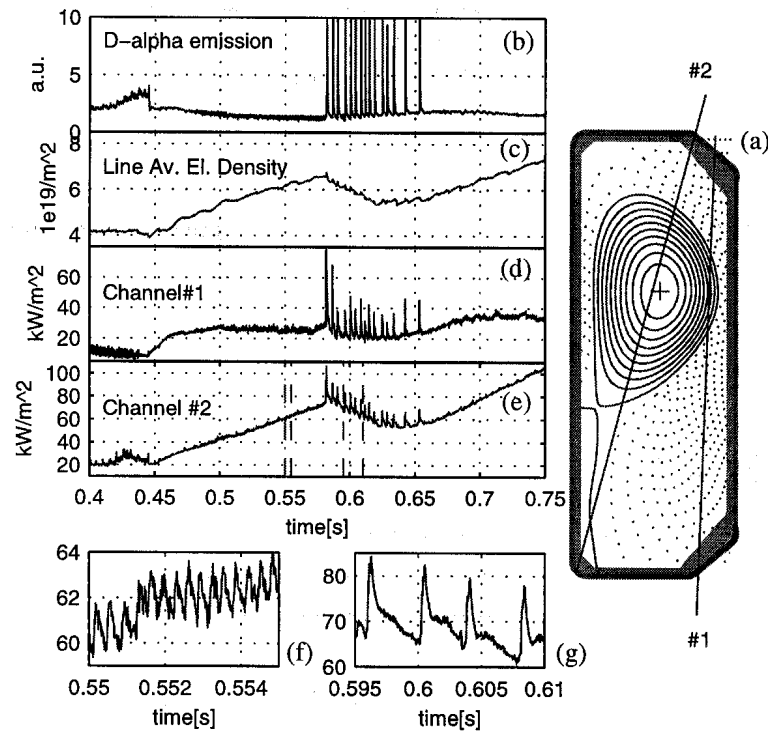


Fig. 3.14 Evolution of an ohmic H-mode in TCV. Right: plasma configuration at $t = 0.6$ s together with two lines of sight of the fast bolometric system, from the upper (#2) and lower (#1) cameras. Left: From top to bottom: D_{α} emission, line integrated central density, a signal (channel#1) from an AXUV photodiode looking through the plasma edge, a signal (channel#2) from an AXUV photodiode viewing the divertor region, expanded view of "mossy ELMs" (left) and of large ELMs (right).

During the ELM-free phase, the central photodiode signal increases approximately as the square of \bar{n}_{e0} (indicating the dominance of recombination and Bremsstrahlung radiation from the core plasma), whilst the edge channel signal amplitude remains constant following an initial fast rise after the L-H transition. Qualitatively, these relative differences are the result of an abrupt steepening of the temperature profile and an increase in the electron temperature itself near the plasma edge following the transition. As a consequence, rapid modifications occur to both the spatial location and absolute concentration of the impurity species responsible for the emission. To understand this behaviour quantitatively requires modelling of the impurity transport, necessitating detailed measurements of density and temperature profiles in the localised region where strong gradients occur. The increase in \bar{n}_{e0} is interrupted by several large ELMs, visible as spikes in the D_{α} emission, Fig. 3.14(b), which expel particles and heat from the plasma on a ms timescale [40] and which are also

easily observed in the AXUV signals as shown in the expanded view in Fig. 3.14(g). Spikes in the radiated power of similar amplitude are also seen in those channels (not shown in Fig. 3.14) of the upper camera viewing the outer divertor strike zone. Although the lack of chords crossing the X-point region prevents tomographic inversion of the data, comparison of these divertor viewing channels with those of the lower camera viewing the same region of plasma indicates the presence of a highly radiating region around the divertor strike point during each ELM. This is confirmed by tomographic inversion of the standard bolometric signals during the ELMing period. The amplitude of the spikes on the photodiode signals indicates that significant quantities of heat and particles are expelled in the divertor region during large ELMs.

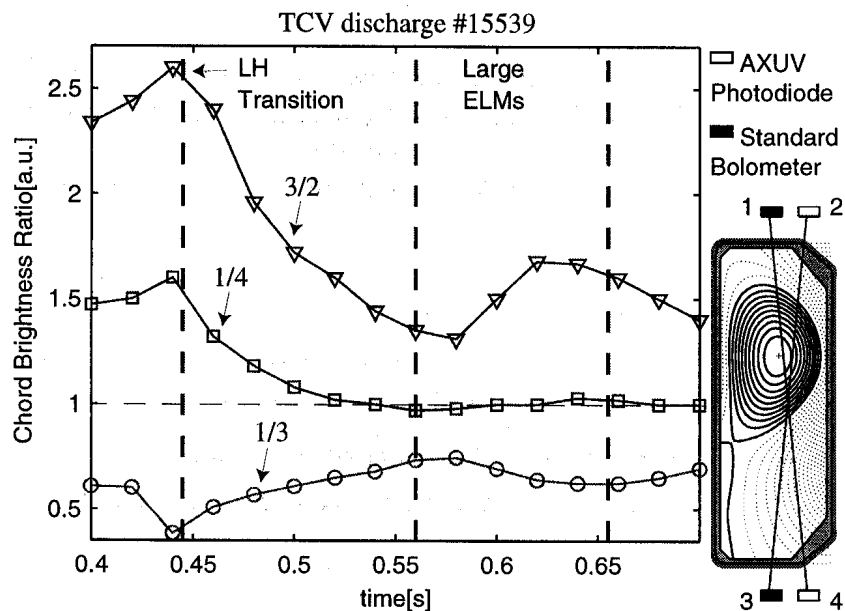


Fig. 3.15 Time evolutions of the absolute chord brightness measured by metal foil bolometers and by AXUV photodiodes for the same discharge as in Fig. 4. Right: plasma configuration at $t = 0.6$ s together with the detector line-of-sight (standard bolometers, 1 and 3, AXUV photodiodes, 2 and 4) used for the comparison. Left: various chord brightness ratios.

For the same discharge, the absolute chord brightness measured by pairs of standard bolometer detectors and AXUV photodiodes viewing the plasma along the same lines-of-sight are compared in Fig. 3.15. The time variation of three ratios of the detector signals are plotted (see caption in Fig. 3.15) demonstrating the differences in response of the two diagnostics. In L-mode the power detected by the metal foil bolometers is significantly higher than that measured by the photodiodes.

3.4 Fast AXUV bolometric system

This difference is more pronounced when using the standard bolometer signal viewing the plasma from below to take the ratio (signal pair 3/2 in Fig. 3.15). During H-mode, agreement between the standard bolometers and the AXUV photodiodes is considerably improved; the ratio of detectors 1 and 4 is close to unity and the ratio of detectors 3 and 2 is significantly decreased. For the latter signal pair, however, the outburst of the ELM activity leads to a large increase in the ratio. One likely interpretation of this behaviour is in terms of low energy neutral losses, to which only the standard bolometers are sensitive. Recycling of neutrals is generally higher in L-mode compared with H-mode, as indicated by the D_{α} emission. The ELM instability temporarily destroys the edge transport barrier formed during the H-mode, leading to an increase in neutral recycling. The latter is more intense in the divertor region of the plasma where the particle exhaust is concentrated during ELM activity. As a result, the lower standard bolometer sees a higher neutral flux and the ratio 3/2 increases. In contrast, the hot plasma core (central electron temperature ≈ 1 keV) prevents the upper metal foil bolometer from seeing the neutral particle production localised in the divertor volume. These results show that more than half of the power detected by the foil bolometers can originate from low energy neutral losses, depending on discharge conditions.

Considerable support for this interpretation comes from tomographic inversion of data from the standard bolometer camera signals. Reconstructions which are consistent with raw data are not possible in the cases such as those in Fig. 3.15 in which neutral emission is strongly poloidally localised. Those channels which view neutral particle sources through the plasma give lower values than those with a direct view. The signal behaves as if the plasma were optically thick, indicating that neutral particles contribute substantially to the measured signal level.

In addition to their vastly improved time response, the AXUV photodiodes therefore also promise to be a valuable tool in helping to separate the component of the total power losses due to neutral particles. In view of the encouraging results obtained during these preliminary experiments, the system has been recently improved by adding a third pinhole camera and by reconfiguring the viewing chord geometry of the upper and lower pinhole cameras. This arrangement of the system provides a better coverage of the TCV vessel as shown in Fig. 3.16. The new pinhole camera (camera #2 in Fig. 3.16) is installed on a lower lateral port and used to view the radiation from the divertor region of high recycling and detached discharges [41] with magnetic equilibria similar to that shown in Fig. 3.15. Future plans include a full tomographic system, consisting of up to 7 pinhole cameras at the same toroidal position, allowing a detailed reconstruction of the total radiation distribution in the poloidal plane.

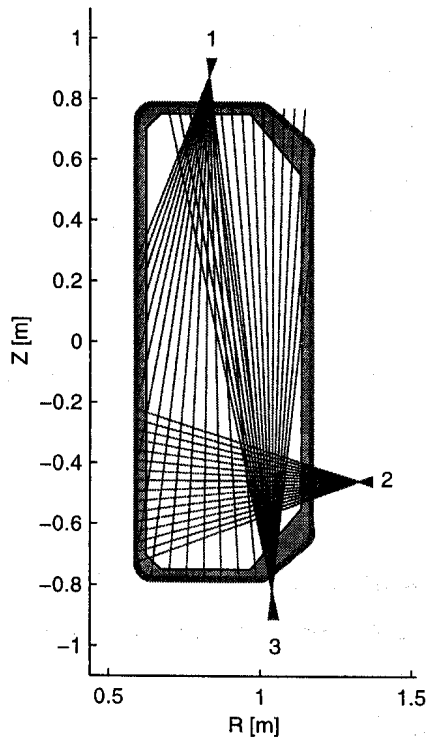


Fig. 3.16 Location and viewing chord geometry of the fast bolometric system in its present arrangement. New features include a lateral pinhole camera (#2) viewing the divertor region and a better coverage of the TCV vessel provided by the upper (#1) and lower (#3) pinhole cameras.

3.5 Concluding remarks

The study of transport phenomena during sawtooth activity requires diagnostics with temporal resolution higher than $\approx 100 \mu\text{s}$, which is the typical sawtooth crash duration in TCV plasmas. The 200 channel soft x-ray system provides measurements with a temporal resolution of $13 \mu\text{s}$ and is therefore well adapted for this study. The local soft x-ray emissivity distribution is reconstructed by means of the minimum Fisher information regularisation method on a grid of square pixels of typical side 3 cm. Local electron density and temperature are provided by a Thomson scattering system at a maximum repetition rate of 0.4 ms. For fast transport studies, this is complemented by a foil-absorption system, which provides central electron temperature at 250 kHz of acquisition frequency, and by the multichord far infrared interferometer. The latter provides line integrated electron density measurements that are inverted by means of a modified Abel inversion method. The total radiated power is monitored by a metal foil bolometric system and by new AXUV photodiodes. The latter are used in the TCV fast bolometric system and allow the study of fast transport at the plasma edge with a temporal resolution of up to $13 \mu\text{s}$ which is inaccessible to standard metal foil bolometry detectors.

3.5 Concluding remarks

References

- [1]M. Anton, et al., *Rev. Sci. Instrum.* **66** (1995) 3762.
- [2]R. H. Kingston, *Detection of Optical and Infrared radiation*, Springer, New York, 1978.
- [3]W. M. J. Veigele, *Atomic Data* **5** (1973) 51.
- [4]M. Anton, et al., *Plasma Phys. Control. Fusion* **38** (1996) 1849.
- [5]R. A. Brooks, et al., *Phys. Med. Biol.* **21** (1976) 689.
- [6]A. P. Thorne, *Spectrophysics*, Chapman and Hall, London, 1998.
- [7]W. H. Press, *Numerical Recipes in FORTRAN*, Cambridge University Press, Cambridge, 1992.
- [8]I. H. Hutchinson, *Principles of plasma diagnostics*, Cambridge University Press, Cambridge, 1987.
- [9]A. M. Cormack, *J. Appl. Phys.* **9** (1963) 2722.
- [10]A. M. Cormack, *J. Appl. Phys.* **10** (1964) 2908.
- [11]J. F. Camacho, et al., *Rev. Sci. Instrum* **57**, (1986) 417
- [12]G. Kuo-Petravic, PPPL-2555 Princeton Plasma Physics Laboratory (1988)
- [13]R. S. Granetz, et al., *Nucl. Fusion* **28** (1988) 457.
- [14]S. Tsiji, et al., *Nucl. Fusion* **22** (1982) 1082.
- [15]G. Fuchs, et al., *Plasma Phys. Control. Fusion* **36** (1994) 307.
- [16]B. R. Frieden, *J. Mod. Opt.* **35** (1988) 1297.
- [17]B. R. Frieden, *Probability Statistical Optics and Data Testing* 2nd Ed., Springer, New York, 1987
- [18]S. Barry, *The extension of the FIR interferometer on TCV to a polarimeter and measurements of the Faraday rotation caused by the poloidal magnetic field*, PhD thesis, National University of Ireland, Cork, 1999. Published as Lausanne Report LRP 638/99.
- [19]D. Veron, *Infrared and Millimeter Waves*, Academic Press, New York, 1979.
- [20]F. Hofmann, et al., *Nucl. Fusion* **28** (1988) 1871.
- [21]H. Reimerdes, *MHD stability limits in the TCV tokamak*, PhD thesis No. 2399, Ecole Polytechnique Fédérale de Lausanne, Lausanne (2001), Switzerland.
- [22]R. Behn, et al., *Proc. 7th Int. Symp. Laser Aided Plasma Diagnostics* (Fukuoka 1995), page 392.
- [23]J. Kiraly, et. al., *Nucl. Fusion* **27** (1987) 397.
- [24]T. P. Donaldson, *Plasma Phys. Control. Fusion* **20** (1978) 1279.
- [25]Equipe TFR, *Nucl. Fusion* **17** (1977) 213.
- [26]I. N. Bogatu, *Diagnostics for Contemporary Fusion Experiments*, Eds. P. E. Scott, D. K. Akulina, G. Gorini and E. Sindoni, SIF Bologna, 1991.
- [27]H. Weisen, et al., *Proc 23rd EPS Conf. on Controlled Fusion and Plasma Physics*, (Kiev 1996), vol. **20C** part I, page 111.

- [28]J. Schivell, *Rev. Sci. Instrum.* **56** (1985) 972.
- [29]E. R. Muller, et al., *J. Appl. Phys.* **55** (1984) 2635.
- [30]B. Joye, et al., *Rev. Sci. Instrum.* **57** (1986) 2449.
- [31]K. F. Mast, et al., *Rev. Sci. Instrum.* **62** (1991) 744.
- [32]S. F. Paul, et al., *Rev. Sci. Instrum.* **64** (1993) 2423.
- [33]R. Korde, et al., *Appl. Opt.* **26** (1997) 5284.
- [34]R. J. Maqueda, et al., *Rev. Sci. Instrum.* **63** (1992) 4717.
- [35]R. L. Boivin, et al., *Rev. Sci. Instrum.* **70** (1999) 260.
- [36]I. Furno, et al., *Rev. Sci. Instrum.* **64** (1999) 4552.
- [37]International Radiation Detectors, 2545 W. 237th Street Unit I, Torrance CA 90505-5229.
- [38]E. M. Gullickson, et al., *Journal of Electron Spectroscopy and Related Phenomena* **80** (1996) 313.
- [39]H. Weisen, et al., *Plasma Phys. Control. Fusion* **38** (1996) 1137.
- [40]H. Weisen, et al., *Plasma Phys. Control. Fusion* **38** (1996) 1415.
- [41]R. A. Pitts, et al., *Proc. 26th EPS Conf. on Controlled Fusion and Plasma Physics* (Maastricht 1999), Vol. 23J, page 1085.

4 ANALYSIS OF SOFT X-RAY DATA

A multivariate technique, which has in recent years gained increased prominence in the analysis of multichannel data, is the singular value decomposition (SVD), also known as the Karunen-Loeve transform, principal component analysis or biorthogonal decomposition. Originally, the SVD was developed in the context of numerical analysis [1], but other applications have been investigated in various fields such as magneto hydrodynamics (MHD) mode analysis [2], [3], signal [4] and image processing [5]. Since this technique is extensively used in this thesis, a brief description of the method and its properties are given in this chapter using applications to TCV soft x-ray data as special examples. The method is presented in section 4.1 and its differences with respect to Fourier harmonic decomposition are examined. In section 4.2, the basic tools for the physics investigations in the following chapters are introduced: the MHD mode identification and the evaluation of the sawtooth inversion radius using soft x-ray data. Readers interested in a more rigorous mathematical derivation of the SVD can refer for example to Ref. [6]. Finally, in section 4.3 we present a method to determine local values of the effective ion charge Z_{eff} from tomographically inverted soft x-ray measurements in conjunction with measurements of electron density and temperature profiles.

4.1 Singular value decomposition (SVD)

We consider a physical quantity, $y = y(x, t)$, which depends on a spatial, x , and a temporal, t , variables. The measurement process consists of sampling the quantity y at different times and spatial locations, leading to an $N \times M$ matrix of data

$$\mathbf{Y} = \begin{bmatrix} y(x_1, t_1) & \dots & y(x_1, t_M) \\ y(x_2, t_1) & \dots & y(x_2, t_M) \\ \dots & \dots & \dots \\ y(x_N, t_1) & \dots & y(x_N, t_M) \end{bmatrix} \quad (4.1)$$

where N and M are respectively the number of spatial and temporal sampling. In what follows, we assume $N \geq M$; if this is not the case, the transpose of the data matrix will be considered. Furthermore, we assume that y is a real scalar quantity but the representation can be easily extended to complex quantities in other spaces (for example Fourier space).

The fundamental matrix decomposition theorem states that \mathbf{Y} can be decomposed as a product [7]

$$Y = U \cdot S \cdot V^T \quad (4.2)$$

where the superscript T denotes transposition and the symbol \cdot indicates the usual matrix multiplication. U and V are respectively $N \times M$ and $M \times M$ unitary matrices, i.e. $U^T \cdot U = V^T \cdot V = I$, and S is an $M \times M$ diagonal matrix. This decomposition is usually referred to as singular value decomposition and is the equivalent of the biorthogonal decomposition [8] of the sampled signal which consists in expanding the discrete signal $y(x_j, t_i)$ into a set of eigenmodes which are orthogonal in space and time

$$Y = \sum_{k=1}^K S_k \mathbf{u}_k \mathbf{v}_k^T \Leftrightarrow (Y)_{ij} = \sum_{k=1}^K S_k u_k(x_j) v_k(t_i) \quad (4.3)$$

where \mathbf{u}_k , and \mathbf{v}_k are respectively N - and M - dimensional vectors. The size of the expansion K is equal to the rank of the data matrix Y , which in practice corresponds to the smallest of N and M . Comparison of Eq. (4.3) to Eq. (4.2) gives

$$V = [\mathbf{v}_1 \ \mathbf{v}_2 \ \dots \ \mathbf{v}_M], \quad (4.4)$$

$$U = [\mathbf{u}_1 \ \mathbf{u}_2 \ \dots \ \mathbf{u}_M], \quad (4.5)$$

$$S = \begin{bmatrix} S_1 & & \\ & \dots & \\ & & S_M \end{bmatrix}. \quad (4.6)$$

Following the nomenclature introduced in Ref. [8], the spatial eigenmodes \mathbf{u}_k will be called *topos* and the temporal eigenmodes \mathbf{v}_k *chronos*. The weights S_k are either positive or equal to zero and conventionally they are sorted in descending order such that $S_1 \geq S_2 \geq \dots \geq S_{K-1} \geq S_K$. We will refer to the weights S_k as *singular values*.

The orthonormality condition for topos and chronos reads

$$\sum_{j=1}^M u_k(x_j) u_l(x_j) = \sum_{i=1}^N v_k(t_i) v_l(t_i) = \delta_{kl} \quad (4.7)$$

or equivalently in matrix notation

4.1 Singular value decomposition (SVD)

$$\mathbf{u}_k^T \cdot \mathbf{u}_l = \mathbf{v}_k^T \cdot \mathbf{v}_l = \delta_{kl}. \quad (4.8)$$

Using Eqs. (4.2)-(4.8), it can be shown that topos and chronos components, \mathbf{u}_k and \mathbf{v}_k , satisfy the eigenequations of the temporal and spatial scatter matrices of \mathbf{Y}

$$\mathbf{A}_x \cdot \mathbf{u}_k = S_k^2 \mathbf{u}_k, \text{ with } \mathbf{A}_x = \mathbf{Y}^T \cdot \mathbf{Y} \quad (4.9)$$

$$\mathbf{A}_t \cdot \mathbf{v}_k = S_k^2 \mathbf{v}_k, \text{ with } \mathbf{A}_t = \mathbf{Y} \cdot \mathbf{Y}^T. \quad (4.10)$$

The scatter matrices \mathbf{A}_x and \mathbf{A}_t do not necessarily have the same size, unless $N = M$. However, they have the same rank and their K largest eigenvalues are identical. In principle, the eigensystems, defined by Eqs. (4.9)-(4.10), together with Eq. (4.2) can be used to calculate the SVD. In practice, this is to be avoided because of potential numerical stability problems and sensitivity to roundoff errors. For this reason, the most robust SVD algorithm [9] is usually preferred.

From Eqs. (4.9) and (4.10) an important physical interpretation of the SVD can be given, namely that it projects the data onto an orthonormal basis along which both spatial and temporal coherences of the signals are maximised. To demonstrate this, we consider the spatial scatter matrix $\mathbf{A}_x = \mathbf{Y}^T \cdot \mathbf{Y}$. The elements of \mathbf{A}_x are the time average of the product of the signal at different positions

$$(\mathbf{A}_x)_{ij} = \sum_{k=1}^M y(x_i, t_k) y(x_j, t_k). \quad (4.11)$$

Equation (4.11) defines the space-covariance matrix of the data matrix \mathbf{Y} , thus the eigenvector, corresponding to the maximum eigenvalue in Eq. (4.9), is the vector along which the spatial covariance is maximised. Similarly, the temporal scatter matrix $\mathbf{A}_t = \mathbf{Y} \cdot \mathbf{Y}^T$ represents the temporal average of the product of the signals at different times such as

$$(\mathbf{A}_t)_{ij} = \sum_{k=1}^N y(x_k, t_i) y(x_k, t_j) \quad (4.12)$$

\mathbf{A}_t defines the time-covariance matrix of the data matrix \mathbf{Y} . Again the eigenvector, corresponding to the maximum eigenvalue in Eq. (4.10), is the vector along which the time covariance is maximised. Therefore, Eqs. (4.9)-(4.10) define a solution which has maximum temporal and spatial

coherences. Coherent spatio-temporal structures, such as travelling waves, are strongly correlated in time and space and they would appear more evident in this new basis (section 4.1.1).

The SVD is in many aspect similar to techniques such as the principal component analysis, which are also based in eigensolutions of Eqs. (4.9)-(4.10). The main difference resides in the way the presence of degeneracies in the spectra of the correlations matrices is treated. Degeneracies occur whenever the signal has spatiotemporal symmetries, such as travelling waves, and they imply that the one-to-one correspondence between the spatial and temporal components is lost. This is recovered by the SVD using the isomorphism between the topos and the chronos as an additional constraint to Eqs. (4.9)-(4.10)

$$\mathbf{Y} \cdot \mathbf{u}_k = S_k \mathbf{v}_k. \quad (4.13)$$

As seen in Eq. (4.13), each topo corresponds always to a unique chrono even when some singular values are identical. Techniques such as the principal components analysis fail to keep this unique correspondence because they formally treat the spatial and temporal behaviour separately.

4.1.1 Some properties of the SVD

An important property of the SVD is the ability to concentrate most of the signal features in a limited and usually small number of biorthogonal components. For any $L \leq K$, the truncated expansion

$$\tilde{\mathbf{Y}}_{ij} = \sum_{k=1}^L S_k u_k(x_j) v_k(t_i) \quad (4.14)$$

is the best approximation in the least-squares sense of the data among all possible sums of L components. In practice, the singular values are strongly ordered and the largest one exceeds the smallest one by a few orders of magnitude. This allows the signal to be reconstructed, retaining in Eq. (4.14) only the most significant biorthogonal components. This ability of the SVD technique to concentrate dominant features into few spatial and temporal modes makes it well suited for the analysis of spatially extended systems.

As we will see in section 4.2, the topos-chronos pairs which are dominant in the data set can be recovered simply inspecting the features of each topo/chrono pair. Several parameters allow to quantify the singular value distribution and the degree of compressibility of the data set.

4.1 Singular value decomposition (SVD)

We define the global signal energy

$$E = \sum_{i=1}^N \sum_{j=1}^M (Y_{ij})^2 \quad (4.15)$$

which is equal to the sum of the squared singular values

$$E = \sum_{k=1}^K S_k^2. \quad (4.16)$$

The dimensionless energy

$$p_k = \frac{S_k^2}{E} \quad (4.17)$$

measures the relative amount of energy, which is stored in each topo/chrono couple and it is a useful parameter for comparing different data set. It has the properties of a probability distribution $\sum p_k = 1$ where the summation is over $k = 1, \dots, K$ and $0 \leq p_k \leq 1$. Several statistical methods allow the assessment of the number of significant components for a given data set [10], [11]. In the following, we present a more qualitative approach having in mind the application to the experimental soft x-ray signals.

Another interesting property of the singular value distribution is the occurrence of two identical and non-negligible singular values in the presence of a spatio-temporal symmetry of the signal [12]. To illustrate this, we consider a sinusoidal travelling wave $y(x, t) = \alpha \cos(\omega t - \kappa x)$ which has the spatiotemporal symmetry $y(x, t + t_0) = y(x - x_0, t)$ being Δt and Δx respectively the spatial and temporal sampling periods. Provided that $N\omega\Delta t \gg 1$, $M\kappa\Delta x \gg 1$, then the scatter matrices in Eqs. (4.9)-(4.10) are

$$(A_x)_{ij} = \frac{1}{2} N \alpha^2 \cos[\kappa(x_i - x_j)] \quad (4.18)$$

$$(A_t)_{ij} = \frac{1}{2} M \alpha^2 \cos[\kappa(t_i - t_j)]. \quad (4.19)$$

The singular values are $S_k = \frac{\alpha}{2} \sqrt{MN}$ for $k = 1, 2$ and $A_k = 0$ for $k > 2$ and the corresponding topos, chronos are

$$u_1(x_j) = \sqrt{2/M} \sin(\kappa x_j) \quad (4.20)$$

$$u_2(x_j) = \sqrt{2/M} \cos(\kappa x_j) \quad (4.21)$$

$$v_1(t_i) = \sqrt{2/N} \sin(\omega t_i) \quad (4.22)$$

$$v_2(t_i) = \sqrt{2/N} \cos(\omega t_i). \quad (4.23)$$

In this case, as can be seen from Eqs. (4.20)-(4.23), the biorthogonal components of the data matrix Y are coincident with its Fourier discrete components and thus the decomposition is equivalent to the Fourier decomposition. In experimental soft x-ray data, coherent structures are often observed but these are not necessarily purely sinusoidal and may have modulation and phase which vary in time. In this case, a large number of Fourier harmonics is required to describe the signal, whereas only a small number of topos/chronos couples is usually necessary. Therefore, the SVD can dramatically simplify the mode analysis of soft x-ray data in tokamak plasmas where toroidicity and shaping further complicate the structure of the modes.

4.2 Application of the SVD to TCV soft x-ray signals

On TCV, the SVD is applied to soft x-ray data from the 200-channel tomographic system after the tomographic inversion [13], in contrast to previous applications in other fusion experiments [2], [14], [15], [16]. The major advantage of 'post-inversion' SVD is that the amplitude of parasitic signal components, such as magnetic pick-up noise, is reduced by the smoothing effect and the built-in boundary conditions of the reconstruction method resulting in a more efficient noise rejection with respect to the 'pre-inversion' SVD. The latter provides an analysis tool which is independent of the tomographic inversion process and therefore insensitive to artifacts of the reconstruction method or to unreliable reconstructed emissivity distributions. In cases where only a few single noisy channels may lead to improbable reconstructed soft x-ray emissivity distributions, the pre-inversion method is to be preferred as a tool for the analysis. Furthermore, since the tomographic inversion of large amounts of data is quite time-demanding [13], the post-inversion approach is limited to off-line data treatment when high speed of the analysis is not a fundamental requirement.

In what follows, which is not meant to be an extensive physics study, an illustration of the post-inversion SVD analysis is presented.

4.2 Application of the SVD to TCV soft x-ray signals

4.2.1 Mode identification

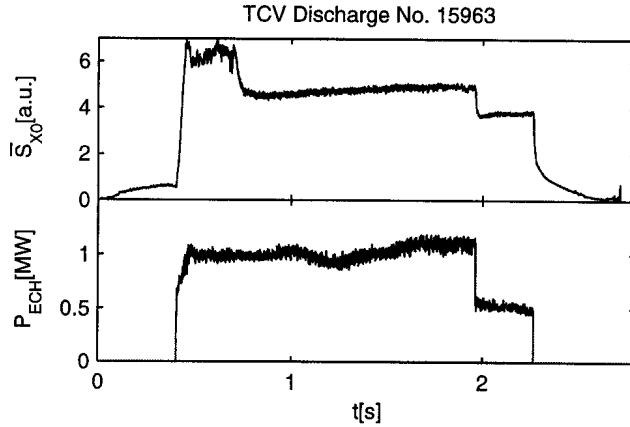


Fig. 4.1 Evolution of an ECH discharge in TCV. On the top, the line integrated soft x-ray emissivity. On the bottom, the ECH power.

The first example is an ECH discharge in which a large MHD mode is destabilised after the onset of the additional heating power. The plasma parameters are:

$\delta_a = 0.09$, $\kappa_a = 1.44$, $I_P = 400$ kA,
 $\bar{n}_{e0} = 1.1 \cdot 10^{19} \text{ m}^{-2}$. In Fig. 4.1, the temporal

evolution of the line integrated central soft x-ray emissivity \bar{S}_{X0} is shown together with the ECH power. A total power of $P_{ECH} = 1$ MW is injected by two gyrotrons with a large component of current drive in the direction of the ohmic current. A toroidal array of magnetic probes identifies a dominant $n = 1$ mode rotating in the direction of the electron

diamagnetic drift at a frequency of ≈ 4 kHz. The poloidal mode structure, as determined by an array of 38 poloidal probes, is $m = 2$. The mode is identified as a neoclassical tearing mode (NTM) [17] and causes a degradation of the energy confinement clearly (albeit qualitatively) visible on the \bar{S}_{X0} signal about 300 ms after the onset of the ECH power, Fig. 4.1. In Fig. 4.2, the SVD analysis of the inverted soft x-ray emissivity is shown in a time interval between $t = 0.80096 - 0.801295$ s. The distribution of the singular values S_k , shown in Fig. 4.2(b), reveals approximately three significant components which contain together more than 99.98% of the total signal energy. The first topo/chrono pair, corresponding to the largest singular value, $S_1^2/E = 99.77\%$, describes the temporal evolution of the average emissivity profile and is not relevant to mode identification.

Analysis of the singular value distribution shows two topo/chrono pairs, corresponding to $k = 2, 3$, whose singular values $S_2 = 498$ and $S_3 = 451$ are closed enough to suggest the existence of a spatiotemporal symmetry. The presence of a rotating mode is confirmed by the corresponding chronos v_2 and v_3 , which are oscillating at a frequency of ≈ 4 kHz and phase shifted by $\pi/2$. The topos u_2 and u_3 are also phase shifted by $\pi/2$ in the poloidal direction and they exhibit an $m = 2$ poloidal structure (each topo has two maxima and two minima along the poloidal direction). The toroidal mode number, as obtained from the toroidal photodiodes, is $n = 1$ which confirms the mode identification by magnetic measurements.

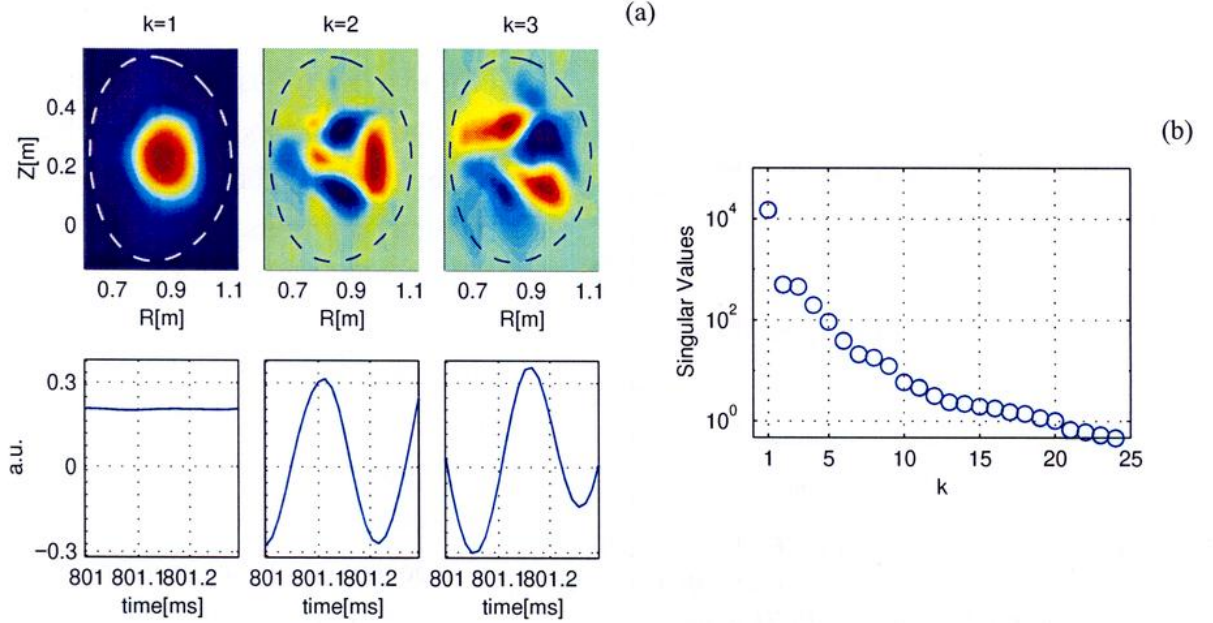


Fig. 4.2 SVD analysis of the reconstructed soft x-ray emissivities of the TCV discharge No. 15963 in the time interval $t=0.80096-0.801295$ s. Shown are the topo/chrono pairs corresponding to first three largest eigenvalues, $S_k = 1, 2, 3$. (a) The top row shows the spatial eigenmodes (topos) with the Last Closed Flux Surface LCFS (dashed line). The corresponding temporal eigenvectors (chronos) are shown in the bottom row. (b) Distribution of the singular values S_k . Only the 40 largest singular values are shown.

4.2.2 The determination of the sawtooth inversion radius

The SVD method also provides a reliable tool in the determination of the sawtooth inversion surface of the local soft x-ray emissivity. In the following, the sawtooth inversion contours are defined by the equation:

$$\widehat{S}_X(r, t_{before}) - \widehat{S}_X(r, t_{after}) = 0. \quad (4.24)$$

Here, \widehat{S}_X is obtained from the SVD expansion in Eq. (4.14) by discarding topo/chrono couples which are not poloidally symmetric, i.e. corresponding to poloidal mode numbers $m \geq 1$, and the times t_{before} , t_{after} are relative to the sawtooth crash time.

The effective and normalised inversion radius are defined respectively as $r_{inv} = \sqrt{A_{inv}/\pi}$ and $\rho_{inv} = \sqrt{A_{inv}/A_p}$, where A_{inv} is the cross sectional area within the inversion contour defined by

4.2 Application of the SVD to TCV soft x-ray signals

Eq. (4.24) and A_p is the total cross sectional area of the plasma. The size of the grid used in the tomographic reconstruction is taken as an estimate of the uncertainty in r_{inv} (typically $\approx \pm 2$ cm). An illustration of the use of the SVD analysis for the determination of the sawtooth inversion surface is given for an ohmic ELMy H-mode discharge (Fig. 4.3, right). Plasma parameters are: $\delta_a = 0.61$, $\kappa_a = 1.74$, $I_p = 400$ kA, $\bar{n}_{e0} \approx 3.7 \cdot 10^{19} \text{ m}^{-2}$. The temporal evolution of the tomographically inverted soft x-ray emissivity is shown for three different radial positions, Fig. 4.3(a,b,c), together with a signal from a bolometric AXUV photodiode looking through the plasma edge at the outer midplane, Fig. 4.3(d).

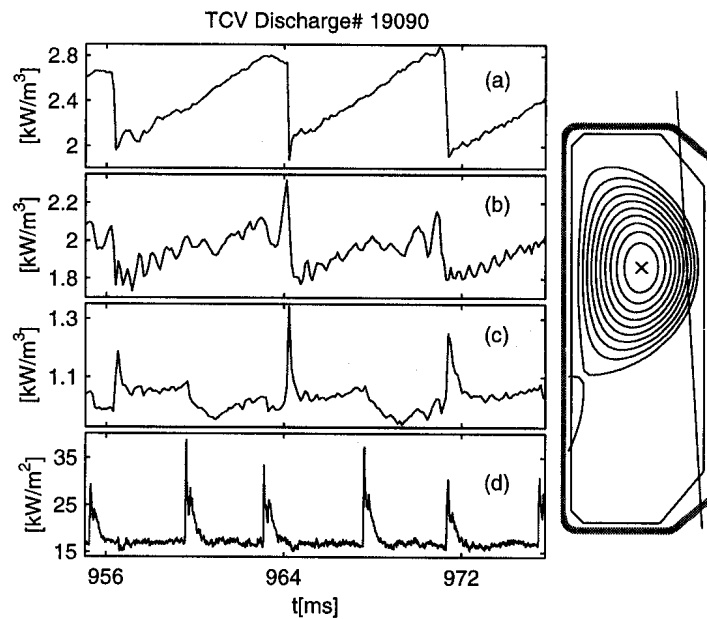


Fig. 4.3 Evolution of an ohmic H-mode in TCV discharge No. 19090. Right: plasma configuration at $t=0.96$ s. Left: soft x-ray emissivity at different radial positions r . (a) On-axis $r = 0$. (b) Just inside the inversion radius. (c) Just outside the inversion radius. (d) A signal from a bolometric AXUV photodiode looking through the plasma edge at the outer midplane (its line of sight is shown on the right).

The temporal evolution of the central soft x-ray emissivity shows the triangular sawtooth shape, Fig. 4.3(a), typical of the TCV ohmic discharges. In Fig. 4.4, the effect of the sawtooth crash on the soft x-ray emissivity profiles is shown for a time just before, $t_{before} = 0.9634$ s, and a time just after $t_{after} = 0.9643$ s the sawtooth crash. During the crash phase, the peaked pre-crash profile flattens inside the inversion surface and heat and particles are expelled beyond this surface. The

following reheat phase is accompanied by mode activity, visible as off-axis oscillations with a frequency of ≈ 1.5 kHz, Fig. 4.3(b). Several large ELMs are clearly visible on the AXUV photodiode signal, Fig. 4.3(d), and barely visible on the off-axis soft x-ray signals, Fig. 4.3(c). Particles and heat are expelled from the plasma core on a ms time scale during ELMs [18]. As a consequence, rapid modifications occur of both the spatial location and absolute concentration of the impurity species responsible for the emission near the plasma edge. This results in a strong enhancement of the emitted power in this region as shown by the amplitude of the spikes on the AXUV photodiode signal.

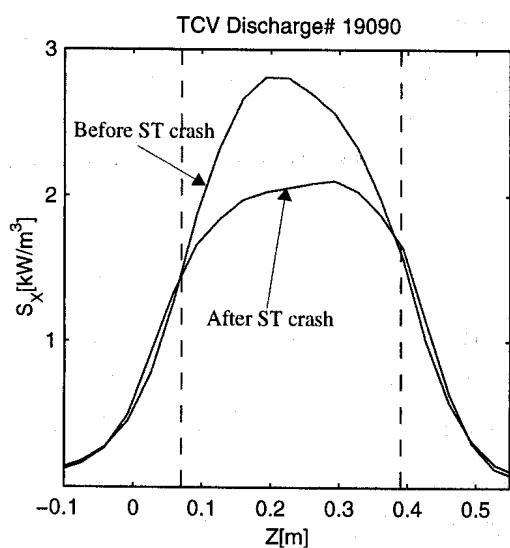


Fig. 4.4 Soft x-ray emissivity profiles along a central vertical cut showing the result of the sawtooth crash for an ohmic ELMy H-mode in TCV. The position of the sawtooth inversion surface is shown as a dashed line.

In Fig. 4.5, the SVD analysis of inverted soft x-ray emissivities is shown in the time window of Fig. 4.3. The distribution of the singular values S_k (not shown here) reveals that five topo/chrono couples contain together more than 99.98% of the total signal energy. The first topo/chrono pair, corresponding to the largest singular value, represents the evolution of the average soft x-ray emissivity profile. The peaking of the profile during the ohmic reheating and the subsequent flattening at the sawtooth crash are represented by the second topo/chrono couple, $k = 2$. This can be seen in the shape of the v_2 chrono, which shows the typical temporal evolution of the sawteeth, and from the u_2 topo which is poloidally symmetric and has a closed nodal surface. The presence of two oscillating topo/chrono pairs, $k = 3, 4$, in quadrature (i.e. both topo and chrono are phase shifted by $\pi/2$) reveals a rotating MHD mode with poloidal mode number $m = 1$, as shown by the dipole structure of the $u_{3,4}$ topos. The toroidal mode number, as obtained from the toroidal photodiodes, is $n = 1$. The mode rotates in the diamagnetic drift direction at a frequency of ≈ 1.5 kHz and its amplitude peaks at the sawtooth crash. The fifth topo/chrono component represents only 0.01% of the total signal energy, which corresponds to somewhat less than 30 times the energy content of the $k = 2$ component. The effect of the ELM events, Fig. 4.3(d), on the plasma emissivity is represented by this component, as suggested by the $m = 0$ symmetry of the u_5 topo and the temporal evolution of the v_5 chrono, which presents few maxima corresponding to the spikes of the AXUV photodiode signals, Fig.

4.2 Application of the SVD to TCV soft x-ray signals

4.3(d). A certain degree of correlation between the u_2 and u_5 topos can be observed, indicating that the SVD method cannot fully separate the dynamics of the sawteeth from the ELMs in this case. Nevertheless, the method is efficient in separating the dynamics of the sawteeth (whose dominant structure is $m = 0$) from the rotation of the $m = 1$ mode and this feature is exploited in the determination of the sawtooth inversion radius as outlined at the beginning of this section. In the present case, the filtered emissivity \widehat{S}_X of Eq. (4.24) is calculated as follows

$$(\widehat{S}_X)_{ij} = \sum_{k=1,2,5} S_k u_k(x_j) v_k(t_i) \quad (4.25)$$

since only the topos $u_{1,2,5}$ have isocontours approximately coincident with the magnetic flux surfaces. The sawtooth inversion surface, as obtained from Eq. (4.24) is shown in Fig. 4.6 together with the LCFS.

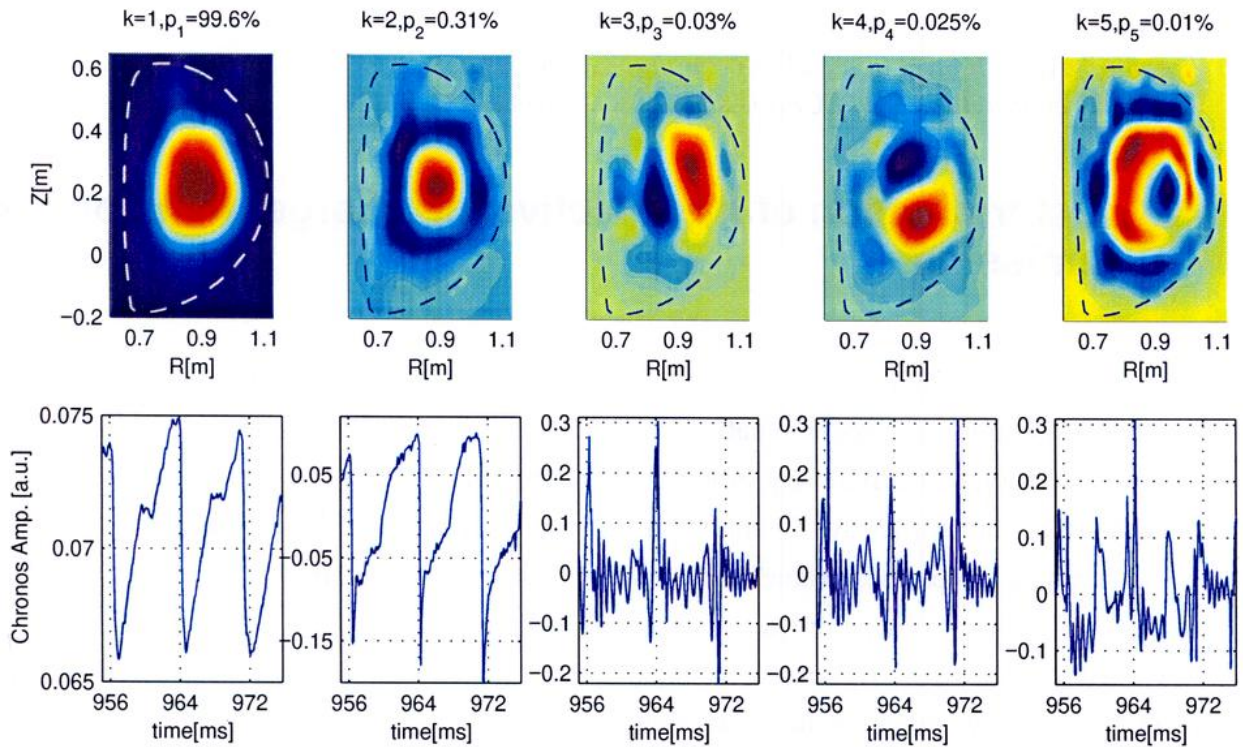


Fig. 4.5 SVD analysis of the reconstructed soft x-ray emissivities during the ELMy H-mode phase shown in Fig. 4.3. Shown are the topo/chrono pairs corresponding to first five largest eigenvalues, S_k , $k = 1, 2, 3, 4, 5$. The top row shows the spatial eigenmodes (topos) with the LCFS (dashed line). The normalised energy content p_k of topo/chrono couple is indicated in the title of each subplot. The corresponding temporal eigenvectors (chronos) are shown in the bottom row.

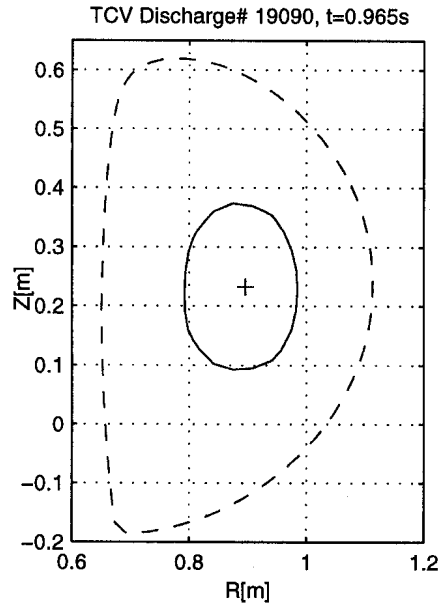


Fig. 4.6 Sawtooth inversion radius (continuous line) as determined from SVD analysis of inverted soft x-ray emissivities. The LCFS is shown as a dashed line.

4.3 Determination of the effective ion charge from soft x-ray emission

In the majority of TCV plasmas, the soft x-ray emission at energies above about 1 keV is dominated by Bremsstrahlung and recombination radiation from carbon (see chapter 2). Local values of impurity density, or alternatively of the effective charge of the ion mixture Z_{eff} , can be derived from simultaneous soft x-ray, T_e and n_e measurements in the manner proposed in Ref. [19]. Under certain circumstances, these values are fundamental in the interpretation of the soft x-ray emissivity in terms of basic plasma parameters, as we will see in chapter 6.

In the following, we briefly review the method described in Ref. [19] and discussed an application to TCV soft x-ray data from the tomographic system.

The local plasma emissivity $E(r)$ is related to local plasma parameters by Eq. (2.47) which we recall

$$E(r) = \sum_Z n_e(r) n_Z(r) \epsilon_Z(r) \quad (4.26)$$

4.3 Determination of the effective ion charge from soft x-ray emission

where n_Z and n_e are the ion and electron density respectively and ε_Z is the energy integrated spectral emissivity, normalised with respect to n_e and n_Z . For applications on TCV, the normalized emissivities ε_Z are calculated by the IONEQ code as a function of the electron temperature T_e assuming corona equilibrium (see chapter 2). Experimentally, the electron temperature and density profiles are provided by Thomson scattering measurements and the soft x-ray emissivity distribution is obtained from tomographic inversion of soft x-ray data from the 200 channel tomographic system. Under usual plasma conditions on TCV, the corona equilibrium assumption is of little consequences since transport significantly affects only line radiation from light impurities near the plasma edge (see chapter 2). These do not contribute to the measured emissivities since their wavelength are below the cut-off of the beryllium filter. Both the spectral sensitivity of the photodiodes and the attenuation in the transmitted power due to the 47 μm beryllium filters of the soft x-ray tomographic system are accounted for in the normalised emissivities ε_Z .

It is convenient to define impurity proportions $p_Z = n_Z/n_{imp}$, where $n_{imp} = \sum_{Z \neq b} n_Z$ is the overall density of impurity particles, excluding the background ion density n_b .

Provided that the quasi-neutrality condition is satisfied, $n_e = \sum n_i Z_i$, from Eq. (4.26) the overall impurity concentration relative to the electrons $c_{imp} = n_{imp}/n_e$ can be expressed as

$$c_{imp} = \frac{bE(r)/n_e^2 - \varepsilon_b(T_e)}{\sum_{Z \neq b} p_Z [b\varepsilon_Z(T_e) - z\varepsilon_b(T_e)]} \quad (4.27)$$

where b is the charge of the background ions.

From Eq. (4.27) and using the definition of the effective ion charge, Z_{eff} , given in Eq. (2.16), we obtain

$$Z_{eff} = b + \frac{n_{imp}}{n_e} \left[\sum_{Z \neq b} z(z-b) \frac{n_Z}{n_{imp}} \right]. \quad (4.28)$$

Equations (4.27)-(4.28) contain the basis of the method for evaluating the effective ion charge. This method is illustrated for the TCV discharge No. 15539 in which a transition occurs from the L-mode to H-mode confinement regime (the same discharge was already presented in section 3.4). The evolution of the soft x-ray emissivity profile along a vertical cut is shown in Fig. 4.7 obtained from the soft x-ray tomographic system. For the same discharge, in Fig. 4.8(a) the D_α emission is shown together with the central electron density n_{e0} and temperature T_{e0} from the Thomson scattering system, Fig. 4.8(b,c). The figure also shows the central soft x-ray emissivity, Fig. 4.8(d), and the derived values of the effective ion charge in the plasma centre Z_{eff0} , Fig. 4.8(e). A carbon to oxygen

density ratio of 4 to 1 was assumed in the calculation.

The L-H transition is clearly visible by the rapid drop of the D_α signal together with the increase of central electron density at $t = 0.445$ s. During the first ELM-free phase the central effective ion charge Z_{eff0} increases from approximately 2 to 4.5, corresponding respectively to values of the overall impurity concentration n_{imp} equal to 3% and 8% of the central electron density.

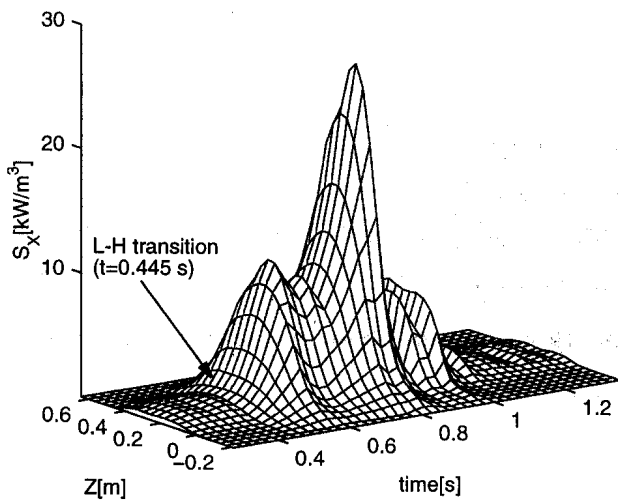


Fig. 4.7 Time evolution of the soft x-ray emissivity profiles along a central, vertical cut in TCV discharge No. 15539.

Fig. 4.9 shows, along a central vertical cut, the profiles of electron density and temperature, Fig. 4.9(a,b), and of the reconstructed soft x-ray emissivity, Fig. 4.9(c), at $t = 0.7258$ s during the second ELM-free phase. The profiles are shown for $\rho \leq 0.5$, being ρ the normalised radius, and the plasma centre is located at $z \approx 0.23$ m. Also shown are the calculated Z_{eff} profiles at the same time and during the ohmic L-mode phase, Fig. 4.9(d). At both times, the Z_{eff} profiles are flat to within 20% over the central half of the plasma. The slope of Z_{eff} appears to be associated with a slope in the n_e profile which is attributed to systematic calibration errors of the Thomson

scattering system. For $\rho > 0.5$, a sharp increase of Z_{eff} is observed (not shown in Fig. 4.9(d)) which is not believed to be real. This outer region corresponds to electron temperatures below 400 eV and to a level of the soft x-ray emission which is 10 times smaller than the soft x-ray emission in the centre. Under these conditions, small errors on the electron temperature and density or on the impurity proportions may result in large errors on the calculated values of Z_{eff} making the method unreliable as discussed in detail in Ref. [19].

4.3 Determination of the effective ion charge from soft x-ray emission

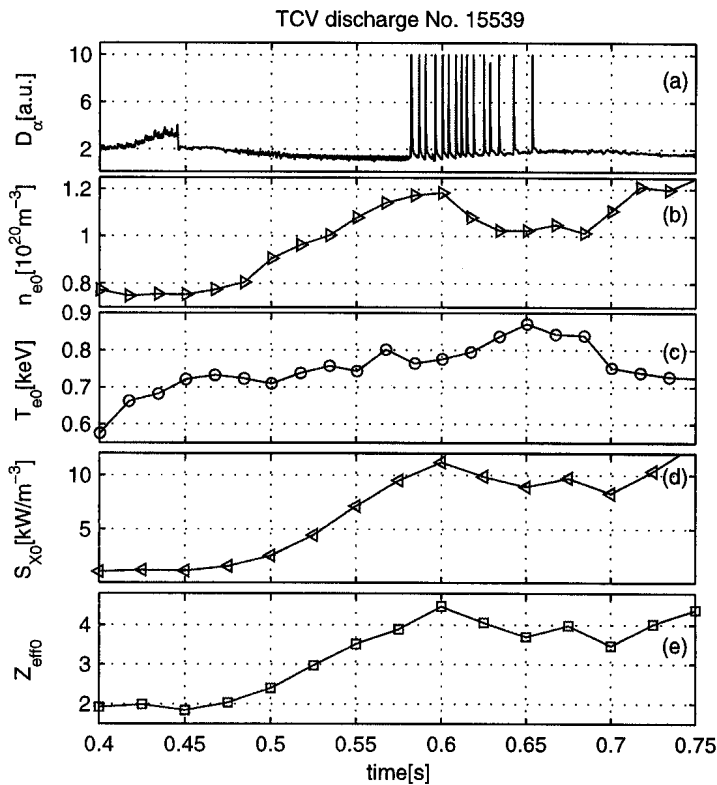


Fig. 4.8 Evolution of an ohmic H-mode discharge in TCV. (a) D_{α} emission. (b,c) Central electron density and temperature from the Thomson scattering system. (d) Central soft x-ray emissivity from the tomographic system. (e) Inferred values of Z_{eff} in the plasma centre.

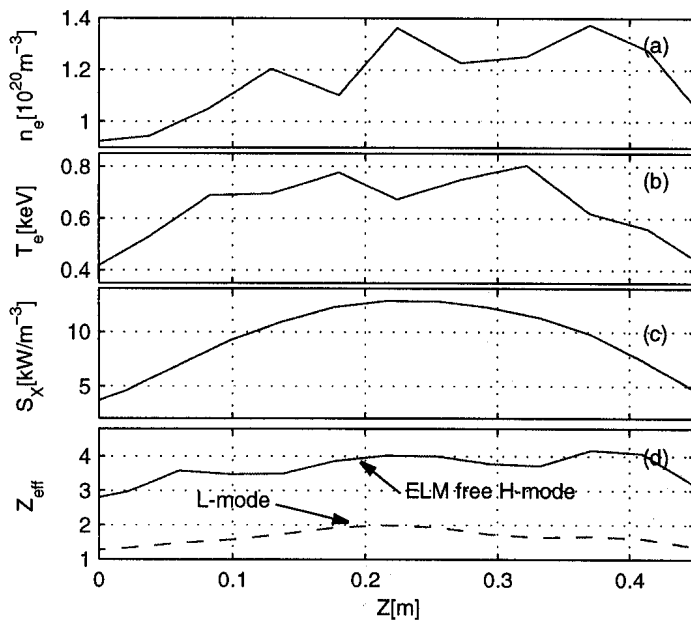


Fig. 4.9 Profiles along a vertical central cut in TCV discharge No. 15539 at $t = 0.7258$ s. (a,b) Electron density and temperature from Thomson scattering. (c) Soft x-ray emissivity. (d) Corresponding Z_{eff} profile at the same time (dashed line) together with the Z_{eff} profile during the ohmic L-mode (continuous line).

References

- [1] G. H. Golub and C. F. Van Loan, *Matrix Computations*, John Hopkins University Press, Baltimore, MD, 1989.
- [2] C. Nardone, *Plasma Phys. Control. Fusion* **34** (1992) 1447.
- [3] J. S. Kim, et al., *Plasma Phys. Control. Fusion* **41** (1999) 1399.
- [4] E. F. Deprettere, *SVD and Signal Processing*, North-Holland, Amsterdam, 1988.
- [5] T. S. Huang, et al., *Appl. Opt.* **14** (1975) 2213.
- [6] J. Stoer and R. Bulirsch, *Introduction to Numerical Analysis*, Springer, New York, 1980.
- [7] C. Eckart, et al., *Bull. Amer. Soc.* **45** (1939) 118.
- [8] T. Dudok de Wit, et al., *Phys. Plasmas* **1** (1994) 3288.
- [9] W. Press, et al., *Numerical Recipes in FORTRAN*, Cambridge University Press, Cambridge, 1992.
- [10] K. V. Mardia, et al., *Multivariate Analysis*, Academic London Press, London, 1987.
- [11] R. W. Preisendorfer, *Principal Component Analysis in Meteorology and Oceanography*, Elsevier, Amsterdam, 1988.
- [12] N. Aubry, et al., *Journal of Statistical Physics* **81** (1995) 793.
- [13] Anton, M., et al., *Plasma Phys. Control. Fusion* **38** (1996) 1849.
- [14] T. Dudok de Wit, *Plasma Phys. Control. Fusion* **37** (1995) 117.
- [15] M. Bessenrodt-Weberpals, et al., *Proc. 21st EPS Conf. on Controlled Fusion and Plasma Physics* (Montpellier 1994), vol. 3, page 1312.
- [16] M. Bessenrodt-Weberpals, et al., *Plasma Phys. Control. Fusion* **38** (1996) 1543.
- [17] H. Reimerdes, et al., *Proc. 27th EPS Conf. on Controlled Fusion and Plasma Physics* (Budapest 2000), P1-025.
- [18] H. Weisen, et al., *Plasma Phys. Control. Fusion* **38** (1996) 1415.
- [19] H. Weisen, et al., *Rev. Sci. Instrum.* **62** (1991) 1531.

5 DEPENDENCE OF SAWTOOTH INVERSION RADIUS AND PROFILES ON PLASMA PARAMETERS

5.1 Introduction

Experimental observations and theoretical models supporting the idea that electron temperature and/or the pressure and/or current density in tokamaks preferentially assume certain privileged profile shapes have been reported for more than two decades [1], [2], [3], [4], [5], [6], [7], [8]. Whereas many observations point to a remarkable degree of resilience of the electron temperature profiles [9],[10], some observations [11] suggest that the plasma pressure profile rather than the temperature profile is most resilient to changes in plasma conditions such as confinement mode or heating. The idea that transport in plasmas adjusts itself in order to establish profiles which together satisfy some equilibrium conditions, such as stability criteria to microscopic or macroscopic modes, the power and particle balance, became known as the ‘principle of profile consistency’ [2]. According to this principle plasma profiles relax to a class of shapes depending only (in the case of circular cross-sections) on the safety factor at the boundary q_a . Experimentally a broadening of the electron temperature profile and of the sawtooth inversion radius, r_{inv} , with $1/q_a$ was observed already in early tokamak experiments [1].

In Ref. [5], Arunasalam and co-workers have proposed a practical working definition of this principle motivated by tearing mode stability considerations. It postulates the existence of unique, natural profile shapes for $j(r)$ and because of ohmic relaxation, for the shape of $T_e(r)$. The consequences of the postulate, as given in Ref. [5], are that the sawtooth inversion radius (which is linked to the safety factor profile), normalised to the minor radius, $\rho_{inv} = r_{inv}/a$ and the broadness of the temperature profile $\langle T_e \rangle / T_{e0}$ are device independent and are functions of $1/q_a$ only. The same authors propose a third consequence expressed as $T_{e0}^{3/2} \propto I_p R_0 / (c_\sigma a^2 V_{loop} F(1/q_a))$, which merely combines the postulation of universal current profiles characterised by $\langle j \rangle / j_0 = F(1/q_a)$ and the assumption of Spitzer conductivity, $\sigma_{Spit} = c_\sigma T_e^{3/2}$. The proposed form is of no predictive value because V_{loop} and I_p cannot be controlled independently in an ohmic discharge. A useful equation for the behaviour of T_{e0} in ohmic plasmas can however be obtained by combining the power balance equation with the temperature dependence of the conductivity [12].

A variety of theories have been proposed to explain the observed features. They differ essentially in the nature of the criteria which are postulated to govern the relations between the relevant plasma profiles. In some theories a relationship between relaxed current and pressure profiles is derived

Chapter 5. DEPENDENCE OF SAWTOOTH INVERSION RADIUS AND PROFILES ON PLASMA PARAMETERS

from a variational principle such that the poloidal magnetic energy [3] or the total (poloidal magnetic plus kinetic) energy [4] is minimised for a given plasma current. Both lead for plasmas with circular cross section to ‘natural’ current and pressure profiles of the form $j/j_0 = p/p_0 = [1 + (q_a/q_0 - 1)\rho^2]^{-2}$, where $\rho = r/a$ is the normalised minor radius, q_0 being the value of the safety factor at the magnetic axis. The broadness $\langle j \rangle/j_0$ and $\langle p \rangle/p_{e0}$ of these natural profiles is equal to $1/q_a$ if $q_0 = 1$ is assumed and to $1/(q_a + 1)$ if $q = 1$ is assumed at the experimentally observed sawtooth inversion radius $\rho_{inv} \approx 1/q_a$ [3], [5]. Assuming Spitzer conductivity a relation between temperature and pressure, respectively density profiles has been inferred [4] with the results $p_e/p_{e0} = T_e^{3/2}/T_{e0}^{3/2}$ and $n_e/n_{e0} = \sqrt{T_e/T_{e0}}$. Note that the natural current and pressure profiles above have finite and substantial boundary ‘pedestals’ which are not supported by experimental measurements and in many conditions would be unstable to external kink modes or to ballooning modes. We note however that minimum energy equilibrium profiles with $j(a) = 0$ have been proposed, although not in a formulation which lends itself to a comparison with experimental data [13]. Relaxed current profiles of the form $j/j_0 = [1 + (q_a/q_0 - 1)\rho^2]^{-2}$, have also been obtained assuming a microscopically filamented, chaotic current structure [6]. There is however in this case no preferred pressure profile. A strong relationship between the pressure and current profiles is also predicted by maximum entropy configurations [7], where the requirement of stationary entropy, together with the equilibrium equation leads, in sawtooth-free tokamak plasmas, to a pressure profile such that $j(\rho)/j_0 = p_e(\rho)/p_{e0} = \Psi(\rho)/\Psi_0$ where $\Psi(\rho)$ is the poloidal flux between the plasma boundary and ρ . Assuming Spitzer resistivity again leads to the above relations between pressure, electron temperature and density profiles. This theory has been recently reformulated to include the effect of sawteeth [14] and the theoretical predictions have been compared to the experimental profiles in a large variety of TCV plasma shapes, showing a remarkable agreement.

In the following we document profile behaviour in the ohmic and ECH L-mode confinement regime for the large variety of plasma shapes which can be produced in TCV.

5.2 Experimental observations in ohmic TCV plasmas

Relations between profile widths, which appear to be consistent with the above theoretical models, are indeed observed in ohmic L-modes in TCV as reported earlier and are independent of plasma shape [12]. The observation is expressed as $\langle p_e \rangle/p_{e0} \approx 1/q_{95}$, where the brackets indicate a volume (or practically equivalently cross sectional area) averages and data were taken over a wide range of plasma shapes including elongations up to 2.6, triangularities in the range -0.5 to +0.7,

5.2 Experimental observations in ohmic TCV plasmas

'square' and 'rhomboidal' shapes and diverted ohmic L-mode plasmas. The electron temperature and density measurements were obtained with the TCV Thomson scattering system with 10-25 measurement locations in the plasma depending on plasma size and mapped onto the flux contours calculated using the equilibrium reconstruction code LIUQE [15] for calculation of the relevant averages. The measurement times, as determined by the probe laser pulses, were not synchronised to the sawtooth cycle. Uncertainties on the broadness factors are dominated by the 1-2 measurements contributing to the determination of the central values and are typically 10%. The confinement properties of these plasmas have been reported previously [16].

In the following, the data are from the same database augmented by a small number of discharges at lower line average density and range from $1.2 \cdot 10^{19}$ to $1.2 \cdot 10^{20} \text{ m}^{-3}$. The plasma currents in the database range from 100 kA to 1.02 MA and the ohmic heating power from 130 kW to 2.1 MW, with energy confinement times ranging from 10 ms to 60 ms. The vacuum toroidal magnetic field was approximately 1.4 T for most discharges except those with $\kappa_a > 2.2$, most of which were obtained for $B_{0vac} = 1$ T. In the case of some of the calculations involving a large number of diagnostic measurements, only 230 discharges out of 350 in the database could be processed. Nonetheless these data are a representative subset of the variety of plasmas created in TCV. A few examples reflecting the variety of plasma shapes in the data set is presented in Fig. 5.1.

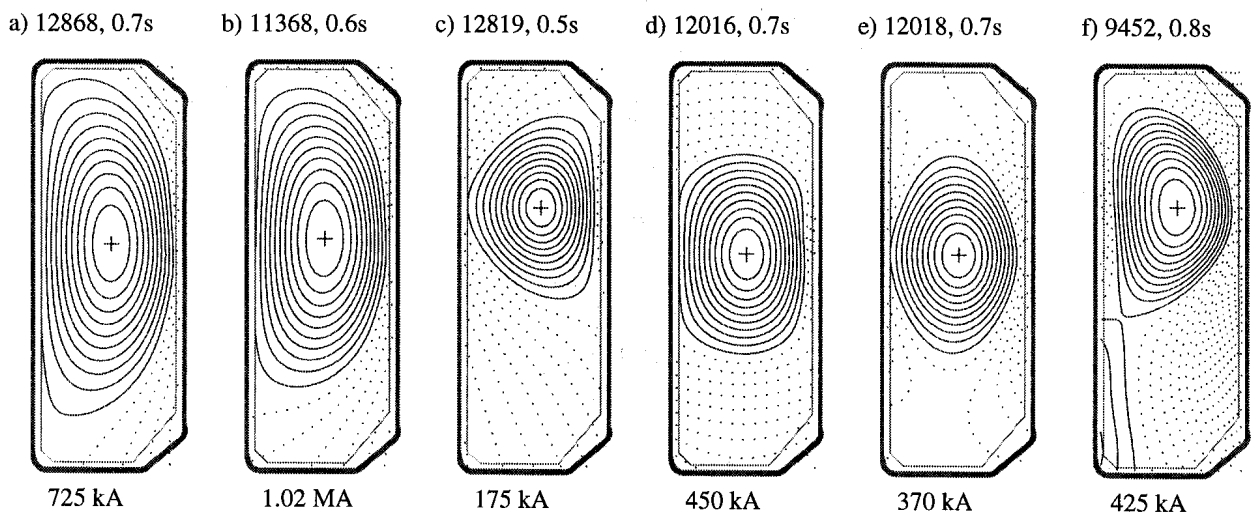


Fig. 5.1 Examples of plasma cross sections in the dataset.

Chapter 5. DEPENDENCE OF SAWTOOTH INVERSION RADIUS AND PROFILES ON PLASMA PARAMETERS

The above mentioned theories deal with the total pressure profile rather than the electron pressure profile measured in TCV. At densities above about $5 \cdot 10^{19} \text{m}^{-3}$, representing 50% of the samples in the database, electron-ion energy equipartition is such that central electron and ion temperatures cannot differ by more than 20% even if half of the ohmic input power density in the core is assumed to be transferred from the electrons to the ions. Hence, at least for those plasmas, the shape of the electron pressure profile is a good reflection of the shape of the total pressure profile and hence suitable for comparison with theory. Also the shapes of the electron temperature and density profiles are found to be insensitive to the average density. The widths of the pressure profile increases approximately as the inverse safety factor at 95% of the poloidal flux, q_{95} , in approximate agreement with the minimum energy model above, assuming $q_0 = 1$ (Fig. 5.2). q_{95} is widely used instead of q_a for characterising shaped plasmas because it is less sensitive to the shape of the plasma boundary, especially the presence or proximity of (an) X-point(s). (For cylindrical plasmas $q_{95} = q_a(1 - 0.05 \ln q_a)$). Note that the most elongated plasmas have so far only been produced in a narrow range of q_{95} due to conflicting requirements for vertical stability and kink stability [17].

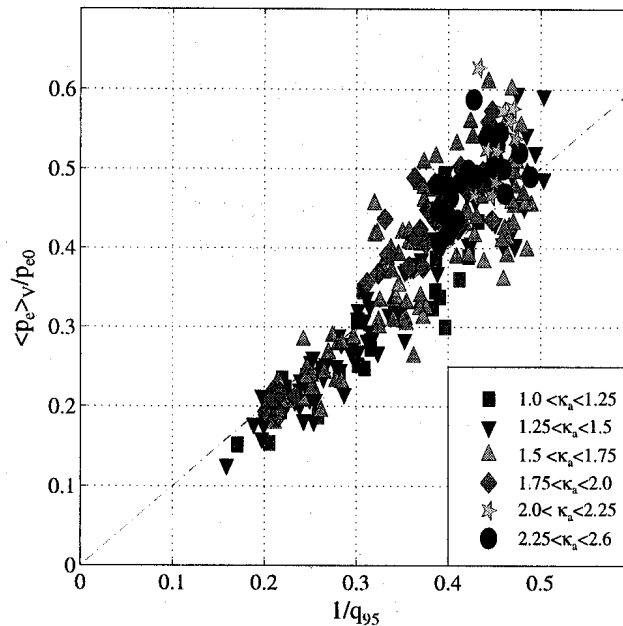


Fig. 5.2 Width of electron pressure profiles versus safety factor at 95% of the poloidal flux.

Inspection of the profiles of electron temperature and density in Fig. 5.3 illustrates some of these features in selected configurations. In this figure, we show T_e , Fig. 5.3(a), and n_e , Fig. 5.3(b),

5.2 Experimental observations in ohmic TCV plasmas

profiles for two discharges having the same shape as shown on the right in Fig. 5.3, but which differ by more than a factor of 2 in q_{95} and have profiles of different broadness.

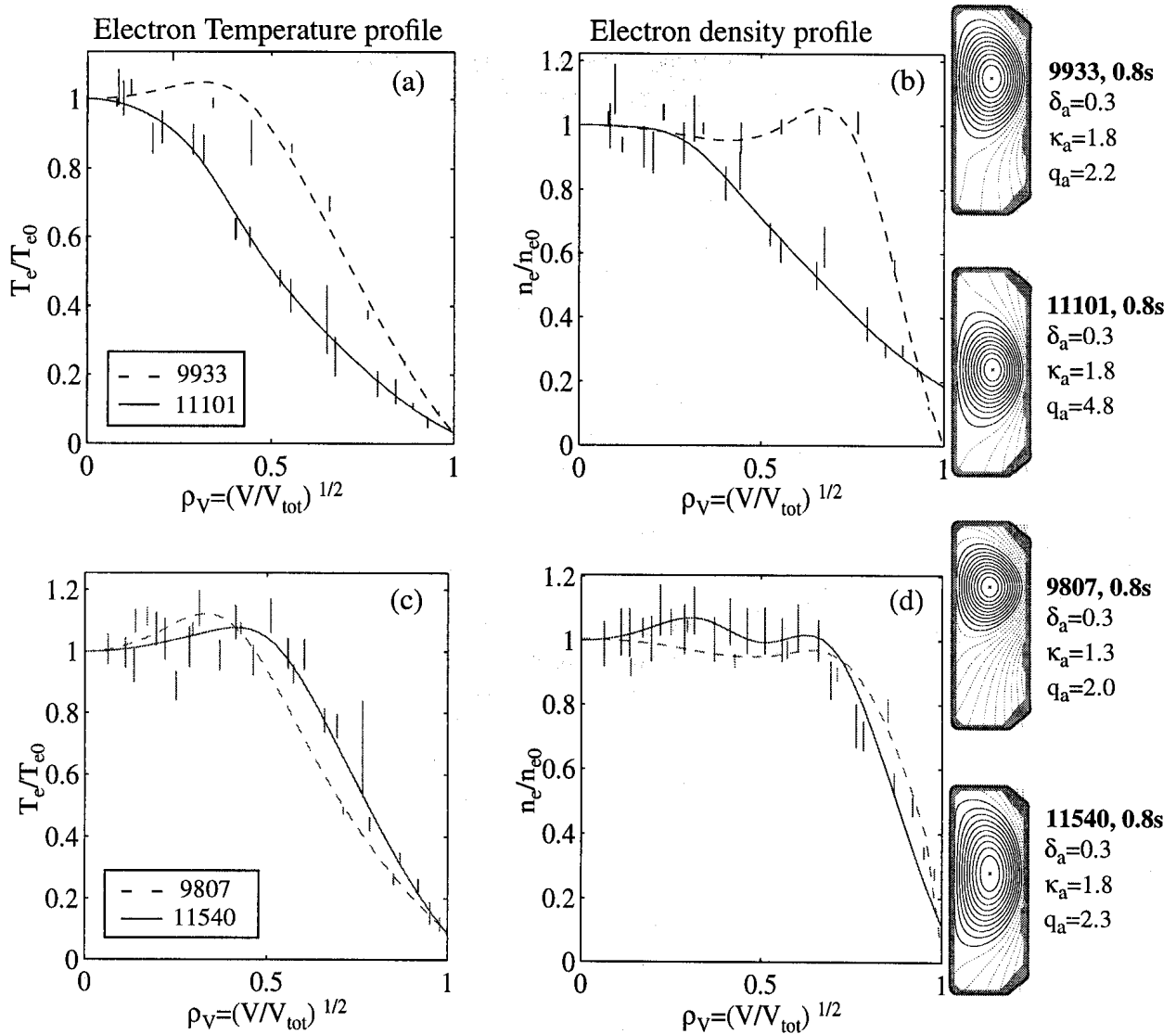


Fig. 5.3 Electron temperature (a,c) and density profiles (b,d) for different plasma configurations shown on the right. Error bars are shown at the positions of measurements. Plasmas in the top row (a,b) have almost the same shape and relevant parameters $T_{e0} = 1.04$ keV, $n_{e0} = 3.9 \cdot 10^{19} \text{ m}^{-3}$ for the discharge No. 9933 and $T_{e0} = 0.62$ keV, $n_{e0} = 6.5 \cdot 10^{19} \text{ m}^{-3}$ for the discharge No. 11101 but different q_{95} . Plasmas in the bottom row (c,d) have similar values of q_{95} and relevant parameters $T_{e0} = 0.66$ keV, $n_{e0} = 3.6 \cdot 10^{19} \text{ m}^{-3}$ for the discharge No. 9807 and $T_{e0} = 0.58$ keV, $n_{e0} = 7.4 \cdot 10^{19} \text{ m}^{-3}$ for the discharge No. 11540 but different elongation.

Chapter 5. DEPENDENCE OF SAWTOOTH INVERSION RADIUS AND PROFILES ON PLASMA PARAMETERS

The profiles are shown as a function of an effective minor radius defined as $\rho = \sqrt{V/V_{plasma}}$ where V is the volume enclosed within the flux surface considered and V_{plasma} is the total plasma volume. Conversely plasmas with very different elongations, but similar values of q_{95} have similar profiles, Fig. 5.3(c,d). Density profiles are systematically broader (by factor ranging from 1 to 1.75) than temperature profiles. The broadness of the density profile is independent of the absolute value of density, which may seem surprising since neutral penetration in these gas-fuelled plasmas depends on density.

5.3 Current profile modelling

We could stop the discussion at this point and declare that the concurrent mechanisms of the various theories are responsible for shaping the profiles as observed. This view is however unsatisfactory for at least two reasons. First it is inappropriate to take the $T_e^{3/2}$ profile as a reflection of the current profile because at low collisionality the conductivity in a tokamak configuration departs significantly from Spitzer conductivity due to friction of the current carrying passing electrons with trapped electrons. But even the neoclassical conductivity σ_{neo} [18] profile alone provides an unsatisfactory (excessively peaked) model of the current profile. The reason for this is that a sawtooth tokamak core, although quasi-stationary on average, is never in resistive equilibrium. Since sawtooth periods in ohmic plasmas are much shorter ($< 10^{-2}$ s in TCV) than current diffusion times ($\approx 10^{-1}$ s for the plasma core) the core remains far from resistive equilibrium and the current profile must not be expected to be proportional to the conductivity profile. The second concern is the applicability of the above theories to plasmas dominated by gross MHD phenomena, such as sawteeth, which are a hallmark of 'normal' ohmic discharges and are governed by MHD stability criteria not contained in their basic assumptions.

We therefore propose a model current profile given as $j = E\sigma_{neo} + j_{boot}$ outside the sawtooth zone and by a prescribed parabolic safety factor profile of the form

$$q(\rho) = q_0 + (1 - q_0)(\rho^2/\rho_1^2) \quad (5.1)$$

inside the $q = 1$ surface, where ρ_1 is the normalised radius of the $q = 1$ surface. For $\rho \leq \rho_1$ the corresponding current profile is well approximated by

$$j_{in}(\rho) = j_0 \cdot \frac{q_0}{q(\rho)} \cdot \frac{B(\rho)}{B_0} \cdot \frac{(\kappa(\rho) + 1/\kappa(\rho))}{\kappa_0 + 1/\kappa_0} \cdot \left\{ 1 - \frac{\rho^2 \cdot (1 - q_0)}{\rho_1^2 \cdot q(\rho)} \right\} \quad (5.2)$$

5.3 Current profile modelling

where

$$j_0 = \frac{(\kappa_0 + 1/\kappa_0)B_0}{\mu_0 R_0 q_0} \quad (5.3)$$

is the central current density, κ is the local elongation, B the average toroidal field and zero suffixes here refer to quantities on the magnetic axis. The safety factor on axis, q_0 and the radius ρ_1 are free parameters. The correction term $\kappa + 1/\kappa$ arises from Ampère's equation in the presence of elongated flux surfaces and the toroidal field correction is necessary to account for effect of the plasma equilibrium, which for these ohmic plasmas is mostly paramagnetic and is as high as 12% for the plasmas with the highest current densities, which are also the most elongated ones.

For $\rho > \rho_1$ the discharge is assumed to be ohmically relaxed, e.g.

$$j(\rho) = E\sigma_{neo}(\rho) + j_{boot}(\rho) \quad (5.4)$$

where $E = V_{loop}/(2\pi R_0)$ is the externally induced electric field, $\sigma_{neo}(\rho)$ is the neoclassical conductivity and j_{boot} is the bootstrap current, which in these ohmic plasmas only contributes a few percent to the total current. The neoclassical expressions were taken from Refs. [19], [20] and evaluated using the measured electron density and temperature profiles and Z_{eff} obtained from soft x-ray measurements [21], as detailed in section 4.3.

The profile of Z_{eff} was assumed to be flat, in accordance with profile measurements on a subset of the data. The trapped electron fraction was obtained from a formulation by Lin-Liu and Miller [22]. The collisionality in our data set ranges over two orders of magnitude, $0.1 \leq \nu^*_{75} \leq 10$, where ν^*_{75} is the collisionality at 75% of the poloidal flux. The corresponding reduction (from the Spitzer value) in cross sectional area average conductivity ranges from 45% to 12% and can be substantially more if only the plasma outside the $q = 1$ surface is considered.

We did not use the absolute values of $E\sigma_{neo}$ because of uncertainties in Z_{eff} , but rescaled $E\sigma_{neo}$ such as to satisfy the matching condition $j_{out}(\rho_1) = j_{in}(\rho_1)$ and then varied ρ_1 such as to satisfy $\int j dA = I_p$, where I_p is the measured total plasma current. This procedure leads to the determination of ρ_1 for a given choice of q_0 which will be compared to the experimentally determined sawtooth inversion radius in section 5.4.

Chapter 5. DEPENDENCE OF SAWTOOTH INVERSION RADIUS AND PROFILES ON PLASMA PARAMETERS

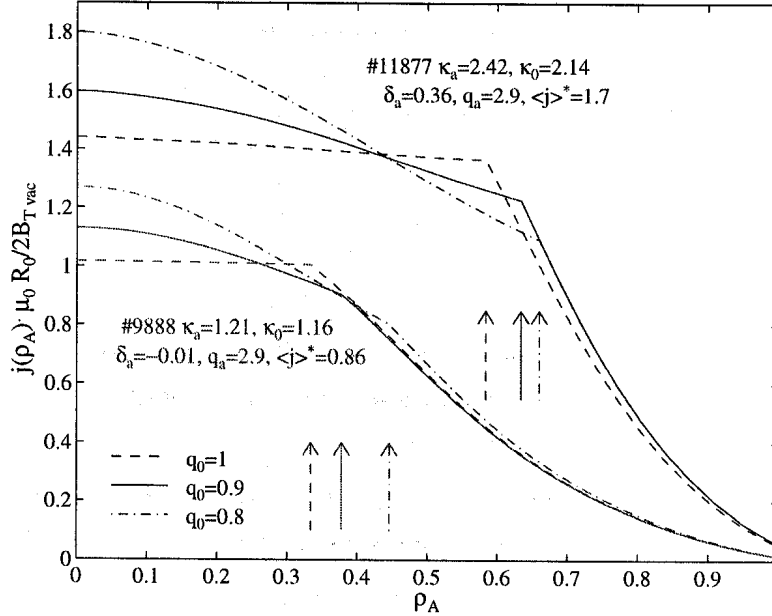


Fig. 5.4 Examples of model current profiles for two different TCV discharges and three choices of q_0 . The safety factor profile inside the $q=1$ surface is prescribed to have a parabolic shape. The ohmic current profile outside the $q=1$ surface is proportional to the neoclassical conductivity. The arrows indicate the $q=1$ radii resulting from the requirement $\int j dA = I_p$.

Fig. 5.4 shows model current profiles for two discharges in the database with the same value of the safety factor at the boundary, but different core elongations, as indicated in the figure. The profiles are shown for $q_0 = 0.8, 0.9$, and 1 and lead to slightly different $q = 1$ radii. The radial coordinate is defined as $\rho_A = \sqrt{A/A_p}$, where A_p is the total cross sectional area of the plasma. (In practice $\rho_A \approx \rho_V$). Also apparent in the figure is the effect of elongation on the current carrying capacity of the discharge. Despite having the same value of q_a the normalised core current density $j_0^* = \mu_0 R_0 j_0 / B_{0vac}$ and ρ_1 are 1.4 times higher, the average dimensionless current density $\langle j \rangle^* = \mu_0 R_0 I_p / B_{0vac}$ is 2 times higher and the total normalised plasma current $\mu_0 R_0 I_p / B_{0vac}$ is 4 times higher for $\kappa_a = 2.4$ than for $\kappa_a = 1.2$ (B_{0vac} is the vacuum toroidal field at the magnetic axis). One interesting feature of these model profiles is that the fraction of the total toroidal current which flows inside the $q = 1$ surface is approximately equal to the normalised $q = 1$ radius, $I(\rho_1) / I_p \approx \rho_1$. More importantly, the modelled $q = 1$ radii are closely approximated by $\rho_1 \approx (\kappa_0 + 1/\kappa_0)^{-1} B_{0vac} / (B_0 \langle j \rangle^*)$ as shown in Fig. 5.5.

5.4 Scaling of the sawtooth inversion radius

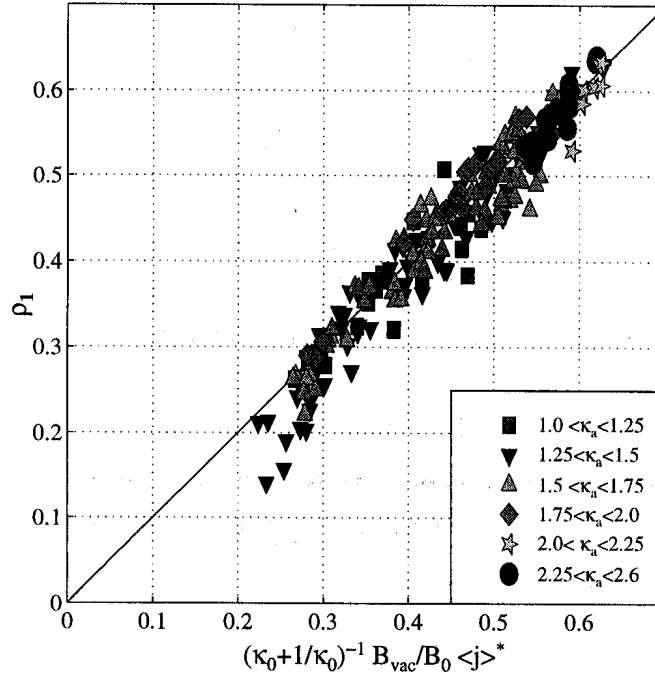


Fig. 5.5 Scaling of effective radius of the $q = 1$ surface from the model.

5.4 Scaling of the sawtooth inversion radius

Time sequences of tomographically inverted soft x-ray signals of typically 10 ms duration, comprising 2-3 sawtooth crashes, were then analysed using the SVD method to yield the spatial structures (*topos*) and corresponding time evolution (*chronos*). The contour of the sawtooth inversion surface is reconstructed as described in section 4.2.2. The normalised inversion radius is defined as $\rho_{inv} = \sqrt{A_{inv}/A_p}$, where A_{inv} is the cross sectional area within the sawtooth inversion surface and A_p is the total cross sectional area of the plasma. Depending on plasma size the accuracy of ρ_{inv} is in the range 0.05-0.1. An advantage of the SVD-based method is that inversion contours can be determined even in the presence of very weak sawtooth activity and strong $m > 0$ modes, as frequently observed at negative triangularity and low average current density. Fig. 5.6 shows examples from four discharges with the same average density, elongation and edge safety

Chapter 5. DEPENDENCE OF SAWTOOTH INVERSION RADIUS AND PROFILES ON PLASMA PARAMETERS

factor, but different triangularity. The top traces are line integrated soft x-ray signals from detectors viewing the plasma core and show sawtoothing and superimposed MHD mode activity (mainly $m = 1$). The lower subplots show the inversion contour and the last closed flux surface.

For $\kappa_a \approx 1$ and $\delta_a \approx 0$ the inversion radius in TCV scales as observed in tokamaks with circular cross section, and $\rho_{inv} \approx 1/q_a$ as proposed as one of the manifestations of ‘profile consistency’. This scaling becomes unsatisfactory even for moderately shaped plasmas.

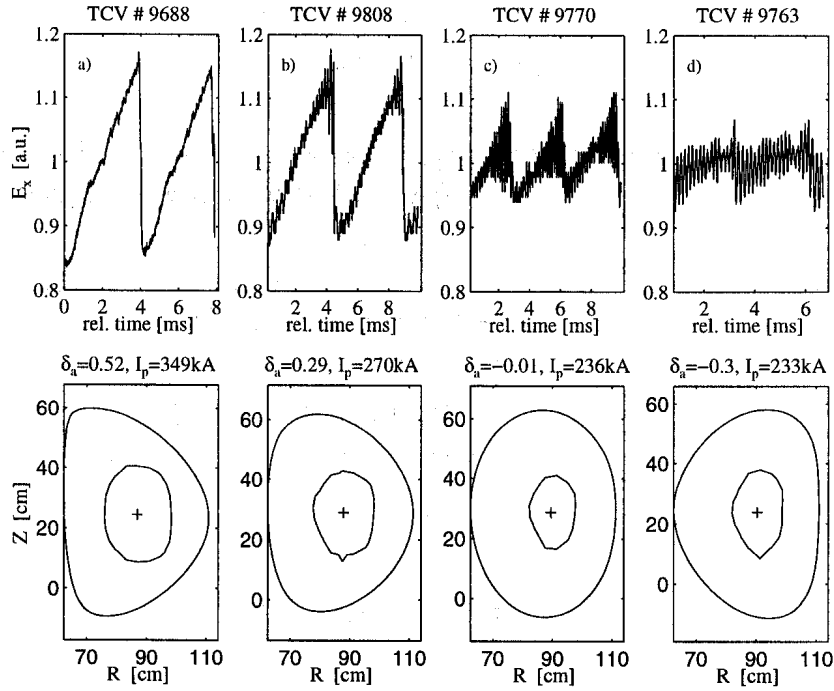


Fig. 5.6 Examples of line integrated soft x-ray signals (top) and sawtooth inversion contours as obtained by tomographical inversion of the data (bottom) in a triangularity scan with $q_a = 3.5$.

An empirical scaling of the sawtooth inversion radius, based on discharges with $\kappa_a < 1.9$, has previously been given as $\rho_{inv} \approx \langle j \rangle^* / 2$, where $\langle j \rangle^* = \mu_0 R_0 I_p / A_p B_{0vac}$ is the dimensionless average current density [12]. This parameter also permits a better empirical scaling of global confinement than safety factor based scalings for a wide range of plasma shapes [12], [16] and relates to q_{95} roughly as

$$\langle j \rangle^* \approx 1.14 [1/\kappa_a + \kappa_a (1 + H(\delta_a) \delta_a^2)] / q_{95} \quad (5.5)$$

5.4 Scaling of the sawtooth inversion radius

where δ_a and κ_a are the triangularity and elongation at the last closed flux surface and $H(\delta_a) = 1$ for $\delta_a > 0$ and $H(\delta_a) = 0$ for $\delta_a < 0$. It also relates to the ‘engineering q ’, $q_{eng} = 5\kappa_a a^2 B_c / R_c I_p$, where the subscript c refers to the geometric centre of the discharge, as $\langle j \rangle^* \approx 2/q_{eng}$. For extreme elongations even the scaling $\rho_{inv} \approx \langle j \rangle^* / 2$ becomes unsatisfactory because of the increased current carrying capacity of the core. This effect is accounted for by a corrective factor proportional to $(\kappa_0 + 1/\kappa_0)^{-1} B_{0vac} / B_0$ as discussed in the previous section. In Fig. 5.7 we show the measured effective inversion radius as a function of the proposed scaling expression,

$$\rho_{inv} = \frac{\langle j \rangle^*}{\kappa_0 + 1/\kappa_0} \cdot \frac{B_{0vac}}{B_0} = \frac{\langle j \rangle}{q_0 j_0}. \quad (5.6)$$

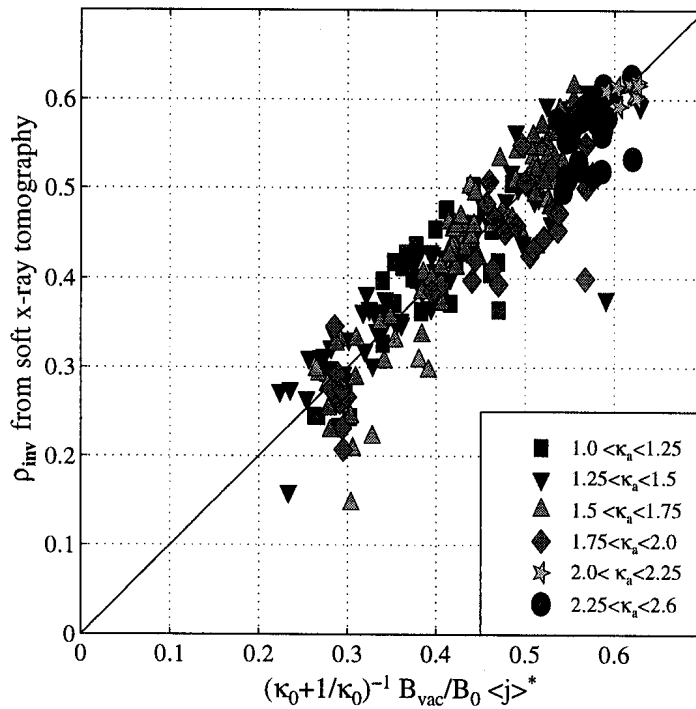


Fig. 5.7 Semi-empirical scaling of inversion radius as determined from soft x-ray tomography for arbitrary shape and elongation in TCV ohmic plasmas.

Chapter 5. DEPENDENCE OF SAWTOOTH INVERSION RADIUS AND PROFILES ON PLASMA PARAMETERS

The correction factors for elongation and toroidal field are the central values obtained from the equilibrium reconstruction. For a predictive scaling expression it is however preferable to use global parameters instead. For this purpose we have fitted the corrective parameters for the whole database, with the results $\kappa_0 \approx 1 + 0.5(\kappa_{95} - 1) + 0.2(\kappa_{95} - 1)^2$ and $B_0/B_{0vac} \approx 1 + 0.054(1 - \beta_p)\langle j \rangle^2$. The latter provides an accurate approximation of diamagnetic and paramagnetic corrections. For moderately shaped plasmas, neglecting equilibrium corrections to B_0 , the scaling reduces to $\rho_{inv} \approx 0.9/q_{95}$.

The measured inversion radii are in good agreement with the radii of the flat core region from the current profile models in section 5.3 for $0.8 \leq q_0 \leq 1$. The best overall match of ρ_{inv} and ρ_1 is obtained for $q_0 = 0.9$ and is shown in Fig. 5.8.

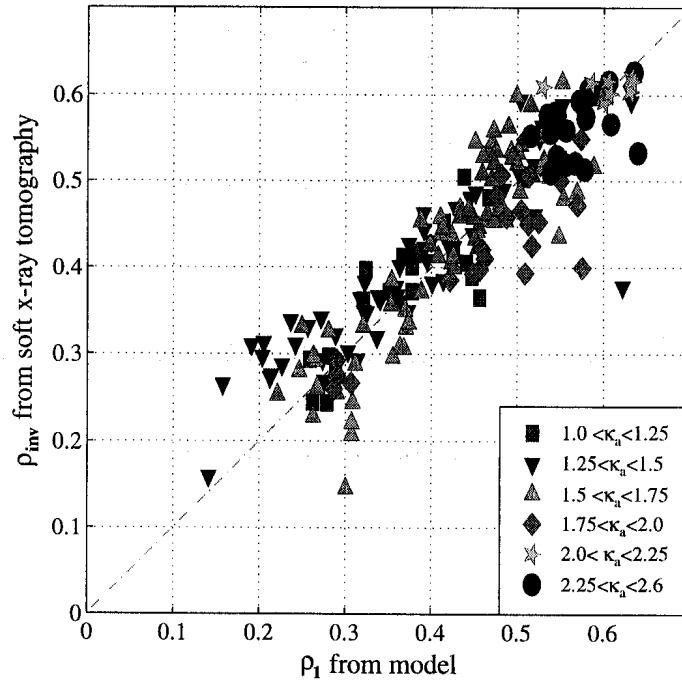


Fig. 5.8 Measured inversion radius versus outermost $q=1$ surface from current profile model.

If we choose $q_0 = 0.8$, the modelled $q = 1$ surface exceeds the measured inversion radius by typically 0.05 minor radii ($\rho_1 \approx \rho_{inv} + 0.05$), while with $q_0 = 1$, corresponding to a flat q -profile, the inversion radius exceeds the $q = 1$ radius by typically 0.05 minor radii ($\rho_1 \approx \rho_{inv} - 0.05$). The latter is consistent with marginal stability to the internal kink mode throughout the plasma core [23].

5.5 Profile shape dependence on plasma parameters

Let's note that the value of q_0 , which is difficult to measure, has been (and still is) a matter of controversy for more than a decade. While some experiments have reported q_0 profiles which are flat in the core region with values very close to unity such as [24], [25], [26], [27], [28], [29] other experiments have reported values of q_0 significantly below unity, with typically $q_0 \approx 0.8$ [30], [31]. It is not clear whether these differences result from experimental uncertainties or from a natural variability of the q -profile in the core and the completeness of the reconnection process during the collapse. We should also note that ρ_{inv} is not expected to be equal to ρ_1 on theoretical grounds [32], see also chapter 6. Fortunately the important physics for the current discussion lies in the limitation of the central current density by sawtooth activity, not in the exact value of q_0 . For the remainder, therefore we assume $q_0 = 0.9$, corresponding to the solid lines in Fig. 5.4. For a different assumption the corresponding broadness of the current profile $\langle j \rangle / j_0$ just needs rescaling with q_0 .

The broadening of current profiles with the inverse edge safety factor, which is proposed as one of the hallmarks of "profile consistency" is a consequence of the limitation of j_0 by sawtoothing. In fact, a better scaling, taking account of the shape and equilibrium corrections discussed above is given by

$$\frac{\langle j \rangle}{j_0} = \frac{I_p}{A_p} \cdot \frac{\mu_0 R_0 q_0}{(\kappa_0 + 1/\kappa_0) \cdot B_0} = \frac{q_0 \cdot B_{0vac}}{(\kappa_0 + 1/\kappa_0) \cdot B_0} \langle j \rangle^* \quad (5.7)$$

Up to the factor q_0 this is just the same as the normalised $q = 1$ radius resulting from the current profile model and as our semi-empirical scaling for the sawtooth inversion radius, Eq. (5.6). For moderately shaped plasmas and with the neglect of equilibrium corrections, all of these reduce to $\langle j \rangle / (j_0) \approx \langle j \rangle^* / 2 \approx \rho_1 \approx \rho_{inv}$.

5.5 Profile shape dependence on plasma parameters

In Fig. 5.9, the widths of the electron pressure, temperature and density profile from Thomson scattering measurements are shown as a function of the current profile width parameter $\langle j \rangle / (j_0 q_0)$ showing a remarkable degree of correlation, irrespective of plasma shape. Such a correlation can be understood from the 'clipping' effect of the sawtooth activity which limits the core peaking of the current and the pressure or temperature profiles at least when, as in TCV, the sawtooth period is substantially shorter than both the energy confinement time and the resistive skin time for the plasma within the $q = 1$ surface.

Chapter 5. DEPENDENCE OF SAWTOOTH INVERSION RADIUS AND PROFILES ON PLASMA PARAMETERS

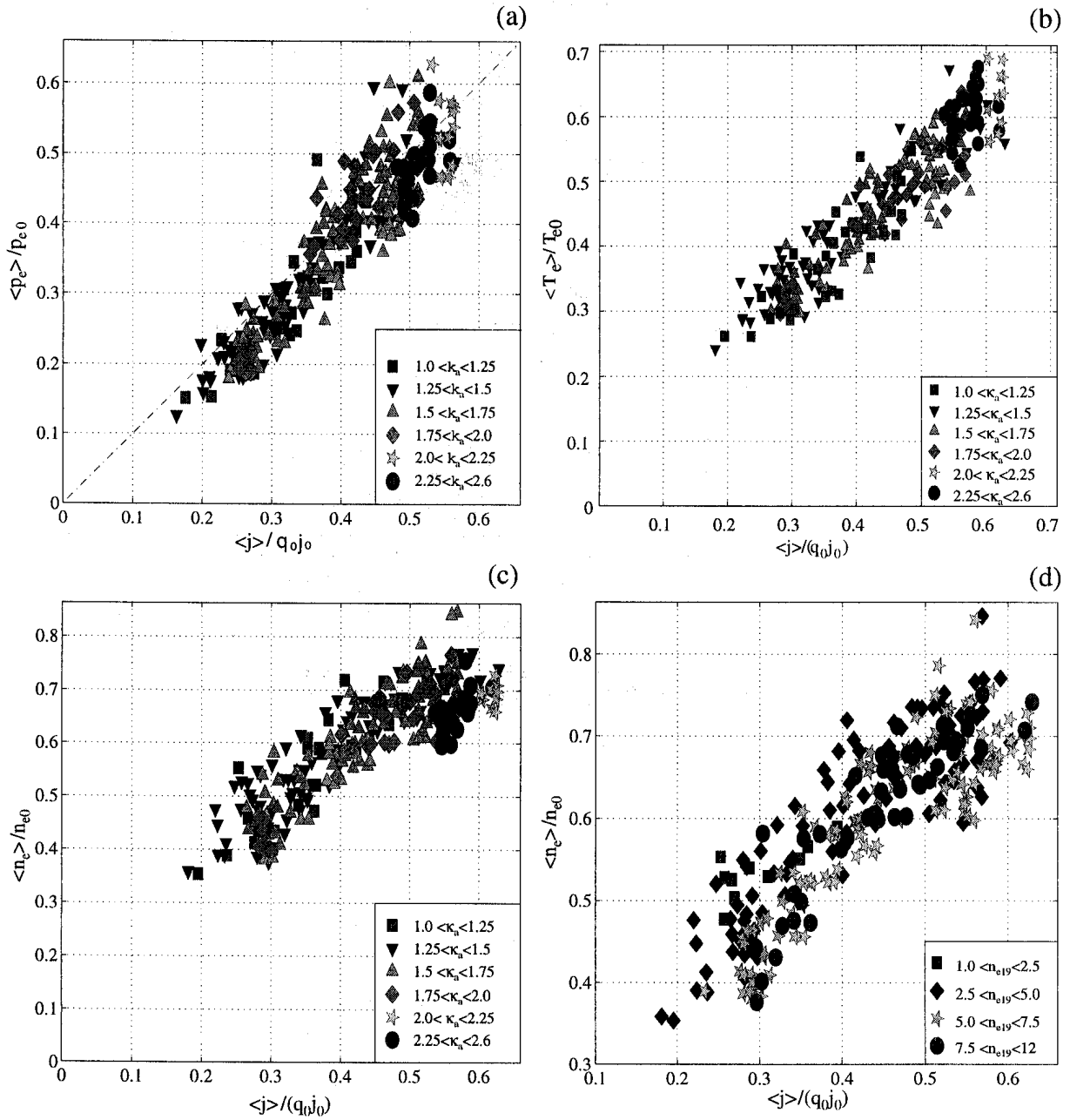


Fig. 5.9 Profiles widths from Thomson scattering measurements as a function of the current profile width parameter $\langle j \rangle / (j_0 q_0)$. (a) Electron pressure; (b) electron temperature (c,d) electron density. Symbols refer to classes of elongations at the LCFS in (a,b,c) and classes of electron density in (d).

5.5 Profile shape dependence on plasma parameters

Sawteeth affect all ohmic discharges operating in the usual range of edge safety factor, usually $q_a < 10$, and they produce post-crash plasma profiles which are nearly flat inside the $q = 1$ surface. Due to the rather low reheat power in ohmic discharges, only a moderate temperature increase is observed before the next sawtooth crash flattens the profiles again. As a result, profiles remain fairly flat and their widths are closely correlated to the normalised inversion radius. An example of the clipping effect of the sawtooth activity on the electron temperature profile is shown in Fig. 1.10 of chapter 1.

One feature of potential importance is the behaviour of the density profile which, unlike the temperature, is not directly linked to the current profile. The greater widths of the density profiles, Fig. 5.9(c,d), is qualitatively consistent with the fact that the source of the particles is peripheral, rather than localised in the plasma core as is the case of the ohmic heating power. The relatively strong peaking at low current densities, Fig. 5.3(a), together with the observation that the profile broadness is not dependent on the electron density Fig. 5.9(d) are indicative of the existence of a particle pinch.

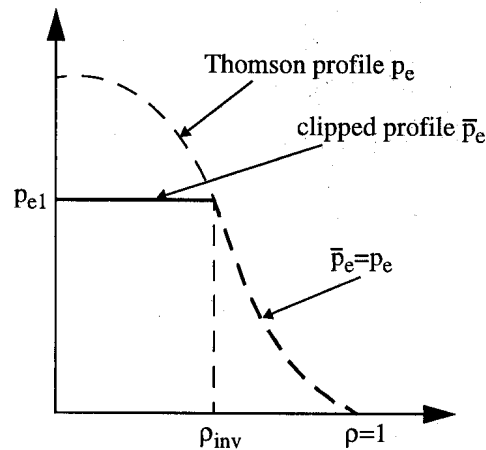


Fig. 5.10 Schematic clipped profile \bar{p}_e together with the Thomson profile p_e . The two profiles are coincident for $\rho > \rho_{inv}$, being ρ_{inv} the experimental inversion radius.

The scaling of profile broadness factor appears to be a robust feature which is essentially related to the position of the $q = 1$ surface or the sawtooth inversion radius and is quite insensitive to the detailed physics governing transport in the confinement zone. The essential features and scalings reported here are the same as those predicted by the theories quoted in the introduction. Nevertheless, these observations should not be regarded as supportive of theories predicting similar relations without accounting for sawtooth activity. It can not be excluded however that the physics

Chapter 5. DEPENDENCE OF SAWTOOTH INVERSION RADIUS AND PROFILES ON PLASMA PARAMETERS

processes of the mentioned theories may also be at work. Conversely, the clipping effect produced by sawteeth cannot explain more subtle features of the profiles in the confinement zone, i.e. outside the $q = 1$ surface. Pressure and temperature profiles are close to trapezoidal outside the inversion radius for high values of $\langle j \rangle / (j_0 q_0)$, whereas they become increasingly concave as $\langle j \rangle / (j_0 q_0)$ is reduced, as can be observed in Fig. 5.3. These features in the confinement region have little influence on profile widths defined as $\langle p_e \rangle / p_{e0}$, etc. Moreover, this definition depends on the time during the sawtooth cycle at which measurements are taken, using a repetitively pulsed Thomson scattering system, resulting in a significant amount of scatter in the data.

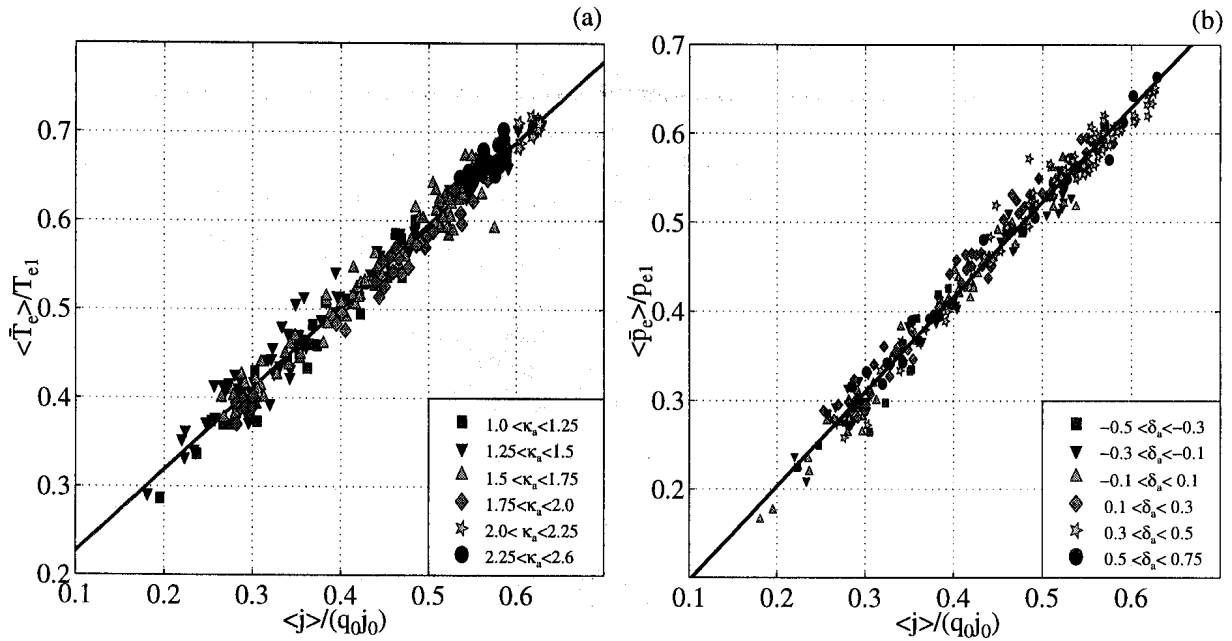


Fig. 5.11 Scaling of inverse peaking factors (confinement zone only) in ohmically heated TCV discharges. (a) Electron temperature inverse peaking factor. Symbols refer to different classes of plasma elongation at the LCFS. Fit: $\langle T_e \rangle / T_{e1} = 0.92 \langle j \rangle / (q_0 j_0) + 0.13$. (b) Electron density inverse peaking factor. Symbols refer to different classes of plasma triangularity at the LCFS. Fit: $\langle \bar{p}_e \rangle / p_{e1} = 1.1 \langle j \rangle / (q_0 j_0) - 0.05$.

To overcome these difficulties, we have introduced ‘clipped’ profile widths such as $\langle \bar{p}_e \rangle / p_{e1}$ where p_{e1} is the electron pressure at the sawtooth inversion radius and $\bar{p}_e = p_{e1}$ for $\rho < \rho_{inv}$ and $\bar{p}_e = p_e$ for $\rho \geq \rho_{inv}$, as it is illustrated in Fig. 5.10. In the latter region, profiles change only little during the sawtooth cycle. As a result, these ‘clipped’ profile peaking factors are a measure of the shape in the confinement zone (degree of convexity) and can be considered as the idealised profile

5.6 Experimental observations in ECH plasmas

widths just after the sawtooth crashes, when the core profiles are flattened.

These widths are shown in Fig. 5.11(a) and Fig. 5.11(b) for electron pressure and temperature respectively and show a remarkably narrow distribution as a function of $\langle j \rangle / (j_0 q_0)$. The standard deviations from the fitted lines in the figures are 0.0173 and 0.0172. Electron density profile widths (not shown) $\langle \bar{n}_e \rangle / n_e$ vary from typically 0.55 to 0.79 as $\langle j \rangle / (j_0 q_0)$ increases from 0.3 to 0.6.

Fig. 5.11 suggests that the current profile determines all other profiles, but clearly they cannot be accounted for by sawteeth alone, since they only marginally affect the profiles in the confinement region. Recently, these observations have been compared with theoretical predictions based on the assumption that magnetic entropy is constant in time [14]. The experimental sawtooth inversion radii and electron temperature profile are in good agreement with predictions in the frame of this theory.

5.6 Experimental observations in ECH plasmas

On TCV, a correlation between clipped profile peaking factor and the current profile width parameter $\langle j \rangle / (j_0 q_0)$ is also observed in ECH L-mode plasmas as shown in Fig. 5.12.

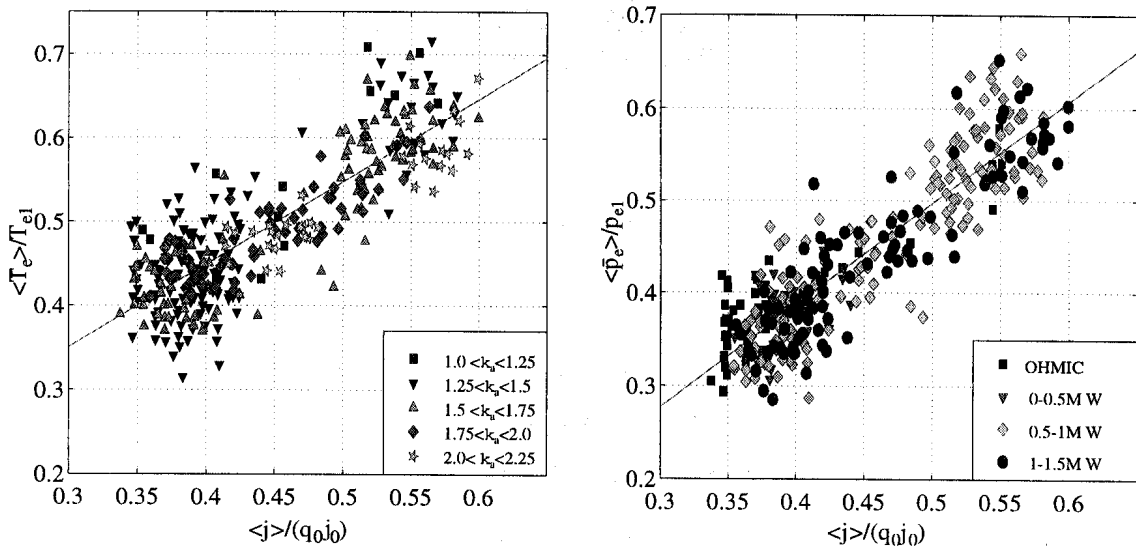


Fig. 5.12 Scaling of inverse peaking factors (confinement zone only) in ECH discharges. (a) Electron temperature inverse peaking factor. Symbols refer to different classes of plasma elongation at the LCFS. Fit: $\langle T_e \rangle / T_{e1} = 0.99 \langle j \rangle / (q_0 j_0) + 0.05$. (b) Electron density inverse peaking factor. Symbols refer to different classes of heating power. Fit: $\langle \bar{p}_e \rangle / p_{e1} = 1.1 \langle j \rangle / (q_0 j_0) - 0.05$.

Chapter 5. DEPENDENCE OF SAWTOOTH INVERSION RADIUS AND PROFILES ON PLASMA PARAMETERS

Data were taken over a wide range of plasma shapes including elongations up to 2.15 and triangularities in the range -0.65 to $+0.65$. All discharges were limited L-mode discharges with central electron density $n_{e0} \approx (2 - 2.5) \cdot 10^{19} \text{ m}^{-3}$ and the plasma current was varied from 200 kA to 700 kA. The confinement properties of this set of experiments, which includes ECH powers up to 1.4 MW, has been presented in Ref. [33] showing that the experimental scaling of the energy confinement time follows the Rebut-Lallia-Watkins confinement scaling [34].

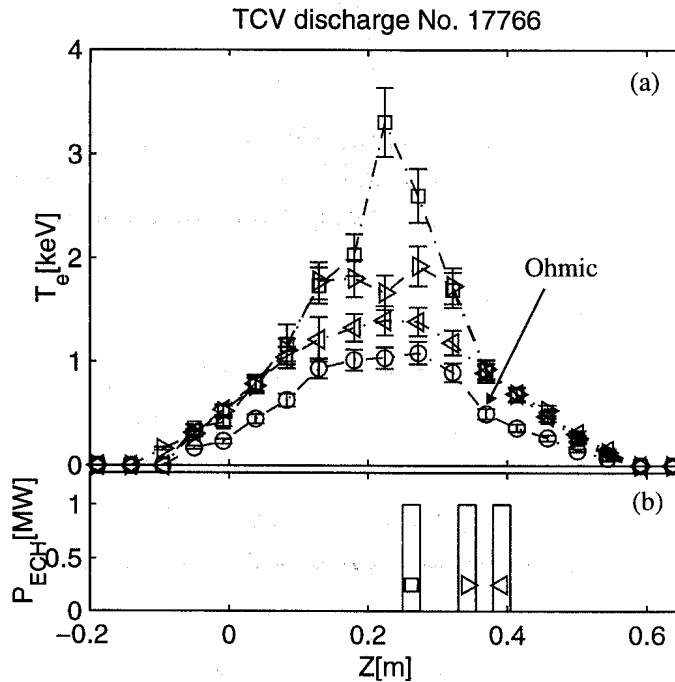


Fig. 5.13 Radial sweep of the ECH power absorption location. (a) Electron temperature profiles from Thomson scattering measurements at different times during ohmic and ECH phases. (b) ECH power deposition location at the times of the temperature profile measurements. The correspondance is indicated by the symbols.

Although the main scaling parameter for profile peaking is still $\langle j \rangle / (j_0 q_0)$, the electron temperature profiles are no longer determined by this parameter alone in ECH plasmas. In Ref. [35], the scatter of $\langle \bar{T}_e \rangle / T_{e1}$ in Fig. 5.12 for any given value of $\langle j \rangle / (j_0 q_0)$ has been interpreted as resulting from the existence of a range of power deposition profiles. This interpretation is supported also by direct comparison of temperature profiles from individual discharges with on-axis versus off-axis power deposition, as it is illustrated in Fig. 5.13 for the TCV discharge No. 17766. The plasma parameters are $\delta_a = 0.17$, $\kappa_a = 1.33$, $q_a = 2.8$, $I_p = 220 \text{ kA}$,

5.6 Experimental observations in ECH plasmas

$P_{ECH} = 900$ kW and during the discharge the heating location is moved radially in minor radius, Fig. 5.13(b), by sweeping the launching angle of two X2-gyrotrons. In Fig. 5.13(a), the electron temperature profiles from Thomson scattering measurements are shown at different times during the sweep of the ECH deposition location and during the ohmic phase. The electron temperature profiles broaden, and central temperatures decrease, as power is deposited further away from the axis, which is located at $z = 0.22$ m, as expected from diffusive transport.

In the experiments of the data set presented in Fig. 5.12, three X2-gyrotrons were used and one gyrotron was inadequately adjusted to produce an O-mode ECH beam which is absorbed after multiple reflection on the TCV wall. This results in large uncertainties in the power deposition profiles. Although heating was fairly central in ECH discharges in this data set, no attempt was made to scale the power deposition profiles to the large variety of plasma shapes and sizes, nor to $\langle j \rangle / (j_0 q_0)$, as occurs naturally in ohmic plasmas.

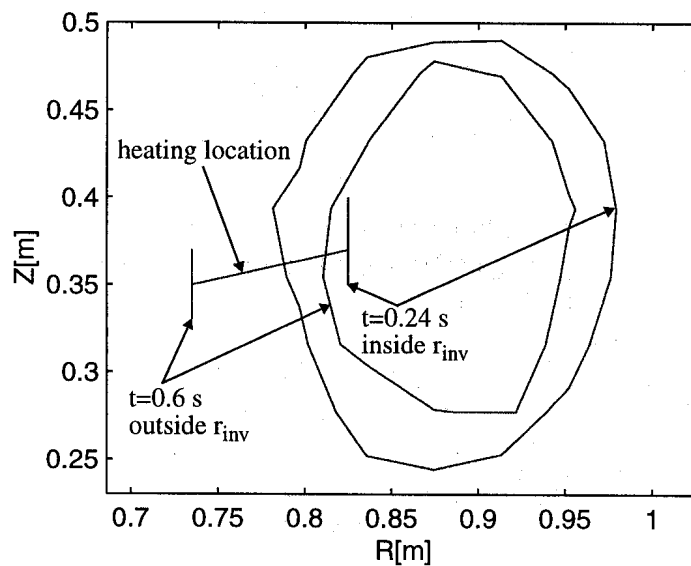


Fig. 5.14 Modification of the sawtooth inversion surface location during ECH in the TCV discharge No. 12348. The sawtooth inversion surface, obtained from tomographically inverted soft x-ray measurements, is shown together with the heating location at different times.

Another main concern arises from the observation that the sawtooth inversion radius can be slightly modified depending on the ECH deposition profiles [36]. This is illustrated for the TCV discharge No. 12348 in Fig. 5.14, which compares the heating position with the sawtooth inversion surface as determined from soft x-ray tomography. The plasma parameters are: $\delta_a = 0.13$, $\kappa_a = 1.29$,

Chapter 5. DEPENDENCE OF SAWTOOTH INVERSION RADIUS AND PROFILES ON PLASMA PARAMETERS

$q_a \approx 3.5$, $P_{ECH} = 500$ kW and the heating location is moved outward in minor radius with a radial velocity of about 3 cm / 100 ms by changing the toroidal magnetic field. During the sweep, the safety factor at the edge shows a slightly increase from $q_a \approx 3.38$ at $t = 0.24$ s to $q_a \approx 3.54$ at $t = 0.6$ s. The ECH deposition location, as determined by the ray tracing code TORAY [37], crosses the inversion surface at $t = 0.37$ s. The inversion surface increases when heating at the surface or inside it whereas it is strongly reduced when heating outside it. This observation is consistent with transport simulations using PRETOR transport code [38] which show that the increase of the sawtooth inversion radius is related to a broadening of the current profile and consequently to a radially outward displacement of the $q = 1$ surface [39].

Modifications to the sawtooth inversion radius may also result from changes in the pre-crash electron temperature profile [36]. On the theoretical grounds, the sawtooth inversion surface, as defined in chapter 4, is not necessarily coincident with the $q = 1$ surface (see for example appendix B in Ref. [36]). The difference between the two depends on the pre-crash profiles of the safety factor, temperature and density, and on the assumed relaxation model. This difference can be large especially for extremely peaked electron temperature profiles such as those obtained with strong central power deposition.

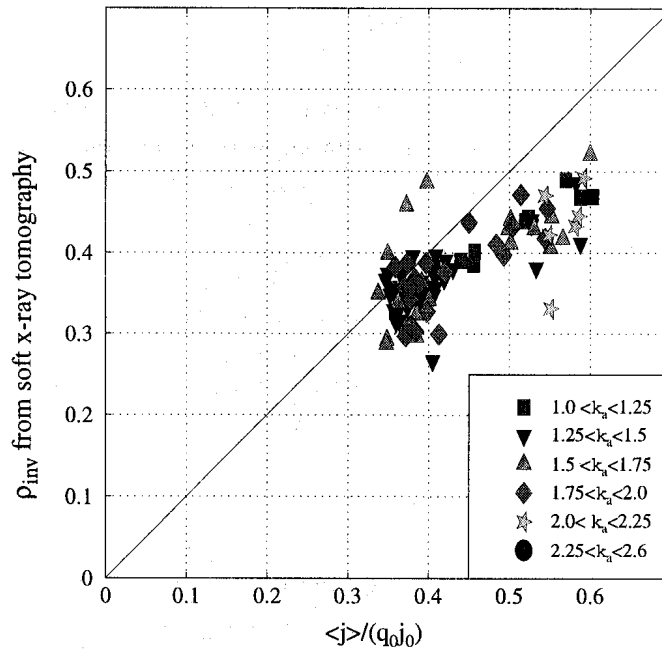


Fig. 5.15 Semi-empirical scaling of inversion radius as determined from soft x-ray tomography for arbitrary shape and elongation in TCV plasmas during ECH. The continuous line shows the scaling obtained under ohmic conditions, given by Eq. (5.6).

5.7 Summary and discussion

In Fig. 5.15, the normalised inversion radius ρ_{inv} in ECH L-mode plasmas is shown as a function of $\langle j \rangle / (j_0 q_0)$. The data set in this figure is extracted from the series of experiments presented in Fig. 5.12 and it is limited to those discharges for which the experimental inversion radius could be obtained. Under ECH conditions, the experimental normalised inversion radii are smaller than those expected from the ohmic scaling, given by Eq. (5.6), which is shown by the continuous line in Fig. 5.15. This does not necessarily imply that the current profiles are significantly broadened in these experiments. The measured inversion radii are more likely a result of increased peaking of pre-crash electron temperature profile, as it will be shown in chapter 6 in the frame of the Kadomtsev's reconnection model [40].

5.7 Summary and discussion

Sawtooth activity affects TCV ohmic L-mode discharges operating at edge safety factors up to 10. A large number of ohmic L-mode discharges including elongations up 2.6 to and triangularities in the range -0.5 to +0.7 have been investigated. We observe that the normalised inversion radius, determined by soft x-ray tomography, and the profile inverse peaking factors $\langle p_e \rangle / p_{e0}$, $\langle T_e \rangle / T_{e0}$ and $\langle n_e \rangle / n_{e0}$ for electron pressure, temperature and density, depend on the current profile width via the parameter $\langle j \rangle / (q_0 j_0)$ where $\langle j \rangle$ is the cross-sectionally averaged current density, irrespective of plasma shape and electron density. This scaling parameter can be evaluated without knowledge of the central current density or safety factor, which is a still a matter of controversy, since $j_0 q_0 = B_0 (\kappa_0 + 1/\kappa_0) / (\mu_0 R_0)$, where κ_0 is the elongation on the magnetic axis. Using the observed scaling of the normalised sawtooth inversion radius $\rho_{inv} = \langle j \rangle / (j_0 q_0)$, the total plasma current can be expressed as

$$I_p = \rho_{inv} \frac{\pi B_0 a^2}{\mu_0 R_0} \kappa_a (\kappa_0 + 1/\kappa_0) \quad (5.8)$$

which is similar to that obtained when scaling the plasma current at fixed safety factor q_{95} , where $I_p \propto \kappa_{95} (\kappa_{95} + 1/\kappa_{95})$ [35]. Eq. (5.8) allows to scale plasma current and elongation for a fixed normalised inversion radius. This is of particular importance for the design of a future reactor where excessively large sawtooth inversion surface may pose severe problems of operation (see chapter 1). Eq. (5.8) together with the empirical relation obtained from the database

$$\frac{(\kappa_0 + 1/\kappa_0)}{(\kappa_{95} + 1/\kappa_{95})} \approx 1 - 0.09 \kappa_{95} (\kappa_{95} + 1) \left(1 - \frac{\langle j \rangle^2}{4} - \frac{\beta_p}{4} \right) \quad (5.9)$$

Chapter 5. DEPENDENCE OF SAWTOOTH INVERSION RADIUS AND PROFILES ON PLASMA PARAMETERS

show that the plasma elongation κ_{95} can be scaled up while keeping fixed the normalised sawtooth inversion radius with only a modest penalty in plasma current (typically 10% at $\kappa_a = 2$), as compared to scaling at fixed q_{95} . Thus, most of the current carrying capacity resulting from high elongation is retained, even when optimising a design with the constraint of a fixed normalised inversion radius.

In TCV, experimental observations, supported by internal kink stability calculations, show that sawtooth periods and amplitudes decrease at high elongation for constant $\langle j \rangle / (j_0 q_0)$ both in ohmic and ECH discharges [41]. These results together with the scaling of the normalised inversion radius presented in this chapter show that the frequently expressed fear of excessively large inversion radii and sawtooth amplitude at high plasma elongation, which may trigger neoclassical tearing modes, are ill founded.

The scaling of profile broadness factor and normalised sawtooth inversion radius appears to be largely a consequence of the ‘clipping’ effect of the sawtooth activity which limits the core peaking of the current and the pressure or temperature profiles at least when, as in TCV ohmic L-mode plasmas, the sawtooth period is shorter than both the energy confinement time and the resistive skin time. Although, the scalings reported here are the same as those predicted by the theories quoted in the introduction, this should not be regarded as supportive of theories predicting similar relations without accounting for sawtooth activity. Conversely, profile features in the confinement zone, i.e. outside the $q = 1$ surface, cannot be accounted for by sawteeth alone since they affect only marginally the profiles in this region.

The profile shape in the confinement zone has been studied by introducing clipped profile widths such as $\langle \bar{p}_e \rangle / p_{e1}$, where p_{e1} is the electron pressure at the sawtooth inversion radius and $\bar{p}_e = p_{e1}$ for $\rho < \rho_{inv}$ and $\bar{p}_e = p_e$ for $\rho \geq \rho_{inv}$. Interestingly, these widths for electron temperature and density show a remarkable correlation with the parameter $\langle j \rangle / (q_0 j_0)$, again suggesting that the current profile determines all other profiles. This is consistent with a recently developed theoretical model based on the assumption that magnetic entropy is constant in time [14], which predicts sawtooth inversion radii and electron temperature profile in good agreement with our experimental observations.

In ECH L-mode plasmas, the parameter $\langle j \rangle / (q_0 j_0)$ remains the main scaling parameter for the clipped profile widths. Nevertheless the electron temperature profiles are no longer determined by this parameter alone and they depend strongly from the ECH power deposition profile showing a broadening of the profile as the ECH power is deposited further away from the axis, as expected from diffusive transport.

5.7 Summary and discussion

The sawtooth inversion surface, which is not necessarily coincident with the $q = 1$ surface, can also be modified by injecting ECH power into the plasma. Modifications may arise either from changes in the pre-crash current or temperature profiles.

References

- [1]TFR Group, presented by D. Launois, *Proc. 7th EPS Conf. on Controlled Fusion and Plasma Physics* (Lausanne 1975), vol. 2, page 1.
- [2]B. Coppi, *Comments on Plasma Phys. Control. Fusion* **5** (1980) 261.
- [3]D. Biskamp, *Comments on Plasma Phys. Control. Fusion* **10** (1986) 165.
- [4]B. Kadomtsev, *Proc. International Conference on Plasma Physics*, (Kiev 1987), page 1273. edited by A.G. Sitenko, published by World Scientific.
- [5]V. Arunasalam, et al., *Nucl. Fusion* **30** (1990) 2111.
- [6]J. B. Taylor, *Phys. Fluids B* **5** (1993) 4378.
- [7]E. Minardi, et al., *Plasma Phys. Control. Fusion* **32** (1990) 819.
- [8]E. Minardi, *Physics Letters A* **240** (1998) 70.
- [9]R. J. Goldston, *Plasma Phys. and Control. Fusion* **26** (1984) 87.
- [10]E. D. Fredrickson, et al., *Nucl. Fusion* **27** (1987) 1897.
- [11]O. Gruberet, et al., *Proc. 14th EPS Conf. on Controlled Fusion and Plasma Physics* (MAdrid 1987) vol. 11D, page 45.
- [12]H. Weisen, et al., *Plasma Phys. Control. Fusion* **40** (1998) 1803.
- [13]E. Lazzaro, et al., *Physics Letters A*, **143** (1990) 393.
- [14]E. Minardi, et al., *Nucl. Fusion* **41** (2000) 113.
- [15]F. Hofmann, et al., *Nucl. Fusion* **28** (1988) 1871.
- [16]H. Weisen, et al., *Plasma Phys. Control. Fusion* **39** (1997) B135.
- [17]F. Hofmann, et al., *Proc. 24th EPS on Controlled Fusion and Plasma Physics* (Berchtesgaden 1997), vol. 21A part II, page 525.
- [18]S. P. Hirshman, et al., *Nucl. Fusion* **21** (1981) 1079.
- [19]O. Sauter, et al., *Theory of Fusion Plasmas*, Lausanne-Varenna Int. Workshop (1994) 337.
- [20]O. Sauter, *ITER EDA memo IDoMS No s19 MD 18 96-08-06 F1* (1996).
- [21]H. Weisen, et al., *Rev. Sci. Instrum.* **63** (1991) 1531.
- [22]Y. R. Lin-Liu, et al., *Phys. Plasmas* **2** (1995) 1666.
- [23]M. N. Bussac, et al., *Phys. Rev. Lett.* **35** (1975) 1638.
- [24]K. McCormick, et al., *Phys. Rev. Lett.* **58** (1987) 491.
- [25]D. Wróblewski, et al., *Phys. Rev. Lett.* **61** (1988) 1724.

- [26]D. Wróblewski, et al., *Phys. Rev. Lett.* **71** (1993) 859.
- [27]H. Weisen, et al., *Phys. Rev. Lett.* **62** (1989) 434.
- [28]B. W. Rice, *Fusion Engineering and Design* **34-35** (1997) 135.
- [29]B. W. Rice, *Private communication on q_0 measurements on the DIII-D tokamak* (1998).
- [30]H. Soltwisch, *Plasma Phys. and Control. Fusion* **34** (1992) 1669 and references therein.
- [31]F. M. Levinton, et al., *Phys. Rev. Lett.* **72** (1994) 2895.
- [32]F. Porcelli, et al., *Plasma Phys. Control. Fusion* **38** (1996) 2163.
- [33]A. Pochelon, et al., *Nucl. Fusion* **39** (1999) 1807.
- [34]P. H. Rebut, et al., *Proc. 12th Int. Conf. on Plasma Phys. and Control. Nuclear Fusion Research* (Nice 1988), Vol 2, page 191.
- [35]H. Weisen, I. Furno, and TCV Team submitted for publication to *Nucl. Fusion*, CRPP report LRP 685/00.
- [36]Z. A. Pietrzyk, et al., including I. Furno, *Nucl. Fusion* **39** (1999) 587.
- [37]G. Smith, et al., *Proc. 9th Joint Workshop and Electron Cyclotron Heating*, Borrego Springs, Editor: John Lohr, Publisher: World Scientific (1995) 651.
- [38]D. Boucher, et al., *Proc. IAEA Tech. Com. on Advances in Simulation and Modell. of Thermonuclear Plasmas* (Montreal 1993), page 142.
- [39]C. Angioni, *Private communications*.
- [40]B. B. Kadomtsev, *Fizika Plazmy* **1** (1975) 710; *Sov. J. Plasma Phys.* **1** (1976) 389.
- [41]H. Reimerdes, et al., *Plasma Phys. Control. Fusion* **42** (2000) 629.

6 SAWTOOTH ACTIVITY IN ECH PLASMAS IN TCV

Different types of central relaxation oscillations are observed in the presence of electron cyclotron heating (ECH) depending on the location of the deposited power. In TCV, standard sawteeth, i.e. triangular sawteeth similar to ohmic sawteeth, and saturated sawteeth are observed with central ECH power deposition, while giant sawteeth and ‘humpback oscillations’ occur when heating close to the sawtooth inversion surface of the local soft x-ray emissivity. New measurements with high temporal resolution show that the crash phase of these sawtooth types is accompanied by a reconnection process associated with an $m/n = 1$ resistive internal kink mode. After the sawtooth crash, full magnetic reconnection is observed in normal and in saturated sawteeth, while for giant and humpback sawteeth the reconnection process is incomplete and poloidally asymmetric temperature profiles persist after the crash. The detailed dynamics of the magnetic island, associated with the resistive internal kink mode, are described by a displacement function which is inferred from the experimental data. In normal sawteeth, the kink mode is destabilised just before the crash, while in all other sawtooth types a magnetic island exists for a significant fraction of the sawtooth period. The different types of sawteeth have been simulated using a numerical code based on a theoretical model which describes the evolution of the electron temperature in the presence of localised heat sources and of a magnetic $m/n = 1/1$ island.

6.1 Introduction

Sawtooth oscillations in tokamak discharges are periodic relaxations of the central electron temperature and density which develop when the safety factor on axis, q_0 , drops below unity (see chapter 1). A slow rise (sawtooth ramp) of these plasma parameters in the central region of the discharge, determined by heat deposition and transport, is followed by a rapid drop (sawtooth crash) resulting in an expulsion of energy and particles from the plasma core. Although these internal instabilities have long been observed and studied in all tokamaks, the understanding of the underlying physical mechanism is incomplete. Furthermore, recent experiments have revealed new peculiar plasma features when localised ECH is applied in sawtooth tokamak discharges. Examples are the observation on the RTP tokamak [1] of sharp temperature gradients just outside the sawtooth inversion radius and the multi-peaked temperature profiles observed in the TEXT-U [2] and RTP [1] experiments. On TCV [3], the sawtooth activity is strongly dependent on ECH deposition conditions. In Ref. [4], a classification of the different types of observed sawteeth was proposed, from usual triangular sawteeth, obtained with on-axis power deposition, to non-standard

behaviour when the location of the resonance position is moved off-axis. In particular, when the ECH power is deposited close to the $q = 1$ surface, the line integrated soft x-ray traces can exhibit ‘humpback’-like features. These internal relaxation oscillations, which were first observed with central electron cyclotron counter current drive [5] in the T-10 tokamak, can also occur under similar conditions on TCV [6], although current drive is not essential.

In previous TCV studies of this subject [4], [7], [8], understanding the sawtooth dynamics was hampered by the limited temporal resolution of the available diagnostics which could not resolve the sawtooth crash phase. In the frame of this thesis, this limitation has been overcome. The TCV soft x-ray tomographic system has been equipped by a new acquisition system which allows the monitoring of the sawtooth crash ≈ 10 times faster than the crash time, which is typically $\approx 100 \mu\text{s}$. In this chapter, we report on high temporal resolution measurements of the sawtooth oscillations during ECH. In section 6.2, the experimental set-up and the tools for the analysis are described. In section 6.3, the experimental results are presented and an interpretation of the observed phenomena is provided. Many of the experimental results can be interpreted using a recently developed theoretical model [9] which is detailed in section 6.4. In section 6.5, the experimental features during the different types of sawteeth are reproduced by a numerical code which is based on this theoretical model. It is shown that specific features in the electron temperature profiles during sawtooth activity may be accounted for by ECH and the advection and mixing of electron thermal energy associated with an $m/n = 1/1$ resistive internal kink mode [10]. Possible explanations of the remaining inconsistencies are proposed, showing that a single model can explain the variety of different sawteeth observed. Finally in section 6.6, conclusions are drawn.

6.2 Experimental set-up

For these experiments, TCV was operated with three 82.7 GHz, 500 kW gyrotrons, with a 2 s pulse length, for heating at the second cyclotron harmonic resonance using the X-2 mode. The vertical microwave beam width near the plasma centre is $w = 2.5$ cm in free-space (beam intensity $\propto \exp[-2(l/w)^2]$ where l is the distance transverse to the direction of the beam propagation). Local ECH flux surface averaged power densities in excess of 10 MW/m^3 can be obtained.

The local soft x-ray emissivity distribution is reconstructed from the line integrated measurements by means of the minimum Fisher information regularisation method [11] on a grid of square pixels of side 3 cm (see chapter 3). The time sequences of the reconstructed emissivities, $S_X(r, t)$, are analysed using the SVD method [12] to obtain the spatial structures, u_k , (*topos*) and their corresponding temporal evolution, v_k , (*chronos*) such that $S_X(r, t) = \sum u_k(r)v_k(t)s_k$, where s_k

6.3 Experimental observations and heuristic understanding

are the singular values (see chapter 4). Structures with poloidal mode numbers up to $m = 3$ are resolved by the SVD and coherent rotating structures such as MHD modes can be identified. It has been shown [4], [13], [14] that there is a strong correlation between the sawtooth shape and the heating location relative to the sawtooth inversion surface, in the sense that small changes in the location of the ECH deposition with respect to the inversion surface lead to large changes in sawtooth period, amplitude and MHD activity. In this study, the sawtooth inversion surface is determined from the SVD analysis of tomographically inverted soft x-ray data as described in section 4.2.2.

The radial displacement, $\xi(t)$, of the position of the maximum emissivity, associated with the kink instability during the sawtooth crash, is also extracted from the reconstructed soft x-ray emissivities. The time evolution of $\xi(t)$ is assumed to represent the displacement of the magnetic axis, which is not predicted theoretically by the model to be described in section 6.4. In what follows, we define the effective displacement

$$\xi(t) = \sqrt{\kappa_0 \left[(R - R_0)^2 + \frac{(Z - Z_0)^2}{\kappa_0^2} \right]} \quad (6.1)$$

where (R, Z) is the position of maximum emissivity within the hot core, (R_0, Z_0) refers to the same point before the instability develops and κ_0 is the elongation at the plasma centre. From this definition, $\xi(t)$ is constant on flux surfaces and therefore can be directly compared with the effective inversion radius r_{inv} . The elongation of the magnetic flux surfaces varies little inside the $q = 1$ surface, which justifies the use of the central elongation in Eq. (6.1).

The position of the ECH absorption region and the total absorbed power are determined by the ray-tracing code TORAY [15].

At the time of the experiments presented in this chapter, the foil-absorption system for the electron temperature measurement (see chapter 3) was not operational. The evolution of T_e on timescales faster than the repetition rate of the Thomson scattering system (≥ 0.4 ms) is derived by combining soft x-ray and electron density measurements in the manner explained later.

6.3 Experimental observations and heuristic understanding

In this section, we report on high temporal resolution measurements of the various types of relaxation oscillations under localised and intense ECH. The injected power, P_{ECH} , exceeds the power in the ohmic target by up to a factor of 4 and the microwave beam is launched perpendicular

to the toroidal magnetic field. In this geometry, a small amount of current (typically less than 2% of the inductive plasma current) is driven by the microwave beam due to the magnetic field lines pitch when the ECH power is deposited off-axis. Although it has recently been shown that the sawtooth period is strongly sensitive to small amounts of current driven close to the $q = 1$ surface [16], this turns out not to be the case for the sawtooth shape which is not seen to vary dramatically as a consequence of small variations of the driven current.

Standard and saturated sawteeth, related to central heating, together with large, almost triangular sawteeth and humpback oscillations, which occur with ECH power deposited close to the sawtooth inversion surface, are analysed.

6.3.1 Standard sawteeth

An example of a standard, triangular sawtooth obtained with on-axis ECH power deposition is shown in Fig. 6.1. In what follows, the plasma parameters are referred to the last closed flux surface (LCFS) which in the present case are: $\delta_a = 0.42$, $\kappa_a = 1.41$, $I_P = 400$ kA, $P_{ECH} = 900$ kW. The sawtooth period, τ_{ST} , is ≈ 3.4 ms, the electron energy confinement time, τ_E , is 3.3 ms and the resistive diffusion time, τ_η , can be estimated to be ≈ 450 ms. The relative crash amplitude of the central soft x-ray emissivity, S_{X0} , is $\Delta S_{X0} / \langle S_{X0} \rangle \approx 0.65$, where the brackets indicate the average of a quantity evaluated before and after the sawtooth crash. The temporal evolution of the local emissivities is shown in Fig. 6.1(a,b,c) for three different radial positions together with radial displacement $\xi(t)$ of the hot core (region of high emissivity) in Fig. 6.1(d). In Fig. 6.2, the soft x-ray emissivity distribution is shown at different times during the sawtooth collapse together with the LCFS, the sawtooth inversion radius, as calculated from soft x-ray tomography, and the hot core trajectory.

During the sawtooth ramp, the soft x-ray emissivity is poloidally symmetric, Fig. 6.2(a), with no detectable MHD mode activity. At the sawtooth crash, an $m/n = 1/1$ instability grows and causes the hot core to move outward in minor radius as a nearly rigid structure in ≈ 120 μ s. The hot core does not spiral in the poloidal plane as one would expect for a toroidally rotating plasma. The rapidity of the hot core displacement during the sawtooth crash (≈ 120 μ s) compared to the frequencies of the modes usually observed on TCV, which are between 3 and 6 kHz, suggests a minimum poloidal rotation of $\approx 120^\circ$, which is not observed in Fig. 6.2. At present, this discrepancy is not understood.

6.3 Experimental observations and heuristic understanding

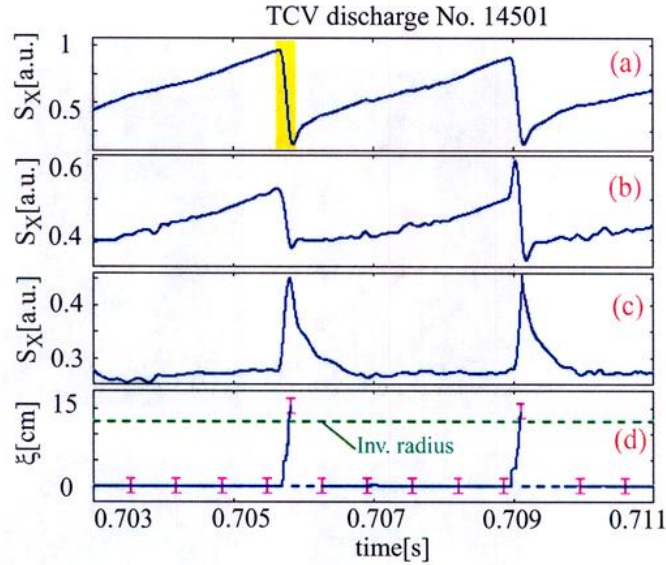


Fig. 6.1 Evolution of the soft x-ray emissivity at different radial positions, r , during triangular sawteeth in TCV discharge No. 14501. (a) On-axis, $r = 0$. (b) Just inside the inversion radius, $r = 0.82 \cdot r_{inv}$. (c) Just outside the inversion radius, $r = 1.21 \cdot r_{inv}$. (d) The hot core radial displacement $\xi(t)$ (blue line) together with the sawtooth inversion radius (green, dashed line). The position of the hot core is not shown immediately after the sawtooth collapse since it is not well defined.

The final radial shift of the hot core from the initial position is $\xi_{max} \approx 15$ cm. During the displacement, the hot core intensity diminishes, Fig. 6.2(b), and the expelled heat redistributes on a hot ring localised, within the error bars, at the sawtooth inversion radius $r_{inv} \approx 12$ cm, Fig. 6.2(c). The soft x-ray emissivity profile is poloidally symmetric at the end of the sawtooth crash, Fig. 6.2(d). The heat redistribution on the annular ring, probably due to heat transport along magnetic field lines, appears to be much faster than the hot core radial displacement and cannot be resolved with the $13 \mu\text{s}$ time resolution of the tomographic system. Small regions of locally lower or higher emissivity at the inversion surface, visible in Fig. 6.2(d) can be explained by artefacts of the tomographic reconstruction technique.

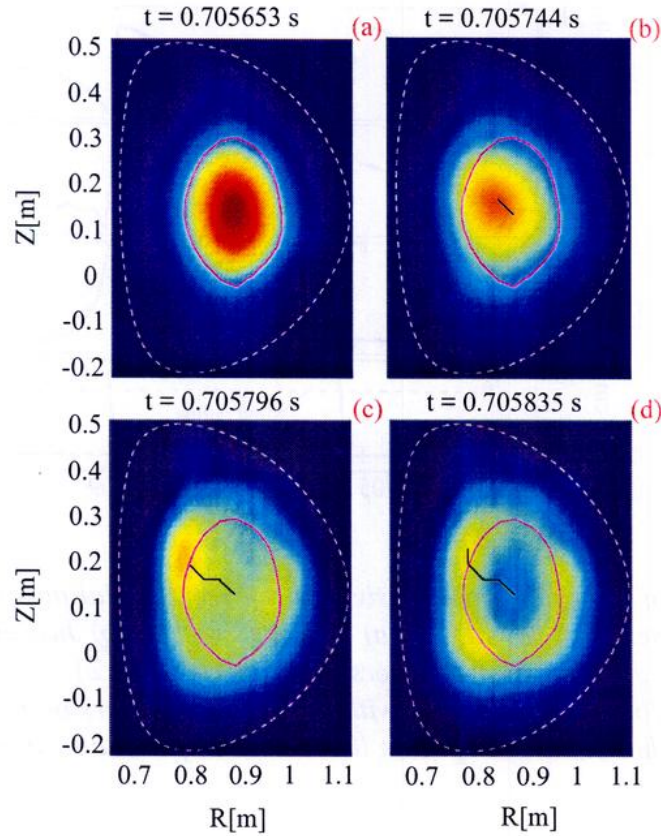


Fig. 6.2 Series of tomographic reconstructions of the soft x-ray emissivity, during the phase of the sawtooth crash highlighted in yellow in Fig. 6.1. The hot core displacement (b,c) and the formation of the hot ring (d) are shown. The units are normalised and the color scale is such that red and blue correspond respectively to high and low emissivities. The LCFS is shown as a white, dashed line and the sawtooth inversion surface as a magenta line. The superimposed black line indicates the hot core trajectory from its position before the instability develops to the position corresponding to the time at each frame.

The effect of the sawtooth oscillation on the soft x-ray emissivity profiles is shown in more detail in Fig. 6.3. The peaked pre-crash profile evolves into a hollow post-crash profile, with $S_X(r_{inv})/S_{X0} \approx 1.35$. The timescale of the evolution of the post-crash profile depends both on heating conditions and plasma parameters. In the present case, the hot ring is visible for $\approx 150 \mu\text{s}$ then the profile gradually becomes more peaked as the plasma is heated until the next sawtooth collapse. In order to quantify the uncertainties due to random errors, a set of 100 tomographic reconstructions were calculated from the line integrated data adding, to all channels, a normally distributed random

6.3 Experimental observations and heuristic understanding

noise with a mean value of zero and a standard deviation of 3% of the signal amplitude, which is worse than the experimental measurements imply [11]. The error bars shown in Fig. 6.3 are the standard deviations of the local emissivities evaluated for this set of reconstructions. Systematic errors due to uncertainties in the position of the lines of sight of the tomographic system and in the efficiency of the silicon photodiodes are taken into account by the procedure described in [11], [17]. Sufficiently large statistical errors were chosen and weighted with the inverse of the etendue for each line of sight, since a small etendue implies a large angle of incidence and thus a larger uncertainty on the value of the etendue and misestimated photodiode efficiency. Another systematic error comes from the tomographic inversion method itself. Simulated line integrated data from hollow soft x-ray emissivity profiles were tomographically inverted using the minimum Fisher regularisation method. The reconstructed profiles are seen to underestimate the initial $[S_X(r_{inv}) - S_{X0}]/S_{X0}$ ratio by about a factor of two. We can thus conclude that a hot ring does indeed exist for which our inversion technique only provides a lower limit for the hollowness.

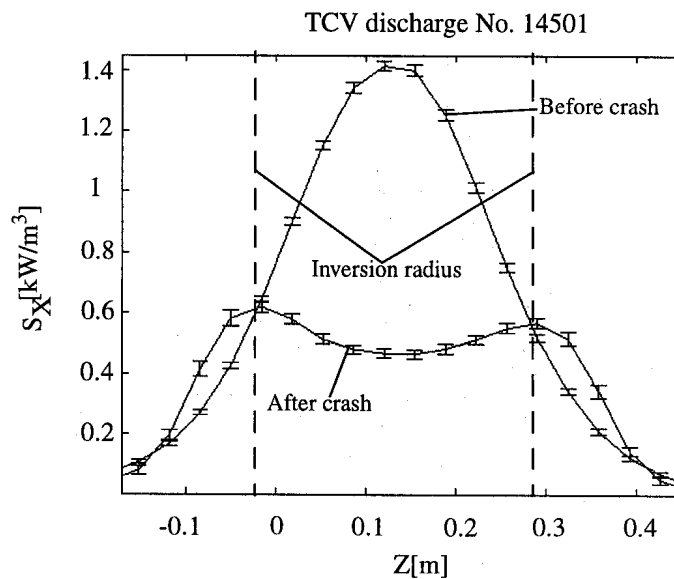


Fig. 6.3 Soft x-ray emissivity profiles along a central, vertical cut showing the result of the crash for a triangular sawtooth with on-axis ECH power deposition. The position of the sawtooth inversion radius is shown as dashed lines.

Interpretation of the variation in the soft x-ray emissivity in terms of changes in the electron temperature is not straightforward. Although the Thomson scattering system provides direct measurements of T_e and n_e profiles, no measurement of the electron temperature profiles during

the short life time of the hot ring have been obtained so far. This is due to the limited repetition rate and the difficulty of synchronising the Thomson scattering laser pulses with the sawtooth crash. A rough estimate of the hollowness in the electron temperature profile can be obtained from soft x-ray measurements, assuming $\Delta T_e/T_e = \gamma \Delta S_X/S_X$, where $\gamma = d(\ln S_X)/d(\ln T_e)$ is the factor describing the temperature dependence of the soft x-ray emissivity of the dominant impurity, which is carbon in TCV [18]. For the case shown in Fig. 6.3, the estimate gives $T_e(r_{inv})/T_{e0} \approx 1.2$, assuming flat electron density, n_e , and Z_{eff} profiles. Interferometric measurements of the electron density have been inverted using the modified Abel inversion method described in chapter 3. The temporal evolution of the tomographically inverted electron density shows that particles are expelled from the plasma centre ($\Delta n_{e0}/\langle n_{e0} \rangle \approx 0.09$), during the sawtooth crash, resulting in a flattening of the n_e profile with $n_e(r_{inv})/n_{e0}$ below the error bars (5%) of the inversion technique. Since there is no independent measurement of the Z_{eff} profile during the lifetime of the hot ring, we cannot exclude the possibility that a local enhancement of Z_{eff} at the hot ring position may contribute to the soft x-ray intensity. Such an enhancement could result from a highly peaked Z_{eff} profile in the plasma core before the sawtooth crash. The Z_{eff} profile can be obtained from simultaneous soft x-ray, T_e and n_e measurements in the manner proposed in Ref. [19] which has been outlined in chapter 4. This has been done for the present case and pre-crash Z_{eff} profiles, which are flat inside the inversion radius were obtained. This result does not support the existence of impurity accumulation and hence makes it implausible that the hot ring emissivity is due to an enhanced impurity density inside the ring.

In section 6.5, it will be shown that the formation of the hot ring can be explained as a consequence of the advection and mixing of the electron thermal energy during the growth of the $m/n = 1/1$ magnetic island. However, the hot ring only forms when the pre-crash temperature profile is sufficiently peaked, as in the case for on-axis ECH deposition. With ohmic heating only, this condition is normally not fulfilled and the hot ring is not observed.

The absence of post-cursor oscillations on both Mirnov coils and soft x-ray traces suggests a full reconnection process, in the sense that poloidal magnetic symmetry is restored at the end of the sawtooth crash. This requires that the original magnetic axis moves up to the mixing radius, r_{mix} , at the end of the reconnection process, i.e. $\xi_{max} \approx r_{mix}$ (see section 6.4 for the mathematical definition of r_{mix}). This radius is slightly larger than the sawtooth inversion radius, by an amount which depends on the safety factor and electron temperature profiles before the crash (see appendix in Ref [4]). The maximum value of the hot core displacement, $\xi_{max} \approx 15$ cm, compared with $r_{inv} \approx 12$ cm, is consistent with this interpretation.

6.3 Experimental observations and heuristic understanding

6.3.2 Saturated sawteeth

Tomographic reconstructions of a saturated sawtooth are shown for the TCV discharge No. 14385 with central ECH. Plasma parameters are: $\delta_a = 0.37$, $\kappa_a = 1.46$, $I_p = 266$ kA, $P_{ECH} = 850$ kW, $\tau_E = 3.6$ ms, $\tau_\eta \approx 250$ ms. The ECH resonance position is located on the magnetic axis with a radial power deposition width, $\delta_{abs} \approx 6$ cm. This discharge has a lower current than the previous case with a consequently smaller inversion radius of $r_{inv} \approx 9$ cm. In Fig. 6.4, the temporal evolution of the tomographically inverted soft x-ray emissivity at different radial positions is shown together with the hot core radial displacement, $\xi(t)$.

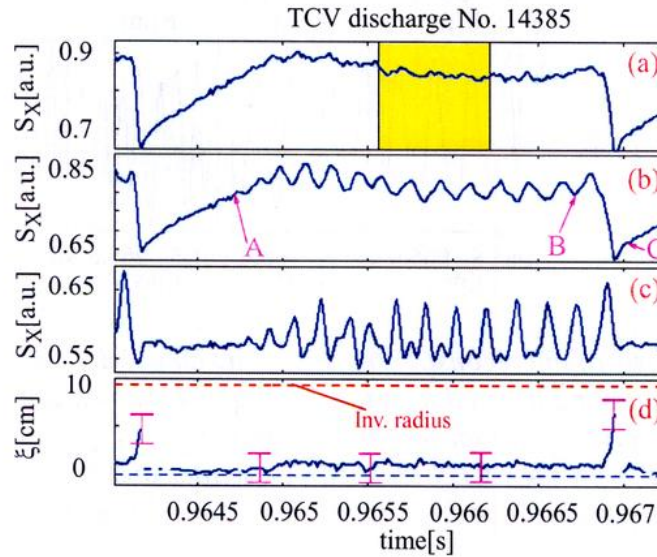


Fig. 6.4 Time evolution of the soft x-ray emissivity at different radial positions, r , during a saturated sawtooth in TCV discharge No. 14385. (a) Close to the magnetic axis, $r = 0.02 \cdot r_{inv}$. (b) Slightly off-axis, $r = 0.28 \cdot r_{inv}$. (c) Just inside the inversion radius, $r = 0.9 \cdot r_{inv}$, where the frequency doubling is clearly visible. (d) The hot core radial displacement $\xi(t)$ (blue line) together with the sawtooth inversion radius (red, dashed line) are shown. The position of the hot core is not shown immediately after the sawtooth collapse since it is not well defined.

The sawtooth crash is followed by a reheating phase, in which the soft x-ray emissivity profiles peak, conserving the poloidal symmetry. This phase is followed for $t > 0.965$ s by a saturated phase during which the central soft x-ray emissivity remains almost constant or even decreases until the following sawtooth crash. The saturated phase is accompanied by strong mode activity, resulting in off-axis oscillations, Fig. 6.4(b). The frequency of the oscillations (≈ 6 kHz in the

present case) can vary between 3 and 7 kHz, depending on ECH and plasma conditions. Close to the inversion radius, Fig. 6.4(d), a frequency doubling is sometimes observed. During the saturated phase, the plasma hot core appears to rotate around the position it had before mode onset at a distance $\xi \approx 1$ cm.

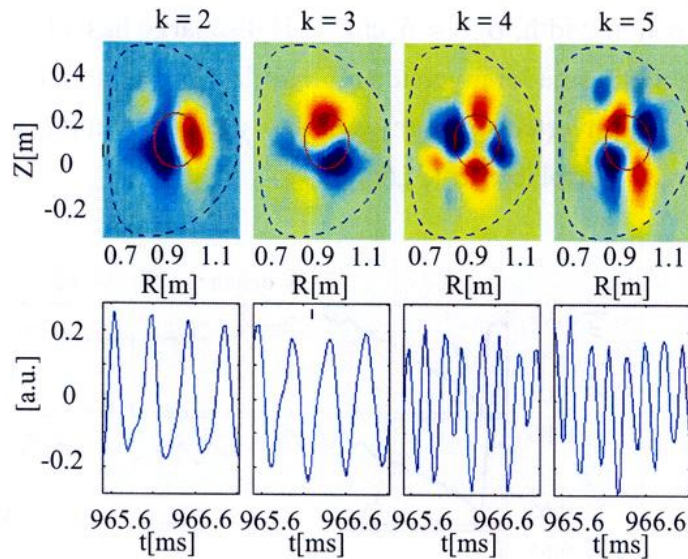


Fig. 6.5 SVD analysis of the reconstructed soft x-ray emissivity distribution during the saturated phase of the sawtooth, highlighted in yellow in Fig. 6.4. Shown are the topo/chrono pairs corresponding to the second to fifth largest eigenvalues, $S_k = 2, 3, 4, 5$. The top row shows the spatial eigenmodes (topos) with the LCFS (dashed black line) and the sawtooth inversion radius (red line). The corresponding temporal eigenvectors (chronos) are shown in the bottom row.

In Fig. 6.5, the mode structure of the soft x-ray emissivity, from SVD analysis, is shown in a small time window during the saturated phase, highlighted in yellow in Fig. 6.4(a). The first topo/chrono pair, corresponding to the largest singular value, is not shown because it describes the temporal evolution of the average emissivity profile and thus is not relevant to the mode identification. Inspection of Fig. 6.5 reveals the presence of two rotating modes, each consisting of two oscillating topo/chrono pairs in quadrature (i. e. both topo and chrono are phase shifted by $\pi/2$) and having poloidal mode numbers $m = 1$ (topo/chrono pairs $k = 2, 3$) and $m = 2$ (topo/chrono pairs $k = 4, 5$). Both modes rotate in the electron diamagnetic drift direction at a frequency of ≈ 6 kHz and their maxima and minima are located at the sawtooth inversion radius, within experimental uncertainties. The toroidal mode number, n , as obtained from the toroidal photodiodes, is such that $m = n$ for both modes. Although the modes appear to rotate in the poloidal direction, we

6.3 Experimental observations and heuristic understanding

believe that this rotation is primarily due to a nearly rigid toroidal rotation of the plasma and modes. The saturation phase terminates with the sawtooth crash when the rapid growth of the $m/n = 1/1$ mode causes the hot core to move outward in minor radius within $80 \mu\text{s}$, Fig. 6.4(d). Fig. 6.6 shows different soft x-ray emissivity profiles, at times corresponding to the arrows indicated in Fig. 6.4, together with the location of the sawtooth inversion radius. The poloidal symmetry is restored and the soft x-ray emissivity profile is seen to flatten up to $r = r_{inv}$ at the end of the sawtooth crash. The relative crash amplitude is less pronounced for a saturated than for a standard sawtooth. In the present case $\Delta S_{X0} / \langle S_{X0} \rangle \approx 0.28$.

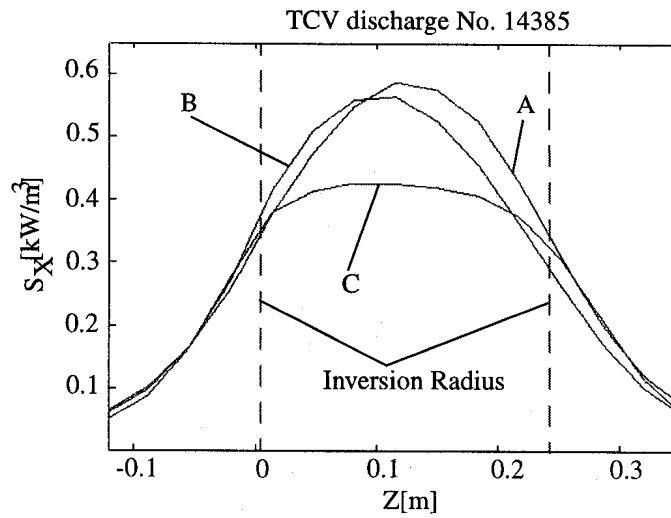


Fig. 6.6 Soft x-ray emissivity profiles along a central, vertical cut corresponding to the different times indicated by the arrows in Fig. 6.4. A: the S_X profile is poloidally symmetric at the end of the sawtooth ramp before the instability develops. B: during the sawtooth saturated phase the profile is not poloidally symmetric and the hot core is displaced by ≈ 1 cm from its position before the onset of the oscillations. C: immediately after the sawtooth crash, $t - t_{crash} \approx 0.005 \cdot \tau_{saw}$, the poloidal symmetry is restored. Dashed lines indicate the position of the sawtooth inversion radius.

The lack of post-cursor oscillations on both soft x-ray traces and Mirnov coil signals again suggests a full reconnection process. The absolute value of the displacement, $\xi_{max} \approx 7$ cm, compared with the inversion radius, $r_{inv} \approx 9.3$ cm, may be too small to explain a complete mixing of the plasma core inside r_{mix} . However, it should be noted that in the very last phase of the reconnection process the maximum of the emissivity profile may no longer be at the position of the displaced magnetic axis in the hot core, making the determination of the displacement function, ξ , difficult.

6.3.3 Heating close to the sawtooth inversion surface

In earlier ECH experiments on TCV [4], it was observed that small changes in the relative position between the ECH location and the sawtooth inversion surface can lead to large changes in the sawtooth shape, period and MHD activity. More recent experiments with three independent gyrotrons heating close to the sawtooth inversion surface suggested that even the beam width may play a role in determining the sawtooth shape [16]. In particular, two types of sawteeth are observed when the power is deposited close to the sawtooth inversion surface: large, almost triangular sawteeth, which we shall refer to as giant sawteeth, and non-standard sawteeth which were termed humpback oscillations when they were observed in the T-10 tokamak [5]. A detailed study of the plasma parameters and heating conditions under which giant sawteeth occur, rather than humpbacks, has already been presented [4], [8], [16]. In what follows, an experimental account of the two types of sawteeth is given and an interpretation of the observed behaviour is proposed. Despite the strong difference in the soft x-ray signals in the two types of sawteeth, we show that the gross features of the temporal evolution of the electron temperature and the MHD activity are similar and that they may result from the combined action of local ECH and a saturated magnetic island.

The sawtooth behaviour for giant sawteeth and the humpback oscillations is presented in Fig. 6.7 and Fig. 6.8 respectively. In both figures, the temporal evolution of the central soft x-ray emissivity, S_{X0} , is shown in frame (a), together with the central electron density, n_{e0} , from interferometer measurements inverted using the modified Abel method described in section 3.3, frame (b). The quantity $\tilde{T}_{e0} = S_{X0}/n_{e0}^2$, in frame (c), is indicative of the evolution of the central electron temperature (the exponent γ , introduced above is close to unity in the present cases).

We examine the giant sawtooth case for which the plasma parameters are: $\delta_a = 0.5$, $\kappa_a = 1.47$, $I_p = 330$ kA, $q_a = 3.25$, $P_{ECRH} \approx 500$ kW, $\tau_E = 3.1$ ms, $\tau_\eta \approx 300$ ms. The ECH absorption layer is located in the plasma midplane on the high field side of the magnetic axis inside the interval $r/a = [0.55, 0.65]$. The sawtooth inversion surface is located at the normalised radius $r_{inv}/a = 0.6$. In Fig. 6.9, the electron temperature and density profiles are shown for the different times indicated by letters A-C in Fig. 6.7. In this case, the Thomson scattering lasers were operated in the ‘burst-mode’ to obtain 3 profiles in a few milliseconds.

6.3 Experimental observations and heuristic understanding

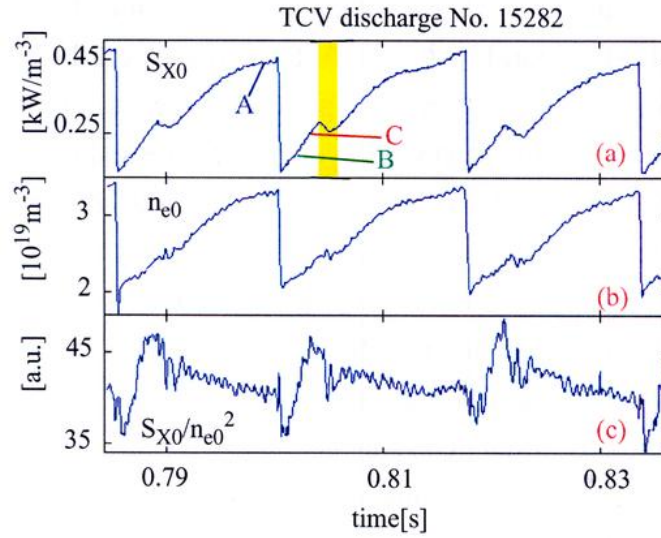


Fig. 6.7 Giant sawteeth during TCV discharge No. 15282 with ECH power deposited close to the sawtooth inversion surface: (a) the central inverted soft x-ray emissivity, S_{X0} ; (b) the central electron density, n_{e0} ; (c) a signal proportional to the variation of the electron temperature, S_{X0}/n_{e0}^2 .

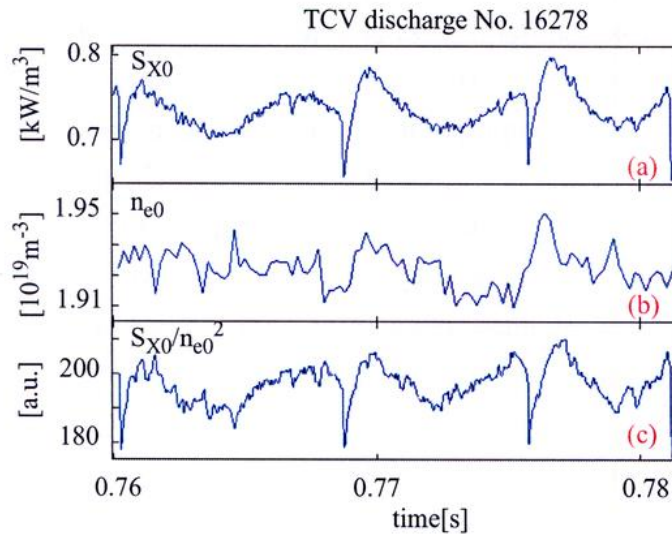


Fig. 6.8 Humpback relaxation oscillations obtained with ECH power deposited close to the sawtooth inversion surface in TCV discharge No. 16278: (a) central inverted soft x-ray emissivity, S_{X0} ; (b) central electron density, n_{e0} ; (c) a signal proportional to the variation of the electron temperature, S_{X0}/n_{e0}^2 .

The sawtooth period, $\tau_{ST} \approx 15$ ms, is significantly longer than the standard sawtooth period. During a single sawtooth period, three distinct phases can be identified during which \tilde{T}_{e0} shows different temporal behaviour, Fig. 6.7(c). At the sawtooth crash, \tilde{T}_{e0} is observed to drop on a fast time scale, typically $\tau_{crash} < 0.1$ ms. The pre-crash electron temperature profile (Fig. 6.9, profile A) is relatively flat inside the sawtooth inversion surface and the sawtooth crash results only in a small variation of the central electron temperature. Both the central soft x-ray emissivity and electron density also drop during the crash phase. For instance, in Fig. 6.7, $\Delta S_{X0} / \langle S_{X0} \rangle \approx 0.66$ and $\Delta n_{e0} / \langle n_{e0} \rangle \approx 0.48$. The tomographic reconstructions of the soft x-ray emissivity (not shown here) and the electron temperature profile (see Fig. 6.9, B) show that the poloidal symmetry is not restored after the sawtooth crash, suggesting an incomplete reconnection process.

The sawtooth crash is followed by a ramp phase during which the central electron temperature and density increase. The time scale of this phase, typically $\tau_{ramp} \approx 2$ ms, is slower than τ_{crash} and is the same as that of triangular sawteeth with central ECH deposition and comparable ECH power, safety factor and plasma energy content. The electron temperature profile C, Fig. 6.9, shows that the poloidal symmetry is not restored during the ramp phase which terminates with the onset of strong oscillations in the soft x-ray traces as seen in the time interval corresponding to the shaded box in Fig. 6.7(a). Typical oscillations in the soft x-ray signals due to the presence of a saturated magnetic island are not easy to distinguish early in the sawtooth ramp since the time scale of the rise is close to the rotation frequency of the mode which produces the oscillations (see below).

In Fig. 6.10, the mode structure of the soft x-ray emissivity during the oscillations is shown: a mode (Fig. 6.10, $k = 2, 3$) having poloidal mode number $m = 1$ and rotating in the electron diamagnetic drift direction at a frequency of ≈ 1.5 kHz is clearly present. The toroidal mode number is $n = 1$. The sawtooth ramp is followed by a diffusive phase during which the central electron temperature undergoes small changes on an even slower time scale ($\tau_{slow} \approx 10$ ms). During this phase, a strong influx of particles into the plasma core is seen, leading to a very peaked electron density profile. The profiles are poloidally symmetric and the electron temperature profile is flat inside the sawtooth inversion radius at the end of the sawtooth ramp. This phase lasts until the onset of precursor oscillations ≈ 500 μ s before the subsequent sawtooth crash.

Fig. 6.8 shows the humpback oscillation which can occur when heating close to the sawtooth inversion surface. The plasma parameters are: $\delta_a = 0.2$, $\kappa_a = 1.37$, $I_P = 200$ kA, $q_a = 4.8$, $P_{ECH} = 900$ kW, $\tau_E = 3.6$ ms, $\tau_\eta \approx 200$ ms. The ECH resonance position is located below the magnetic axis resulting in a comparatively broader absorption layer located inside the interval $r/a = [0.2, 0.4]$. The sawtooth inversion surface is located at the normalised radius $r_{inv}/a = 0.32$.

6.3 Experimental observations and heuristic understanding

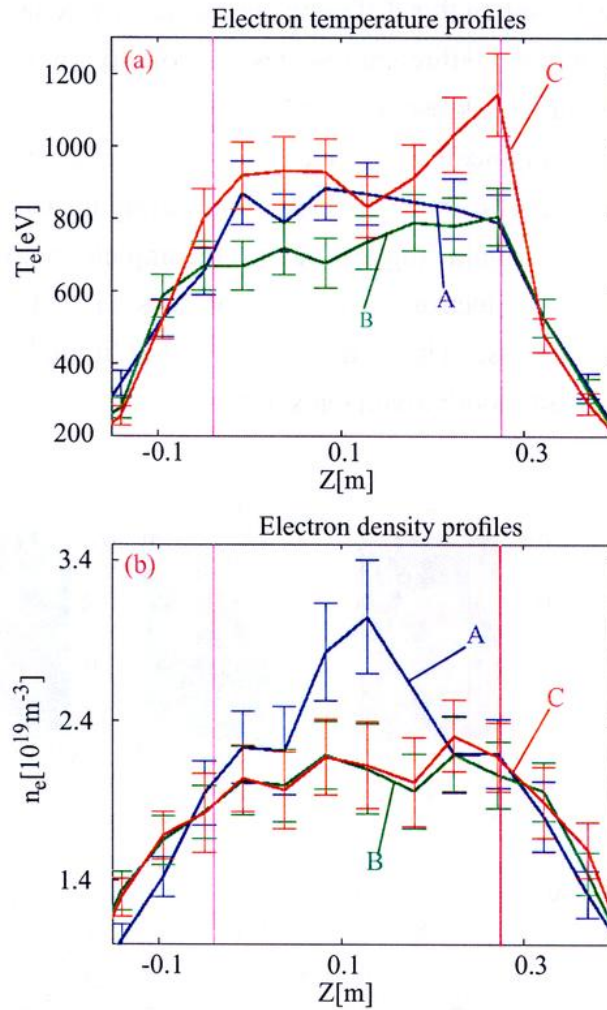


Fig. 6.9 Thomson scattering profiles for TCV discharge No. 15282, shown in Fig. 6.7(a). The electron temperature (a) and the electron density (b) profiles relative to the times, t , indicated by colors in Fig. 6.7: $t_A = 0.8004$ s, just before the sawtooth crash; $t_B = 0.8014$ s, early during the sawtooth ramp; $t_C = 0.8024$ s, before the onset of the oscillations. The position of the sawtooth inversion radius, from reconstructed soft x-ray emissivity, is shown in magenta.

For the humpback case, like for the giant sawteeth, $\tau_{ST} \approx 8$ ms is significantly longer than the ohmic sawtooth period. At first sight, the evolution of the central soft x-ray emissivity in the humpback case suggests that the electron temperature behaviour is radically different from that of the giant sawteeth. However, as can be seen from Fig. 6.8(c), the temporal evolution of the central soft x-ray emissivity is mainly dependent on \tilde{T}_{e0} , since n_{e0} has only small variations (1-2%)

during a sawtooth period in the humpback case, as compared with the large variations of the density during the giant sawteeth. When this difference in the density behaviour is accounted for, the \tilde{T}_{e0} evolution is very similar and the three timescales of evolution of \tilde{T}_{e0} , found in the giant sawtooth case, also apply to the humpback oscillations.

SVD analysis of tomographically inverted soft x-ray measurements together with toroidal photodiodes reveal that an $m/n = 1/1$ mode exists during the early sawtooth ramp immediately after the sawtooth crash, again suggesting an incomplete reconnection process. Poloidally asymmetric structures in the electron temperature profiles due to the presence of the mode are not easy to be observed in this case. This is mainly due to the limited number of Thomson scattering measurements inside the sawtooth inversion surface.

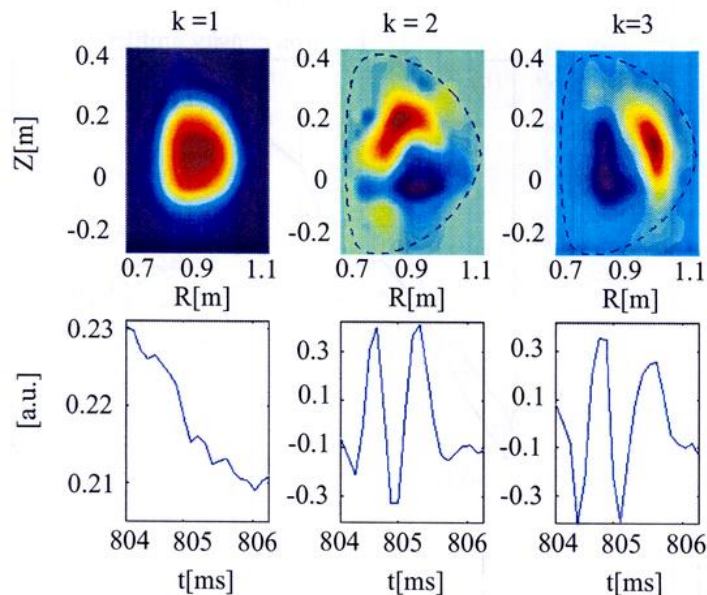


Fig. 6.10 SVD analysis of the reconstructed soft x-ray emissivity distribution during the phase of the giant sawtooth highlighted in yellow in Fig. 6.7(a). The top row shows the spatial eigenmodes (topos) with the LCFS (blue dashed line). The corresponding temporal eigenvectors (chronos) are shown in the bottom row.

The difference in the electron density behaviour between giant sawteeth and humpback oscillations is not completely understood, nevertheless we suppose that it can be ascribed to the pumpout effect which is studied in detail in chapter 7. In plasmas with modest triangularities [20], pumpout is observed in the presence of $m/n = 1/1$ mode activity when sufficiently high electron temperature gradients develop inside the $q = 1$ surface. In the giant sawtooth case, this last

6.3 Experimental observations and heuristic understanding

condition is not fulfilled because of the narrow off-axis ECH absorption region and thus no pump-out effect is observed resulting in a peaking of the electron density during the sawtooth ramp as in the case of triangular sawteeth with central heating. In the case of the humpback oscillations, because of the broad ECH absorption region a considerable amount of the power is deposited inside the sawtooth inversion region. This may result in an increased peaking of the electron temperature profile causing particle pumpout by thermodiffusion and thus preventing the electron density from peaking after the sawtooth crash. Although this explanation of the difference in the electron density behaviour is qualitatively consistent with our interpretation of pumpout, given in chapter 7, an accurate modelling would require quantitative measurements of the electron temperature gradients inside the $q = 1$ surface. In the future, this will be possible on TCV using the recently installed electron cyclotron emission diagnostic providing measurements of the local temperature.

Our interpretation for the electron temperature behaviour, in both sawtooth types described above, is based on the following heuristic picture. When the ECH power is deposited near the sawtooth inversion surface, the electron temperature profile tends to acquire distinctive features. In particular, T_e becomes relatively flat (see Fig. 6.9, T_e profile A) in the central region up to the $r = r_{inv}$ and relatively steep outside this radius, as the result of localised heating and diffusive transport during a period of relative MHD quiescence. The formation of these features in the electron temperature profile requires improved stability against $m/n = 1/1$ modes leading to a relatively long quiescent period.

Different stabilisation mechanisms can be envisaged through changes of the plasma pressure and/or current density profile. Recent simulations [21] using the PRETOR transport code [22] which contains a sawtooth trigger model based on a critical shear value at the $q = 1$ surface, s_{1crit} , [23] suggest that the improvement in the $m/n = 1/1$ mode stability, reported here, may result from a modification of the electron pressure gradient at the $q = 1$ surface (resulting in an increased s_{1crit}) and a slower growth of the magnetic shear at the $q = 1$ after the sawtooth crash. The stabilisation of the internal kink mode due to resonant interaction with suprathermal electrons [24] is not believed to be effective in the present case, since in TCV a suprathermal population of electrons is observed only with a significant toroidal injection angle [25]. This period of quiescence is terminated by the appearance of an $m/n = 1/1$ magnetic island [10], [26] indicated by brief precursor oscillations in the soft x-ray traces. In this first phase, as long as magnetic reconnection takes place, the island moves radially outwards and the soft x-ray emissivity decreases. The magnetic topology during this phase, described in detail in section 6.4, is such that crescent-shaped surfaces inside the magnetic island separatrix directly connect the heated ring with the plasma centre. Therefore, the central plasma region is still heated even

though radially separated from the ECH deposition region due to the large thermal conduction along field lines. When the hot core starts to move outwards again and the reconnection process continues, the central temperature remains almost constant. The brief oscillations present in the experimental traces in this phase are in agreement with the existence of an $m/n = 1$ mode and the picture of a magnetic island which is now close to the mixing radius, with the reconnection process close to completion. Subsequently, the poloidal symmetry is re-established and no further oscillations are seen in the soft x-ray signals.

6.4 Theoretical model

Many of the experimental results in the previous section can be interpreted using a theoretical model, first presented in Ref. [9], which describes the evolution of the electron temperature in the presence of $m/n = 1$ magnetic island and localised heat sources. The derivation of this model is detailed in this section.

The part of the model that describes the evolution of $m/n = 1$ magnetic islands is fairly standard and the evolution of these islands is assumed to follow the characteristic spatial structure of a resistive internal kink mode [10] and the topological constraints of Kadomtsev's model [27]. Although this model is fairly old, its consequences in the presence of localised auxiliary heating have only recently been fully appreciated. In Ref. [9], it was proposed that the temperature 'filamentary' structures and sharp gradients observed in RTP [1] and in TEXT-U [2] may be consistent with the Kadomtsev's model. In this paper, we show that the model may also account for the variety of experimental observations in sawtoothing TCV discharges, although we do not strictly follow Kadomtsev model.

We do not use Kadomtsev's prediction for the timescale of the sawtooth crash. This prediction would be valid for a plasma obeying resistive MHD equations [27]. High temperature tokamak experiments, such as TCV, are ill-described by resistive MHD. For instance, TCV is better described by a semi-collisional kinetic model [4], where diamagnetic and ion Larmor effects are important for the island evolution. Toroidal effects, not treated by Kadomtsev, are also important. Unfortunately, a fully consistent non-linear theory for the island dynamics that accounts for all these effects is not yet available. Therefore, the model used contains a free parameter, which describes the evolution of the $m/n = 1$ magnetic island width, or alternatively, of the displacement function $\xi(t)$ which is measured experimentally, as shown in section 6.3.

The original Kadomtsev's model assumes full magnetic reconnection. Single-helicity, $m/n = 1$ island growth occurs until this island reaches its maximum amplitude, $w_{max} = 2r_{mix}$, where the

6.4 Theoretical model

mixing radius, r_{mix} , is defined below. We suspect that the single-helicity assumption is not valid in a strict sense in a three-dimensional toroidal system. Satellite harmonics of the internal kink magnetic perturbation localised within the $q = 1$ volume, such as the $m/n = 2/2$ harmonic driven by toroidal coupling, may cause some degree of magnetic stochasticity [28]. This, in turn, may cause the decoupling of the electron pressure and q profiles: the pressure may flatten in the stochastic region independently of the q profile. This would lead to incomplete reconnection and may explain why the safety factor on axis, q_0 , is observed to remain below unity after the sawtooth crash in certain tokamak experiments [29], [30]. According to this picture, the extent of the stochastic region determines the degree of departure from complete reconnection. For small departures, the model presented here may satisfactorily reproduce gross features of the experimental observations. Conversely, we are tempted to conclude that if the model results agree with the experimental data, then full reconnection is really obtained in the experiment. A direct measurement of the q profile would settle this issue, but unfortunately such a measurement is not available on TCV.

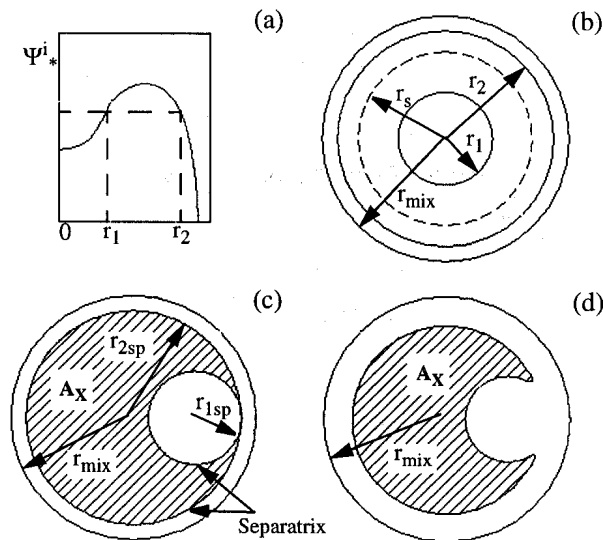


Fig. 6.11 Magnetic reconnection process according to the Kadomtsev model: (a) pre-crash normalised helical flux for a monotonic q profile; (b) helical flux surfaces before reconnection starts; (c) the flux surface originally at $r = r_1$ reconnects with the flux surface, corresponding to the same helical flux, originally at $r = r_2$; (d) at a later time, the separatrix of (c) has deformed into a crescent-shaped surface maintaining a constant area A_X .

6.4.1 Derivation of the model.

We assume, for simplicity, a cylindrical plasma column of length L with periodic boundary conditions. In absence of an $m/n = 1$ island, the magnetic flux surface cross sections are concentric circles of constant normalised helical flux [31],

$$\Psi_{*in}(r) = \int_0^{r^2} [q_{in}(x)^{-1} - 1] dx \quad (6.2)$$

where $x = r^2$ and the subscript “in” stands for initial, i.e. before the island formation. An elliptical deformation of the flux surfaces with constant elongation can be introduced trivially if desired. For a typical case (i.e. a monotonic q profile), $\Psi_{*in}(r)$ has a maximum at the $q = 1$ radius, $r = r_s$, as shown in Fig. 6.11(a).

Our problem is now to specify the helical flux function, $\Psi_{*in}(r, \alpha, t)$, during the growth of the $m/n = 1$ island, where $\alpha = \vartheta - 2\pi z/L$, ϑ being the poloidal angle. We note that this function is not explicitly determined in Kadomtsev’s paper [27], where only $\Psi_{*rel}(r)$ is derived as a function of $\Psi_{*in}(r)$, with the subscript “rel” referring to the relaxed helical flux at the full reconnection. Nevertheless, the two basic rules for the reconstruction of $\Psi_{*in}(r, \alpha, t)$ are to be found in that paper. These rules are:

- (i) conservation of the normalised helical flux, i.e.

$$\frac{\partial}{\partial t} \Psi_* + \mathbf{v} \cdot \nabla \Psi_* = 0$$

which describes the evolution of Ψ_* everywhere except in a narrow layer around the island X-point where magnetic reconnection occurs.

- (ii) toroidal flux conservation.

These rules do not define a unique solution for the functional $\Psi_{*in}(r, \alpha, t)$, although they represent a strong mathematical constraint. A prescribed model for the velocity field, \mathbf{v} , is assumed corresponding to a resistive internal kink motion. Accordingly, helical flux surfaces within the $q = 1$ surface are shifted rigidly. The motion is thus specified by a single function, $\xi(t)$, representing the radial displacement of the magnetic axis from its original position. The assumption of a given velocity field greatly simplifies the analysis, but is not fully self-consistent with the solution of the set of resistive MHD equations. An improved analytical model was the one proposed

6.4 Theoretical model

by Waelbroeck [32]. Alternatively, the resistive-MHD equations could be solved numerically, which is not the spirit of the present analysis.

According to the procedure outlined above, at each time t during the reconnection process, the island separatrix is formed by two circles of radii $r_{1sp} < r_s$ and $r_{2sp} > r_s$, where $\Psi_{*in}(r_{1sp}) = \Psi_{*in}(r_{2sp})$, with the centre of the inner circle (i.e. the original magnetic axis) displaced from its original position by a distance

$$\xi(t) = r_{2sp} - r_{1sp} \quad (6.3)$$

(see Fig. 6.12). With $B_z = const$, toroidal flux conservation is equivalent to area conservation. Thus, the area A_X enclosed by the magnetic separatrix equals that of the annular region between the initial position of the two reconnecting circles, i.e. $A_X = \pi(r_{2sp}^2 - r_{1sp}^2)$.

The magnetic island has a width

$$w_{isl}(t) = 2\xi(t). \quad (6.4)$$

At a later time, the island separatrix evolves into a crescent-shaped surface, maintaining a constant area A_X indicated by the dashed regions in Fig. 6.11(d). The contour of the crescent is also a surface of constant helical flux, specifically

$$\Psi_{*in}(r, \alpha, \xi) = \Psi_{*in}(r_{1sp}) \quad (6.5)$$

where the function Ψ_* now depends on time through $\xi(t)$. Eventually, at full reconnection when poloidal symmetry is restored, each reconnected surface becomes a circle of radius r_k such that $\pi r_k^2 = A_X$, or

$$r_k^2 = r_{2sp}^2 - r_{1sp}^2. \quad (6.6)$$

The relaxed normalised helical flux must satisfy the relationships

$$\Psi_{*rel}(r_k) = \lim_{\xi \rightarrow r_{mix}} \Psi_* \Big|_{r=r_k} = \Psi_{*in}(r_{1sp}). \quad (6.7)$$

The magnetic axis of the initial configuration reconnects with the flux surface at $r = r_{mix}$, such that

$$\Psi_{*in}(0) = \Psi_{*in}(r_{mix}). \quad (6.8)$$

This formula defines the mixing radius. Observe that, at full reconnection, the initial magnetic axis and the island O-point annihilate each other, while the new axis of the relaxed configuration corresponds to the O-point of the expanding $m/n = 1$ island.

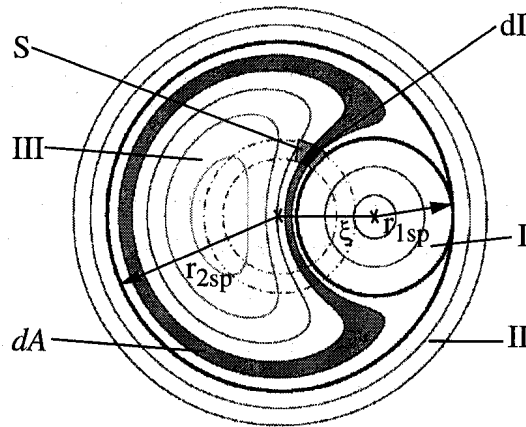


Fig. 6.12 Magnetic topology during the reconnection. The island separatrix is formed by the circles of radii, r_{1sp} and r_{2sp} and S is the region where the ECH power is deposited. Outside the island separatrix (regions I and II) the magnetic flux surfaces are circular while inside (region III) they are crescent shaped. In the plasma rest frame, with the assumption of rigid toroidal rotation, the toroidally averaged heated region is the ring indicated by dot-dashed circles. dI shows the intersection of the heated ring with a generic flux tube of cross sectional area dA .

So far, we have specified the constraints that the function Ψ_* must obey but we have not derived this function explicitly. This is done now in two steps. In the first step, we find convenient to introduce a Hamiltonian function, $H = H(\Psi_*) = H(r, \alpha, \xi)$, whose constant energy contours correspond to the crescent-shaped surfaces within the island separatrix. This region is indicated as “region III” in Fig. 6.12. A suitable choice for this function, as detailed in [9], is

$$H = \frac{(r^2 + \xi^2 - r_{1sp}^2 - 2r\xi \cos \alpha)(r_{2sp}^2 - r^2)}{r^2 + \xi^2 - 2r\xi \cos \alpha}. \quad (6.9)$$

6.4 Theoretical model

The parameters r_{1sp} and r_{2sp} can readily be obtained as a function of $\xi(t)$ and $\Psi_{*in}(r)$, both assumed as given. The island separatrix for a given ξ corresponds to the contour level $H = 0$, while H reaches a maximum value, $H_{max}(\xi)$, on the island O-point. Crescent-shaped surfaces correspond to contour levels $H = H_0 \in [0, H_{max}]$. Note that the curves $H(\alpha, r, t) = H_0$ become circles in both the limits $\xi = 0$ and $\xi = r_{mix}$ (in the latter limit, $r_{1sp} = 0$).

In the second step, the function $A = A(H, \xi)$ can be evaluated numerically after computing the area, A_X , pertaining to each $H = 0$ surface; from this, using the area conservation rule, the function $\Psi_* = \Psi_*(H)$ can be constructed. A simple analytic fit can also be obtained:

$$A(H, \xi) = A_X(\xi) \left(1 - \frac{H}{H_{max}}\right) \quad (6.10)$$

For an inverse parabolic q profile,

$$\frac{q_0}{q_{in}(r^2)} = 1 - \Delta q \left(\frac{r}{r_s}\right)^2 \quad (6.11)$$

where $\Delta q = 1 - q_0$ is positive definite, we obtain [27]

$$\Psi_{*rel}(r^2) = \frac{\Delta q}{2q_0} r_s^2 \left(1 - \frac{r^4}{4r_s^4}\right) \quad (6.12)$$

and through Eqs. (6.5)-(6.7) and (6.10)

$$\Psi_*(\alpha, r, \xi) = \frac{\Delta q}{2q_0} r_s^2 \left\{ 1 - \frac{A_x^2(\xi)}{4\pi^2 r_s^4} \left[1 - \frac{H(\alpha, r, \xi)}{H_{max}(\xi)} \right]^2 \right\}. \quad (6.13)$$

This function Ψ_* is valid within the island region III of Fig. 6.12. In regions I and II, the magnetic surface cross sections and the function Ψ_* are trivially determined from $\Psi_{*in}(r)$.

Let us now derive an equation for the electron temperature, T_e . Since in a magnetised, high temperature plasma the heat transport along magnetic field lines is large compared to the transport perpendicular to magnetic field lines, the electron temperature is constant on magnetic flux surfaces, i.e. $T_e = T_e(\Psi_*, t)$. Similarly, since electron parallel diffusion is very large, we may conclude that $n_e = n_e(\Psi_*, t)$. Surfaces of constant Ψ_* move with the fluid and it is convenient to express the heat transport equation in a Lagrangian frame. We consider the limit of intense electron heating and relatively low density, where the collisional energy transfer between electrons

Chapter 6. SAWTOOTH ACTIVITY IN ECH PLASMAS IN TCV

and ions can be neglected. This is certainly the case in TCV with intense ECH, where the electron temperature can exceed the ion temperature by a factor of 10. The relevant equation becomes

$$\frac{3}{2}n_e\frac{\partial T_e}{\partial t} = -\bar{\nabla} \cdot \mathbf{q} + S \quad (6.14)$$

where S is the heat source and

$$\mathbf{q} = -n_e\chi_{\perp}\bar{\nabla}_{\perp}T_e \quad (6.15)$$

is the heat flux, with χ_{\perp} the perpendicular heat diffusion coefficient. The flux surface averaging (denoted by angular brackets) of Eq. (6.14) gives

$$\frac{3}{2}n_e\frac{\partial T_e}{\partial t} = \langle \bar{\nabla} \cdot \left(n_e\chi_{\perp}\frac{\partial T_e}{\partial \Psi_*}\bar{\nabla}\Psi_* \right) \rangle + \langle S \rangle. \quad (6.16)$$

This equation is coupled to the equation for the electron density, which reads

$$\frac{\partial n_e}{\partial t} = \langle \bar{\nabla} \cdot \left[\left(D_{\perp}\frac{\partial n_e}{\partial \Psi_*} - \frac{n_e v_{pe}}{|\bar{\nabla}\Psi_*|} \right) \bar{\nabla}\Psi_* \right] \rangle \quad (6.17)$$

where D_{\perp} is the electron diffusion coefficient across the field lines and v_{pe} is the pinch velocity. Eqs. (6.16) and (6.17) describe the evolution of the electron density and temperature on magnetic flux tubes frozen to the plasma flow. At a particular instant in time when two flux tubes with equal helical flux reconnect, mixing rules for the particle density and thermal energy density must be implemented which means that both the temperature and the density evolve during the reconnection process even if $\chi_{\perp} = S = 0$.

The mixing rules are derived from particle and energy conservation relations. Particle conservation can be written in integral form:

$$\int_A n_e(A')dA' = \pi \int_{r_1}^{r_2} n_{in}(r^2)dr^2 \quad (6.18)$$

where, as before, A is the area between two circles with equal helical flux before they reconnect. After the reconnection, A is the area of the crescent-shaped surface with the same value of Ψ_* . Differentiating Eq. (6.18), we obtain

6.4 Theoretical model

$$n_e[A(\Psi_*)] = \pi \left[n_e(r_{2sp}^2) \frac{dr_{2sp}^2}{dA} - n_e(r_{1sp}^2) \frac{dr_{1sp}^2}{dA} \right] \quad (6.19)$$

where the metric elements dr_{1sp}^2/dA and dr_{2sp}^2/dA can be obtained from the initial $\Psi_{*in}(r)$. For instance, for the inverse parabolic q profile in Eq. (6.11), one finds

$$-dr_{1sp}^2/dA = dr_{2sp}^2/dA = 1/2\pi. \quad (6.20)$$

The mixing rule for the thermal energy is obtained with similar considerations. However, we should consider that magnetic energy is transformed into heat during the reconnection process. A simple calculation shows that typically the transformed magnetic energy is smaller than the energy associated with the equilibrium poloidal magnetic field by two orders of magnitude and therefore can be neglected. Thermal energy conservation gives

$$p_e[A(\Psi_*)] = \pi \left[p_e(r_{2sp}^2) \frac{dr_{2sp}^2}{dA} - p_e(r_{1sp}^2) \frac{dr_{1sp}^2}{dA} \right] = n_e(\Psi_*) T_e(\Psi_*) \quad (6.21)$$

Since $p_e = n_e T_e$, Eqs. (6.19) and (6.21) can be combined to give the mixing rule for the electron temperature.

The appropriate boundary conditions for the temperature are as follows: an initial temperature $T_e(r, t=0) = \tilde{T}(r)$, where $\xi(t=0) = 0$; a condition at the plasma edge, $r = a$, located in region II of Fig. 6.12, normally $T(a, t) = 0$; the geometrical conditions $\partial T_e / \partial \tilde{r}|_{I,II} = 0$, where \tilde{r} is the distance from the magnetic axis in the two regions. Finally, a condition at the separatrix is required. Note that, with $\chi_\perp = 0$, a discontinuity of n_e and T_e across the separatrix is in general allowed by Eq. (6.21). With finite χ_\perp , a common temperature is found, approaching the separatrix from any of the three regions I, II, III. This common temperature is determined by the continuity of the heat flux. The boundary conditions for the density are similar. Eqs. (6.16), (6.17), (6.19), (6.21) with the appropriate boundary conditions and the determination of the helical flux function, as described above, completely specify the theoretical model.

In applying our model to the interpretation of the TCV experimental results, a number of simplifying assumptions were made:

- Rigid plasma toroidal rotation, with a period τ_{rot} .
- The ECH power source, S , is located on the poloidal midplane between radii, r_{h1} , r_{h2} (Fig. 6.12).

Chapter 6. SAWTOOTH ACTIVITY IN ECH PLASMAS IN TCV

To understand the toroidal averaged ECH pattern, indicated by the dot-dashed circles in Fig. 6.12, let us suppose that at the time $t = t_1$ the ECH beam heats the poloidal cross section at $\varphi = \varphi_1$ and $\alpha = \alpha_1$, being φ the toroidal angle and α the helicoidal angle defined above. All the flux surfaces that intersect the region $\{r \in [r_{h1}, r_{h2}], \alpha = \alpha_1\}$ are heated. Due to the plasma toroidal rotation, with angular velocity $\omega_{rot} = 1/\tau_{rot}$, and to the $m/n = 1/1$ symmetry of the mode, at the time $t_2 = t_1 + \Delta t$ the poloidal cross section at $\varphi = \varphi_1 - \omega_{rot}\Delta t$ will be heated by the ECH beam at $\alpha_2 = \alpha_1 - \omega_{rot}\Delta t$ resulting in a heating of all the flux surfaces intersecting the region $\{r \in [r_{h1}, r_{h2}], \alpha = \alpha_2\}$.

If the condition

$$\tau_{rot} \ll \frac{1}{\xi} \frac{d\xi}{dt} \quad (6.22)$$

is satisfied, the geometry of the flux surfaces is the same in the time interval $t \in [t_1, t_2]$ and thus all the flux surfaces intersecting the region $\{r \in [r_{h1}, r_{h2}], \alpha \in [0, 2\pi]\}$ are heated during the toroidal plasma rotation resulting in the toroidal averaged ECH pattern of Fig. 6.12. Over timescales longer than the rotation period, τ_{rot} , the heated region in the plasma rest frame is a ring in the poloidal cross-section, indicated by the dashed-dotted lines in Fig. 6.12. The region obtained by rotating the heated ring in the toroidal direction has a volume V_h . Thus, in the plasma frame, we take for simplicity

$$S = \rho \mathcal{H}[(r - r_{h1})(r_{h2} - r)] \quad (6.23)$$

where \mathcal{H} is the Heaviside function and $\rho = P_{ECH}/V_h$. Since parallel heat conduction is dominant, the deposited heat spreads rapidly over all flux tubes intersecting the heated ring. Thus, if we denote by dA the cross-sectional area of a generic flux tube and by dI its intersection with the heated ring, we can write the ECH power density averaged over flux surfaces as $\langle S \rangle(A) = \rho dI/dA$. Note that the heat is transported radially by parallel diffusion in a complex magnetic structure, such as that of Fig. 6.12, resulting in an apparent non-local transport process.

6.5 Simulation results

- The perpendicular heat diffusion coefficient, χ_{\perp} , is taken to be of the form

$$\left\{ \begin{array}{l} \chi_{\perp} = \left(\frac{r}{a}\right)^{\beta} \chi_{max} \quad \text{for } r \geq r_{2sp} \\ \chi_{\perp} = \left(\frac{r_{2sp}}{a}\right)^{\beta} \chi_{max} = \text{const for } r < r_{2sp} \end{array} \right. \quad (6.24)$$

with χ_{max} and β constant parameters; $r \geq r_{2sp}$ corresponds to the region II of Fig. 6.12, where $\Psi_* = \Psi_{*in}(r)$.

- The initial q profile is taken as inverse parabolic, Eq. (6.11). Note that this profile is used only up to $r = r_{mix}$; for this profile, $r_{mix} = \sqrt{2}r_s$. For $r \geq r_{mix}$, the magnetic topology is unchanged and the q profile can differ from inverse parabolic. The precise value of q_0 is found not to affect the resulting temperature evolution. Electron cyclotron current drive effects are neglected.

- The electron density profile is flat inside the mixing radius and fixed during the sawtooth period. This is the crudest of all our simplifications. It is justified on the basis that, with intense ECH, the electron temperature profile tends to become rather peaked and, during a sawtooth period, $\Delta T_e/T_e \gg \Delta n_e/n_e$. This condition is satisfied for the standard and saturated sawteeth discussed in section 6.3, but it is only marginal for the humpback oscillations and giant sawtooth.

- The temperature profile at $t = 0$ is chosen to be $T(r, t = 0) = T_0 \left(1 - \frac{r^2}{a^2}\right)$, with $T_0 = 1$ keV. However, after an initial transient, which may last for a few sawtooth periods, the temperature evolution settles into a periodic cycle independent of $T(r, t = 0)$.

6.5 Simulation results

In this section, we discussed numerical simulations with the code M1TEV [9], [33], which is based on the previous theoretical model. The parameters used in the simulations are given in Table 6.1.

Simulation	r_{h1}/r_{mix}	r_{h2}/r_{mix}	χ_{max} [m ² /s]	β	P_{ECH} [kW]
Standard Sawtooth	0	0.25	3.5	1.8	500
Saturated Sawtooth	0	0.25	10.5	3	460
Deposition on $q = 1$	0.55	0.8	4.8	2	450

Table 6.1 : Simulation parameters

6.5.1 Standard sawtooth

Fig. 6.13 presents the simulation of a standard, triangular sawtooth in the presence of central ECH. The function $\xi(t)$ is taken to be zero for $0 \leq t \leq 0.975 \cdot \tau_{saw}$ and then to increase linearly up to r_{mix} during the crash, i.e. for $0.975 \cdot \tau_{saw} \leq t \leq \tau_{saw}$, consistent with the experimental displacement function shown in Fig. 6.1. Fig. 6.13 shows local temperature traces and Fig. 6.14 the simulated temperature profiles corresponding to different times in the shaded box of Fig. 6.13. The most striking experimental feature reproduced by our simulation is the formation of a hot ring in the relaxed temperature profile. This is not observed in TCV ohmic discharges, but it occurs with intense central ECH when the pre-crash temperature profile is very peaked.

The formation of the hot ring is a straightforward consequence of Kadomtsev's full reconnection model for cases where the crash phase is very rapid, so that diffusion and heating can be neglected during this phase, and the pre-crash temperature profile is sufficiently peaked. An analytic calculation provides a better understanding of this point. Assume, for simplicity, a constant density profile, a pre-crash q profile as in Eq. (6.11) and a rather peaked pre-crash temperature profile,

$$T_{in}(r) = T_0 \left(1 - \frac{r^2}{a^2}\right)^\alpha \quad (6.25)$$

with $\alpha = 2$.

Using Eq. (6.21), the relaxed temperature profile is

$$T_{rel}(r) = T_{in}(r_s) \left[1 + \frac{r^4}{4(a^2 - r_s^2)^2} \right] \text{ for } r \leq r_{mix}, \quad (6.26)$$

while for $r > r_{mix}$, $T_{rel}(r) = T_{in}(r)$. This profile is hollow up to $r = r_{mix}$ and the discontinuity at $r = r_{mix}$ would be smoothed out by perpendicular heat diffusion. The resulting profile has a hot ring structure centred in the proximity of r_{mix} .

In general, a hot ring forms if $\alpha > 1$ in Eq. (6.25). For less peaked temperature profiles with $\alpha \leq 1$, as more typical for ohmic discharges, the relaxed profiles is flat or perhaps slightly peaked on axis. For instance, assuming $\alpha = 1$, a constant density profile, an inverse parabolic q profile as in Eq. (6.11), Eq. (6.21) yields a constant temperature up to $r = r_{mix}$, $T_{rel} = T_0 = T_{in}(r_1)$.

6.5 Simulation results

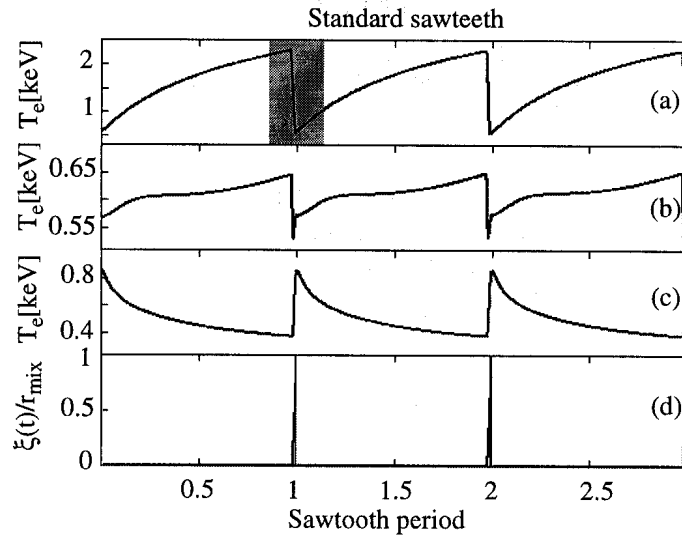


Fig. 6.13 Simulation of triangular sawteeth with on-axis ECH power deposition. The electron temperature is shown at different radial positions. (a) On-axis, $r = 0$. (b) Just inside the inversion radius, $r = 0.85 \cdot r_{inv}$. (c) Just outside the inversion radius, $r = 1.27 \cdot r_{inv}$. (d) Displacement function $\xi(t)$.

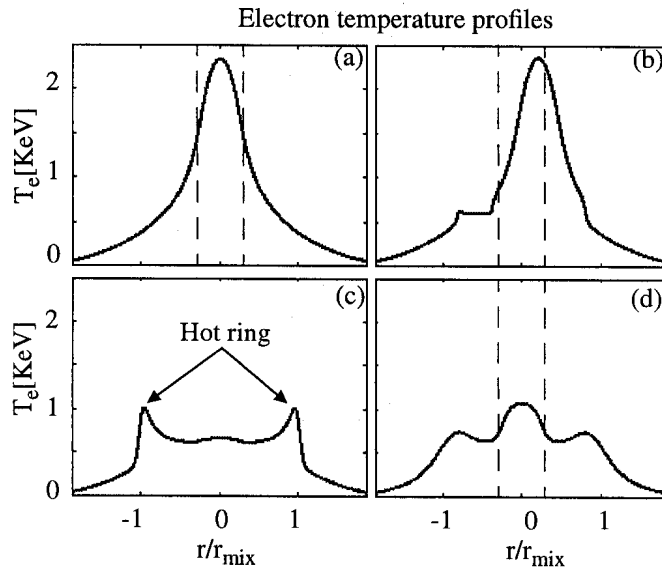


Fig. 6.14 Simulated electron temperature profiles for the time window indicated in Fig. 6.13. (a) Pre-crash, $\xi = 0$. (b) During hot core displacement, $\xi = 0.41$. (c) Just after the sawtooth crash, $\xi = r_{mix}$, the hot ring is formed. (d) Early during reheat ramp, corresponding to $t - t_{crash} = 0.125 \cdot \tau_{saw}$. The power deposition region is shown as dashed lines.

Chapter 6. SAWTOOTH ACTIVITY IN ECH PLASMAS IN TCV

The inversion radius r_{inv} for the electron temperature satisfies

$$T_{rel}(r_{inv}) = T_{in}(r_{inv}). \quad (6.27)$$

In particular for $\alpha = 2$, using Eq. (6.25) and Eq. (6.26) numerical evaluation of Eq. (6.27) yields

$$r_{inv} \approx 0.73 \cdot r_s. \quad (6.28)$$

This is consistent with the reduction of the sawtooth inversion radius observed under central ECH conditions compared to ohmic conditions, as reported in chapter 5.

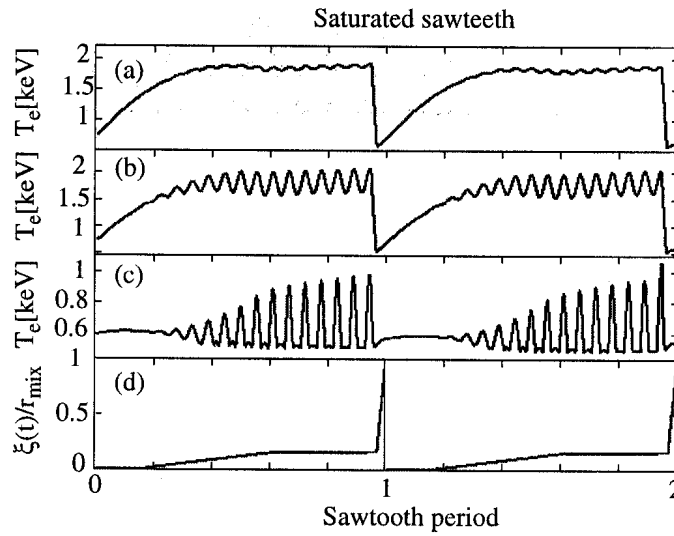


Fig. 6.15 Simulation of saturated sawtooth with on-axis ECH power deposition. The electron temperature is shown at different radial positions. (a) Close to the magnetic axis, $r = 0.01 \cdot r_{inv}$. (b) Slightly off-axis, $r = 0.15 \cdot r_{inv}$. (c) Just inside the inversion radius, $r = 0.85 \cdot r_{inv}$, where the frequency doubling is visible. (d) The hot core radial displacement $\xi(t)$.

6.5 Simulation results

6.5.2 Saturated sawtooth

Saturated sawteeth can be obtained with our model with central or slightly off-axis heating, provided the heat is deposited well within the $q = 1$ radius, Fig. 6.15, with the simulation parameters in Table 6.1. The key to obtaining saturated sawteeth is to assume a displacement function which moves the magnetic axis early in the sawtooth ramp, by a distance comparable to the outer radius of the heat deposition region. In this way, the heating power is no longer deposited near the magnetic axis. Consequently, the electron temperature saturates at the plasma centre, i.e. at the original position of the magnetic axis before the onset of the $m/n = 1$ island. The displacement function used for this simulation, shown in Fig. 6.15(d), was chosen to reproduce the experimentally measured displacement, Fig. 6.4.

With a magnetic island width, $w_{isl} = 2\xi$, the temperature profile is not poloidally symmetric. In the presence of toroidal plasma rotation, this gives rise to oscillations of the simulated electron temperature traces, Fig. 6.15(b,c). Of particular interest is the doubling of the oscillation frequency, in agreement with the experimental traces, Fig. 6.4.

6.5.3 Deposition close to the sawtooth inversion surface

Recent attempts to simulate the humpback oscillations [34], using the same model, resulted in a sawtooth shape in which the drop and rise of the central electron temperature occur on the same timescale. This was mainly due to the choice of the displacement function, $\xi(t)$, and to the assumption of full magnetic reconnection after the sawtooth crash. This condition was, however, not fulfilled in the two examples presented in section 6.3.

In the present simulation, the function $\xi(t)$ shown in Fig. 6.16(b) increases rapidly up to $0.5 \cdot r_{mix}$ during the crash and then remains constant during the sawtooth ramp, i.e. for $0 \leq t \leq 0.3 \cdot \tau_{saw}$. After the sawtooth ramp, for $0.3 \cdot \tau_{saw} \leq t \leq 0.4 \cdot \tau_{saw}$, $\xi(t)$ reaches the mixing radius completing the reconnection process. The ECH power is deposited on the $q = 1$ surface and the parameters are given in Table 6.1. The main features of the overall evolution of the central electron temperature are in agreement with the time traces shown in Fig. 6.7(c) and Fig. 6.8(c). In particular, the three distinct phases with different timescales, previously described, are correctly reproduced by the simulation and the electron temperature profiles are qualitatively consistent with the Thomson scattering measurements, Fig. 6.17.

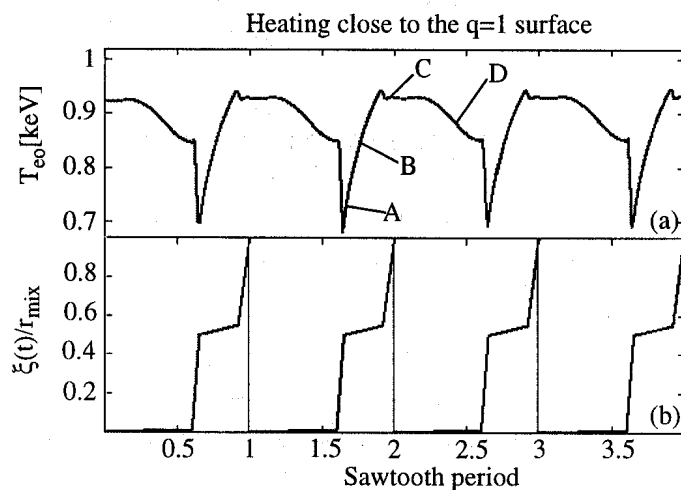


Fig. 6.16 Simulation results of sawtooth oscillations with ECH power deposited close to the $q = 1$ surface: (a) the central electron temperature; (b) the displacement function $\xi(t)$.

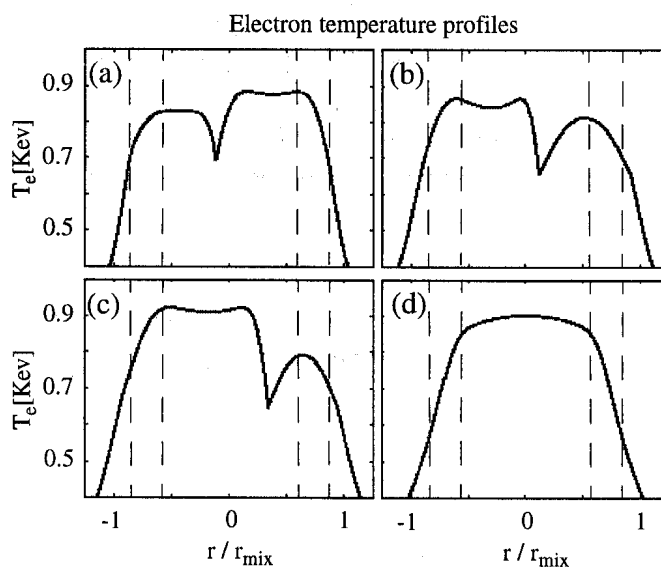


Fig. 6.17 Simulated electron temperature profiles obtained with ECH power deposited on the $q = 1$ surface. The T_e profiles shown in (a,b,c,d) correspond respectively to the times A, B, C, D indicated in Fig. 6.16: (a,b) post-crash profiles during the sawtooth ramp, $\xi = 0.5$, $\xi = 0.518$; profiles are not poloidally symmetric since the reconnection process is incomplete; (c) during hot core displacement, $\xi = 0.719$; (d) at complete magnetic reconnection, $\xi = 1$. The power deposition region is shown by dashed lines.

6.6 Concluding remarks

However, there are many open issues which call for extensions. One issue relates to current drive effects, which probably play an important role for the detailed interpretation of humpback events observed in the T-10 tokamak [5]. Since current drive modifies the q profile and the local magnetic shear we expect this to have consequences on the internal kink stability which could be taken into account by different choices of the displacement function in our simulation. Another open issue is the overall detailed shape of a humpback trace. More accurate comparisons of simulation and experiment require an improved spatial resolution of the electron temperature profile measurement. Moreover, the assumption of flat electron density profile inside the mixing radius during subsequent sawtooth crash is only marginally satisfied in the case of giant sawteeth and humpbacks. This limitation will be overcome in the future by a recent improvement of the M1TEV code which has been upgraded to include the temporal evolution of the electron density [35].

6.6 Concluding remarks

In the TCV tokamak, different types of sawtooth oscillations, ranging from triangular to non-standard sawteeth, are observed in the presence of ECH as the location of the power deposition is moved from the magnetic axis to the sawtooth inversion surface. Measurements with high temporal resolution have shown that the different sawtooth shapes and their features in the electron temperature profiles are compatible with the strong localisation of the heating region, which is specific to the ECH method, and of the advection and mixing of electron thermal energy associated with a resistive internal kink mode. This mode produces precursor oscillations which have been identified to have $n = 1$ and dominant $m = 1$ mode numbers for all sawtooth types. This shows that all the different sawtooth relaxation cycles can be reproduced by a single model. The detailed dynamics of the magnetic island, associated with the resistive internal kink mode, is described by the displacement function, $\xi(t)$, which is inferred from the experimental data for the different sawtooth types.

In triangular sawteeth, obtained with on-axis heating, the $m/n = 1$ mode develops immediately before the crash, whereas, when the deposition is off-axis but still within the sawtooth inversion surface, it grows early in the sawtooth ramp and remains at a saturated level until the sawtooth crash, resulting in saturated sawteeth. In both cases, the sawtooth crash is consistent with a full reconnection process and its overall effect is to expel particles and heat from the plasma centre resulting in a flattening of both the electron temperature and density profiles. In the case of on-axis heating, when the pre-crash electron temperature profile is sufficiently peaked, the formation of a hot ring around the sawtooth inversion surface is observed at the end of the reconnection process.

When the ECH power is deposited slightly off-axis, the electron temperature profile is less peaked and the hot ring is not observed.

With ECH power deposited close to the sawtooth inversion surface, improved stability against the internal kink mode is obtained, leading to a long period of relative MHD quiescence and to pre-crash electron temperature profiles which are relatively flat inside the $q = 1$ region. The subsequent sawtooth crash, observed during giant and humpback sawteeth, results in a small variation of the central electron temperature, which shows similar temporal evolution, despite a large difference in the electron density behaviour. This difference is not completely understood, but may be ascribed to the ECH associated pump-out. The post-crash electron temperature profiles in both sawtooth types are not poloidally symmetric, indicating an incomplete magnetic reconnection process.

The different types of sawteeth have been simulated using a numerical code based on a theoretical model [9] which describes the evolution of the electron temperature in the presence of localised heat sources and of an $m/n = 1$ magnetic island whose temporal evolution is inferred from the experimental displacement function, $\xi(t)$. Despite the relative simplicity of this model, the simulated sawtooth shapes under the different heating conditions are in agreement with the experimental observations.

References

- [1]N. J. Lopez-Cardozo, et al., *Phys. Rev. Lett.* **73** (1994) 256.
- [2]G. Cima, et al., *Plasma Phys. Control. Fusion* **40** (1998) 1149.
- [3]F. Hofmann, et al., *Plasma Phys. Control. Fusion* **36** (1994) B277.
- [4]Z. A. Pietrzyk, et al. including I. Furno, *Nucl. Fusion* **39** (1999) 587.
- [5]K. A. Razumova, et al., *Plasma Physics Reports* **23** (1997) 13.
- [6]T. P. Goodman, et al., *Proc. 2nd Europhys. Top. Conf. on Radiofrequency Heating and Current Drive of Fusion Devices* (Brussels 1998), Vol. 22A, page 249.
- [7]A. Pochelon, et al., *Nucl. Fusion* **39** (1999) 1807.
- [8]T. P. Goodmann, et al., *Proc. 25th EPS Conf. on Controlled Fusion and Plasma Physics* (Prague 1998), vol. 22C, page 1324.
- [9]F. Porcelli, et. al., *Phys. Rev. Lett.* **82** (1999) 1458.
- [10]B. Coppi, et al., *Fiz. Plazmy* **2** (1976) 961; *Sov. J. Plasma Phys.* **1** (1976) 389.
- [11]M. Anton, et al., *Plasma Phys. Control. Fusion* **38** (1996) 1849.
- [12]T. Dudok de Wit, et al., *Phys. Plasmas* **1** (1994) 3288.
- [13]R. T. Snider, et al., *Phys. Fluids B* **1** (1989) 404.

6.6 Concluding remarks

- [14]K. Hanada, et al., *Phys. Rev. Lett.* **66** (1991) 1974.
- [15]G. Smith, et al., *Proc. 9th Joint Workshop and Electron Cyclotron Heating*, Borrego Springs, Editor John Lohr, Publisher World Scientific (1995) 651.
- [16]T. P. Goodman, et al., *Proc. 26th EPS Conf. on Controlled Fusion and Plasma Physics* (Maastricht 1999), vol. 23J, page 1101.
- [17]M. Anton, et al., *Rev. Sci. Instrum.* **66** (1995) 3762.
- [18]H. Weisen, et al., *Nucl. Fusion* **37** (1997) 1741.
- [19]H. Weisen, et al., *Rev. Sci. Instrum.* **62** (1991) 1531.
- [20]I. Furno, et al., *Proc. 27th EPS Conf. on Controlled Fusion and Plasma Physics* (Budapest 2000), P1-026.
- [21]C. Angioni, et al., *Proc. Joint Varenna-Lausanne International Workshop on Theory of Fusion Plasmas* (Varenna 2000), page 73.
- [22]D. Boucher, et al., *Proc. IAEA Tech. Com. on Advances in Simulation and Modell. of Thermonuclear Plasmas* (Montreal 1993), page 142.
- [23]F. Porcelli, et al., *Plasma Phys. Control. Fusion* **38** (1996) 2163.
- [24]K.-L. Wong, et al., *Proc. 27th EPS Conf. on Controlled Fusion and Plasma Physics* (Budapest 2000), P1-108.
- [25]S. Coda, et al., *Proc. 26th EPS Conf. on Controlled Fusion and Plasma Physics* (Maastricht 1999), vol. 23J, page 1097.
- [26]W. Park, et al., *Nucl Fusion* **30** (1990) 2413.
- [27]B. B. Kadomtsev, *Fizika Plazmy* **1** (1975) 710; *Sov. J. Plasma Phys.* **1** (1976) 389.
- [28]A. J. Lichtenberg, *Nucl. Fusion* **24** (1984) 1277.
- [29]J. O'Rourke, *Plasma Phys. Control. Fusion* **33** (1991) 289.
- [30]W. P. West, et al., *Phys. Rev. Lett.* **58** (1987) 2758.
- [31]J. Wesson, *Tokamaks*, Clarendon Press, Oxford, 1987.
- [32]F. L. Waelbroeck, *Phys. Fluids B* **1** (1989) 2372.
- [33]E. Rossi, *Isole magnetiche e trasporto d' energia nei plasmi*, Tesi di Laurea, Politecnico di Torino (Torino 1998), Italy.
- [34]F. Porcelli, et al., including I. Furno, *Nucl. Fusion* **40** (2000) 1691.
- [35]E. Rossi, *Private communication*.

7 PARTICLE TRANSPORT WITH HIGH POWER CENTRAL ECH AND ECCD

7.1 Introduction

Electron cyclotron heating and current drive appear to be at the origin of unexpected transport phenomena which are potentially important in the confinement of fusion plasmas. In several past and present tokamak experiments, ECH is often seen to lead to a reduction in the plasma particle density and confinement [1], [2]. Such phenomena are also observed in stellarators, where they are at least qualitatively explained by neoclassical transport processes (thermodiffusion) arising from the presence of locally trapped particles due to the existence of magnetic field modulations throughout the plasma cross section [3], [4]. Since the toroidal magnetic field ripple is very small on axis in most tokamaks, there are, in principle, no locally trapped particles in the core of axisymmetrical tokamaks. As a result, the particle pumpout in tokamaks has remained unexplained. Evidence from TCV tokamak suggests that pumpout in stellarators and in the core region of tokamaks is most probably of the same physical origin. Whereas in stellarators the field modulation is a built-in feature of the magnetic configuration, in tokamaks it can result from MHD perturbations caused by instabilities affecting the plasma core, especially inside the $q = 1$ surface. The presence of an $m/n = 1/1$ island causes the plasma core to be helically displaced. As a result, trapped particles exist even on the axis, similarly to the heliac configuration. The coexistence of locally and toroidally trapped particles within the $q = 1$ surface can be expected to give rise to competing transport phenomena, including pumpout, since the off-diagonal terms associated with these two classes of particles have opposite signs.

7.2 Experimental observations

The plasma response to a radial sweep of the ECH power absorption location is shown in Fig. 7.1 for the TCV discharge No. 17766. Plasma parameters are: $\delta_a = 0.17$, $\kappa_a = 1.28$, $I_p = 193$ kA, $q_a = 4.4$, $P_{ECH} = 900$ kW. The ECH power absorption location is scanned through the plasma along the vertical resonance position for the X2-mode at a velocity of 3.5 cm / 100 ms by sweeping the poloidal injection angle of the heating beam. The plasma shape is kept constant during the

sweep. The interval, indicated by the shaded box in Fig. 7.1(d), corresponds, within the experimental uncertainties, to power deposition inside the sawtooth inversion surface determined by tomographic inversion of soft x-ray measurements as described in chapter 4.

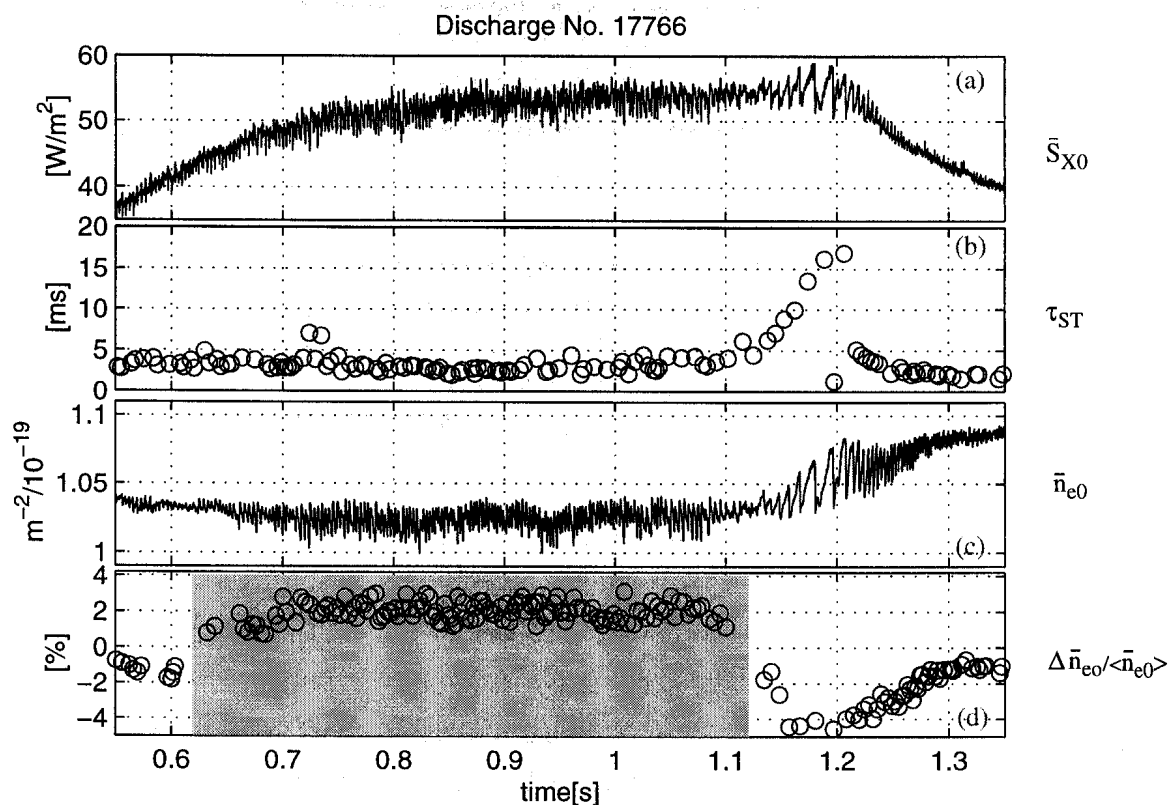


Fig. 7.1 Plasma response to a radial sweep of the ECH power absorption location. (a) Central line integrated soft x-ray signal. (b) Sawtooth period. (c) Central line integrated density from 2 mm interferometer. (d) Relative variation of \bar{n}_{e0} at the sawtooth crash, Fig. 7.2(c). The interval [A,B] (shaded box) corresponds to ECH power deposition inside the sawtooth inversion surface determined from soft x-ray tomography.

For the same discharge, Fig. 7.2 gives an expanded view of sawtooth oscillations corresponding to ECH power deposition outside, Fig. 7.2(a,c,e), and inside, Fig. 7.2(b,d,f), of the sawtooth inversion surface. The line integrated central soft x-ray emissivity \bar{S}_{X0} , Fig. 7.2(a,b), is shown together with the line integrated central electron density \bar{n}_{e0} from a microwave interferometer operating at 140 GHz, Fig. 7.2(c,d), and the central electron temperature T_{e0} , Fig. 7.2(e,f), from foil-absorption measurements using 150 μm Be and 650 μm Be filters.

In the previous chapter, the sawtooth behaviour has been discussed for power deposition close to the sawtooth inversion surface which corresponds approximately to the interval $t \in [1.12, 1.2]$ s in Fig. 7.1. Also, the behaviour of the sawtooth period, Fig. 7.1(b), has been recently simulated [5] using the PRETOR transport code [6] which contains a sawtooth trigger model based on a critical shear value at the $q = 1$ surface, s_{1crit} [7]. These simulations suggest that the increase in the sawtooth period observed when the ECH power is deposited close to the $q = 1$ surface may result from an increase of the electron pressure scale length at the $q = 1$ surface (resulting in an increased s_{1crit}) and from a slower growth of the magnetic shear at the same surface after the sawtooth crash.

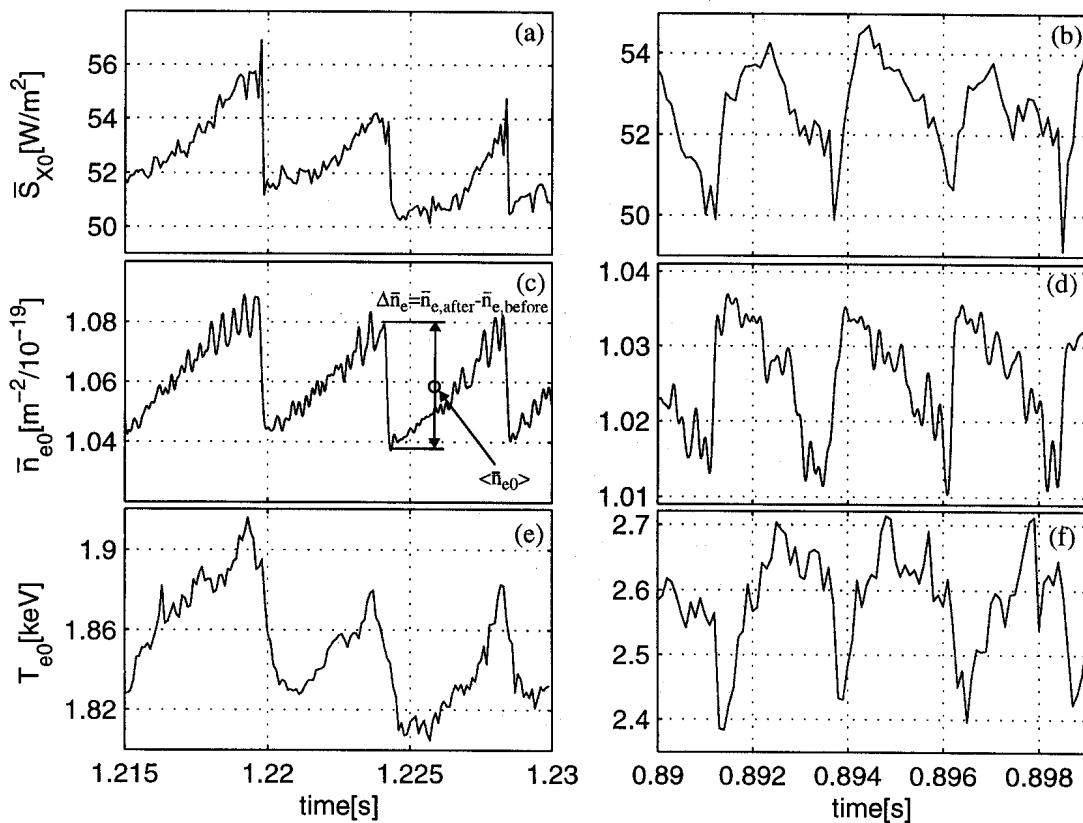


Fig. 7.2 Discharge No. 17766. Sawtooth oscillations corresponding to ECH power deposition well outside (left) and inside (right) the sawtooth inversion surface. (a, b) Central line integrated soft x-ray emissivity filtered by $50 \mu\text{m}$ Be foil. (c, d) Line integrated central density from a microwave interferometer operating at 140 GHz. (e, f) Central electron temperature from the foil-absorption system using $150 \mu\text{m}$ Be + $650 \mu\text{m}$ Be filters.

Chapter 7. PARTICLE TRANSPORT WITH HIGH POWER CENTRAL ECH AND ECCD

For power deposition well outside the inversion radius, both \bar{n}_{e0} and T_{e0} increase during the reheating and then drop at the sawtooth crash on a fast time scale (typically $\tau_{crash} < 100 \mu\text{s}$), Fig. 7.2(c,e). The relative crash amplitude of the line integrated central electron density is $\Delta\bar{n}_{e0}/\langle\bar{n}_{e0}\rangle \approx -4\%$, where the brackets $\langle \rangle$ indicate the average of a quantity evaluated before and after the sawtooth crash as illustrated in Fig. 7.2(c). During the early sawtooth ramp, the soft x-ray emissivity is poloidally symmetric with no detectable MHD mode activity; 2–3 ms before the sawtooth crash, $m/n = 1/1$ precursor oscillations are observed, Fig. 7.2(a,c).

When the ECH power deposition is moved inside the sawtooth inversion radius, particles are expelled from the plasma centre during the reheat phase, resulting in inverted sawteeth on the line integrated central electron density, Fig. 7.2(d). The sawtooth period τ_{ST} is ≈ 2.5 ms. The central electron temperature increases from approximately 2.4 keV to 2.7 keV for $t - t_{crash} < 0.4\tau_{ST}$ and then remains almost constant until the following sawtooth crash. In the present case, the soft x-ray emissivity from dominant carbon impurities depends on the electron temperature and density as $S_X \propto n_e^2 T_e^\gamma$, with $\gamma \approx 0.4$. This accounts for the time evolution of the central soft x-ray emissivity, Fig. 7.2(b), which shows an inverted ramp similar to the \bar{n}_{e0} signal. This inverted ramp is accompanied by a strong $m/n = 1$ rotating mode, as obtained from SVD analysis of tomographically inverted soft x-ray measurements (not shown here).

The inverted ramp is terminated by the sawtooth crash, during which \bar{n}_{e0} recovers rapidly (typically $\tau_{recover} \approx \tau_{crash}$), whereas T_{e0} drops from ≈ 2.6 keV to ≈ 2.4 keV. The relative amplitude of the recovery of the line integrated density, $\Delta\bar{n}_{e0}/\langle\bar{n}_{e0}\rangle \approx 2\%$, is approximately constant for injection angles inside the inversion surface, as shown in Fig. 7.1(d).

The dependence of sawtooth behaviour on the injected ECH power is presented in Fig. 7.3 and Fig. 7.4 for the TCV discharge No. 14475. The temporal evolution of the central soft x-ray emissivity, Fig. 7.4(c,d), is shown together with the central electron density n_{e0} , Fig. 7.4(a, b). The latter has been estimated using the TCV 14-channel far infrared interferometer, the signals of which were inverted by means of a modified Abel inversion method taking into account the non-circular shape of the flux surfaces in TCV (see chapter 3). Plasma parameters are: $\delta_a = 0.23$, $\kappa_a = 1.54$, $I_p = 393$ kA, $q_a = 2.9$. The ECH resonance position is located inside the sawtooth inversion radius and P_{ECH} is increased in three steps from 0.5 MW to 1.4 MW. For this plasma shape, the central ECH deposition strongly perturbs the triangular ohmic sawteeth. With $P_{ECH} = 1.4$ MW, the sawtooth period, $\tau_{ST} \approx 3$ ms, is significantly longer than the ohmic sawtooth period $\tau_{ST} \approx 2$ ms and the n_{e0} behaviour changes from triangular to inverted. In the latter case, the electron density recovery $\Delta\bar{n}_{e0}/\langle\bar{n}_{e0}\rangle$ increases from 1.6% at $P_{ECH} = 0.8$ MW to 2.3% at $P_{ECH} = 1.4$ MW.

7.2 Experimental observations

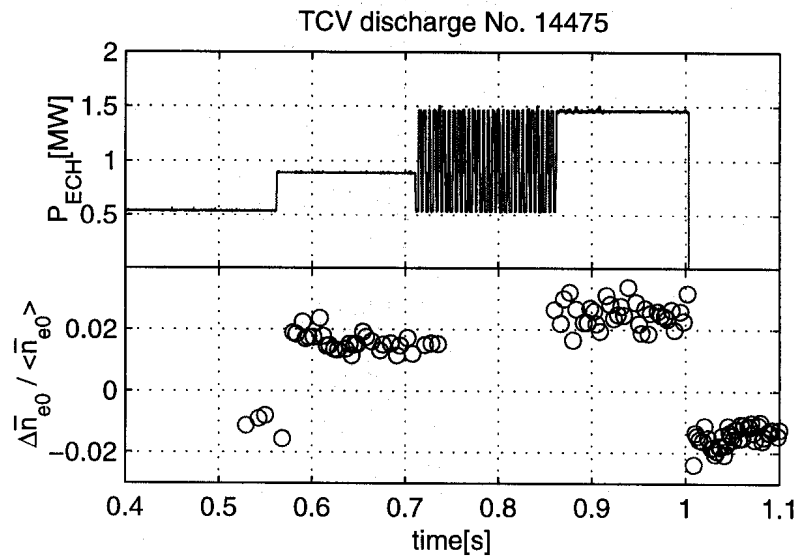


Fig. 7.3 Dependence of the density recover at the sawtooth crash on the injected ECH power. The ECH resonance position is located inside the sawtooth inversion radius. (a) Stepping up of the ECH power. (b) Relative variation of \bar{n}_{e0} at the sawtooth crash.

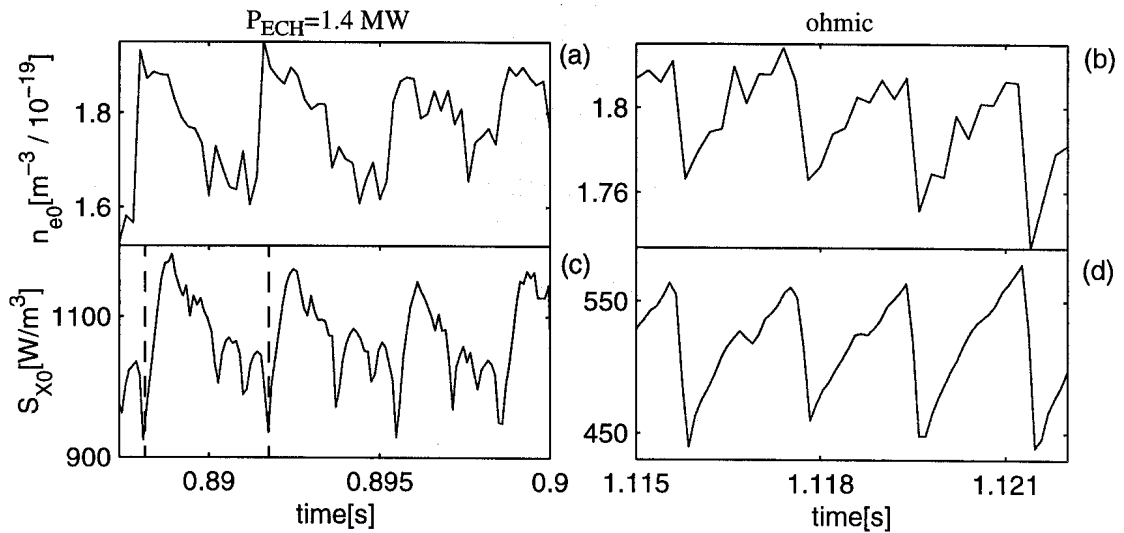


Fig. 7.4 Discharge No. 14475. Sawtooth behaviour with 1.4 MW of ECH (left) and ohmic heating only (right). Top traces show inverted central electron density (a,b) and bottom traces show local soft x-ray emissivity from tomography (c,d). Dashed lines (c) indicate the time interval in which the SVD analysis is applied to local soft x-ray emissivities which is shown in Fig. 7.5.

Chapter 7. PARTICLE TRANSPORT WITH HIGH POWER CENTRAL ECH AND ECCD

During the associated inverted sawtooth ramp, the decrease in n_{e0} results from a flattening of the electron density profile and is correlated with the presence of $m/n = 1$ mode activity as shown in Fig. 7.5. In this figure, the mode structure of the soft x-ray emissivity, from SVD analysis, is shown in a small time window during the inverted sawtooth ramp indicated in Fig. 7.4(c) by dashed lines. Inspection of Fig. 7.5 reveals the presence of a rotating $m = 1$ mode at a frequency of ≈ 5 kHz which is represented by the topos/chronos pair $k = 3, 4$. The toroidal mode number, as obtained from toroidal soft x-ray photodiodes, is $n = 1$. Partial collapses of the soft x-ray emissivity are observed during the particle pump-out and are particularly evident in the topos/chronos couple $k = 2$ which result in a flattening of the soft x-ray emissivity profile.

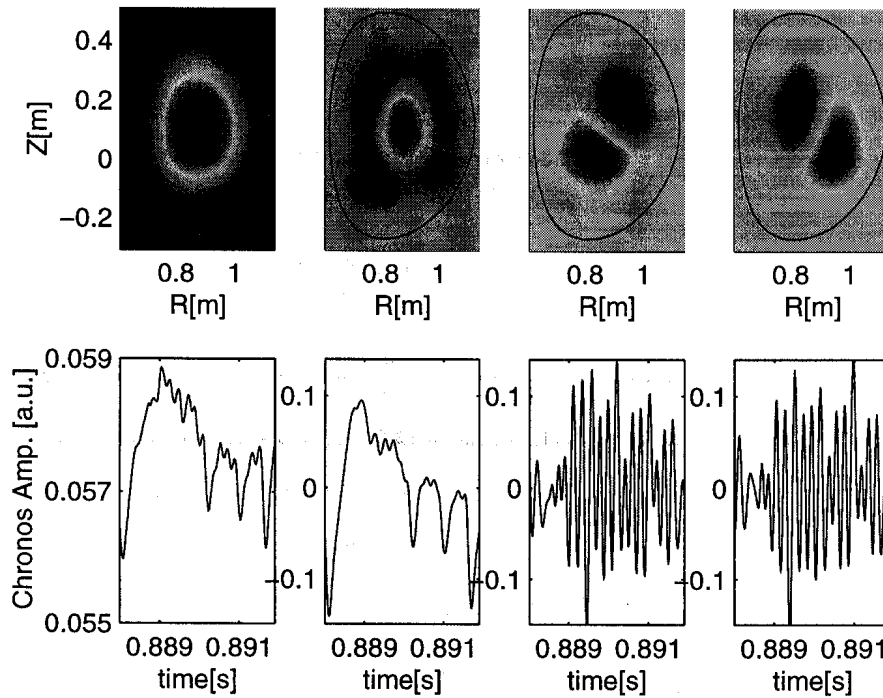


Fig. 7.5 SVD analysis of the reconstructed soft x-ray emissivities during the phase shown in Fig. 7.4(c) by dashed lines. Shown are the topo/chrono pairs corresponding to four largest eigenvalues. The top row shows the spatial eigenmodes (topos) with the LCFS. The corresponding temporal eigenvectors (chronos) are shown in the bottom row.

Fig. 7.6 shows the crash amplitude $\Delta \bar{n}_{e0} / \langle \bar{n}_{e0} \rangle$ from an ECH power scan for low and high triangularity obtained from a line integrated central electron density signal.

At high triangularity no pumpout is observed. It is a generally observed feature in TCV, both in

7.2 Experimental observations

ohmic [8] and ECH plasmas [9], that $m/n = 1/1$ pre-and postcursor oscillations are absent at high triangularity and are increasingly present as triangularity is reduced, suggesting a link between mode activity and the observed particle transport.

We may estimate the heat convected away from the core during the sawtooth ramp if we can assume that the electrons lost from the core have close to thermal energies. This assumption is justified for pure ECH (as in the examples of Fig. 7.4) by the absence of hard x-ray [10] and suprathermal ECE emission [11]. The heat carried away by electrons exiting from within the volume V_{inv} delimited by the inversion radius, can be then estimated as $P_{conv} \approx 1.5k_B \langle T_e \Delta N_e \rangle / \tau_{saw}$, where $\Delta N_e = \langle \Delta n_e \rangle V_{inv}$ is the number of electrons that haven been ‘pumped out’ between consecutive sawtooth crashes and τ_{saw} is the sawtooth period. The brackets refer to averages over V_{inv} . For the example in Fig. 7.4(a) we have $V_{inv} \approx 0.25 \text{ m}^3$, $\tau_{saw} \approx 3 \text{ ms}$, $\langle T_e \rangle \approx 2 \text{ keV}$ and may estimate $\langle \Delta n_e \rangle \approx 0.5 \Delta n_{e0} \approx 5 \cdot 10^{17} \text{ m}^{-3}$ and hence $P_{conv} / P_{ECH} \approx 0.02$. Although this is only a rough estimate, it shows that the convective heat losses associated with ‘pumpout’ do not significantly affect the overall power balance.

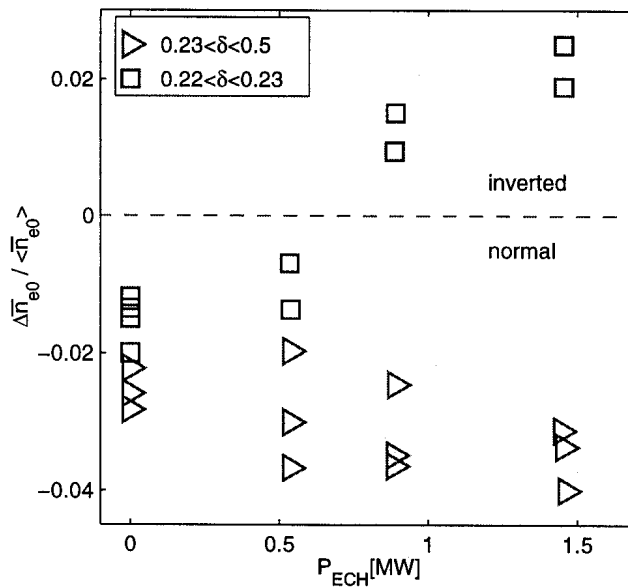


Fig. 7.6 Relative variation of \bar{n}_{e0} at the sawtooth crash for different plasma triangularity and injected ECH power. Positive and negative $\Delta \bar{n}_{e0} / \langle \bar{n}_{e0} \rangle$ values indicate respectively inverted and normal sawteeth.

Chapter 7. PARTICLE TRANSPORT WITH HIGH POWER CENTRAL ECH AND ECCD

In sawtoothing plasmas, significantly hollow density profiles cannot develop because the crashes regularly flatten density and temperature profiles. However with ECH and ECCD many situations arise when sawteeth are stabilised for long enough (typically 10 ms or more) for profiles to approach steady-state and the hollowness to become significant enough for measurements using the TCV Thomson scattering system. Fig. 7.7 shows two examples of electron density in a Counter-ECCD and in fully sustained Co-ECCD plasmas, showing that the pumpout phenomenon is very general and does not depend on the parallel velocity of the electrons interacting with the heating beams. In the case of the Counter-ECCD discharge, Fig. 7.7(b,d), plasma parameters are: $\delta_a = 0.25$, $\kappa_a = 1.71$, $q_a = 7.6$, $I_p = 220$ kA. In this discharge, the absence of sawteeth, which are completely stabilised, is accompanied by a saturated $m = 1$ mode as shown in Fig. 7.8 by the SVD analysis of the inverted soft x-ray emissivities.

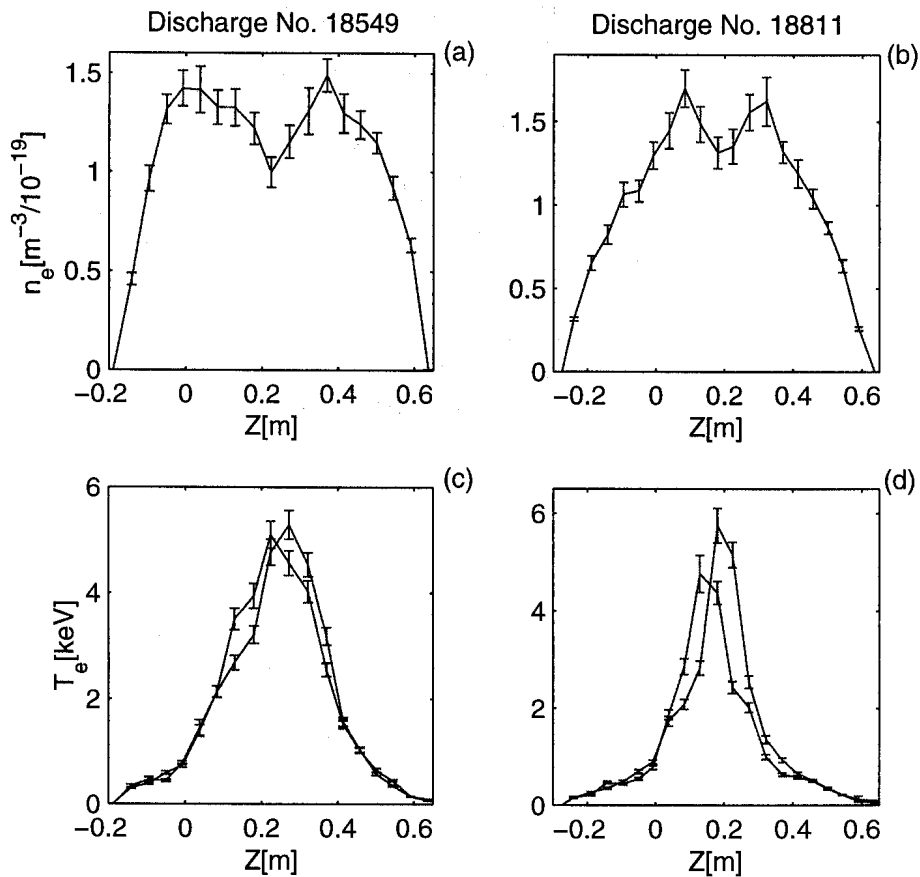


Fig. 7.7 Examples of electron density (a,b) and temperature (c,d) profiles in a Co-ECCD (left) and a Counter-ECCD discharge (right). Electron temperature profiles are shown at different times during mode activity revealing a kink distortion of the plasma core of a few centimeters.

7.2 Experimental observations

The mode appears to rotate at a frequency of ≈ 3 kHz and results in a displacement of the soft x-ray emissivity hot core of ≈ 1 cm determined from the reconstructed soft x-ray emissivities using Eq. (6.1). The mode activity results also in oscillations of the line integrated central electron density \bar{n}_{e0} (not shown here) at the frequency of ≈ 3 kHz and relative amplitude $\Delta\bar{n}_{e0}/\bar{n}_{e0} \approx 1\%$. During mode activity, hollow electron density profiles are sustained as shown in Fig. 7.7(b), where $n_{e,max}/n_{e0} \approx 1.3$.

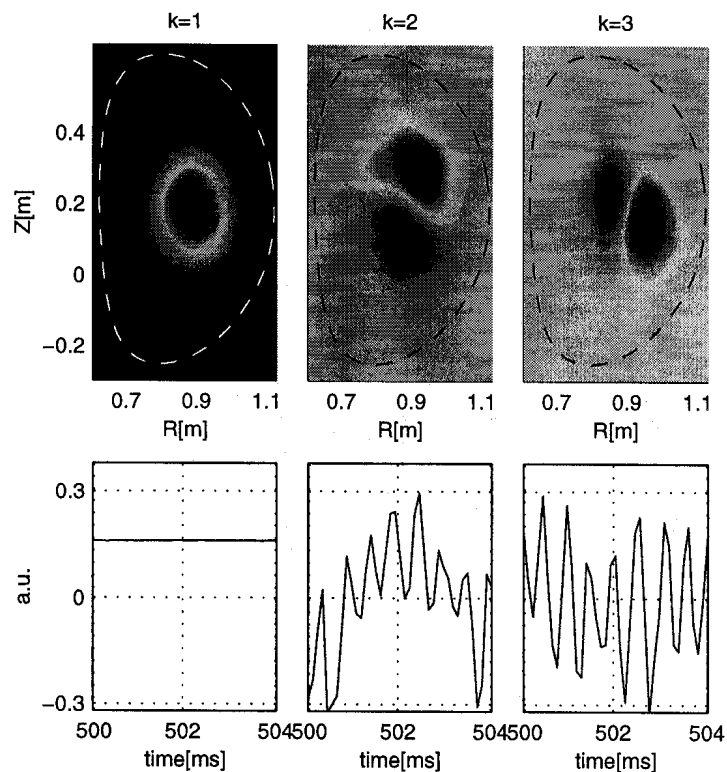


Fig. 7.8 SVD analysis of the reconstructed soft x-ray emissivities in TCV Counter-ECCD discharge No. 18811. Shown are the topo/chrono pairs corresponding to three largest eigenvalues. The top row shows the spatial eigenmodes (topos) with the LCFS (dashed line). The corresponding temporal eigenvectors (chronos) are shown in the bottom row.

Another extreme example of electron density pump-out has been obtained in the case of full current replacement with Co-ECCD [12] at an injected power $P_{ECH} = 2.7$ MW and plasma parameters: $\delta_a = 0.42$, $\kappa_a = 1.62$, $q_a = 7.8$, $I_p = 200$ kA. In this discharge, hollow electron density profiles are sustained during the whole sawtooth cycle. Fig. 7.7(a) shows the electron density profile relative to a time just before the sawtooth crash where $n_{e,max}/n_{e0} \approx 1.4$. The sawtooth behaviour

is presented in Fig. 7.9 which shows the temporal evolution of the line integrated central soft x-ray emissivity \bar{S}_{X0} , Fig. 7.9(a), together with the line integrated central electron density \bar{n}_{e0} , Fig. 7.9(b), from a microwave interferometer operating at 140 GHz and the central electron temperature T_{e0} , Fig. 7.9(c), from foil-absorption measurements using 150 μm Be and 650 μm Be filters.

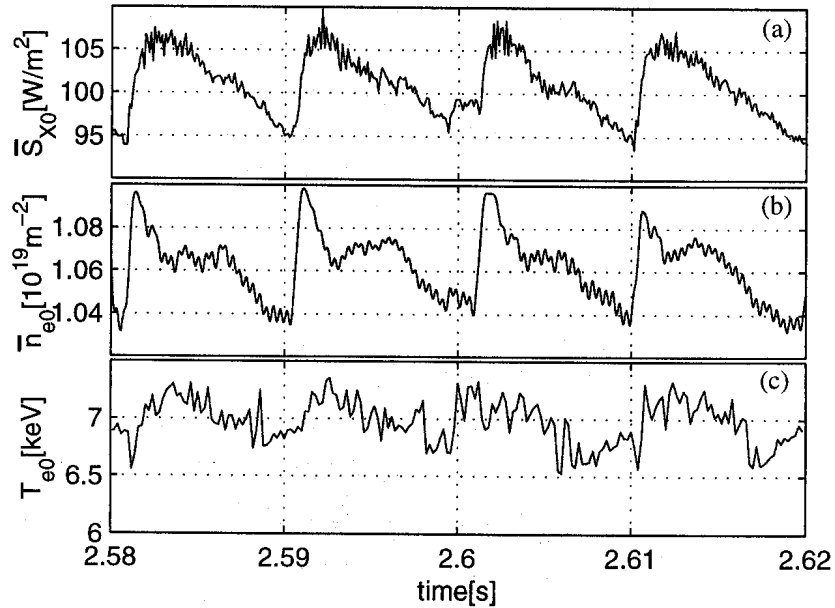


Fig. 7.9 Sawtooth behaviour in TCV discharge No. 18549 where full current replacement with electron cyclotron Co-Current drive was obtained with 2.7 MW of injected power. (a) Central line integrated soft x-ray emissivity. (b) Line integrated central density from a microwave interferometer operating at 140 GHz. (c) Central electron temperature from the foil-absorption system using 150 μm Be + 650 μm Be filters.

The sawtooth period is $\tau_{ST} \approx 12$ ms and the density recovery at the sawtooth crash is such that $\Delta\bar{n}_{e0}/\langle\bar{n}_{e0}\rangle \approx 5.5\%$ resulting in flatter n_e profiles (not shown here) with $n_{e,max}/n_{e0} \approx 1.08$. During a sawtooth cycle, the central electron temperature shows a relative variation $2\Delta T_{e0}/(T_{e0,max} - T_{e0,min}) \approx 10\%$ which is below the estimated error bars obtained from the foil-absorption system at this average temperature. It should be noted that measurements from the Thomson scattering system indicate central electron temperatures of about 5 keV, Fig. 7.7(c). The overestimate of T_{e0} provided by the foil absorption system may be due to an enhancement of the emission by suprathermal electrons. These are observed on TCV with significant toroidal injection angle of the ECCD beam [13] as in the present case. Fortunately, the absolute value of T_{e0} is not

7.3 Discussion and interpretation

crucial for the present discussion.

A reliable tomographic inversion of the line integrated soft x-ray signals was hampered by soft x-ray emission from carbon tiles of the TCV vessel probably due to impacts of suprathermal electrons. Thus, the method for the identification of the MHD activity described in chapter 4 is not applicable in this case. Nevertheless, the presence of a kink distortion of the plasma core is revealed during the inverted sawtooth ramp by the displacement of the electron temperature profile, as shown in Fig. 7.7(c) by two profiles measured at different times during this phase. This kink distortion is probably due to a $m = 1$ mode which results in off-axis oscillations in the soft x-ray emissivity (not shown here) at a frequency of ≈ 3 kHz and which are barely visible on the \bar{S}_{X0} time traces in Fig. 7.9(a). The oscillations on line integrated soft x-ray signals along lines of sight viewing the plasma on different sides of the magnetic axis have opposite phase. This also indicates a $m = 1$ poloidal mode number. Strong oscillations of the line integrated central electron density \bar{n}_{e0} also suggest the presence of a mode during the inverted sawtooth ramp. The frequency of these oscillations is ≈ 3 kHz and the relative amplitude $\Delta\bar{n}_{e0}/\bar{n}_{e0} \approx 4\%$. In Fig. 7.9(b), the relative amplitude of the oscillations is reduced by a factor of 8 because the \bar{n}_{e0} signal was digitally filtered to improve the visibility of the inverted sawtooth ramp.

7.3 Discussion and interpretation

Several explanations for pumpout have been suggested. Pondermotive effects [14] are the least likely, both because the potentials are easily shown to be far smaller than electron temperatures and because the beams are very localised poloidally and toroidally, whilst the phenomenon is observed outside the beam region. In principle the thermal force [15] could transfer parallel momentum to ions in the presence of a parallel electron temperature gradient. Such an explanation might fit into the (controversial) picture of electron diffusion in stochastic magnetic fields, but would not make the economy of considering ion orbits. The first explanation based on particle orbits was proposed by Hsu et al. [16]. According to this theory, the ECH, by increasing the perpendicular energy of electrons of low parallel velocity, causes many of these to become toroidally trapped, leading to the buildup of an excess of banana-electrons and thereby a poloidal charge asymmetry which produces a net electric field oriented in the direction of the major radius (“banana pile-up”). The resulting increased ion vertical drift velocity, by widening ion orbits, would then increase the neoclassical diffusivity and lead to increased particle losses.

The banana pile-up explanation however does not explain why pumpout is observed with heating on the high field side of the magnetic axis, which is the case in most TCV experiments, nor with

large toroidal injection angles as in ECCD experiments, when the power is deposited to electrons with large v_{\parallel} . A model which only predicts increased diffusivities cannot explain the observed gradient reversal. Finally banana pile-up cannot account for the observed importance of MHD modes.

We propose that loss of axisymmetry provides the crucial physics for this phenomenon by allowing the existence of locally trapped particles, which are not confined in the core region. Fig. 7.10 shows a schematic of the magnetic configuration inside the $q = 1$ surface when a magnetic island causes a helical displacement of the magnetic axis by a distance ξ . This displacement is typically of order 10% of the minor radius, as determined from soft x-ray tomography. The magnetic field modulation produced by the displacement inside the $q = 1$ surface is $\Delta B/B \cong \xi/R_0$. Particles with $|v_{\parallel}/v| < \sqrt{2\xi/R_0}$ on the low field side are mirrored back before they can reach the high field side on the same flux surface. They are not confined and can be expected to drift vertically outside of the $q = 1$ volume where they find themselves in an (approximately) axisymmetrical field configuration, from where on their trajectories become 'ordinary' banana orbits. Particle orbits of this kind have been theoretically investigated in relation with the 'snake' phenomenon in JET [17].

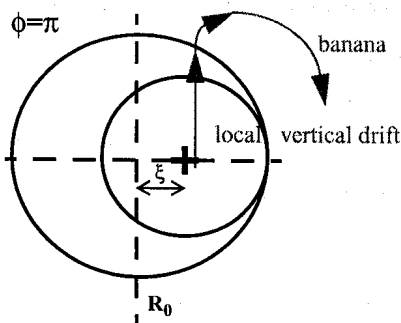


Fig. 7.10 Helically displaced plasma core and locally trapped particle orbit (schematic).

The nature of a configuration can be characterised by the parameter $\alpha = \epsilon B / (\Delta B q n)$, where ϵ is the inverse aspect ratio and n the number of toroidal modulations [18]. For the configuration considered in Fig. 7.10, we have $\alpha \cong \rho / \xi$. It is stellarator-like for $\rho < \xi$ and becomes increasingly like an ideal tokamak when $\rho > \xi$.

In principle both collisions and direct perpendicular energy transfer by ECH can cause electrons to become trapped [19].

Since pumpout occurs even with ECH on the high field side, where trapped electrons cannot be created directly, as is the case in most experiments in TCV, and with ECCD, when the trapped-passing boundary in velocity space is far from the electron cyclotron resonance, we must assume that collisional trapping by pitch angle scattering is the most important of these mechanisms. It cannot be excluded however, from the available experimental evidence, that resonant velocity space diffusion driven by the ECH power may play a contributory role. Trapping as a result of velocity space diffusion may be important when the ECH power is deposited at the low field side. Low field side deposition experiments are still to be carried out in TCV. In combination with pitch angle scattering, ECH driven resonant diffusion may also contribute with high field side ECH deposition by increasing the velocity space density in the trapped-passing

7.3 Discussion and interpretation

boundary region, thereby enhancing the collisional trapping rate beyond that of a purely Maxwellian plasma.

The vicinity of the displaced magnetic axis may act as a sink from where particles which become locally trapped (due to collisional or driven velocity space diffusion) are lost on wide orbits to beyond the non-axisymmetrical region (typically outside the $q = 1$ surface), causing particle depletion in the core. Some of the particles escaping from the core region may subsequently also become trapped in the toroidal field ripple (which increases with distance from the core) and drift out of the plasma altogether.

Since from the arguments above, collisional trapping appears to be the dominant mechanism, we may attempt an interpretation in the frame of neoclassical theory, assuming Maxwellian distribution functions. The coexistence of the two classes of trapped particles (toroidally and locally) can be expected to give rise to competing transport phenomena, which may, at least qualitatively, explain our observations. In neoclassical theory [18], [19] trapped particles give rise to coupled heat and particle transport, of the generic form

$$\Gamma_{e,i} = D_{11}^{e,i} n_{e,i} \left[\left(\frac{n'_{e,i}}{n_{e,i}} + \frac{qZ_{e,i}\Phi'}{T_{e,i}} \right) + d_{12}^{e,i} \frac{T'_{e,i}}{T_{e,i}} \right] \quad (7.1)$$

where d_{12} gives rise to thermodiffusion and primes designate spatial derivatives. A steady state solution is obtained in the usual way by setting the ion flux to zero and inserting the ambipolar potential Φ into the electron equation, with the result

$$\frac{n'_e}{n_e} = -d_{12}^e \left(1 + \frac{d_{12}^i T'_i}{d_{12}^e Z T'_e} \right) / \left(1 + \frac{T_i}{Z T_e} \right) \cdot \frac{T'_e}{T_e} \approx -d_{12}^e \frac{T'_e}{T_e} \quad (7.2)$$

where the last approximation pertains to typical conditions in ECH heated plasmas in TCV, where $T_e \gg T_i$. For fluxes caused by toroidally trapped particles we have $d_{12}^i = -0.5$, corresponding to an inward pinch, while for locally trapped particles $d_{12}^i \approx 1$ in the long mean free path regime and $d_{12}^i = 3.5$ in the $1/\nu$ regime [18], corresponding, for peaked temperature profiles, to an outward flux. In a realistic situation both processes, as well as anomalous transport, must be expected to compete. A competition between outward thermodiffusion and an anomalous inward pinch has been reported from the W7-AS stellarator [4].

Formally, we may write the total flux as a sum $\Gamma = \Gamma^t + \Gamma^l + \Gamma^a$, with $D_{11} = D_{11}^t + D_{11}^l + D_{11}^a$ and the superscript a refers to all fluxes not due to thermodiffusion and to anomalous transport. For simplicity, we may assume that these fluxes have the form of Eq.

Chapter 7. PARTICLE TRANSPORT WITH HIGH POWER CENTRAL ECH AND ECCD

(7.1), with $d_{12}^a = -v_d T_e / (D_{11}^a T_e')$, where v_d is a phenomenological pinch velocity. The resulting off-diagonal term is then

$$d_{12} = (d_{12}^t \cdot D_{11}^t + d_{12}^l \cdot D_{11}^l + d_{12}^a \cdot D_{11}^a) / D_{11} \quad (7.3)$$

(Note that D_{11}^x may depend on electric fields). A reversed density gradient, and hence a hollow density profile, is expected where

$$d_{12}^l \cdot D_{11}^l + d_{12}^t \cdot D_{11}^t - v_d T_e / T_e' > 0 . \quad (7.4)$$

The second and third term in Eq. (7.4) are negative. A gradient reversal region does not exist if the (negative) inward pinch velocity is too high and/or the temperature gradient is too small. This is the usual situation in tokamaks, unless localised core heating, such as obtained with ECH and ECCD, is applied, leading to strong peaking of the electron temperature profiles. In the limit when the third term in Eq. (7.4) can be neglected, we can expect hollow profiles for $D_{11}^l / D_{11}^t > -d_{12}^t / d_{12}^l \approx 0.5$, e.g. sufficiently close to the displaced axis, where locally trapped particles dominate off-diagonal transport, whatever the value of the diffusion coefficient. Low values of particle diffusivities (and inward pinches), as are frequently reported to prevail in the plasma core in the absence of sawteeth, or between consecutive sawtooth crashes [20], will however allow a more pronounced gradient reversal to be established, thereby making the observation of the effect easier.

Fig. 7.11 shows the relations between the temperature and density gradients obtained in a variety of discharges with Co- and Counter-ECCD. Although the results are qualitatively consistent with the existence of neoclassical outward fluxes due to locally trapped particles, the observed density gradients $\langle \nabla n_e \rangle / n_{e0} \approx -0.5 \cdot \langle \nabla T_e \rangle / T_{e0}$, for the cases with the most hollow profiles, are smaller than expected from locally trapped particles alone, Eq. (7.2). From the denominator in Eq. (7.3), we see that the effect of anomalous diffusion, which generally can be expected to dominate, is to erode the strong steady-state gradients predicted by Eq. (7.2), which would be produced by neoclassical effects alone. We also note on Fig. 7.11 that hollow profiles have, at least so far, only been observed for $\langle \nabla T_e \rangle / T_{e0} < 4 m^{-1}$. This is consistent with the existence of an inward pinch v_d , which must be overcome, as expressed in Eq. (7.4), by a sufficiently large temperature gradient before density gradient reversal can occur.

7.3 Discussion and interpretation

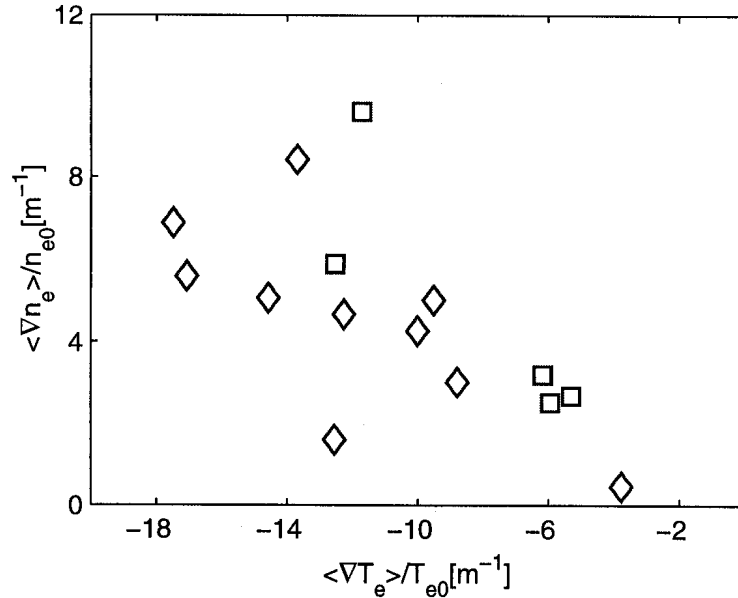


Fig. 7.11 Average electron density versus average T_e gradients over region with hollow n_e profiles. Squares: Co-ECCD. Diamonds: Counter-ECCD.

The observation of ‘normal’ density sawteeth with $m/n = 1/1$ mode in ohmic discharges or for ECH deposition well outside the inversion surface, Fig. 7.2(a,c,e), when temperature gradients are small, indicates the existence of components to the inward pinch which are not due to thermodiffusion. The existence of flat density profiles in the presence of finite temperature gradients in Fig. 7.11 is similarly suggestive. Possible candidates are the Ware and Varma pinches ($v_D \propto E_{||}/B_{pol}$) [21] or coupled anomalous energy and particle transport processes constrained by the (approximate) conservation of the first and second particle adiabatic invariants, which have been proposed to tend to establish density profiles roughly of the form $n_e \propto 1/q$ [22].

The above considerations should be regarded as tentative since it is not clear whether standard neoclassical theory can be applied. Locally trapped particle orbits for instance, even in the presence of orbit squeezing by electric fields, may well be larger than the stellarator-like region near the magnetic axis, as indicated in Fig. 7.10. Clearly future work to test and refine the emerging physical picture of the pumpout phenomenon in tokamaks will require numerical orbit calculations and an improved understanding of neoclassical transport in the particular magnetic configurations which result when MHD instabilities break the symmetries of the ideal tokamak.

Chapter 7. PARTICLE TRANSPORT WITH HIGH POWER CENTRAL ECH AND ECCD

References

- [1]TFR-GROUP, *Nucl. Fusion* **25** (1985) 1011.
- [2]V. Erckmann, et al., *Plasma Phys. Control. Fusion* **36** (1994) 1862.
- [3]H. Renner, et al., *Plasma Phys. Control. Fusion* **31** (1989) 1579.
- [4]U. Stroth, et al., *Phys. Rev. Lett.* **82** (1999) 928.
- [5]C. Angioni, et al., *Proc. Joint Varenna-Lausanne International Workshop on Theory of Fusion Plasmas* (Varenna 2000), page 73.
- [6]D. Boucher, et al., *Proc. IAEA Tech. Com. on Advances in Simulation and Modell. of Thermonuclear Plasmas* (Montreal 1993), page 142.
- [7]F. Porcelli, et al., *Plasma Phys. Control. Fusion* **38** (1996) 2163.
- [8]H. Weisen, et al., including I. Furno, *Nucl. Fusion* **37** (1997) 1741.
- [9]H. Reimerdes, et al., *Plasma Phys. Control. Fusion* **42** (2000) 629.
- [10]O. Sauter, et al., *Fusion Engineering and Design* **53** (2001) 289.
- [11]P. Blanchard, et al., submitted to the *28th EPS Conf. on Controlled Fusion and Plasma Physics* (Portugal 2001).
- [12]O. Sauter, et al., *Phys. Rev. Lett.* **84** (2000) 3322.
- [13]S. Coda, et al., *Proc. 26th EPS Conf. on Controlled Fusion and Plasma Physics* (Maastricht 1999), Vol. 23J, page 1097.
- [14]R. A. Cairns, *Plasma Physics*, Blackie and Son Ltd, Glasgow, 1985.
- [15]S. I. Braginskii, *Review of Plasma Physics* **1**, Ed. M. A Leontovich (1965), page 205.
- [16]J. Y. Hsu, et al., *Phys. Rev. Lett.* **53** (1984) 564.
- [17]S. Putvinskii, *JET report JET-RP(42)* (1992).
- [18]L. M. Kovrizhnykh, *Nucl. Fusion* **24** (1984) 851.
- [19]H. Maassberg, et al., *Phys. Plasmas* **7** (2000) 295.
- [20]R. Dux, et al., *Nuclear Fusion* **39** (1999) 1509, and references therein.
- [21]R. K. Varma, *Plasma Phys. Control. Fusion* **40** (1998) 1999.
- [22]D. R. Baker, et al., *Phys. Plasmas* **5** (1998) 293.

8 SUMMARY

Analysis of sawtooth activity in hot, shaped deuterium plasmas in the TCV tokamak has revealed new features of heat and particle transport which have potentially important effect on the confinement of fusion plasmas and thereby of interest to the community of experimental and theoretical fusion physics. The exceptional shaping capability of TCV has been used to explore a wide range of plasma parameters, including high elongation and high positive and negative triangularity. Similarly, the flexibility of the electron cyclotron heating (ECH) and current drive (ECCD) system on TCV was used to probe the sawtooth behaviour and the plasma response to a localised auxiliary power deposition.

A large part of the work presented in this thesis results from the analysis of a 200 channel soft x-ray tomographic system, for measuring the soft x-ray emission which originates from the central plasma region. Tomographic reconstruction of line integrated measurements from this system provided the poloidal soft x-ray emissivity distribution. The temporal resolution required to resolve the sawtooth crash, which occurs on TCV on a typical timescale of 100 μs , was obtained by installing a transient recorder with minimum sampling period of 13 μs which permits the study of fast transport phenomena and magnetohydrodynamic (MHD) activity hitherto inaccessible on TCV. Singular value decomposition of the tomographically inverted soft x-ray emissivity has proven to be an efficient technique for extracting the poloidal mode structure of MHD perturbations, the associated displacement of the soft x-ray emissivity hot core and the sawtooth inversion surface. Soft x-ray tomography was complemented by magnetic Mirnov coils and a toroidal array of four silicon photodiodes for mode identification. The TCV Thomson scattering system was augmented by a foil absorption system and by a 14 chord far infrared interferometer which provide respectively electron temperature and density measurements. To obtain the local electron density from interferometer data, a modified Abel inversion method was developed which is based on a base function expansion in magnetic flux coordinates provided by the TCV magnetic equilibrium reconstruction code (LIUQE).

A fast bolometric system was also developed in the course of this thesis, for monitoring the total radiated power during fast transport events, like sawteeth, ELMs and impurity injection, which are not accessible to standard, slow reaction metal foil bolometers. The comparison of these two systems showed that low-energy neutral fluxes can be a significant contribution to foil bolometer measurements under certain operating conditions such as in high recycling discharges. This result

cautions against the use of tomographic inversion techniques for reconstruction of the radiation distribution using metal foil bolometers as is the case in many magnetic fusion experiments. For the future, a fast bolometric system consisting of up to seven pinhole cameras is under consideration. This system is being designed to allow fast time scale tomographic reconstruction of the total radiated distribution in a poloidal plane of TCV.

In the present study, the effect of sawtooth activity on profile shape has been investigated in a wide variety of ohmic L-mode discharges including plasma configurations with elongation up to 2.6 and triangularities in the range -0.5 to $+0.7$. Our observations show that, independently of plasma shape and electron density, the normalised sawtooth inversion radius ρ_{inv} , as obtained from soft x-ray tomography, and the profile inverse peaking factors $\langle p_e \rangle / p_{e0}$, $\langle T_e \rangle / T_{e0}$ and $\langle n_e \rangle / n_{e0}$ for electron pressure, temperature and density, depend solely on the current profile peaking via the parameter $\langle j \rangle / (q_0 j_0)$, where the parenthesis indicate volume averages. This scaling parameter can be evaluated without knowledge of the central current density j_0 and safety factor q_0 , which are still under debate, since $j_0 q_0 = B_0 (\kappa_0 + 1/\kappa_0) / (\mu_0 R_0)$, where κ_0 is the elongation on the magnetic axis. These new findings extend previous scaling of ρ_{inv} with the inverse of the edge safety factor, obtained for plasmas with circular poloidal cross sections, and appear to be largely a consequence of profile flattening following sawtooth crashes. These limit the core peaking of the current and the pressure and/or temperature profiles when the sawtooth period is shorter than both the resistive skin time and the energy confinement time. Although sawtooth activity cannot account for profile features outside the sawtooth inversion radius, profile shapes in the confinement region also show a good correlation with the parameter $\langle j \rangle / (q_0 j_0)$.

Previous experimental observations in TCV, supported by internal kink stability calculations, show that sawtooth periods and amplitudes decrease at high elongation for constant $\langle j \rangle / (q_0 j_0)$ both in ohmic and ECH discharges. These results together with the scaling of the normalised inversion radius, obtained in this thesis, show that the frequently expressed fear of excessively large inversion radii and sawtooth amplitude at high plasma elongation, which may trigger neoclassical tearing modes, are ill founded. The plasma elongation can be scaled up while keeping fixed the normalised sawtooth inversion radius with only a modest penalty in plasma current as compared to scaling at fixed q_{95} . Thus, most of the current carrying capacity resulting from high elongation is retained, even when optimising a design with the constraint of a fixed normalised inversion radius.

Electron cyclotron heating and current drive are at the origin of unexpected transport phenomena which are potentially important in the issue of confinement of fusion plasmas. In several past and present tokamak experiments, ECH often results in a reduction in the energy and particle

confinement. In TCV, the use of ECH and ECCD results also in different types of sawteeth depending on the power deposition location. Standard sawteeth, i.e. triangular sawteeth similar to ohmic sawteeth, and saturated sawteeth are observed with central ECH power deposition, while giant sawteeth and ‘humpback’ oscillations occur when heating close to the sawtooth inversion surface of the local soft x-ray emissivity.

In the frame of this thesis, measurements with high temporal resolution have shown that heat transport during sawteeth is compatible with a strong localisation of the heating region, as achieved with ECH, and with the advection and mixing of electron thermal energy associated with a resistive internal kink mode. This mode produces precursor oscillations which have been identified to have $n = 1$ and dominant $m = 1$ mode numbers for all sawtooth types. The detailed dynamics of the magnetic island, associated with the resistive internal kink mode, have been described by a displacement function $\xi(t)$ which is inferred from the experimental data. In normal sawteeth, the kink mode is destabilised just before the crash, while in all other sawtooth types a magnetic island exists for a significant fraction of the sawtooth period.

Previous types of sawteeth have been simulated using the numerical code M1TEV based on a theoretical model which describes the evolution of the electron temperature in the presence of localised heat sources and of an $m/n = 1$ magnetic island whose temporal evolution is inferred from the experimental displacement function $\xi(t)$. Despite the relative simplicity of this model, the simulated electron temperature behaviour under the different heating conditions is in agreement with the experimental observations. Nevertheless, an accurate description of these sawtooth types has to account for the evolution of the current profile and the particle transport which were neglected in our simulations. The latter is crucial to understanding the difference in the experimental electron density behaviour between giant and humpback sawteeth which we attributed to particle pumpout.

Particle pumpout is observed in several tokamak and stellarator experiments which employ electron cyclotron resonance heating and current drive. This phenomenon results in a depletion of particles from the plasma centre, causing inverted sawteeth on the central density in sawtoothed discharges and leading to hollow density profiles in the absence of sawteeth. In stellarators, the pumpout is qualitatively explained by neoclassical transport processes arising from the presence of locally trapped particles. This explanation cannot account for the particle pumpout observed in axisymmetrical tokamaks since, in this case, there are no locally trapped particles.

Present experimental observations from TCV suggest that the pumpout from the central region of tokamaks is qualitatively consistent with neoclassical thermodiffusion in the presence of locally

trapped particles, as in stellarators. Whereas in stellarators the field modulation is a built-in feature of the magnetic configuration, in tokamaks it can result from MHD perturbations caused by instabilities affecting the plasma core, especially inside the $q = 1$ surface. The presence of an $m/n = 1/1$ island causes the plasma core to become helically displaced permitting trapped particles even on the magnetic axis. The coexistence of locally trapped particles and toroidally trapped particles within the $q = 1$ surface can be expected to give rise to competing transport phenomena, including pumpout, since the off-diagonal terms associated with these two classes of particles are of opposite sign. The experimental relation between temperature and density gradients is qualitatively consistent with the existence of neoclassical outward fluxes due to locally trapped although the observed density gradients are smaller than expected from locally trapped particles alone. This may be accounted for by the effect of anomalous diffusion which generally is expected to dominate and the existence of an inward pinch which is not due to thermodiffusion. However, from the available experimental evidence, resonant velocity space diffusion, driven by the ECH power, could also play a contributory role. Trapping and ensuing orbit losses resulting from velocity space diffusion may be important when the ECH power is deposited on the low field side. In the future, this could be tested in low field side power deposition experiments in TCV.

Further work to test and refine the emerging physical picture of pumpout phenomena in tokamaks will require numerical orbit calculations and an improved understanding of neoclassical transport in the particular magnetic configurations which arise when MHD instabilities break the symmetries of the ideal tokamak. Recently, the MITEV code has been upgraded to include the evolution of the electron density in the presence of a magnetic island. This will be used to simulate inverted sawteeth in TCV by modelling particle fluxes as a combination of diffusive and convective components, including a thermodiffusion term that changes sign near the magnetic axis.

Energy and particle transport during sawtooth activity in TCV plasmas has been studied in this thesis with high temporal resolution many chord diagnostics. We indicated the influence of sawteeth on plasma profiles in ohmic conditions and in the presence of auxiliary electron cyclotron resonance heating and current drive. A 2-dimensional model for heat transport, including localised heat source and a magnetic island, has been used to interpret the experimental observations. These results provided a new interpretation of a coupled heat and transport phenomenon which is potentially important for plasma confinement.

The observations validate the applicability and show the possibility of improvement of a 2-dimensional theoretical model for the study of heat transport in the presence of localised heat source and a magnetic island. Furthermore, the TCV results showed new possibility for the

interpretation of a coupled heat and particle transport phenomenon previously understood only in stellarators.

Acknowledgements

I am grateful to Prof. F. Troyon who, as Director of the CRPP, provided me with the opportunity to start a Ph.D. in Lausanne, and to Prof. M.Q. Tran who, as his successor, continued to give me the same precious support.

I thank sincerely Dr. H. Weisen who supervised my work despite his other numerous activities and who encouraged and helped me constantly during this work. His approach to physics, combining experimental and theoretical points of view, will serve as an example to me.

I am indebted to Dr. M. Anton who left me in "heritage" the soft x-ray tomographic system and who initiated me to tomographic inversion techniques.

A special thank goes to Drs. X. Llobet and B.P. Duval for their help during the installation of the T-REX3 acquisition system. I also acknowledge the friendship of Basil Duval who has always been available not only as a patient linguistic corrector of my manuscript but also for discussions in more than just professional matters. Along with them, I thank Dr. R.A. Pitts for his help in the installation of the divertor bolometric camera and in the interpretation of the fast bolometric measurements.

During this work, I have closely collaborated with Prof. F. Porcelli to whom I am particularly obliged for the support he gave me in the interpretation of sawtooth activity in the presence of ECH. My gratitude also goes to C. Angioni and E. Rossi who carried out the simulations using the code MITEV and with whom I had many fruitful discussions.

I have also benefited from discussions with Drs. R. Behn, S. Coda, T.P. Goodman, M.A. Henderson, F. Hofmann, J.M. Moret, Z.A. Pietrzyk and A. Pochelon which I kindly acknowledge.

It would not have been possible to accomplish this work without the competent and efficient support of the CRPP technical staff. My gratitude goes to G. Pochon for designing the bolometric system, to the whole mechanical workshop for its realisation, to E. Bader for assembling and testing its pinhole cameras and to P. Conti and M. Ries for installing them on TCV. A special thank goes to A. Centra and C. Raggi for their availability and readiness to help me whenever solicited. I would like to extend these acknowledgements to P. Marmillod and B. Marletaz for designing the electronics and for their constant assistance with the electronics through the years.

For running the TCV tokamak, heating the plasma as well as diagnosing it I sincerely acknowledge the whole TCV team and especially all the Ph.D students with whom I shared the hard task of "diagnosticien du jour".

A big thank goes to the CRPP secretaries (Edith Grueter, Paula Halter, Raymonde Vincent and Elizabeth Braham) whose efficiency and kindness have always been appreciated.

My officemate Holger Reimerdes deserves a particular “danke” not only for the numerous discussions about the meaning of life during the last five years but also for admitting, after the completion of his Thesis, the excellence of Italian cuisine.

Among all the people who made my time in Lausanne most enjoyable, I want to thank Eddy Scavino for his sincere friendship. A big thank also goes to all my dance partners with whom I shared so many “salsas”.

Thanks to Scintilla for her sweetness and patience.

A particular regard goes to my parents Bianca and Tone to whom I dedicate this Thesis.

Curriculum vitae

I was born on the 12th of July 1969, in Ivrea, Italy. I attended primary school in Bairo and secondary school in Rivarolo Canavese where I obtained the Maturità Scientifica from the Liceo "Aldo Moro" in 1988. In the same year, I commenced studies in Nuclear Engineering at the Politecnico di Torino. During the last academic year in 1994, I was given the possibility to carry out my diploma work at the Joint European Torus (JET) in Abingdon (UK) where I spent four months as a student fellow, modelling the slowing down of high energy ions in tokamaks. In February 1995, I received my degree as a "Dottore in Ingegneria Nucleare" from the Politecnico di Torino. Since June 1996, I have been pursuing doctoral research at the Centre de Recherches en Physique des Plasmas in Lausanne. The subject of my research has been fast transient transport events measured by soft x-ray emission in TCV tokamak plasmas.

